



THE UNIVERSITY  
*of* ADELAIDE

Harnessing Hydrokinetic Energy from  
Vortex-Induced Vibration (VIV)

By

**Javad Farrokhi Derakhshandeh**

School of Mechanical Engineering

Faculty of Engineering, Computer and Mathematical

Sciences

This thesis is submitted for the degree of

Doctor of Philosophy

March 2015



*Dedicated to my parents, to my wife Sahar and  
to my son Farbod for their love, support and inspiration*



## Summary

In this dissertation, the application of Vortex-Induced Vibration (VIV) and Wake-Induced Vibration (WIV) of a bluff body for harnessing the kinetic energy of a fluid flow is presented. The application of induced vibration due to vortices in harnessing hydrokinetic energy of the fluid is relatively immature and this research work, which is written as a compilation of journal articles, attempts to address major scientific and technological gaps in this field. The project spans both VIV and WIV, with a particular attention to the development of a better understanding of the wake behaviour in a tandem configuration and the effect of boundary layers for harnessing the kinetic energy of the flow. Accordingly, two separate coupled test cases of tandem bodies comprising Coupled Circular-Cylinder (CCC) and Coupled Cylinder-Airfoil (CCA) configurations were proposed and investigated.

In the first series of tests on the CCC, two circular cylinders were employed to investigate the unsteady wake interactions on the energy yield. The upstream cylinder was fixed, while the downstream one was mounted on a virtual elastic base with one degree of freedom. The virtual elastic system consisted of a motor and a controller, a belt-pulley transmission and a carriage. In the CCC, the influence of the Reynolds number, gap between cylinders and boundary layers on the dynamic response of the downstream cylinder were numerically and experimentally investigated. In a numerical analyse of the system, a dynamic mesh technique within the ANSYS Fluent package was utilized to simulate the dynamic response of the cylinder. The experimental tests confirmed the numerical outcomes and demonstrated that in the WIV mechanisms, a positive kinetic energy transfer from fluid flow to the cylinder was achieved. It is also observed that the dynamic response of the cylinder under the WIV mechanism differs from the dynamic response of VIV. In addition, both numerical and experimental results indicated that a staggered arrangement with  $3.5 \leq x_0/D \leq 4.5$  and  $1 \leq y_0/D \leq 2$  (here,  $D$  is the diameter of the cylinder, and  $x_0$  and  $y_0$  are the

horizontal and vertical offsets, respectively) is the optimum arrangement among all test cases to harness the energy of vortices, resulting in a power coefficient of 28%. This was achieved due to the favourable phase lag between the velocity of the cylinder and force imposed by the fluid. The results revealed that for the staggered arrangement of the cylinders, the WIV responses can occur at frequencies outside the range in which VIV is observed.

In the second series of tests utilizing a CCA, the downstream circular cylinder was replaced by a symmetric airfoil with two degrees of freedom; heave and pitch. The heave degree of freedom employed the same virtual elastic base used for the CCC experiments. The pitch angle of the foil was actively controlled, as opposed to using passive mechanical impedance, since this enables full control over the foil behaviour, thereby facilitating the adjustment of the angle of attack accurately and rapidly. The results of CCA show that both longitudinal and lateral distances play an important role in the Strouhal number, power density and, consequently, the heave response of the airfoil. In addition, it was shown that the circulation of the vortices was influenced by the gap spacing between the cylinder and the airfoil. Furthermore, it was found that an optimum angle of attack of  $\alpha = 10^\circ$  is the most efficient for harnessing the energy of vortices with a maximum power coefficient of 30% for cases with  $3.5 \leq x_0/D \leq 4.5$  and  $1 \leq y_0/D \leq 1.5$  arrangements. Such a range is narrower laterally when compared with the optimum arrangement of the CCC. This work provided the foundation for further work to utilize the potential of this technology and further explore the opportunity to harness the vortical power in shallow water and ocean currents.

# Acknowledgement

First and foremost, I would like to thank **God** almighty, the creator and the guardian, and to whom I owe my existence. **God** has given me the power to believe in myself and pursue my dreams. I could never have written this dissertation without the faith; I have in you.

Apart from my efforts, the success of any project depends mostly on the encouragement and guidelines of many individuals. I take this opportunity to express my sincere gratitude to the people who have been instrumental in the progress of this research.

I would like to show my greatest appreciation to my advisers, **Dr Maziar Arjomandi**, **Professor Benjamin Cazzolato** and **Professor Bassam Dally** for supervising my research using both their knowledge and experience.

I thank **Maziar** for his support and guidelines through my studies. I have been extremely lucky to have a supervisor, who patiently listened to my personal problems during my studies. I am using this opportunity to express my gratitude to Maziar and **Niloufar**, his wife, who offered us the warmest welcome in Adelaide.

I would also like to express my sincere gratitude to **Benjamin** for his brilliant ideas on scientific issues in particular his suggestions regarding the experimental rig and instrumentations. Special thanks for his detailed comments, and important contribution, particularly for the improvement of the publication quality. His feedback helped me improve my writing substantially.

I am highly indebted to **Bassam** for his support and valuable assistance. There is no doubt that this progress would have not been possible without his kind support, attention and encouragement. His advice on both research and on my career have been priceless and it is impossible for me to show my sincere gratitude in few sentences.

I am thankful to my friends **Vahid Alamshah**, **Mohsen Bazghaleh** and **Zahra Bagheri** for their valuable assistance and help. I also wish to thank the many workshop staff members, at the school of the Mechanical Engineering, who manufactured and provided the equipment for my test rig.

I am particularly thankful for the support of **my family**. A special thank goes to my parents, **Fatemeh** and **Naser** and my parents-in-law, **Nooshin** and **Jalal** for giving me their deep love, encouragement and support during my studies.

I am also grateful to my elder sister, **Nasrin** and my brother-in-law, **Arsam** for their guidance and advice. Although Arsam passed away in the middle of my research, his technical and personal skills gave me a great deal of confidence and motivation to carry out my work and study. "*God bless his sole*".

I am most grateful to **Sahar**, my wife, who put up with me through the difficult and challenging journey especially her dedication to our son and for being a kind wife to me. She was always cheering me up and stood by me through the good times and bad times.

I also would like to thank **Farbod**, my son, who had no choice but to join me sometimes when I was studying in my office. He was giving me unlimited happiness and pleasure and relieved all the tiredness and stress with his paintings on my draft.



## **Declaration by Author**

I certify that this work contains no material which has been accepted for the award of any other degree or diploma in my name, in any university or other tertiary institution and, to the best of my knowledge and belief, contains no material previously published or written by another person, except where due reference has been made in the text. In addition, I certify that no part of this work will, in the future, be used in a submission in my name, for any other degree or diploma in any university or other tertiary institution without the prior approval of the University of Adelaide and where applicable, any partner institution responsible for the joint-award of this degree.

I give consent to this copy of my thesis when deposited in the University Library, being made available for loan and photocopying, subject to the provisions of the Copyright Act 1968.

The author acknowledges that copyright of published works contained within this thesis resides with the copyright holder(s) of those works.

I also give permission for the digital version of my thesis to be made available on the web, via the University's digital research repository, the Library Search and also through web search engines, unless permission has been granted by the University to restrict access for a period of time.

*Javad Farrokhi Derakhshandeh*

*Date*

---

---

# Table of Contents

Summary.....	v
Acknowledgement.....	vii
Declaration by Author.....	ix
Chapter 1 .....	1
Background and introduction .....	1
1.1. Motivation .....	1
1.2. Objectives of the Research .....	6
1.4. Thesis structure.....	7
1.5. Publications.....	8
1.6. Thesis format .....	9
Chapter 2 .....	13
Literature review .....	13
2.1. VIV of a circular cylinder .....	15
2.2. Vortex structure in the wake of a cylinder .....	24
2.3. The effects of surface roughness .....	27
2.4. Mass damping ratio and VIV .....	30
2.5. Reynolds number and VIV.....	31
2.6. Effects of walls .....	33
2.7. Non-circular cylinders .....	37
2.8. Power efficiency of a cylinder and an airfoil.....	39
2.9. A pair of circular cylinders.....	40
2.10. Classification of wake interference.....	41
2.11. Wake-Induced Vibration (WIV) .....	46
2.12. Summary .....	50
Chapter 3 .....	65
Harnessing hydropower energy using a circular cylinder.....	65
3.1. Chapter overview.....	65
3.2. Manuscript.....	68
Chapter 4 .....	103
Harnessing hydro power using wake energy.....	103
4.1. Chapter overview.....	103

4.2. Article .....	108
4.3. Manuscript .....	121
Chapter 5 .....	159
Effect of a rigid wall .....	159
5.1. Chapter overview .....	159
5.2. Article .....	161
Chapter 6 .....	179
Effect of Airfoil .....	179
6.1. Chapter overview .....	179
6.2. Manuscript .....	181
Chapter 7 .....	218
Conclusions and future work .....	218
7.1. Conclusions .....	218
7.1.1. Study of power coefficient of a cylinder .....	219
7.1.2. Effect of staggered arrangement on the power coefficient .....	220
7.1.3. Effect of a rigid wall on the power coefficient .....	221
7.1.4. Effect of flutter on energy extraction .....	222
7.2. Future work .....	223
7.2.1. Effect of the location of the pitching axis .....	223
7.2.2. Effect of passive control on the downstream airfoil .....	224
7.2.3. Effect of mass and damping ratios .....	224
7.2.4. Effect of upstream cylinder .....	225
Appendix A .....	227
Conference Papers: .....	227
Article (18 <sup>th</sup> AFMC) .....	230
Article (19 <sup>th</sup> AFMC) .....	234
Appendix B .....	239
Experimental Setup and Apparatus .....	239

# Nomenclature

<b>Symbol</b>	<b>Definition and Unit</b>
<i>Latin Alphabet</i>	
$c$	<i>Damping coefficient (N.s/m)</i>
$C_D$	<i>Drag coefficient</i>
$\bar{C}_x$	<i>Mean drag coefficient</i>
$C_L$	<i>Lift coefficient</i>
$\bar{C}_y$	<i>Mean lift coefficient</i>
$D$	<i>Diameter (m)</i>
$F$	<i>Force (N)</i>
$f$	<i>Natural frequency (Hz)</i>
$f_s$	<i>Vortices frequency (Hz)</i>
$f_n$	<i>Natural frequency in water</i>
$I_\alpha$	<i>Mass moment (kg. m<sup>2</sup>)</i>
$k$	<i>Spring stiffness (N/m)</i>
$k_\alpha$	<i>Spring stiffness (N.m/rad)</i>
$k_e$	<i>Kinetic energy (Joule)</i>
$k_y$	<i>Spring stiffness (N/m)</i>
$L$	<i>Lift force (N)</i>
$M$	<i>Mass (kg)</i>
$M$	<i>Moment (N.m)</i>
$m^*$	<i>Mass ratio</i>
$m_a$	<i>Inviscid added mass (kg)</i>
$m_d$	<i>Mass of displaced fluid (kg)</i>
$m_{osc}$	<i>Oscillating system mass (kg)</i>
$P$	<i>Power (W)</i>
$Re$	<i>Reynolds number</i>
$S$	<i>Gap size (m)</i>
$St$	<i>Strouhal number</i>
$S_\alpha$	<i>Static moment (kg.m)</i>
$t$	<i>Time (s)</i>
$T$	<i>Torque (N.m)</i>
$T_{cyl}$	<i>Time (s)</i>
$U$	<i>Velocity (m/s)</i>
$U_r$	<i>Reduced velocity</i>
$W$	<i>Work (J)</i>
$x_0$	<i>Wake distance between cylinders (m)</i>
$y_0$	<i>Lateral distance between centre of cylinders (m)</i>

$y$  Cylinder displacement (m)

**Greek Alphabet**

$\alpha$  Angle of attack (rad)  
 $\theta$  Angle of rotation (rad)  
 $\delta$  Differential  
 $\eta$  Efficiency  
 $\Phi$  Phase difference between the fluid force and displacement (rad)  
 $\mu$  Dynamic fluid viscosity (Pa s)  
 $\nu$  Kinematic fluid viscosity (m<sup>2</sup>/s)  
 $\rho$  Density (kg/m<sup>3</sup>)  
 $\zeta$  Damping factor

**Acronym**

DOF Degree Of Freedom  
CFD Computational Fluid Dynamics  
FIV Flow Induced Vibration  
FSI Fluid Structure Interaction  
PSD Power Spectral Density  
SAS Scale Adaptive Simulation  
SST Shear Stress Transport  
UDF User Define Function  
VIV Vortex-Induced Vibration  
WIV Wake-Induced Vibration



# Chapter 1

## Background and introduction

### 1.1. Motivation

Fossil fuels supply the majority of the world energy production these days. This finite resource is likely to be continued to be used in the near future until alternative sustainable and affordable alternatives are found. At the same time, the population of the world is growing with the rate of 2.2% annually and is expected to increase to 9 billion by 2050 (Trevor 2013). It has been predicted that the growth rate in energy consumption over the next 20 years is approximately 5%. The reason is largely related to the increase in electricity demand by developing countries (Trevor 2013). Therefore, it is predicted that the production of electricity will increase from 20 petawatt hours in 2010 to 31.2 petawatt hours in 2030. It is argued that electricity production using fossil fuel is not only responsible for producing significant carbon dioxide emissions but also producing various harmful gases (CO, NO, SO and CH), as well as soot and ash. These products are released into the environment and cause environmental effects.

It has been reported that due to the environmental pollution, the total harmful effects of only air pollution on human beings health cost was \$147.4 billion in 1985 (Barbir *et al.* 1990). Therefore, it is necessary to seek alternative zero-emission sources of energy to replace conventional sources

delivered primarily from fossil fuels. Renewable energy technologies can meet much of the growing demand on one hand and reduce the environmental effects compared to fossil fuels. It is estimated that by 2050, renewable energy sources could count for three-fifths of the electricity (Johansson *et al.* 1993). This growth is also confirmed by the Energy Information Administration (2014), which anticipates that by 2025 total renewable generating capacity will grow by 25% from 2012 to 2025 (from approximately 150 gigawatts to 200 gigawatts). Here, the main renewable energy sources are categorised into solar, wind, hydropower, and biomass and geothermal. Among these, wind and hydropower are expected to remain the primary sources of renewable capacities. The proportion of wind, hydropower and solar are expected to be approximately 75 gigawatts, 75 gigawatts and 25 gigawatts, respectively. Biomass and geothermal are expected to cover the rest of production with 25 gigawatts. While wind and solar energy will continue to be main sources along with hydropower sources, the two former technologies vary in accessibility and quality because of the limitation of installation (Energy Information Administration 2014).

Hydro energy is easily accessible and abundant, making this the choice for clean energy production (Güney and Kaygusuz 2010). Considering that almost two third of the earth's surface is covered with water and the majority of the world's population live close to water resources, harnessing hydropower energy represent a substantial source of renewable energy for the future. Conventionally, energy extraction from water currents is achieved employing rotating blades commonly referred to as turbine systems (Khan *et al.* 2009). Recently a great deal of attention has been devoted to research in the field of energy production utilising Vortex-Induced Vibration (VIV), which is primarily a non-turbine system (Khan *et*

---



*al.* 2009). In this process, the VIV phenomenon is used to capture and convert the hydrokinetic energy of the fluid to electrical energy (Bernitsas *et al.* 2004, Lee *et al.* 2011). The vibration induced by the vortices is a result of the interaction of fluid forces and elastic forces in the structures due to synchronisation between the frequency of the generated vortices and the natural frequency of the structure (Blevins 1990).

One of the biggest advantages of the VIV converters is its scalability and flexibility. It was reported that a VIV converter can be scaled between microwatt and megawatt sizes based on the dimensions of the cylinders, the number of the cylinders and the flow speed (Bernitsas *et al.* 2004, 2008 and 2009). The flexibility of the converter is one of the biggest advantages of the system, which makes this new technique more attractive. In addition, it was shown that this converter has high efficiency (approximately 30%) and can operate at low free stream velocities (Bernitsas *et al.* 2008), where other turbine systems such as watermills cannot be employed effectively.

A comparison between the volume densities of the VIV convertor with wave convertors can provide further insight into the potential of the VIV convertor. The volume energy density, here, is calculated as the ratio of actual energy production to the occupied physical volume of the cylinder. In this comparison, the volume energy density of the VIV energy convertor has been compared with three types of wave energy convertor such as oscillating water column systems (e.g. Pelamis, the Opt Power Buoy and Energetech). For instance, Pelamis is a floating ocean wave convertor; Opt Power Buoy is another floating wave convertor, which is moored to the sea bed and the Energetech is located on the sea bed or moored at a low depth. As a view point of volume energy density it has been shown that VIV convertor is comparable with other wave converters (Bernitsas *et al.* 2008). From Figure 1.1 it is clear that the volume energy density of VIV is higher

than three wave convertors giving a value of  $0.33 \text{ kW/m}^3$  (Bernitsas *et al.* 2008). Furthermore, among different hydropower sources of energy, it has been shown that a VIV converter has more advantages than other alternative sources in terms of production cost and volumetric power density (Bernitsas and Raghavan 2004, Bernitsas *et al.* 2008). It has been estimated that the energy extracted from VIV costs USD  $\sim$  \$0.055 per kilowatt hour, which is comparable with wind and solar energy costs, which are estimated at \$0.07 per kilowatt hour and \$0.16 per kilowatt hour, respectively (Bernitsas *et al.* 2008).

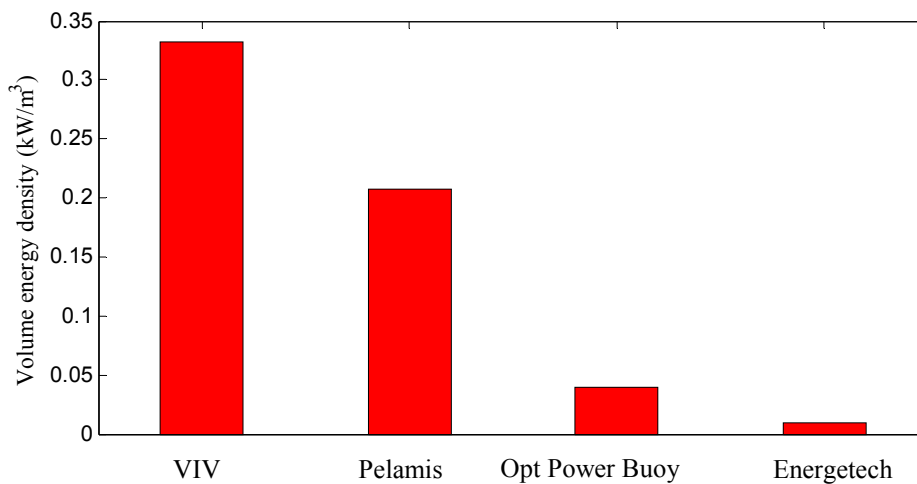


Figure 1.1: Comparison of volume energy density of VIV with three types of wave convertors (reproduced from Bernitsas *et al.* 2008).

The complexity of the VIV of bluff bodies increases considerably by having two cylinders arranged in tandem. The resultant interaction leads to what is known as Wake-Induced Vibration (WIV). For a tandem arrangement of the cylinders, the spacing gap between the cylinders changes the dynamic response of the elastically mounted cylinder. The WIV of two circular cylinders was thoroughly studied by Assi *et al.* (2006), Assi (2009), and Assi *et al.* (2010). Despite the numerous numerical and experimental studies of VIV (Bearman 1984, Khalak and Williamson 1996, Govardhan and Williamson 2000, Govardhan and Williamson 2004, Jauvtis, and

Williamson 2004) and WIV (Assi *et al.* 2006, Assi 2009) of an elastically mounted circular cylinder, the resulting power of the cylinder has drawn less attention in the literature. Under the WIV mechanism, the second bluff body is affected by both its own vortices and upstream vortices. Under these conditions, no comparison has been conducted between the power coefficients of a single cylinder under VIV mechanism and a pair of circular cylinders under WIV phenomenon with a view to harness the kinetic energy of the vortices. The power coefficient, here, is defined as VIV power divided by fluid power.

It is worth noting that using the VIV mechanism as a source of energy has its own limitations. One of the disadvantages of a VIV converter is that the maximum amplitude of oscillation of the cylinder occurs in a narrow range of free stream velocities, in which the vortex shedding frequency is matched to the frequency of oscillation of the cylinder. Despite this constraint, employing a new technology to harness the abundant clean energy from currents and oceans with high density, sensible efficiency and long period life is always desirable. On the other hand, to the knowledge of the author, no study has been conducted to employ the WIV mechanism to generate power.

This project aims to employ both VIV and WIV mechanisms to harness the energy of a fluid flow in a turbulence flow regime for Reynolds numbers up to 15,000. This flow regime has been selected as it can cover most of available free stream velocities in the nature (Bernitsas *et al.* 2008).

In the WIV mechanism, the downstream cylinder is under the influence of two types of vortices; first it is subjected to oncoming vortices due to the separation from the upstream cylinder as well as being affected by its own vortices. This combination of vortices makes the WIV mechanism different from VIV and the frequency of the oscillation of the downstream cylinder is

---

not limited to the lock-in or resonance frequency. In WIV the arrangement of cylinders is important and it is examined to identify the optimum arrangement of the cylinder with maximum power coefficient. Thus, the primary motivation of this project is the increase of the power coefficient of the converter, focusing on fluidic and structural parameters of the VIV and WIV mechanisms. In addition, in order to understand the dynamic response of a non-circular cylinder under the effect of oncoming vortices, an airfoil was employed in the wake of the circular cylinder. In this case, it is intended to find the optimum arrangement and the angle of attack of the airfoil to capture the maximum energy of the vortices.

### **1.2. Objectives of the Research**

The project aim is to investigate the parameters and mechanisms that maximise the power generation from a WIV of two bluff body structures in tandem under different flow regimes. To achieve the main aim of the thesis, the following objectives have been set:

- Study and compare the dynamic response of an elastically mounted circular cylinder under two different mechanisms, namely; VIV and WIV and to compare the power coefficient of each one;
- Study the flow and resulting forces over an elastically mounted circular cylinder with one degree of freedom and investigate the dynamic response of the cylinder;
- Understand the flow characteristics around a pair of circular cylinders with different arrangements in a turbulent flow regime to determine the maximum amplitude of oscillation of the downstream cylinder and to evaluate the theoretical power coefficient of the WIV convertor;

- Examine the dynamic response of a circular cylinder with 1 DOF, which is elastically mounted in the wake of the upstream cylinder in order to measure the displacement of the cylinder and to calculate the optimum power coefficient of the WIV mechanism as well as the power content of the convertor;
- Investigate the effect of non-circular cylinder with 2 DOF to estimate the dynamic response of the structure and study the effect of angle of attack in the wake of the cylinder.

### 1.4. Thesis structure

This thesis is divided into seven chapters, including this introduction chapter. Chapter 2 provides detailed background literature, with Chapters 3 to 6 containing copies of manuscripts that have or being published from this work. Chapter 7 contains summary, conclusions and future work. Specifically:

- **Chapter 1** contains the **background and introduction**. It presents a brief overview of the flow induced structure vibrating of bluff bodies and presents the aim and objectives of this work.
- **Chapter 2** presents a comprehensive **literature review** of the topic highlighting the knowledge gap.
- **Chapter 3** describes the dynamic response of an elastically mounted circular cylinder, validates the use of a Scale Adaptive Simulation (SAS) turbulence model for VIV phenomenon, (submitted paper).
- **Chapter 4** presents the numerical and experimental analysis, which investigates the effect of arrangement of two circular cylinders in capturing vortex energy (includes two papers).

- **Chapter 5** focuses on numerical modelling and reports a study of the effect of boundary layer on the vortex structure and maximum captured energy, extracted by the downstream cylinder (Derakhshandeh *et al.* 2014-b).
- **Chapter 6** is combination of the numerical and experimental analysis, investigating the dynamic response of an elastically mounted airfoil in the wake of the fixed cylinder (submitted paper).
- **Chapter 7** is the final chapter, which summarises the findings of the thesis and describes the conclusions and recommendations for future work.

### 1.5. Publications

Publications arising from this thesis:

#### Journal papers

- [1] **Derakhshandeh, J. F.**, Arjomandi, M., Dally, B., Cazzolato, B., A study of the Vortex-Induced Vibration mechanism for harnessing hydrokinetic energy of eddies using a single cylinder, *Journal of Applied Mathematical Modelling*, under review, 2014.
- [2] **Derakhshandeh, J. F.**, Arjomandi, M., Dally, B., Cazzolato, B., Harnessing hydro-kinetic energy from wake induced vibration using virtual mass spring damper system, *Journal of Ocean Engineering*, No: OE-D-14-00232, 2014.
- [3] **Derakhshandeh, J. F.**, Arjomandi, M., Dally, B., Cazzolato, B., The effect of arrangements of two circular cylinders on the maximum efficiency of Vortex-Induced Vibration power using a Scale-Adaptive Simulation model, *Journal of Fluids and Structures*, Vol. 49, Pages 654-666, 2014.

[4] **Derakhshandeh, J. F.**, Arjomandi, M., Dally, B., Cazzolato, B., Effect of a rigid wall on the vortex induced vibration of two staggered cylinders, American Society of Physics (AIP), *Journal of Renewable and Sustainable Energy*, 6, 033114, 2014.

[5] **Derakhshandeh, J. F.**, Arjomandi, M., Dally, B., Cazzolato, B., Flow induced vibration of an elastically mounted airfoil under the influence of oncoming vortices, *Journal of Experimental Thermal and Fluid Science*, under review, 2015.

### **Conference papers**

[1] **Derakhshandeh, J. F.**, Arjomandi, M., Dally, B., Cazzolato, B., Experimental and computational investigation of wake induced vibration, *19<sup>th</sup> Australian Fluid Mechanics Conference*, Melbourne, 2014.

[2] **Derakhshandeh, J. F.**, Arjomandi, M., Dally, B., Cazzolato, B., Numerical simulation of vortex induced vibration of an elastically mounted cylinder, *18<sup>th</sup> Australian Fluid Mechanics Conference*, Launceston, 2012.

### **1.6. Thesis format**

In compliance with the formatting requirements of The University of Adelaide, the print and online versions of this thesis are identical. The exceptions are some images where Copyright approval in the online version was not obtained. In these instances the original images have been replaced with a black box. The online version of the thesis is available as a PDF. The PDF version can be viewed in its correct fashion with the use of Adobe 9.

**References:**

Assi, G., Meneghini, J., Aranha, J. Bearman, P., Experimental investigation of flow-induced vibration interference between two circular cylinders, *Journal of Fluids and Structures*, 22, 819-827, 2006.

Assi, G., Mechanisms for flow-induced vibration of interfering bluff bodies. PhD thesis, Imperial College London, UK, 2009.

Assi, G., Bearman, P. and Meneghini, J., On the wake-induced vibration of tandem circular cylinders: The vortex interaction excitation mechanism. *Journal of Fluid Mechanics*, 661 (1), 365-401, 2010.

Barbir, F., Veziroğlu, T. and Plass, H., Environmental damage due to fossil fuels use. *International Journal of Hydrogen Energy*, 15 (10), 739-749, 1990.

Bearman, P.W., Vortex shedding from oscillating bluff bodies. *Journal of Fluid Mechanics*, 16, 195-222, 1984.

Bernitsas, M. and Raghavan, K., Converter of current/tide/wave energy. *Provisional Patent Application. United States Patent and Trademark Office Serial NO.60/628,252*, 2004.

Bernitsas, M. M., Raghavan, K., Ben-Simon, Y. and Garcia, E., VIVACE (Vortex Induced Vibration Aquatic Clean Energy): A new concept in generation of clean and renewable energy from fluid flow. *Journal of Offshore Mechanics and Arctic Engineering*, 130, 1-15, 2008.

Bernitsas, M.M., Ben-Simon, Y., Raghavan, K. & Garcia, E., The VIVACE converter: Model tests at high damping and Reynolds number around 10. *Journal of Offshore Mechanics and Arctic Engineering*, 131, 1-12, 2009.



Blevins, R.D., Flow-induced vibration. *Krieger Publishing Company, Malabar, Florida, USA*, 1990.

Energy Information Administration (US Dept. of Energy) Energy Statistics, Data and analysis, [www.eia.gov/forecasts/aeo](http://www.eia.gov/forecasts/aeo), 2014.

Govardhan, R. and Williamson, C., Modes of vortex formation and frequency response of a freely vibrating cylinder. *Journal of Fluid Mechanics*, 420, 85-130, 2000.

Govardhan, R. and Williamson, C., Critical mass in vortex-induced vibration of a cylinder. *European Journal of Mechanics-B/Fluids*, 23 (1), 17-27, 2004.

Güney M. and Kaygusuz K., Hydrokinetic energy conversion systems: A technology status review, *Renewable Sustainable Energy Rev.*, 14 (9), 2996–3004, 2010.

Jauvtis, N., Williamson, C. H. K., The effect of two degrees of freedom on vortex-induced vibration at low mass and damping. *Journal of Fluid Mechanics*, 509, 23-62, 2004.

Jamieson, P. and Hassan, G., Beating Betz–Energy Extraction Limits in a Uniform Flow Filed. European Wind Energy Conference, European Wind Energy Association Paper, 2008.

Johansson, T.B. and Burnham, L., *Renewable energy: Sources for fuels and electricity*: Island Press, 1993.

Khalak, A. and Williamson, C., Dynamics of a hydro-elastic cylinder with very low mass and damping, *Journal of Fluids and Structures*, 10 (5), 455-472, 1996.

Khan, M., Bhuyan, G., Iqbal, M. & Quaicoe, J., Hydrokinetic energy conversion systems and assessment of horizontal and vertical axis turbines for river and tidal applications: A technology status review. *Applied Energy*, 86 (10), 1823–1835, 2009.

Lee, J.H., Xiros, N. and Bernitsas, M. M., Virtual damper–spring system for VIV experiments and hydrokinetic energy conversion. *Ocean Engineering*, 38 (5-6), 732-747, 2011.

Peng, Z. and Zhu Q., Energy harvesting through flow-induced oscillations of a foil. *Physics of Fluids*, 21(12): p. 123602, 2009.

Trevor L., Future energy: Improved, sustainable and clean options for our planet, Elsevier, 2013.

Zhu, Q., Optimal frequency for flow energy harvesting of a flapping foil. *Journal of Fluid Mechanics*, 675: p. 495-517, 2011.

## **Chapter 2**

### **Literature review**

The phenomenon of vortex shedding was first recognized by Leonardo da Vinci in the 16<sup>th</sup> century where he observed it behind a piling in a river (Garcia 2008). His famous illustration is shown in Figure 2.1. Following this, the importance of vortex dynamics due to periodic shear forces on a bluff body has been well recognized and many aspects of this phenomenon such as vortex shedding frequency and amplitude of oscillation of the body have been investigated, particularly in the last century (Tritton 1959, Zdravkovich 1977, Sarpkaya 1979, Williamson and Roshko 1988, Williamson and Govardhan 2004). While the phenomena of vortex shedding behind bluff bodies is well understood, the process of extracting energy from these vortices is still immature and further investigations are required.



Figure 2.1: Sketch by Leonardo da Vinci in 1513 showing the wake behind a piling in a river (Garcia 2008).

Flow around bluff bodies can be found in many engineering applications spanning civil, mechanical, aerospace and marine systems. The generated vortices around such bodies have been observed to result in undesirable vibrations and the process is generally identified as Flow-Induced Vibration (FIV). Further sub-classifications of FIV come galloping, Vortex-Induced Vibration (VIV), Wake-Induced Vibration (WIV) and flutter (Blevins 1990), and can be based on the geometry of the bodies or the number of bluff bodies.

In general, galloping occurs when a non-circular cylinder with a single degree of freedom is mounted in a cross flow; thus, it oscillates under the effect of shear and pressure forces. A detailed explanation of the galloping theory has been reported by Parkinson (1971, 1989) and Blevins (1990).

The VIV is a term used to signify the response of a single circular cylinder interacting with an external fluid flow due to the vortices generated around the cylinder (Parkinson and Dicker 1971, Khalak and Williamson 1996). On the other hand, WIV is associated with the vibrations that can occur when a tandem body operates in the wake of an upstream body (Zdravkovich and Pridden 1977, Ruscheweyh 1983, Bokaian and Geoola 1984 and 1985, Zdravkovich 1988, Hover and Triantafyllou 2001, Assi 2006, Huera-Huarte and Bearman 2009). The term VIV is commonly coupled with lock-in

phenomenon, in which the motion of the cylinder follows the shedding frequency of the fluid leading to resonance. Therefore, it is generally known that VIV can occur due to such synchronisation. It is worth noting that the WIV response can occur outside of the natural frequency of the structure (Assi 2009) with higher amplitude of displacement as compared with VIV.

VIV can be categorized into two main mechanisms; fluid oscillators and body oscillators (Naudascher and Rockwell 2012). Here, oscillator is identified as a system of fluid mass or body that is acted upon by restoring forces when oscillating from its equilibrium position. In this research, only the bluff body can oscillate and it consists of a rigid circular cylinder and/or a symmetric airfoil that is elastically mounted in a cross flow, with a linear and/or rotary movements.

A circular cylinder is the common model of a bluff body with wide applications due to its simple axisymmetric geometry without sharp edges. Consequently, a brief review of the phenomenon of flow around a circular cylinder is initially considered, followed by a discussion on the dynamic response of non-circular cylinders.

### **2.1. VIV of a circular cylinder**

Numerous studies of the VIV response of a circular cylinder covered several features of structure and fluid flow including flow separation, the free shear layer, the effects of surface roughness, as well as the structure and behaviour of shed vorticity (Skop and Griffin 1975, Williamson 1996, Khalak and Williamson 1997, Jauvtis and Williamson 2003). There are fluid and structural parameters that influence the VIV phenomenon. On the fluidic side, the Reynolds number is the key non-dimensional parameter that influences the appearance of the vortical structures behind the bluff-body, which is dependent on the fluid density ( $\rho$ ), the free stream velocity ( $U$ ), the

diameter ( $D$ ) of the cylinder and the dynamic viscosity of the fluid ( $\mu$ ). While the mass of the cylinder ( $m$ ), including the added mass of the fluid, and the damping ratios ( $\zeta$ ) are structural parameters that need to be taken into account to characterize the VIV response of the cylinder. Consequently, in order to study the concept of resulting power using VIV, it is necessary to introduce the phenomenological aspects of the VIV phenomenon and analyse these parameters for a single elastically mounted cylinder in a cross-flow.

As the flow approaches a circular cylinder, it splits around the body. The pressure distribution field around the cylinder generates a maximum value at the stagnation point and the minimum value of the pressure generated is observed around the opposite side of the cylinder, as shown in Figure 2.2. By integrating the pressure around the surface of the cylinder, a resultant force is obtained, which can be projected into two components, such as drag and lift forces, relative to the  $x$  and  $y$  axes, respectively. The vortices are alternately shed from one side and then the other side of the cylinder. Due to this vortex formation process, the pressure distribution around the cylinder alters, which can cause a periodic movement at an identifiable frequency.

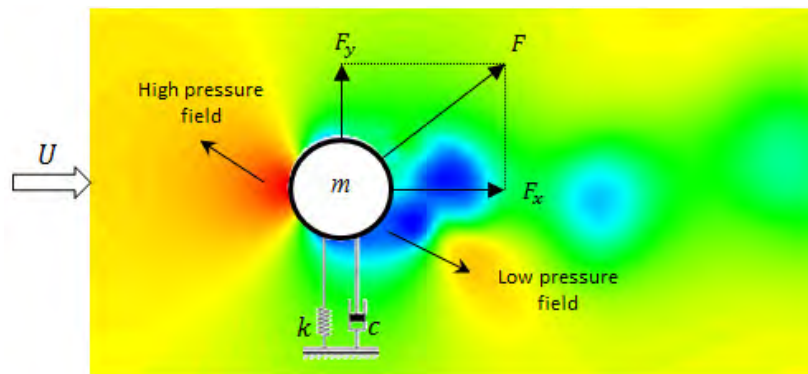


Figure 2.2: Instantaneous pressure field around an elastically mounted circular cylinder in a cross-flow resulting in two components of drag and lift forces in the  $x$  and  $y$ -directions.

The frequency of vortex shedding ( $f_s$ ) is generally normalized by the free stream velocity and the diameter of the cylinder to form the dimensionless parameter known as the Strouhal number ( $St = f_s D/U$ ). During the periodic formation of the vortices, the drag and lift forces fluctuate based on  $f_s$ . Over one complete cycle of vortex formation, two types of vortices are shed and are known as negative and positive vortices; one from each side of the surface of the cylinder. Consequently, for a mounted single cylinder in cross-flow, the component of the force normal to the mean flow  $F_y$ , has the same frequency as the vortex-shedding frequency, whereas, in the direction parallel to the flow, the frequency of  $F_x$  is doubled (Bishop and Hassan 1964). As a consequence of vortex shedding, surface forces periodically act on the cylinder. Therefore, the oscillating forces produce harmonic motion and cause the cylinder to vibrate depending on the degrees of freedom of the cylinder.

The lock-in resonance can happen in both directions of the lift and drag forces. As a consequence, the oscillation of the cylinder may change its form from small to larger vibration amplitudes, depending on the structural parameters (Sumer and Fredsoe 1997, Williamson and Roshko 1988, Sarpkaya 2004, and Williamson and Govardhan 2004). For instance, Williamson and Govardhan (2004) showed that the maximum dimensionless amplitude of oscillation of a cylinder ( $y/D$ ) can be obtained at lock-in range when the reduced velocity is approximately equal to 8 (which is approximately  $y/D \approx 1$ ). Here, the reduced velocity is defined as  $U_r = U/(f_n D)$ . Outside of this range, the amplitude ratio reduces depending on the vortex shedding frequency. According to Bernitsas *et al.* (2008), the amplitude ratio of the cylinder affects the power content of the VIV device. Therefore, to capture the energy of vortices in a fluid flow, synchronisation is an important aspect of VIV and must be considered in any analysis, in

particular for the lift force frequency. The lift force is generally utilised for energy conversion as an active force on the cylinder to produce an effective movement.

Due to the cyclic nature of vortex shedding, if the cylinder is mounted on an elastic base, the excitation of the cylinder can occur, which can be modelled as a mass-spring-damper. Bearman (1984) was the first to suggest that the harmonic displacement of the cylinder with one degree of freedom ( $y$ -axis, normal to the flow direction) can be modelled as:

$$\ddot{y}(t) + 2\zeta\omega_n\dot{y}(t) + \omega_n^2y(t) = F_y(t)/M, \quad (2.1)$$

where,  $y$  (m),  $\dot{y}$  (m/s) and  $\ddot{y}$  (m/s<sup>2</sup>) are the transverse displacement, velocity and acceleration of the cylinder, respectively. The term  $\zeta$  represents the damping ratio of the second order system, and  $\omega_n = 2\pi f_n$ , where  $f_n$  (Hz), represents the natural frequency. On the right hand side of Equation (2.1),  $F_y$  (N) and  $M$  (kg) are the fluid force exerted on the cylinder perpendicular to the flow direction and the effective mass of the system comprised of the mass of the cylinder bounded fluid, respectively.

The time dependent transverse displacement and the lift coefficient can be obtained from the following equations by assuming sinusoidal response of the cylinder:

$$y(t) = y_{\max}\sin(2\pi f_s t), \quad (2.2)$$

$$c_L(t) = C_L\sin(2\pi f_s t + \Phi). \quad (2.3)$$

Note, that here  $y_{\max}$  is the harmonic displacement amplitude,  $c_L$  and  $C_L$  are the time dependent lift coefficient and the lift coefficient amplitude, respectively, and  $\Phi$  (rad) is the force-displacement phase angle, which is

---



vital in the understanding the VIV response of the cylinder, particularly for energy conversion (Khalak and Williamson 1999, Bernitsas and Raghavan 2004, Bernitsas *et al.* 2008, Bernitsas *et al.* 2009). The power content of a circular cylinder is directly proportional to the force-displacement phase angle and any additional force-displacement phase lag to frequency of oscillation would bias the energy conversion (Lee *et al.* 2011).

Govardhan and Williamson (2000 and 2004) exposed that with a low mass damping ratio, three types of responses for the amplitude of oscillation were produced; *initial*, *upper* and *lower* branches. For the VIV response of a single elastically-mounted cylinder, Figure 2.3 shows a typical time series of displacement and highlights the phase difference between the lift force and the displacement of the cylinder at upper branch, transition between the upper to the lower branch,  $U_r = 5.7$ , and the lower branch,  $U_r = 7.9$ , respectively (Assi 2009). It is observed that when the cylinder is under the effect of upper branch at  $U_r = 4.0$ , the lift force and displacement of the cylinder are in phase and consequently the maximum amplitude of oscillation is obtained. Further increasing the reduced velocity to  $U_r = 5.7$ , the amplitude of the lift coefficient degrades significantly. In addition, it can be seen that the phase difference between force and displacement signals increases to 180 degrees.

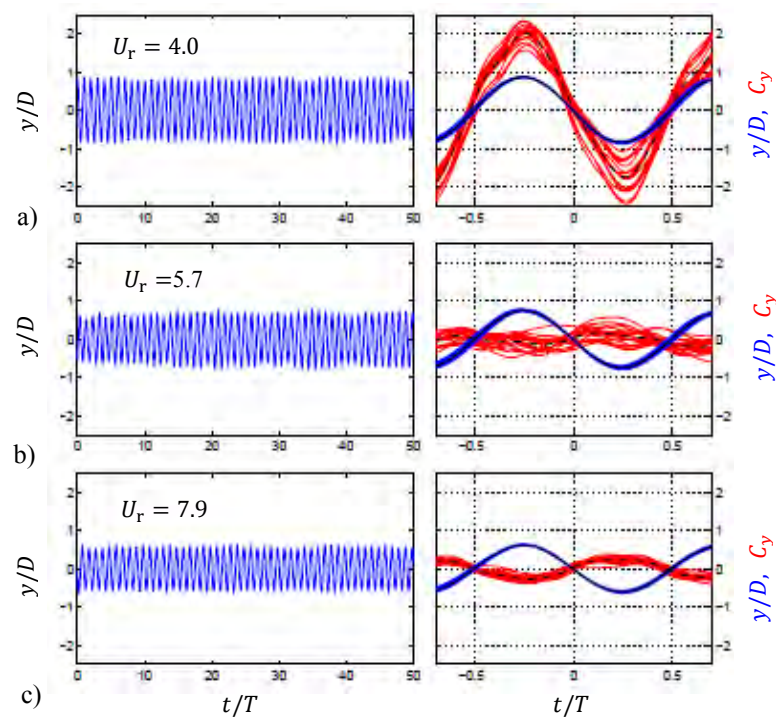


Figure 2.3: Dynamic response of a circular cylinder under VIV mechanism at three different branches of oscillation. Left column: time histories of displacement. Right column: lift coefficient and displacement over one complete cycle,  $y/D$  in blue and  $C_y$  in red with average cycle in dash black, at a)  $U_r = 4.0$ , b)  $U_r = 5.7$ , and c)  $U_r = 7.9$  (Assi 2009).

Figure 2.4 provides a further insight into the phase angle between force and displacement (Assi 2009). Since the reduced velocity of the cylinder increases, the VIV behaviour of the cylinder passes three branches beginning from initial, reaching the upper and finally decreasing to the lower branch (Figure 2.4-a). At the upper branch, it is possible to identify the variation of the frequency of oscillation is extremely close to the natural frequency of the cylinder. It is also evident that the phase angle between force and displacement of the cylinder from zero at initial branch shifts to 180 degree at the lower branch.

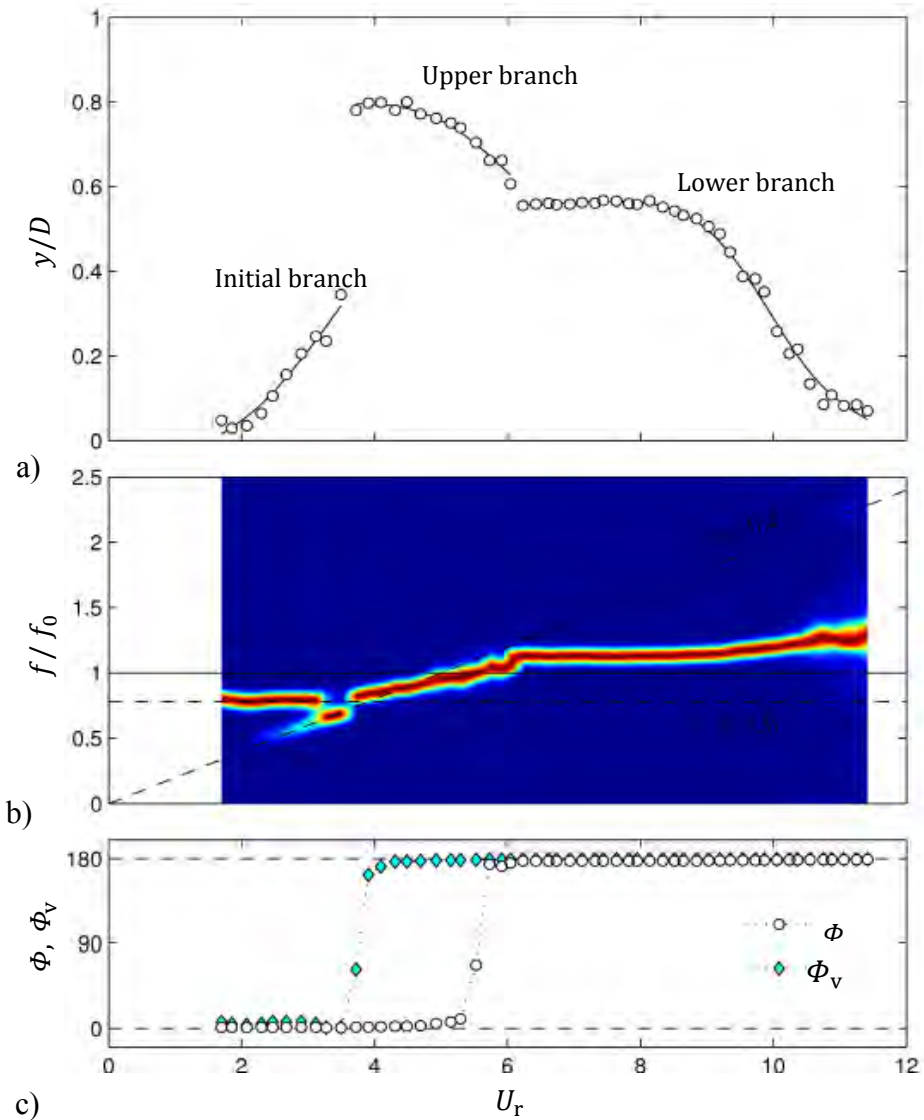


Figure 2.4: Dynamic response of a single circular cylinder under VIV mechanism, including a) amplitude of oscillation, b) normalised frequency of oscillation, Power Spectral Density (PSD), and c) phase angles (Assi 2009).

Numerical investigations have also been conducted to understand the flow over stationary and elastically mounted cylinders using different turbulence models. The flow around a stationary circular cylinder was investigated by Liaw (2005) using Large Eddy Simulation (LES) and Detached Eddy Simulation (DES) models in the transient flow regime. LES solves the

filtered Navier–Stokes equations by directly computing the large scale turbulence structures and modelling the smaller scale of dissipative eddies (Sagaut 2001). On the other hand, DES utilises the RANS model at the boundary layers of the flow. This approach helps save computational cost and switches to the LES in the detached flow region to capture the unsteady scales of the separated shear layers (Liaw 2005). It was found that the LES model is able to capture the flow structure in the wake of the cylinder, while DES shows less significant flow structures. Although LES provides the details of the flow pattern and is less dissipative compared to RANS models, the expense of computational requirements is significantly higher.

A series of numerical studies have also been conducted by Guilmineau and Queutey (2003) using a Shear Stress Transport (SST)  $k-\omega$  model to investigate the VIV response of the cylinder at the three branches of oscillation. The numerical results showed that although SST  $k-\omega$  is able to predict the dynamic response of the cylinder at the initial and lower branches, there is an inability for SST  $k-\omega$  to achieve the upper branch of vibration. Therefore, it is concluded that RANS models fail to appropriately predict the shear forces such as lift and drag, particularly in the transient flow regime in which all numerical studies of this research were performed.

The Shear Stress Transport (SST) model, developed by Menter (1994), combines the  $k-\omega$  and  $k-\varepsilon$  turbulence models to overcome the problems associated with the prediction of length scales close to the walls for the  $k-\omega$  and free stream dependency of the  $k-\varepsilon$  model. For flow around two cylinders, the SST model can be utilized to compute the transport of the turbulence shear stress inside the boundary layers. In this turbulence model, the aim is to increase the accuracy of flow predictions with strong adverse pressure gradients. It has been shown that SST can better predict flow separation compared with either the  $k-\omega$  or  $k-\varepsilon$  (Liaw 2005). Despite the

advantages of the SST model compared with  $k-\omega$  and  $k-\epsilon$ , it behaves similarly to the  $k-\epsilon$  model away from the wall (Fletcher and Langrish 2009). When the SST model is utilised in transient simulations, it generates large length-scales and consequently turbulence viscosities are too high. This feature does not allow a spectrum of length scales to be determined appropriately (Menter and Egorov 2005). Hence, seeking a solution to investigate the flow behaviour around a pair of cylinders can provide both computational efficiency and accurate flow predictions.

Within a transient flow, hybrid models have drawn less attention and no simulations have been yet conducted utilizing a combined formulation of Reynolds Average Navier Stokes (RANS) and Large Eddy Simulation (LES), known as Scale Adaptive Simulation (SAS) model. In the SAS turbulence model, the turbulence length-scale is resolved by considering the definition of von Kármán length scale ( $k$ ). In contrast to previous turbulence models, SAS overcomes the deficiency of SST in resolving the turbulence length-scale by considering the definition of von Kármán length scale. The modification assists in more accurately capturing the vortex structure in the wake of the bluff-body. The von Kármán length scale is given by:

$$L_{vk} = k \left| \frac{\partial U / \partial y}{\partial^2 U / \partial y^2} \right|. \quad (2.7)$$

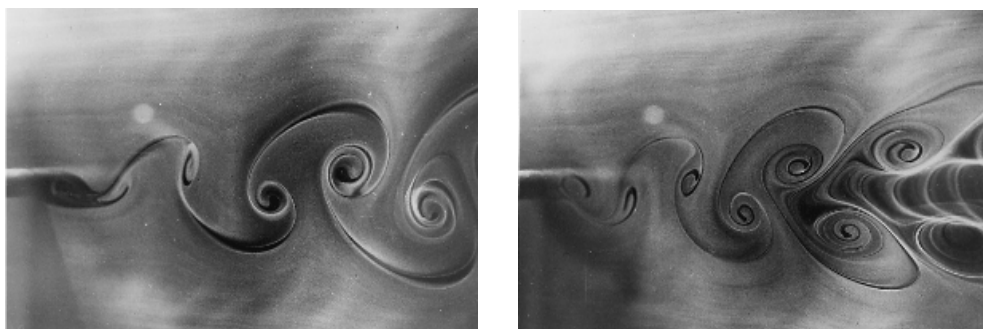
Using the von Kármán length scale, the model is able to adapt its behaviour to Scale Resolving Simulation (SRS) according to the stability parameters of the flow (Egorov *et al.* 2010). This allows the model to provide a balance between the contributions of the simulated and resolved parts of the turbulence stresses. Hence, the model can effectively and automatically switch from the Large Eddy Simulation (LES) mode to the Reynolds Averaged-Navier Stokes (RANS) mode (Menter and Egorov 2010).

With the aim of capturing the energy of the vortices, the fluidic parameters of the vibrated cylinder in a transient flow regime need to be addressed. Therefore, the effects of the shear forces, the Reynolds number, vortex structure and vortex shedding frequency as the critical parameters of the VIV and WIV mechanisms will be analysed using the SAS model.

## 2.2. Vortex structure in the wake of a cylinder

With the aim of harnessing the energy of oncoming vortices, it is important to understand the fundamental behaviour of vortices in the wake of a circular cylinder. The direction or type of vortices known as the mode (Williamson and Govardhan 1988) can influence the dynamic response of a second bluff body mounted in the wake of the first one.

The flow visualizations of VIV phenomenon conducted by Zdravkovich (1996) showed a discontinuous jump (approximately  $180^\circ$ ) in the upper branch of oscillation (refer to Figure 2.4 c) on the phase angle between the force acting on an elastically mounted cylinder and its displacement, where the maximum amplitude is obtained. Figures 2.5-a and 2.5-b depict a mirror-like image of the von Kármán Streets (VKS) due to the alteration in the phase angle at two reduced velocities (Griffins and Ramberg 1976, cited by Zdravkovich 1996).



a)

b)

Figure 2.5: Vortex Kármán Street at a)  $U_r = 5.14$  and b)  $U_r = 6.0$  (Griffin and Ramberg 1974, cited by Zdravkovich 1996).

It was reported that the phase change (approximately  $\pi$ ) between vortex shedding frequencies near synchronization is due to a switch in the timing of vortex shedding. This claim has been later confirmed by Gu *et al.* (1994) and Lu and Dalton (1996). Zdravkovich (1982) also compared the observation of other scholars (Den Hartog, 1934, Angrilli *et al.*, 1972, Griffin and Ramberg, 1974) and it was found that two modes of vortex shedding occur during the lock-in resonance. At the preliminary range of lock-in, the vortex shedding on one side of the cylinder's surface is formed when the cylinder is positioned at the maximum displacement. On the other hand, towards the end of the lock-in range, the vortex is formed again when the cylinder is near its maximum displacement on the same side. In addition, it is argued that these two modes are the limitations of the reduced velocities at which the maximum amplitude of oscillation of the cylinder occurs (Zdravkovich 1982).

Following the observation of Zdravkovich (1982), Williamson and Roshko (1988) conducted a series of experiments by vibrating a vertically mounted circular cylinder in a water channel at a range of Reynolds numbers from 300 to 1,000. Several regimes of vortex shedding were defined based on the mode of vortices in a map of  $y/D$  versus  $\lambda/D = U/f D$ , where  $\lambda$  is the wavelength. The vortex shed in the wake of the circular cylinder manifests a unique vortex mode depending on the wavelength ratio or reduced velocity of the flow. The pattern can involve a single vortex (S) and/or pair of vortices (P) generating patterns such as 2S, 2P modes, or a combination of these.

The term 2S is defined as two single vortices produced during each oscillation cycle. For a two dimensional (2D) flow around a cylinder, Bearman *et al.* (1981) and Williamson (1985) found that the 2S mode of vortices are frequently generated from each side of the cylinder within a

certain range of amplitudes at the initial branch of oscillation. On the other hand, the 2P mode is characterised by two pairs of vortices per cycle, which is known as the principal mode of vortices in the synchronisation region (Williamson and Roshko 1988). Following the proposed map of different modes of vortex shedding, Brika and Laneville (1993, 1995, and 1999) conducted wind tunnel tests utilizing smoke visualisation and were the first to point out that the 2S and 2P modes in the wake of a vibrating cable are produced at the initial and the lower branches of oscillation. Figure 2.6-a shows the sketches of the vortex formation patterns and a detailed description of these modes is mapped in Figure 2.6-b based on the  $y/D$  and  $\lambda$  (Williamson and Govardhan 1988). In Figure 2.6-b, the frequency axis of  $T_e/T_s$  is also drawn parallel to the wavelength ratio axis in order to indicate the lock-in point. Here,  $T_s$  represents the time of vortex formation based on the  $St = D/UT_s$ . Therefore, the parameter  $T_e/T_s$  is related to the wave length ratio  $\lambda/D$  by the expression  $T_e/T_s = St (\lambda/D)$ . As a consequence, near the lock-in, it is assumed that  $T_e \approx T_s$ . It can be observed that close to the fundamental lock-in region, the major vortex patterns are 2S, 2P and P+S. It is worth noting that the 2P\* mode is similar to the 2P mode except that the vortices in one of the half periods of vortex formation move away from the front surface of the cylinder. In this case, a pair of vortices moves downstream rather than in the upstream direction that is observed for the 2P mode. It is seen that the vortex pattern in the wake of the cylinder is directly dependent on the wavelength ratio or the reduced velocity of the flow and can be noticed as one of the primary parameters for capturing the wake energy. Therefore, it can be concluded that stronger circulation would be produced when 2P modes are generated. Stronger circulation then can increase the lift force on the downstream cylinder and consequently causes higher amplitude of displacement and alters the power coefficient of the VIV device.



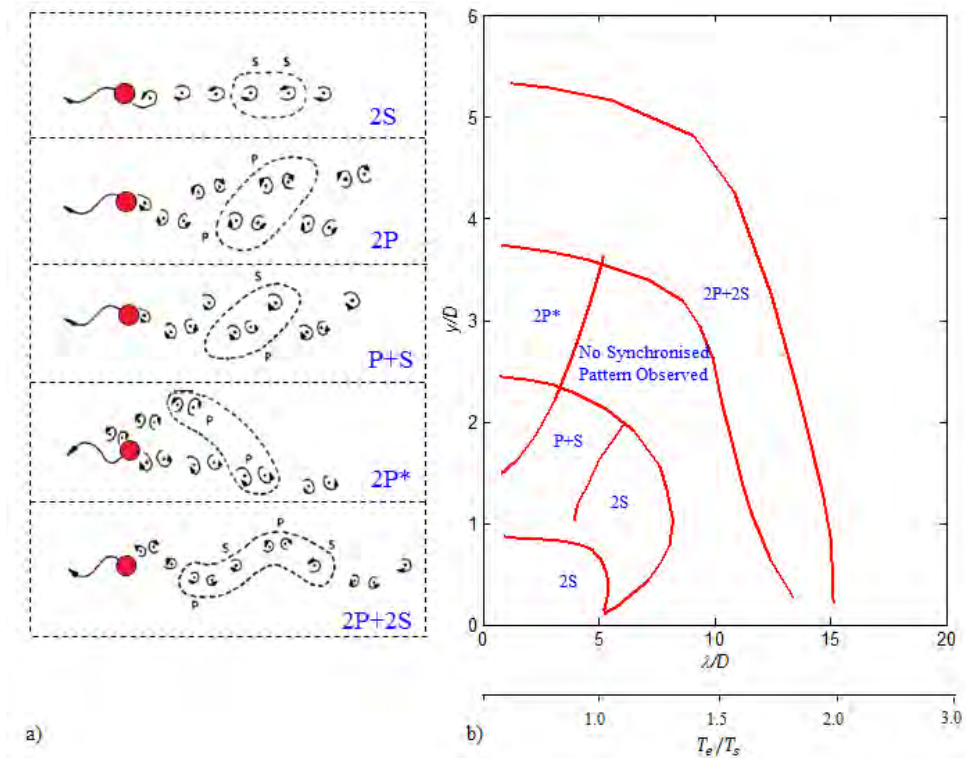


Figure 2.6: a) Modes of vortices in the wake of a circular cylinder. Highlighted vortices indicate one complete cycle of vortex shedding, b) Map of vortex mode as function of the wavelength ' $\lambda/D$ ' and amplitude ' $y$ ' (reproduced from Williamson and Govardhan 1988).

### 2.3. The effects of surface roughness

Surface roughness has also been observed to have a profound impact on the VIV process. Nakamura and Tomonari (1982) conducted experimental tests employing a wind tunnel for Reynolds numbers between 40,000 and 170,000. The effects of surface roughness on the VIV response of the cylinder was measured with different roughness strips located at  $\theta = 50^\circ$  on the surface of the cylinder relative to the free stream. It was found that the flow separation, pressure distribution around the cylinder and Strouhal number were all dependent on the roughness of the cylinder. At lower Reynolds numbers ( $Re < 20,000$ ) the variations in the base pressure

coefficient and the Strouhal number, in which all experimental tests of this project were conducted are insignificant. However, increasing the Reynolds number beyond  $Re > 20,000$  results in significant changes in both base pressure coefficients and Strouhal number due to the added roughness of the cylinder. Figure 2.7 shows the variation of the Strouhal number as function of the Reynolds number and the roughness of the cylinder. Here the roughness of the cylinder is normalized by the diameter of the cylinder, e.g.  $r/D$ , where,  $r$  represents the diameter of the particles on the surface of the cylinder. While the outcomes of Nakamura and Tomonari (1982) were in good agreement with the previously published data of Roshko (1961) and Achenbach (1977), most of the work was limited to a specific location of roughness strip on the cylinder ( $\theta = 50^\circ$ ).

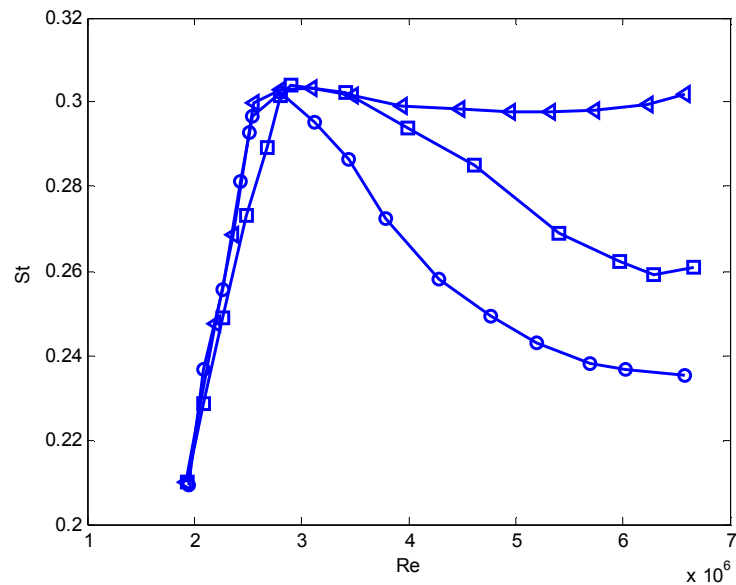


Figure 2.7: Effect of roughness of a cylinder on the Strouhal number, 'St', as a function of the Reynolds number with strip placement at  $\theta = 50^\circ$ . Triangles indicate smooth surface; Squares indicate  $r/D = 9.4 \times 10^{-5}$ ; Circles indicate  $r/D = 9.0 \times 10^{-5}$ ; ( $r$  represents the diameter of the particles) (reproduced from Nakamura and Tomonari 1982).

In addition to the studies by Nakamura and Tomonari (1982), Roshko (1961) and Achenbach (1977), Chang *et al.* (2011) found that beyond a strip placement angle of  $\theta = 64^\circ$ , the VIV mechanism is suppressed. It was also indicated that the frequency of oscillation at this location of the strip sharply declined when the reduced velocity was larger than  $U_r = 7$ . The effect of roughness height was also examined by Chang *et al.* (2011). The results showed that the height does not have considerable impact on the amplitude and frequency of oscillation of the cylinder. However, it was observed to result in earlier galloping.

Chang *et al.* (2011) also examined the effects of straight roughness strips on the surface of the circular cylinder at  $30,000 \leq Re \leq 120,000$ . Three specific features including width, roughness and circumferential location of the strip were considered in these experiments. The significance of this study was the identification of the influence of the roughness and high Reynolds numbers,  $3 \times 10^4 \leq Re \leq 1.2 \times 10^5$  on the flow induced vibration, including galloping and VIV of the cylinder. Surface roughness was changed by placing a strip (one inch wide) on the surface of the cylinder at a different angle relative to the stagnation point of the cylinder. For all test cases, the mean strip location was at  $\theta = 40^\circ$  and it spanned between  $8^\circ$  and  $32^\circ$ . It was found that as the area of coverage increases, the vibration of the cylinder is suppressed when the cylinder is mounted at  $U_r < 10$ . Further increase in the area coverage from  $8^\circ$  to  $24^\circ$  at higher reduced velocities results in significant increase in the amplitude of the cylinder. However, at this range of reduced velocity, the figure depicts that a considerable reduction in the amplitude occurs when the area coverage is  $32^\circ$ . Therefore to avoid the effect of roughness on dynamic response of the cylinder, two main features are considered for all experiments of this work; employing a smooth surface circular cylinder is used in a transient flow regime at  $Re < 20,000$ .

#### 2.4. Mass damping ratio and VIV

The extraction of energy through the VIV mechanism is directly proportional to the displacement of a bluff-body (Bernitsas *et al.* 2008) which itself is inversely proportional to the product of mass ratio and damping factor (Bearman 1984). It is obvious that depending on the mass of the cylinder and the density of the fluid in which the cylinder is mounted, the frequency of oscillation can be considerably affected by the additional mass of fluid due to the acceleration of the cylinder. For this reason, generally, the mass ratio is defined as the ratio of the mass of the cylinder and its components to the displaced mass of the fluid and given by  $m^* = 4m/\rho\pi D^2L$ , based on the mass ( $m$ ), the diameter ( $D$ ) and the length ( $L$ ) of the cylinder. The mass ratio is a very important factor for all types of induced vibrations by the flow. Depending on the density of the fluid, the frequency of the oscillation in air, for instance, is different from the frequency of oscillation when the cylinder is immersed in water.

An extensive number of studies have been performed to investigate the influence of the mass damping ratio on the VIV of a single cylinder ( $m^*\zeta$ ). Here,  $\zeta$  represents the damping ratio of the elastically mounted cylinder. Following Bearman (1984), Govardhan and Williamson (2000) also confirmed that the amplitude of oscillation increases by decreasing the mass damping ratio. Furthermore, it was reported that the synchronisation or lock-in can only be influenced by the mass ratio  $m^*$ .

Simultaneous measurement of force and displacement of an elastically mounted circular cylinder conducted by Govardhan and Williamson (2000 and 2004) revealed that with a low mass damping ratio, three types of responses for the amplitude of oscillation were established; *initial*, *upper* and *lower* branches, compared to only the *initial* and *lower* amplitudes observed with high mass damping ratios conducted by Feng (1968).

Accordingly, the maximum amplitude of the cylinder was captured within the upper branch of oscillation of the cylinder using a low mass damping ratio. The results showed that although the product of mass ratio and damping ratio was equal for both experiments, a larger synchronisation range was achievable by selecting a lower mass ratio (Govardhan and Williamson 2000).

The dependency of the amplitude of oscillation of the cylinder to the mass damping ratio has been confirmed by all previous scholars. However, recently Raghavan and Bernitsas (2011) showed that the mass damping ratio plays a secondary role, after the Reynolds number, on VIV phenomenon. It was found that by increasing the Reynolds number to fully turbulent shear layers,  $2 \times 10^4 - 4 \times 10^4 < Re < 1 \times 10^5 - 2 \times 10^5$ , the 2P modes of vortices are generated and the lower branch of oscillation disappears and replaced by an extended upper branch (Raghavan and Bernitsas 2011).

## **2.5. Reynolds number and VIV**

While the mass damping ratio is identified as one of the key parameters of the VIV phenomenon, it was shown that this parameter has a smaller influence on the VIV process when compared with the Reynolds number. VIV of a circular cylinder has been studied over the entire range of Reynolds numbers from laminar (Koopmann 1967, Anagnostopoulos and Bearman 1992) to transient and turbulent flows (Moe *et al.* 1994, Vikestad 1998, Ding *et al.* 2004, Bernitsas *et al.* 2006, Bernitsas *et al.* 2008). For laminar flow, Koopmann (1967) as a pioneer of Fluid Structure Interaction (FSI) research, studied a few aspects of VIV of a circular cylinder including velocity and frequency measurements, and flow visualisation at low Reynolds numbers,  $Re = 100, 200$  and  $300$ . He found that the displacement of the cylinder is a function of the Reynolds number which can affect the

frequency of the vortices. The frequency of the vortices was estimated using an optical system (Figure 2.8). The response of the cylinder at low Reynolds numbers,  $Re = 90-150$ , has been also investigated by Anagnostopoulos and Bearman (1992) and it was shown that the maximum amplitude of oscillation occurs close to the lower branch of the lock-in, where the motion of the structure dominates, based on the vortex shedding frequency. Therefore, to capture the energy of vortices at low Reynolds numbers using laminar flow regime, this range of frequency can be considered when the cylinder begins to oscillate.

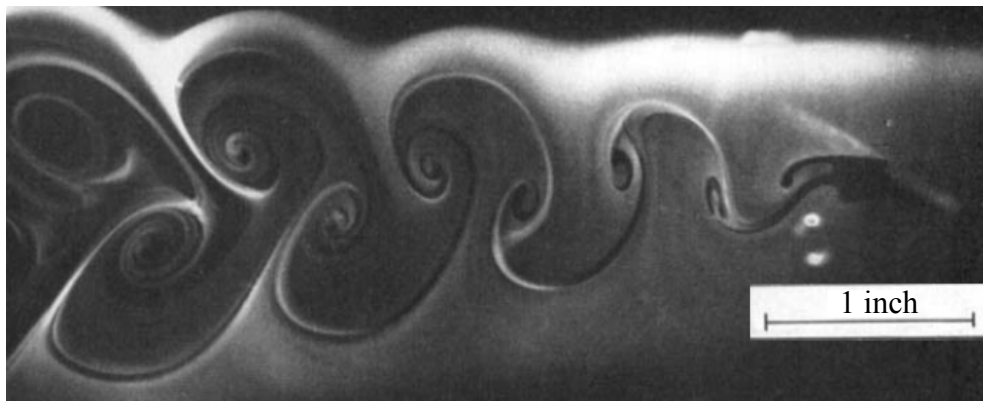


Figure 2.8: Vortex wake pattern around an elastically mounted cylinder at  $Re = 200$  including the first length scale of the initial vortex, flow from right to left (Koopmann 1967).

In general, studies of VIV response of bluff bodies at high Reynolds numbers are generally restricted due to the cost of equipment and instruments. Experimental tests on vibration of cylinders at high Reynolds numbers are limited to those conducted by Moe *et al.* (1994) ( $Re = 8,400$ ), Khalak and Williamson (1996) ( $Re = 12,000$ ), Vikestad (1998) ( $Re = 10,000$ ), Ding *et al.* (2004) ( $Re = 250,000$ ), and Raghavan and Bernitsas (2008 and 2011) ( $Re = 100,000-200,000$ ).

A series of water channel experiments conducted by Raghavan and Bernitsas (2011) confirmed that VIV is strongly dependent on Reynolds number compared to the mass damping ratio,  $m^*\zeta$ . It was found that the amplitude of oscillation of the cylinder increases when a Transition-in-Shear-Layer (TrSL) regime is utilized. The TrSL corresponds to the flow regime in which the Reynolds numbers range between 20,000 and 200,000 (Zdravkovich and Pridden 1977). It was found that although the mass ratio was increased by about 20 times compared to the Govardhan and Williamson value; the maximum achievable amplitude of cylinder was found to be  $1.9D$ , which was approximately two times the amplitude of the cylinders found by Govardhan and Williamson (2000) and Khalak and Williamson (1997). The reason for this achievement is due to the high fluctuating lift coefficient, which is obtained at TrSL flow regime (Raghavan and Bernitsas 2011). The results showed that the effect of the Reynolds number on the amplitude ratio appeared stronger than the mass ratio in VIV phenomenon. It was also found that this alteration is only limited to the upper branch of oscillation and there is no significant change seen at initial and lower branches. As a consequence, it is concluded that in the TrSL flow regime, the high amplitude of vibration was sustained even at high values of mass damping ratio, which demonstrates TrSL can be considered as one of the optimal flow regimes for energy capturing employing the VIV mechanism.

## **2.6. Effects of walls**

All previously mentioned studies were generally conducted to analyse the flow around a bluff body which was mounted at a significant distance from a wall. In this case, the bluff bodies or cylinders do not experience the effect of blockage that is generally encountered when the cylinder is in close proximity to a wall. Several studies focused on the effects of wall boundary layers on a single stationary cylinder (Bearman and Zdravkovich 1978,

---

Taniguchi and Miyakoshi 1990, Mahir and Rockwell 1996, Bosch *et al.* 1996, Mahir 2009, Sarkar and Sarkar 2010). These studies have shown that the dynamics of vortex formation is significantly different from that observed on unbounded bluff bodies away from walls and is a function of the gap ratio  $G/D$ , where  $G$  is the separation between the cylinder and wall.

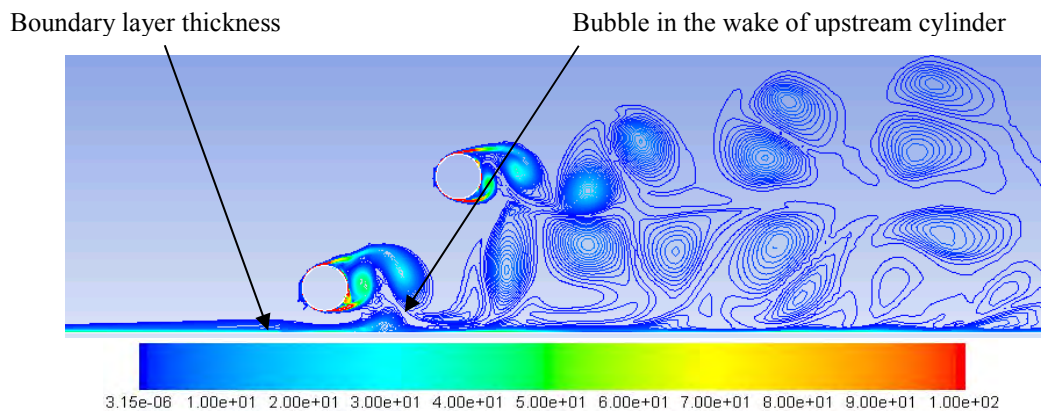


Figure 2.9: Instantaneous vorticity contours ( $s^{-1}$ ) around two staggered cylinders at  $Re = 8,700$ . The upstream cylinder is under the effect of wall located at  $G/D = 0.5$  (Derakhshandeh *et al.* 2014).

Figure 2.9 shows the instantaneous vorticity contours around two circular cylinders when the first one is mounted in vicinity of a rigid wall. When the gap between the cylinder and wall is small, vortices are suppressed in the gap. In this case, a non-uniform velocity profile in the wake of the cylinder is more considerable as compared to an unbounded cylinder. Due to the wall effect, the mean streamwise velocity profiles are not symmetric and tend to be inclined towards one side. This interaction alters the pressure coefficient in the wake of the cylinder and can provide a higher gradient in the shear layers, which can significantly affect the shear forces such as the lift and drag on the cylinder (Sarkar and Sarkar 2010). As a consequence, any subsequent bluff body in the wake of the upstream cylinder will be notably affected by the shear forces generated in the wake of the upstream cylinder.



Experiments of Bosch *et al.* (1996) for a flow around a square cylinder revealed that the gap ratio  $G/D = 0.35-0.5$  is critical since the generated vortices were entirely suppressed between the cylinder and wall. The vortices were still influenced by the presence of the wall when the gap ratio was increased to  $G/D = 0.75$ . However, at  $G/D = 1.5$ , the wall had no effect on the vortices and the dynamic structure of vortices around the cylinder was similar to that of an unbounded cylinder.

The influence of the gap ratio on the lift and drag coefficients over a cylinder of square cross-section has been investigated by Martinuzzi *et al.* (2003) at Reynolds number 18,900. The experiments were conducted at different gap ratios varying between 0.07 and 1.5. Four regimes of operation were identified depending on the behaviour of the shed vortices. These are:

- i) Vortex suppression region:  $G/D < 0.3$ ,
- ii) Regular vortex shedding suppression:  $0.3 < G/D < 0.6$ ,
- iii) The influence of viscous wall:  $0.6 < G/D < 0.9$ ,
- iv) No influence region:  $G/D > 0.9$ .

It was found that at  $G/D \geq 0.9$ , the mean lift force observed by the cylinder near the wall was very similar to that observed on a square cylinder mounted in a free stream without walls. Most previous studies showed that the critical gap ratio ( $G/D$ ) occurs when the gap ratio is approximately  $0.3 \leq G/D \leq 0.45$ . In another scenario, Sarkar and Sarkar (2010) studied the effect of a rigid wall on a circular cylinder at  $Re = 1,400$ . Figure 2.10 shows the vortex structure in the wake of the cylinder at three different gap ratios  $G/D = 0.25, 0.5$  and  $1.0$ . It can be seen that when the cylinder is mounted at critical gap ratio,  $G/D = 0.25$ , vortices tend to move upward in the wake of the cylinder as they are under the effect of the rigid wall. This trend changes the pressure field in the wake of the cylinder. Accordingly, the dynamic of

vortices changes which alters the fluidic parameters of the flow in the wake of the cylinder such as velocity

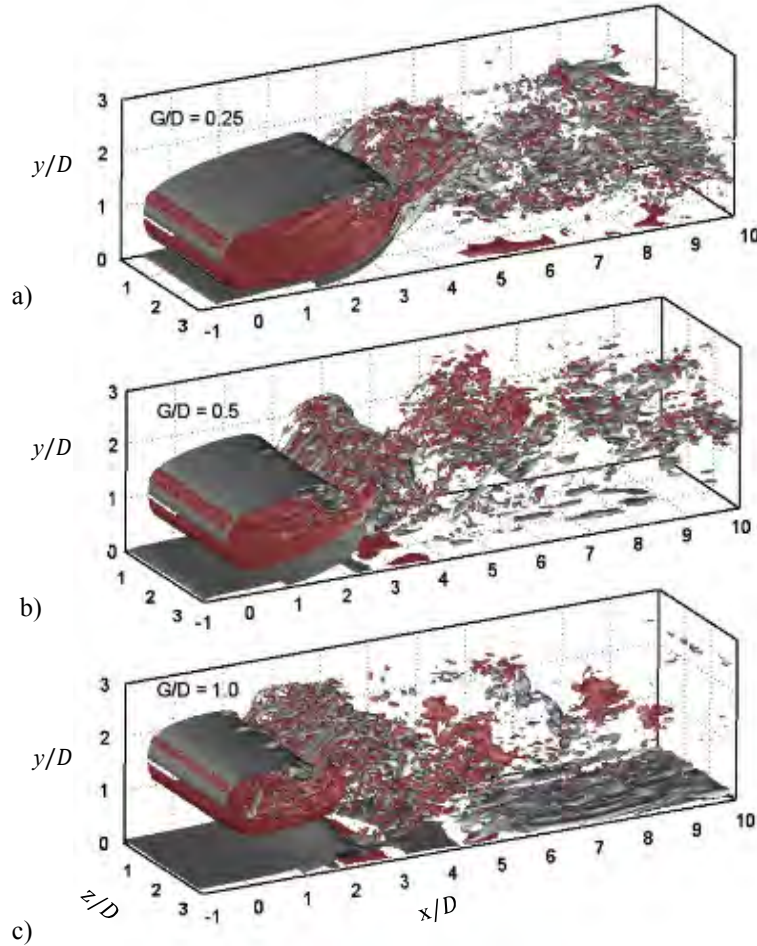


Figure 2.10: Computed vorticity contours for three gap ratio; a)  $G/D = 0.25$ , b)  $G/D = 0.5$ , c)  $G/D = 1.0$  for a circular cylinder at  $Re = 1,440$  (Sarkar and Sarkar 2010).

The dimensionless mean streamwise velocity ( $\bar{u}/U$ ) profiles at several longitudinal distances in the wake of the cylinder ( $x/D = 2, 5,$  and  $10$ ) are shown in Figure 2.11. Here,  $\bar{u}$  is the average of the  $x$ -velocity, which was evaluated over the total running time and the data were normalized against the free stream velocity,  $U$ . It is observed that due to the wall effect, the velocity profiles are non-uniform and tend to be inclined towards one side.

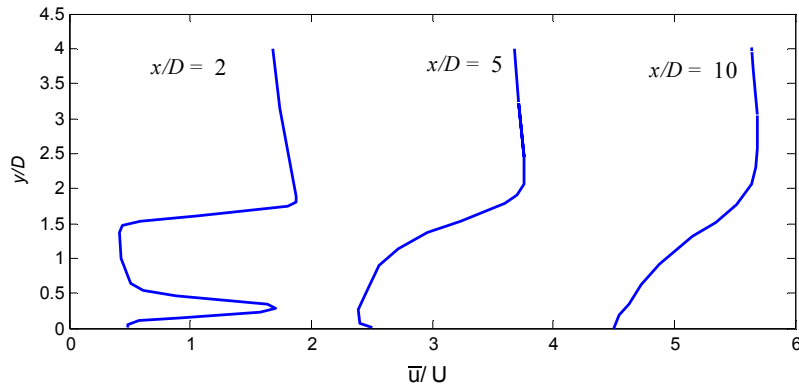


Figure 2.11: Mean streamwise velocities at several longitudinal distances in the wake of a circular cylinder in vicinity of a rigid wall,  $G/D = 0.25$ , at  $Re = 1,440$  (reproduced from Sarkar and Sarkar 2010).

## 2.7. Non-circular cylinders

In general, a square cylinder can be considered as the simplest and most common form of a non-circular cylinder. Therefore, it is initially worthwhile to study the dynamic response of the square cross section under the effect of vortices.

A non-circular cross section bluff body experiences a periodic fluid force similar to bluff bodies with a circular cross section. However, in this case the force alters with the orientation of the body with respect to the free stream velocity. When the square cylinder oscillates its orientation also changes (Blevins 1990). In this case, with a single degree of freedom, galloping might occur. A square cross section cylinder with an elastic support ( $m$ ,  $c$  and  $k$ ) mounted in a cross flow which can only oscillate in a direction normal to the fluid flow is illustrated in Figure 2.12. The separation for the square cylinder with the sharp edges occurs at the leading edges. When the square cylinder provides relative cross-flow motion, a cyclic movement of the shear layers from each side of the edges causes asymmetric flow field resulting in an asymmetric pressure field. This leads to the generation of a fluid force  $F_y$ , which is in the same direction as the

motion of the square cylinder (Blevins 1990). Therefore, for the non-circular bluff bodies the acting force on the structure is in phase with the displacement velocity of the square that contributes to an increase in the amplitude of displacement.

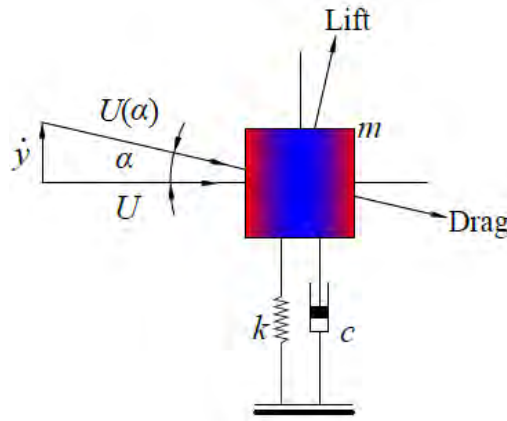


Figure 2.12: An elastically mounted square cylinder with one degree of freedom under the effect of free stream velocity.

The equation of motion for the mass-damper-spring model of an elastic square cylinder can be written as (Blevins 1990)

$$m\ddot{y} + c\dot{y} + ky = \frac{1}{2}\rho \cdot U^2 \cdot D \left[ c_L|_{\alpha=0^\circ} + \frac{\partial c_L}{\partial \alpha} |_{\alpha=0^\circ} \alpha + O(\alpha^2) \right]. \quad (2.4)$$

Here,  $\alpha$  is the angle of the square, and  $c_L$  is the lift coefficient. It is clear that the magnitude of the lift force increases with the angle of attack, which is dependent on the velocity of the cylinder in the normal direction ( $\dot{y}$ ). For non-circular cross sections, the angle of attack therefore plays an important role with an increment of amplitude vibration due to the fluid dynamic instability (Bearman *et al.* 1987). For this dependency, Parkinson and Dicker (1971) concluded that the amplitude of VIV is limited to less than  $1D$ , while the amplitude of galloping can increase many fold.

More experiments have been conducted by Bearman *et al.* (1987) to reveal the dependency of amplitude and the angle of attack at different turbulence intensities. It was found that the maximum lift coefficient for a square cylinder is achievable at angle of approximately  $13^\circ$ . The variation of the vertical force acting on the square at  $\alpha$  can result in lift coefficient of the cylinder. Accordingly, the increment of lift force, which is utilized in this project acting on an airfoil, results in continuous increase in both amplitude of oscillation and velocity. This can cause larger vibrations compared with a circular cylinder. Hence, for circular cylinders where the maximum amplitude of oscillation is limited to the upper branch with approximately  $1D$ , for non-circular bluff bodies the amplitude can be many times  $D$  (Parkinson 1971).

### **2.8. Power efficiency of a cylinder and an airfoil**

Airfoils can also be considered as a slender body that undergoes instantaneous heave and pitch motion. In this case the dynamic response of the airfoil is known as flutter. This concept was initially studied by McKinney and DeLaurier (1981) who analysed the harmonic oscillation of an airfoil to extract wind energy. They showed that the flutter behaviour of the airfoil is capable of efficiencies up to 35%. This high efficiency was observed for a reduced frequency of  $f^* \approx 0.15$  and high pitching amplitude with  $\alpha \approx 75^\circ$ . The mechanism of flutter to harvest the kinetic energy of the fluid is very similar to the energy convertor based upon the VIV phenomenon. However, the efficiency of the energy extracted using an airfoil is larger compared to that of the VIV with a 22% efficiency (Bernitsas *et al.* 2008). Along with the experimental tests on the energy harvesting performance of a fluttering airfoil mechanism, the numerical simulations of Peng and Zhu (2009) showed that a high efficiency of 34% was achievable when the normalized oscillation frequency is around 0.15,

which is also comparable with the theoretical VIV efficiency of 32% shown by Bernitsas *et al.* (2008).

Further investigations have been conducted by Zhu and Peng (2009) and Zhu (2011) using numerical modelling to understand the kinetic energy captured from flapping foils in a uniform flow. Zhu and Peng (2009) found that the behaviour of the airfoil is dependent on the stiffness of the system. It was also shown that the location of the pitching axis plays an important role in the dynamic response of the airfoil. Depending on the location of the pitching axis and the rotational spring stiffness, four distinct responses were identified: static, periodic, irregular and oscillation motions. They showed that excitation of airfoil occurs when an elastic axis distance  $b$  was set between -0.2 and 0.5 from the centre of the airfoil. Among these responses, it was postulated that the periodic motion of the airfoil could be used for energy harvesting and it was found that the energy capacity of the mechanism remains stable as the distance of elastic axis varies from -0.1 to 0.1.

While a few numerical studies have shown the capability of fluttering airfoils for energy capture, the lack of examination of the fluttering response of an airfoil in capturing hydrokinetic energy has motivated further examination of this area in this project.

### **2.9. A pair of circular cylinders**

In order to capture the wake energy of a cylinder, different arrangements of the cylinders can be considered. In this case, since the cylinders are arranged in close proximity to one another, several fluidic parameters are involved and cause a change in the interactions between vortices, the shear layers and consequently the wake field. Numerous comprehensive studies of the flow around a pair of cylinders arranged side-by-side, in tandem and

staggered configurations have been conducted. Figure 2.13 shows two identical circular cylinders immersed in a steady cross-flow.

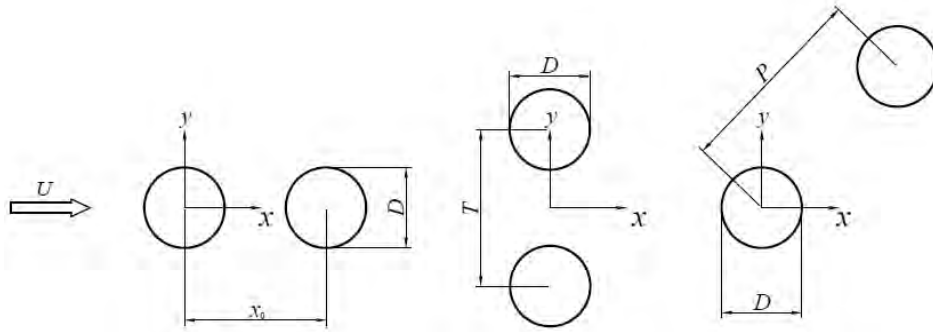


Figure 2.13: Two identical circular cylinders in a cross-flow in different configurations a) tandem, b) side-by-side, c) staggered.

### 2.10. Classification of wake interference

The gap between the cylinders is one of the important features, especially in the WIV mechanism. There are several approaches to classify the wake of two circular cylinders. Zdravkovich (1988) was the first to compile a map of the wake regime for an upstream circular cylinder based on the location of a downstream cylinder. Figure 2.14 depicts three interference regimes according to the longitudinal and lateral distances between cylinders; a) proximity interference, b) wake interference and c) no interference. Proximity interference occurs when the cylinders are located in close vicinity of each other and the second cylinder is under the effect of wake and vortices produced by the first cylinder. In this case, the first cylinder might influence the second one depending on the gap between the cylinders. The most popular configuration for the proximity interference regime is the side-by-side cylinders. In the wake interference regime the second cylinder is affected by the wake generated by the first cylinder. Finally, the no-interference regime is identified when the second cylinder is outside both previous regimes.

---

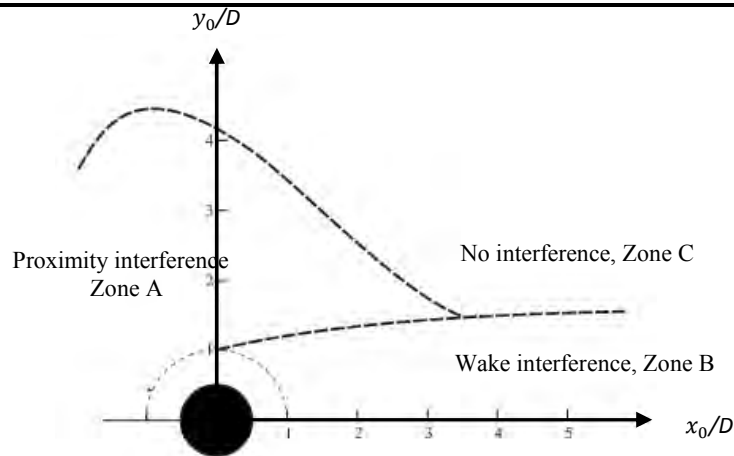


Figure 2.14: A map of wake interference regions with the upstream cylinder fixed (Zdravkovich 1988).

Another approach is to focus on the fluidic parameters such as Strouhal number, pressure coefficient, and shear forces on the cylinder to interpret the wake regimes. In order to investigate the Strouhal number, Kiya *et al.* (1980) conducted a series of wind tunnel tests for staggered arrangements using identical cylinders at  $Re = 15,800$ . It was found that the cylinders can be considered as a single bluff body when the gap between them is less than  $1.4 D$ . In addition, it was reported that for a gap less than  $1.4 D$ , the Strouhal number for the downstream cylinder is about  $St = 0.12$ , which is much lower than that for a single cylinder ( $St \approx 0.2$ ). The smaller gap between the cylinders affects the wake development of the upstream cylinder resulting in a narrower wake behind the first cylinder compared with the wake of the downstream cylinder. As a consequence, narrower wake is associated with a higher Strouhal number while wider wake corresponds to lower Strouhal numbers, (Kiya *et al.* 1980). Under this condition, the resulting vortex splits into smaller vortices without any chance to achieve the maximum circulation.

Similarly, the pressure coefficients developed around the cylinders have been examined by Igarashi (1984), Hiwada *et al.* (1982), Ljungkrona *et al.*

---



(1991) and Ljungkrona (1992). Figure 2.15 shows the mean pressure distributions around the downstream cylinder as a function of the gap between the cylinders and the Reynolds number (Igarashi 1984). It can be observed that at higher separation angles  $\Phi > 70^\circ$ , the effect of the gap on the pressure coefficient is much higher. In addition, this effect appears to be stronger than that of the Reynolds number. As the shear forces are affected by the pressure distribution around the downstream cylinder, the variation of the gap between the cylinders would alter the dynamic response of the cylinders.

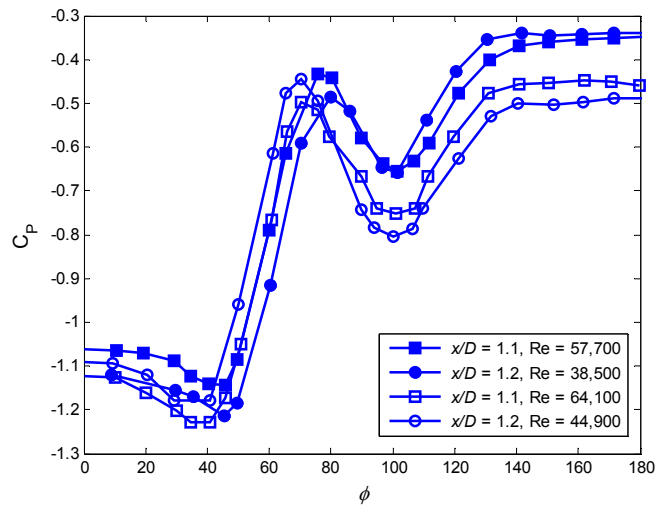


Figure 2.15: Mean pressure distribution around a downstream cylinder as a function of the Reynolds number and longitudinal distance between the cylinders (Igarashi 1984).

For two aligned cylinders, Igarashi (1981) experimentally investigated the wake of the upstream cylinder and found it was highly dependent on the streamwise separation between the cylinders. It was found that the flow may be categorized into six different patterns based on the spacing between the cylinders. This tandem configuration has also been studied experimentally and numerically by Zdravkovich (1988), Carmo (2005) and Carmo *et al.* (2008), respectively and similar observations were made.

The flow patterns of the unstable shear layer as a function of the distance between the two cylinders is illustrated in Figure 2.16. In the case where the distance between cylinders is less than  $1.5D$ , the vortices have no interaction in the wake area (patterns A and B). By increasing the gap distance of the cylinders to  $1.5 < x_0/D < 3$  (patterns C and D), it can be observed that two recirculation regions appear in the wake of the upstream cylinder. Initially, when the distance is smaller, the vortices are symmetric. However, as the distance is increased, these recirculation regions alternate to the asymmetric reattachment of the shear layers. Therefore, it can be concluded that a mean value of the sinusoidal lift force of the upstream cylinder is equal to zero (Assi, 2009). For larger gaps between the cylinders, the shear layer from the upstream cylinder has ample room to roll up in the wake and emerge as a fully developed vortex street in the wake. This was also studied by Ljungkrona and Sunden (1993) by using flow visualization techniques.

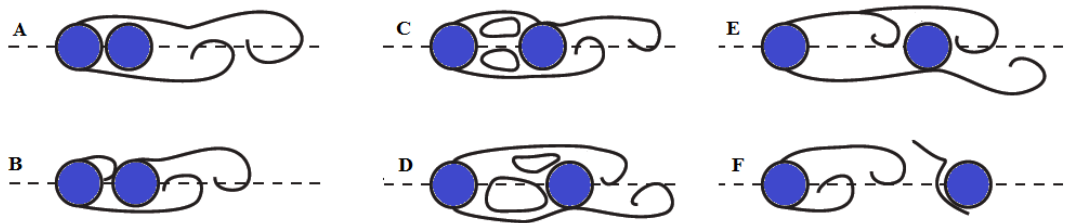


Figure 2.16: Flow patterns around two stationary circular cylinders as a function of streamwise separation (A-F), reproduced from Igarashi (1981).

Figure 2.17 shows the prominent flow patterns around a pair of cylinders in a wind tunnel. In the experiments, the effects of the longitudinal distance between the cylinders and Reynolds number were considered, simultaneously. It was observed that for two similar cylinders, the critical wake spacing with developed vortices is  $3.0D$  for a Reynolds number of 42,000. This was observed to increase as the Reynolds number was

decreased indicating that the complete wake development is prolonged at smaller free stream velocities.

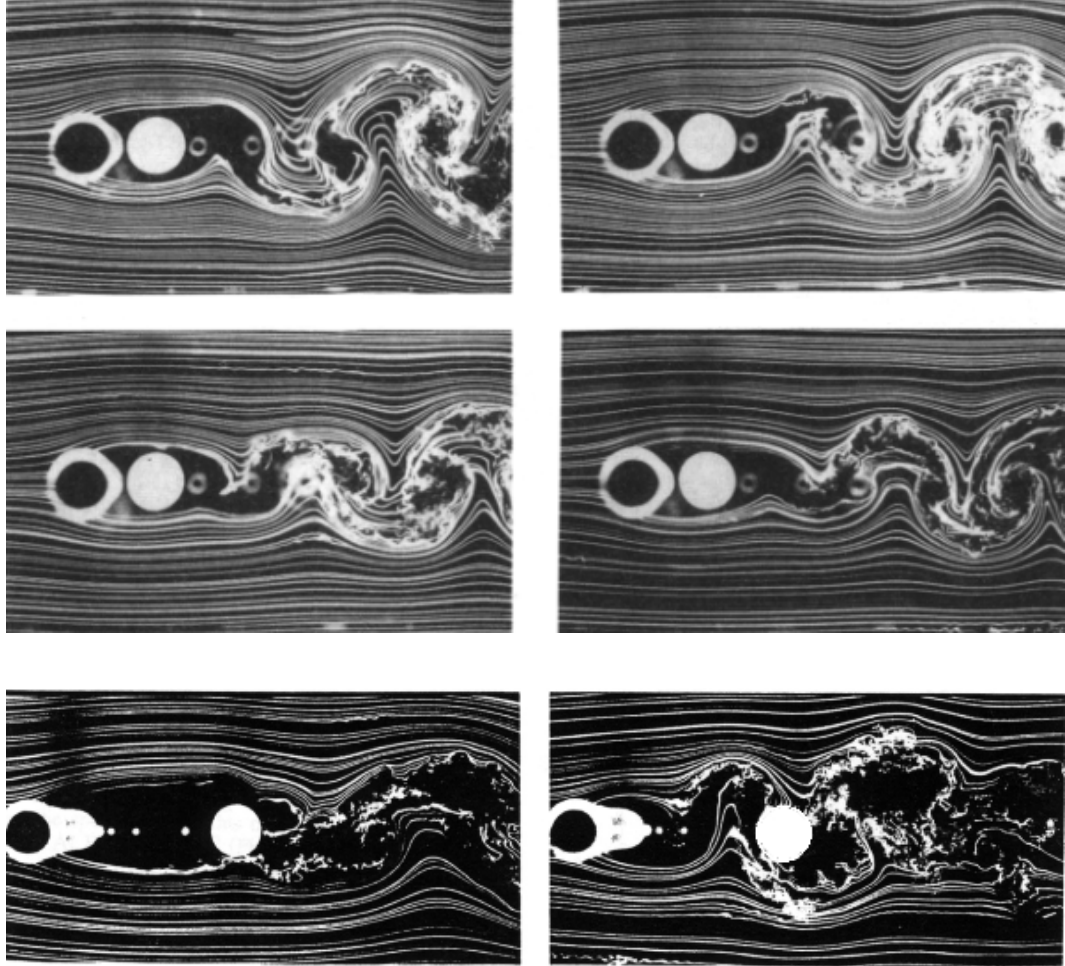


Figure 2.17: Flow past two circular cylinders for  $x/D = 1.25$  at a)  $Re = 3,300$ , b)  $Re = 6,700$ , c)  $Re = 10,000$ , d)  $12,000$ , e) for  $x/D = 4.0$ ,  $Re = 10,000$ , f) for  $x/D = 4.0$ ,  $Re = 12,000$  (Ljungkrona and Sunden 1993).

The critical measured wake spacing by Igarashi (1981) is between  $1.5D$  and  $3.53D$ , while a critical range of  $1.5D$  to  $4D$  was recorded by Kuo *et al.* (2008). Ljungkrona *et al.* (1991) showed that for two similar cylinders the critical wake spacing is  $4.5D$  for a Reynolds number of 1,400 which decreases to  $3.0D$  for a Reynolds number of 42,000.

Further investigations related to the relative sizes of the two cylinders were performed by Alam and Zhou (2007). In their study, the diameter of the upstream cylinder ( $d$ ) was gradually increased from 6 mm to 25 mm, while the diameter of the downstream cylinder ( $D$ ) was kept constant at 25 mm. It was concluded that a decrease in diameter ratio ( $d/D$ ) causes a reduction in the width between the two free shear layers in the wake spacing of the cylinders.

All previous studies indicate that fully developed vortex formation behind the upstream cylinder requires a minimum spacing of  $1.5D$  between two similar cylinders. Due to the spacing between the cylinders, the vortices are formed and become fully developed. This means that at larger gaps fully developed vortices with larger length scales and higher circulations of the vortices are produced. In this case larger shear forces might be generated, which directly affect the dynamic response of the elastically mounted cylinder.

### **2.11. Wake-Induced Vibration (WIV)**

Despite the intensive research into the VIV phenomenon over the past few decades, WIV has not received much attention in the literature, particularly as an application for energy extraction. In general, the WIV of a downstream cylinder can be thought of as the unsteady vortex-structure interaction that occurs between the cylinder and the upstream wake (Assi *et al.* 2010). In the WIV mechanism, when the downstream cylinder is displaced sideways, a lift force acts to move the cylinder towards the centreline (Zdravkovich 1977) and it can occur outside of the resonance frequency. Hence, the WIV response of a circular cylinder is distinctively different from the VIV response of a single cylinder.

A series of experimental investigations of the WIV of an elastically mounted circular cylinder were conducted by Assi (2009), in the range of  $1,000 \leq Re \leq 30,000$ . It was demonstrated that in the WIV mechanism at a high reduced velocity,  $U_r > 17$ , the amplitude of oscillation is much higher than that observed for the VIV response of a single cylinder.

For a pair of cylinders under the WIV mechanism, it is worth noting that the total measured lift force acting on the surface of the cylinder can be divided into two separate components (Govardhan and Williamson 2000). The total lift force on the cylinder includes a potential-force component ( $F_{\text{potential}}$ ) due to the ideal flow inertia and a vortex-force ( $F_{\text{vortex}}$ ), which is only produced by the dynamics of the vorticity field around the downstream cylinder. Therefore:

$$\vec{F}_{\text{total}} = \vec{F}_{\text{potential}} + \vec{F}_{\text{vortex}} \quad (2.5)$$

Here, the potential-force is a function of the cylinder acceleration and its magnitude is proportional to the product of the displaced fluid mass and the acceleration of the cylinder. On the other hand, the vortex-force is dependent on the dynamics of the generated vortices and can be expressed in terms of another phase angle such as ( $\Phi_v$ ) in relation to the displacement of the cylinders (Assi 2009). Assuming  $\Phi$  is the phase angle between displacement and total lift force; the total lift can be formulated in terms of the lift coefficient as follows:

$$\begin{aligned} c_{\text{total}} \sin (2\pi ft + \Phi) = \\ c_{\text{potential}} \sin (2\pi ft + 180^\circ) \\ + c_{\text{vortex}} \sin (2\pi ft + \Phi_v). \end{aligned} \quad (2.6)$$

Consequently, the maximum lift coefficient acting on the cylinder is accessible when both potential lift coefficient and vortex lift coefficient become maximum and the phase angle between total lift force and displacement ( $\Phi$ ) remains close to zero. This concept has been also verified through a series of water channel tests where the force, displacement and frequency of oscillation were measured by Assi (2009). It was reported that that a maximum lift coefficient of 2.5 can be obtained at reduced velocity of  $U_r = 5$  (Assi 2009).

To harness the hydropower of the fluid, Equation (2.6) is important to analyse and evaluate the lift force and later in the experimental tests, this concept will be applied in the experimental tests.

As mentioned earlier, Bearman (1984) was the first to postulate that the response of an elastically mounted circular cylinder can be modelled as a Mass-Spring-Damper system (MSD). Following the proposed model by Bearman (1984), Hover *et al.* (1997), a pioneer of the computer model of Virtual Mass-Spring-Damper (VMSD), designed and employed a force-feedback controller in real time. The VMSD system allowed the operator to electronically set the desired impedance of the MSD. The advantage of VMSD is that it allows a wider range of tests to be conducted rapidly compared to the real physical MSD which requires changes in the physical elements of the system in order to change the impedance. The ease of application of the VMSD allowed Hover *et al.* (1997) to conduct a wide range of air channel tests to analyse the effects of damping ratio and the Reynolds number on the VIV response of a cylinder. They observed that the maximum amplitude of oscillation can be obtained when the damping ratio is zero as would be expected. Although, it was shown that the VMSD is able to record reliable results, such as lift coefficients and the amplitude of oscillation, the system was observed to produce an additional phase lag of

12 degrees. The phase lag between lift and displacement was due to the Chebyshev third-order digital filter used for noise filtering (Hover *et al.* 1997), which can cause a reduction in energy conversion.

The use of VMSD models opened the way for optimisation and further development of energy extraction from VIV. In particular, it was used to explore many unresolved issues including the force-displacement phase lag, the power coefficient of energy harnessing, etc. For example, Lee *et al.* 2011 developed a VMSD of a VIV converter including a circular cylinder, a timing belt-pulley, a motor, and a controller. The VMSD allowed them to perform a wide range of experiments in which the spring stiffness was kept constant and the viscous damping was varied. In this model, there was no artificial phase lag between the force and displacement which could bias the energy conversion. In addition, to eliminate the vibration of the timing belt, an idler was utilized to remove the non-linearity of the oscillations. Furthermore, in order to protect the motor, a coupling was employed between the pulley and the motor shaft. Although significant improvements were made in this model, the mass of the cylinder was imposed on the motor and generated significant frictional force due to the static weight of the cylinder. This caused a nonlinear behaviour for the response of the cylinder at low velocities.

In the current work presented in this thesis, a new developed VMSD system is designed, built and employed to overcome the limitations of the previous devices. In this virtual mechanism, the cylinder is installed vertically in the water channel. This assists in avoiding the static loads on the motor arising from the cylinder, thus reducing friction and improving the response of the cylinders.

## 2.12. Summary

A literature review on VIV and WIV highlights that the dynamic response or displacement amplitude of a bluff body such as circular cylinder under the effect of generated vortices is dependent on several parameters such as geometry and spacing between the cylinders. It is well-understood that the behaviour of a circular or non-circular cylinder can vary in a cross flow and influence the power coefficient of a converter. The complexity of the phenomenon increases when two bluff bodies are arranged in a tandem, side-by-side or in a staggered arrangement. This complexity increases as the number of degrees of freedom of the bluff body increases. Despite the large number of investigations on VIV, only few have focused on the extraction of energy from vortices, particularly using WIV and FIV phenomena. This is mainly because of the fact that harnessing hydropower energy from vortices is a relatively new technique, proposed recently by Bernitsas and Raghavan (2004), Bernitsas *et al.* (2008), Raghavan and Bernitsas (2008), Bernitsas *et al.* (2009) and Chang *et al.* (2011). Consequently, further investigations are necessary to better understand the characteristics of the flow patterns involved and the dynamic response of the bluff bodies. Therefore, the main purposes of this study, in light of the literature review can be defined as follows:

- To understand the effects of the space between, and the arrangement, of circular cylinders on the power content of WIV.
- To investigate the effects of a rigid wall on the behaviour of the downstream elastically mounted cylinder and consequently the amount of power captured by the cylinder.
- To study the effects of a non-circular cylinder such as an airfoil with two degrees of freedom on harnessing energy of oncoming vortices.



To achieve these objectives, **Chapter 3** of the dissertation highlights the availability and amount of the kinetic energy in the wake of a circular cylinder at a transient flow regime using numerical analysis. Two turbulence models have been examined and the numerical models have been validated against previously published data. The mode of vortices, displacement amplitude of the cylinder and vortex shedding frequency of the flow are evaluated due to the importance of the parameters. Following this chapter, the effects of structure such as arrangement of the cylinders are investigated numerically and experimentally in **Chapter 4**. The experimental tests conducted in a water channel confirm the numerical simulations and the outcomes shows similar optimum arrangement for harnessing kinetic energy of the wake. It was found that the staggered arrangement of the cylinders has more potential to capture the energy of the wake of the upstream stationary cylinder as compared to other test cases such as side-by-side arrangements. As the dynamic response of the cylinder is directly proportional to the amount of energy, the displacement amplitude of an elastically mounted cylinder has been investigated when the upstream stationary cylinder was mounted in vicinity of a rigid wall. Therefore, **in Chapter 5**, the effect of the rigid wall on the dynamic response of the downstream cylinder has been studied numerically. Several parameters such as lift coefficient, phase angle between force and displacement and vortex shedding frequency are studied in this chapter. Of all studied test cases, optimum arrangement of the cylinders is introduced. The effect of generated vortices on a symmetric airfoil NACA 0012 as a non-circular body has been numerically and experimentally in the next chapter, **Chapter 6**. Different arrangements were considered for a coupled cylinder-airfoil in this chapter. The wake of the upstream stationary cylinder was divided into three distances based on the length scale of vortices. The fluidic parameters of the flow such as Strouhal number, circulation of vortices and transverse spacing of vortices have been calculated. In this chapter, the numerical results agree

---

with the experiments and the power coefficient of the converter has been evaluated. Finally, in the last section of the thesis, **Chapter 7**, the outlines of the thesis and recommendations for work in the future have been presented.

**References:**

Achenbach, E., Influence of surface roughness on the cross-flow around a circular cylinder. *Journal of Fluid Mechanics*, 46 (2), 321-335, 1971.

Achenbach, E. and Heinecke, E., On vortex shedding from smooth and rough cylinders in the range of Reynolds numbers  $6 \times 10^3$  to  $5 \times 10^6$ . *Journal of Fluid Mechanics*, 109, 239-251, 1981.

Anagnostopoulos, P. and Bearman, P., Response characteristics of a vortex-excited cylinder at low Reynolds numbers. *Journal of Fluids and Structures*, 6 (1), 39-50, 1992.

Angrilli, F., Di Silvio, G. and Zanardo, A., Hydro-elasticity study of a circular cylinder in a water stream. *Flow-Induced Structural Vibrations IUTAM-IAHR Symposium*, 504-512, 1972.

Assi, G., Meneghini, J., Aranha, J. Bearman, P., Experimental investigation of flow-induced vibration interference between two circular cylinders, *Journal of Fluids and Structures*, 22, 819-827, 2006.

Assi, G., Mechanisms for flow-induced vibration of interfering bluff bodies. PhD thesis, Imperial College London, UK, 2009.

Assi, G., Bearman, P. and Meneghini, J., On the wake-induced vibration of tandem circular cylinders: The vortex interaction excitation mechanism. *Journal of Fluid Mechanics*, 661 (1), 365-401, 2010.

Bearman, P.W., Vortex shedding from oscillating bluff bodies. *Journal of Fluid Mechanics*, 16, 195-222, 1984.

Bearman, P. W. and M. Zdravkovich, Flow around a circular cylinder near a plane boundary, *Journal of Fluid Mechanics* 89(1), 33-47, 1978.

Bearman, P. W., Graham, J. M. R., Naylor, P., and Obasaju, E. D., The role of vortices in oscillatory flow about bluff cylinders. *International Symposium on Hydrodynamics and Ocean Engineering*, Norway, 621-626, 1981.

Bearman, P. W., Gartshore, I., Maull, D., Parkinson, G., Experiments on flow-induced vibration of a square-section cylinder, *Journal of Fluids and Structures*, 1, 19-34, 1987.

Bernitsas, M. M. and Raghavan, K., Converter of current/tide/wave energy. *Provisional Patent Application, United States Patent and Trademark Office Serial NO.60/628, 252, 2004.*

Bernitsas, M. M., Raghavan, K., Ben-Simon, Y. and Garcia, E., VIVACE (Vortex Induced Vibration Aquatic Clean Energy): A new concept in generation of clean and renewable energy from fluid flow. *Journal of Offshore Mechanics and Arctic Engineering*, 130, 1-15, 2008.

Bernitsas, M. M., Ben-Simon, Y., Raghavan, K. and Garcia, E., The VIVACE converter: Model tests at high damping and Reynolds number around 10. *Journal of Offshore Mechanics and Arctic Engineering*, 131, 1-12, 2009.

Bishop, R. and Hassan, A., The lift and drag forces on a circular cylinder in a flowing fluid. *Proceedings of the Royal Society of London. Series A. Mathematical and Physical Sciences*, 277 (1368), 32-50, 1964.

Blevins, R.D., Flow-induced vibration. *Krieger Publishing Company, Florida, USA, 1990.*

Bokaian, A. and Geoola, F., Wake-induced galloping of two interfering circular cylinders, *Journal of Fluid Mechanics*, 146, 383-415, 1984.

Bokaian, A. and Geoola, F., Wake displacement as cause of lift force on cylinder pair, *Journal of Engineering Mechanics*, 111, 92-99, 1985.

Bosch, G., M. Kappler, M., and Rodi, W., Experiments on the flow past a square cylinder placed near a wall, *Experimental Thermal and Fluid Science* 13(3): 292-305, 1996.

Brika, D. and Laneville, A., Vortex-induced vibrations of a long flexible circular cylinder, *Journal of Fluid Mechanics*, 250, 481-481, 1993.

Brika, D. and Laneville, A., An experimental study of the aeolian vibrations of a flexible circular cylinder at different incidences. *Journal of Fluids and Structures*, 9(4), 371-391, 1995.

Brika, D. and Laneville, A., The flow interaction between a stationary cylinder and a downstream flexible cylinder. *Journal of Fluids and Structures*, 13 (5), 579-606, 1999.

Carmo, B.S., Estudo numerico do escoamento ao redor de cilindros alinhados. Master's thesis, University of Sao Paulo, Brazil, 2005.

Carmo, B.S., Sherwin, S.J., Bearman, P.W. and Willden, R.H.J., Wake transition in the flow around two circular cylinders in staggered arrangements. *Journal of Fluid Mechanics*, 597, 1-30, 2008.

Chang, C. C. J., Ajith Kumar, R. and Bernitsas, M.M., VIV and galloping of single circular cylinder with surface roughness at  $3.0 \times 10^4 \leq Re \leq 1.2 \times 10^5$ , *Journal of Ocean Engineering*, 38, 1713-1732, 2011.

Cheng, Y., Lien, F., Yee, E. and Sinclair, R., A comparison of large eddy simulations with a standard k-w Reynolds-Averaged Navier–Stokes model for the prediction of a fully developed turbulent flow over a matrix of cubes. *Journal of Wind Engineering and Industrial Aerodynamics*, 91 (11), 1301-1328, 2003.

Den Hartog, J., The vibration problems of engineering. *Proc. 4th Int. Cong. Appl. Mech, Cambridge*, 36-53, 1934.

Derakhshandeh, J. F., Arjomandi, M., Dally, B., Cazzolato, B., Effect of a rigid wall on the vortex induced vibration of two staggered cylinders, American Society of Physics (AIP), *Journal of Renewable and Sustainable Energy*, 6, 033114, 2014.

Ding, Z., Balasubramanian, S., Lokken, R. and Yung, T., Lift and damping characteristics of bare and straked cylinders at riser scale reynolds numbered, *Proceeding of Offshore Technology Conference Paper No.* 16341, 2004.

Egorov, Y., Menter, F., Lechner, R. and Cokljat, D., The scale-adaptive simulation method for unsteady turbulent flow predictions. Part 2: Application to complex flows. *Flow, Turbulence and Combustion*, 85 (1), 139-165, 2010.

Fletcher, D. and Langrish, T., Scale-adaptive simulation (SAS) modelling of a pilot-scale spray dryer. *Chemical Engineering Research and Design*, 87 (10), 1371-1378, 2009.

Garcia, E.M.H., Prediction by energy phenomenology for harnessing hydrokinetic energy using vortex-induced vibrations, PhD thesis, the University of Michigan, 2008.

Govardhan, R. and Williamson, C., Modes of vortex formation and frequency response of a freely vibrating cylinder. *Journal of Fluid Mechanics*, 420, 85-130, 2000.

Govardhan, R. and Williamson, C., Critical mass in vortex-induced vibration of a cylinder. *European Journal of Mechanics-B/Fluids*, 23 (1), 17-27, 2004.

Griffin, O.M. and Ramberg, S.E., 1975. On vortex strength and drag in bluff-body wakes, *Journal of Fluid Mechanics*, 69 (4), 721-728.

Gu, Z., Sun, T., He, D. and Zhang, L., 1993. Two circular cylinders in high-turbulence flow at supercritical Reynolds number, *Journal of Wind Engineering and Industrial Aerodynamics*, 49 (1), 379-388.

Guilmineau, E. and Queutey, P., Numerical simulation of vortex-induced vibration of a circular cylinder with low mass-damping in a turbulent flow, *Journal of Fluids and Structures*, 19 (4), 449-466, 2003.

Hiwada, M., Taguchi, T., Mabuichi, I. and Kumada, M., Fluid flow and heat transfer around two circular cylinders of different diameters in cross flow. *Journal of Strategic Management Education*, 22 (167), 715-723, 1979.

Hover, F.S. and Triantafyllou, M.S., Galloping response of a cylinder with upstream wake interference. *Journal of Fluids and Structures*, 15, 503-512, 2001.

Hover, F., Miller, S. and Triantafyllou, M., Vortex-induced vibration of marine cables: Experiments using force feedback, *Journal of Fluids and Structures*, 11 (3), 307-326, 1997.

Huera-Huarte, F.J. & Bearman, P.W. Wake structures and vortex-induced vibrations of a long flexible cylinder Part 1: Dynamic response, *Journal of Fluids and Structures*, 25, 991-1006, 2009.

Igarashi, T., Characteristics of the flow around two circular cylinders arranged in tandem: I. *JSME International Journal Series B*, 24, 323-331, 1981.

Jauvtis, N. and Williamson, C. H. K., Vortex-induced vibration of a cylinder with two degrees of freedom. *Journal of Fluids and Structures*, 17 (7), 1035-1042, 2003.

Khalak, A. and Williamson, C. H. K., Dynamics of a hydro-elastic cylinder with very low mass and damping, *Journal of Fluids and Structures*, 10 (5), 455-472, 1996.

Khalak, A. and Williamson, C.H.K., Fluid forces and dynamics of a hydroelastic structure with very low mass and damping. *Journal of Fluids and Structures*, 11 (8), 973-982, 1997.

Khalak, A. and Williamson, C., Motions, forces and mode transitions in vortex-induced vibrations at low mass-damping. *Journal of Fluids and Structures*, 13(7-8), 813-851, 1999.

Kiya, M., Tamura, H. and Arie, M., Vortex shedding from a circular cylinder in moderate-reynolds-number shear flow. *Journal of Fluid Mechanics*, 101(4), 721-735, 1980.

Koopmann, G., The vortex wakes of vibrating cylinders at low Reynolds numbers, *Journal of Fluid Mechanics*, 28(3), 501-512, 1967.



Kuo, C., Chein, S. and Hsieh, H., Self-sustained oscillations between two tandem cylinders at reynolds number 1,000. *Experiments in Fluids*, 44(4), 503-517, 2008.

Liaw, K., Simulation of flow around bluff bodies and bridge deck sections using CFD, PhD thesis, University of Nottingham, 2005.

Lu, X.-Y. and Dalton, C., Calculation of the timing of vortex formation from an oscillating cylinder. *Journal of Fluids and Structures*, 10 (5), 527-541, 1996.

Ljungkrona, L., Norberg, C. and Sunden, B., Free-stream turbulence and tube spacing effects on surface pressure fluctuations for two tubes in an in-line arrangement. *Journal of Fluids and Structures*, 5 (6), 701-727, 1991.

Ljungkrona, L., *Characteristics of mean and fluctuating surface pressure distributions on tubes in tandem arrangement and in-line tube bundles*: PhD thesis, Chalmers University of Technology, 1992.

Ljungkrona, L. and Sundén, B., Flow visualization and surface pressure measurement on two tubes in an inline arrangement. *Experimental Thermal and Fluid Science*, 6 (1), 15-27, 1993.

Mahir, N., Three-dimensional flow around a square cylinder near a wall, *Ocean Engineering* 36(5): 357-367, 2009.

Mahir, N. and Rockwell, D., Vortex formation from a forced system of two cylinders. Part I: Tandem arrangement. *Journal of Fluids and Structures*, 10(5), 473-489, 1996.

Martinuzzi, R., S., Bailey, and Kopp G., Influence of wall proximity on vortex shedding from a square cylinder. *Experiments in Fluids*, 34(5): 585-596, 2003.

McKinney, W. and DeLaurier J., The Wing mill: An oscillating-wing windmill, *Journal of Energy*, 5(2), 109-115, 1981.

Menter, F.R., Two-equation eddy-viscosity turbulence models for engineering applications. *AIAA Journal*, 32(8), 1598-1605, 1994.

Menter, F. and Egorov, Y., A scale-adaptive simulation model using two-equation models, 43<sup>rd</sup> AIAA Aerospace Sciences Meeting and Exhibit 1905, 1-13, 2005.

Menter, F. and Egorov, Y., The scale-adaptive simulation method for unsteady turbulent flow predictions. Part 1: Theory and model description, *Flow, Turbulence and Combustion*, 85 (1), 113-138, 2010.

Michelassi, V., Wissink, J., Fr-Ograve, J., Hlich & Rodi, W., Large-eddy simulation of flow around low-pressure turbine blade with incoming wakes. *AIAA journal*, 41 (11), 2143-2156, 2003.

Moe, G., Holden, K. and Yttervoll, P., Motion of spring supported cylinders in subcritical and critical water flows. *The Fourth International Offshore and Polar Engineering Conference*, 3, 468-475, 1994.

Nakamura, Y. and Tomonari, Y., The effects of surface roughness on the flow past circular cylinders at high Reynolds numbers. *Journal of Fluid Mechanics*, 123, 363-378, 1982.

Naudascher, E. and Rockwell, D., Flow-induced vibrations: An engineering guide: Courier Dover Publications, 2012.

Parkinson, G. V., and Dicker D., Wind-induced instability of structures, *Philosophical Transactions of the Royal Society of London*, 269, 395-413, 1971.

Parkinson, G. V., Phenomena and modelling of flow-induced vibrations of bluff bodies, *Progress in Aerospace Science*, 26, 169-224, 1989.

Palau-Salvador, G., Stoesser, T. and Rodi, W., LES of the flow around two cylinders in tandem. *Journal of Fluids and Structures*, 24 (8), 1304-1312, 2008.

Peng, Z., and Zhu Q., Energy harvesting through flow-induced oscillations of a foil, *Journal of Physics of Fluids*, 21(12), 123602, 2009.

Raghavan, K. and Bernitsas, M.M., Enhancement of high damping viv through roughness distribution for energy harnessing at  $8 \times 10^3 < Re < 1.5 \times 10^5$ . *ASME 2008 27th International Conference on Offshore Mechanics and Arctic Engineering*, American Society of Mechanical Engineers, 871-882, 2008.

Raghavan, K. and Bernitsas, M.M., Experimental investigation of Reynolds number effect on vortex induced vibration of rigid circular cylinder on elastic supports. *Ocean Engineering*, 38 (5-6), 719-731, 2011.

Roshko, A., Experiments on the flow past a circular cylinder at very high Reynolds number. *Journal of Fluid Mechanics*, 10 (03), 345-356, 1961.

Ruscheweyh, H. P., Aeroelastic interference effects between slender structures, *Journal of Wind Engineering and Industrial Aerodynamics*, 14, 129-140, 1983.

Sagaut, P., *Large eddy simulation for incompressible flows*: Springer Berlin, 2001.

Sarkar, S. and S. Sarkar, Vortex dynamics of a cylinder wake in proximity to a wall, *Journal of Fluids and Structures*, 26(1), 19-40, 2010.

Sarpkaya, T., A critical review of the intrinsic nature of vortex-induced vibrations, *Journal of Fluids and Structures*, 19 (4), 389-447, 2004.

Skop, R. and Griffin, O., On a theory for the vortex-excited oscillations of flexible cylindrical structures. *Journal of Sound and Vibration*, 41 (3), 263-274, 1975.

Sumer, B. and Fredsoe, J., *Hydrodynamics around cylindrical structures*, World Scientific, 1997.

Sváček, P., Feistauer M., and Horáček J., Numerical simulation of flow induced airfoil vibrations with large amplitudes, *Journal of Fluids and Structures*, 23(3), 391-411, 2007.

Taniguchi, S. and Miyakoshi, K., Fluctuating fluid forces acting on a circular cylinder and interference with a plane wall, *Experiments in Fluids*, 9 (4), 197-204, 1990.

Tritton, D. J., Experiments on the flow past a circular cylinder at low Reynolds numbers, *Journal of Fluid Mechanics*, 6 (04), 547-567, 1959.

Vikestad, K., *Multi-frequency response of a cylinder subjected to vortex shedding and support motions*: Department of Marine Structures, Faculty of Marine Technology, PhD thesis, Norwegian University of Science and Technology, 1998.

Williamson C.H.K., Three-Dimensional Vortex Dynamics in Bluff Body Wakes, Mechanical and Aerospace Engineering, Upson Hall, Cornell University, New York, 1996.

Williamson C. H. K., Sinusoidal flow relative to circular cylinders, *Journal of Fluid Mechanics*, 155, 141–174, 1985.

Williamson C. H. K. and Roshko A., Vortex formation in the wake of an oscillating cylinder, *Journal of Fluids and Structures*, 2, 355-381, 1988.

Williamson, C. H. K. and Govardhan, R., Vortex-induced vibrations. *Annual Review Fluid Mechanics*, 36, 413-455, 2004.

Zdravkovich, M. M., Modification of vortex shedding in the synchronization range. *Journal of Fluids Engineering*, 104 (4), 513-517, 1982.

Zdravkovich, M. M., On origins of hysteretic responses of a circular cylinder induced by vortex shedding, *Zeitschrift für Flugwissenschaften und Weltraumforschung*, 14 (1-2), 47-58, 1990.

Zdravkovich, M. M., Different modes of vortex shedding: An overview. *Journal of fluids and Structures*, 10 (5), 427-437, 1996.

Zdravkovich, M. M. and Pridden D. L., Interference between two circular cylinders; series of unexpected discontinuities, *Journal of Wind Engineering and Industrial Aerodynamics*, 2, 255-270, 1977.

Zdravkovich, M. M., 1988, Review of interference-induced oscillations in flow past two circular cylinders in various arrangements, *Journal of Wind Engineering and Industrial Aerodynamics*, 28, 183-200, 1988.

Zhu, Q., Optimal frequency for flow energy harvesting of a flapping foil.  
*Journal of Fluid Mechanics*, 675, 495-517, 2011.

## Chapter 3

# Harnessing hydropower energy using a circular cylinder

### 3.1. Chapter overview

In this chapter, the VIV response of a single circular cylinder at transient flow regime is studied. Based on the dynamic response of the cylinder the power density of the VIV converter is evaluated numerically using a hybrid turbulence model for a single cylinder.

It is demonstrated that among the many different turbulence models available, Scale Adaptive Simulation (SAS) as a relatively new hybrid model can be utilized to predict the dynamic response of an elastically mounted circular cylinder. The flow pattern and vortex structure in the wake of the cylinder is analysed. Consequently, based on the effective fluidic parameters on the power coefficient, for the rest of study, the SAS model is used to predict the VIV response of the cylinder in the numerical analysis sections. The details of turbulence model including its validation and implementation have been presented and discussed here.

This chapter has been submitted for publication as

### Chapter 3: Harnessing hydropower energy using a single cylinder

---

“A study of a vortex-induced vibration mechanism for harnessing hydrokinetic energy of eddies using an elastically circular cylinder”, by Javad Farrokhi Derakhshandeh, Maziar Arjomandi, Bassam Dally and Benjamin Cazzolato to the *Journal of Applied Mathematical Modelling*, Elsevier.



## Statement of Authorship

Title of Paper	A study of a vortex-Induce vibration mechanism for harnessing hydro kinetic energy of eddies using an elastically circular cylinder
Publication Status	<input type="radio"/> Published, <input type="radio"/> Accepted for Publication, <input checked="" type="radio"/> Submitted for Publication, <input type="radio"/> Publication style
Publication Details	Derakhshandeh, J. F., Arjomandi, M., Dally, B., Cazzolato, B., A study of the Vortex-Induce Vibration mechanism for harnessing hydrokinetic energy of eddies using a single cylinder, Journal of Applied Mathematical Modelling, Ref. No.: APM-D-14-02132, 2014.

### Author Contributions

By signing the Statement of Authorship, each author certifies that their stated contribution to the publication is accurate and that permission is granted for the publication to be included in the candidate's thesis.

Name of Principal Author (Candidate)	Javad Farrokhi Derakhshandeh
Contribution to the Paper	Evaluation of the power content of a single elastically mounted cylinder in a transient flow regime and develop a function for the power coefficient of the VIV based on four dimensionless parameters.
Signature	Date 18/03/2015

Name of Co-Author	Maziar Arjomandi
Contribution to the Paper	Supervised the work, assisted in developing ideas and manuscript evaluation.
Signature	Date 18.03.2015

Name of Co-Author	Bassam Dally
Contribution to the Paper	Supervised the work, assisted in developing ideas and manuscript evaluation.
Signature	Date 18-03-15

Name of Co-Author	Benjamin Cazzolato
Contribution to the Paper	Supervised the work, assisted in developing ideas and manuscript evaluation.
Signature	Date 19/3/15

### **3.2. Manuscript**

#### **A study of a vortex-induced vibration mechanism for harnessing hydrokinetic energy of eddies using an elastically circular cylinder**

Javad Farrokhi Derakhshandeh, Maziar Arjomandi, Bassam Dally and Benjamin Cazzolato

School of Mechanical Engineering

University of Adelaide, Adelaide, South Australia 5005, Australia

#### **Abstract**

This paper aims to study the phenomenon of Vortex-Induced Vibration (VIV) as a potential source of renewable energy. The feasibility of capturing hydrokinetic energy from the vibration of a bluff body such as a cylinder due to cyclic shear forces is explored. The dynamic response of a circular cylinder with one degree of freedom is analysed in a transient flow regime. The theoretical power coefficient of the VIV power is evaluated by employing and assessing two turbulence models. The outcomes of the Scale Adaptive Simulation (SAS) model are compared with results from a Shear Stress Transport (SST) model. To facilitate validation, the fluidic and structural parameters used in the models, including the Reynolds number and the mass and damping ratios, were chosen to be similar to published experimental data. The Reynolds number was varied from 2,000 to 25,000. The vortex structure, the force acting on and the displacement of the cylinder is presented and analysed. It is shown that the power coefficient of the VIV power is a function of four dimensionless parameters comprising the lift coefficient, the Strouhal number, the maximum displacement of the cylinder and phase angle between force and displacement of the cylinder, which vary with the reduced velocity. Furthermore, while the previous

numerical investigations were unable to fully capture all flow regimes using the  $k-\omega$  model (Guilmineau and Queutey 2003). It is observed that the SST model is able to cover all three branches of the flow-induced oscillation of the cylinder. Based on the numerical results of the SST model, the maximum obtained theoretical power coefficient of the VIV power is evaluated to be approximately 10% for a single cylinder.

*Keywords: Vortex Induced Vibration, hydropower energy, vortex shedding frequency, circular cylinder.*

## **1. Introduction**

Flow around an elastically mounted circular cylinder can be found in many engineering applications spanning civil, mechanical, aerospace and marine systems, which can cause a vibration. The phenomenon is known as Vortex-Induced Vibration (VIV) and it is generally associated with the lock-in phenomenon when the motion of the compliant structure couples with the shedding frequency of the fluid leading to resonance. Therefore, it is generally known that VIV can be a disastrous phenomenon to structures due to the undesirable synchronisation. Nevertheless, the feasibility of the VIV to produce hydropower energy as a clean and renewable energy is at the centre of this study.

The practical significance of VIV has led to a large number of investigations and different aspects of fluidic and structural parameters have been experimentally and numerically studied (Bearman 1984, Parkinson 1989, Govardhan and Williamson 2000, Williamson and Govardhan 2004, Carmo 2005). Bearman (1984) studied the oscillation of a cylinder in a cross-flow due to vortices, and found that the maximum amplitude of oscillation is achievable over a range of the reduced velocity,  $U_r = U/(f_n D)$ , where  $U$  is

the free stream velocity,  $f_n$  is the natural frequency of the elastically suspended cylinder and  $D$  is the diameter of the cylinder.

Govardhan and Williamson (2000) showed that three types of resonance are generated when the mass damping ratio is kept low, namely; initial, upper and lower. However, at high mass damping, Feng (1968) showed that only the initial or the lower types of amplitude occur. The response of a circular cylinder at low Reynolds numbers,  $Re = 90$  to  $150$ , has been investigated by Anagnostopoulos and Bearman (1992). It was shown that the maximum amplitude of oscillation occurs close to the lower branch of the lock-in, where the motion of the structure dominates based on the frequency of vortex shedding.

A series of water channel experiments on an array of circular cylinders conducted by Bernitsas *et al.* (2008) determined an empirical expression for the efficiency of VIV power. They showed that the phase lag of the lift force on the cylinder with respect to the displacement of the cylinder would cause a reduction in work production since work is the product of the force and displacement. In addition, it was shown that the VIV phenomenon can be employed as a source of energy production with acceptable theoretical and experimental efficiencies, which were found to be 37% and 22%, respectively (Bernitsas *et al.* 2008).

Despite the numerous experimental studies on VIV of a circular cylinder, the application of VIV to generate environmentally clean energy has drawn less attention in the literature. In most experimental works investigating the VIV phenomenon, the measurements necessary for a deep understanding of the flow mechanics are difficult and time consuming. Therefore, numerical simulations can be employed to give an initial solution to cover all branches of the oscillation of the structures with lower cost. On the other hand, within

a transient flow, no simulations have been yet conducted utilizing a hybrid formulation of Reynolds Average Navier Stokes (RANS) and Large Eddy Simulation (LES), known as Scale Adaptive Simulation (SAS) model. In the SAS turbulence model, the turbulence length-scale is resolved by considering the definition of Von Karman length scale. This assists in more accurately to capturing the vortex structure.

The current study aims to harness hydrokinetic energy of the fluid and to analyse the relative features of the flow, such as vortex structures, utilizing a circular cylinder immersed in a transient flow regime. Within the transient flow regime, the turbulent viscosity reduces with increasing the free stream velocity. Therefore, in a transient turbulent flow using the RANS model, there is a tendency to estimate a larger length scale. This rough estimation does not allow the spectrum of length scale to be resolved correctly (Menter and Egorov 2005). Since the length scale is directly related to the circulation and consequently shear forces, it can alter the dynamic behaviour of the structure. Numerical investigations of the VIV conducted by Guilmineau and Queutey (2003) using  $k-\omega$  turbulence model revealed that although the displacement amplitude of the cylinder at the initial and lower branches of oscillation matched the experimental data of Govardhan and Williamson 2000, the  $k-\omega$  turbulence model is not capable of predicting the upper branch of oscillation.

In the current paper, the application of VIV phenomenon in harnessing hydropower energy is evaluated. The dynamic response of the cylinder with one degree of freedom is studied at a transient flow regime. With the aim of capturing the energy of the vortices, the fluidic parameters of the VIV such as vortex structure need to be addressed. Furthermore, the effects of the shear forces, the Reynolds number and vortex shedding frequency as the critical parameters on the VIV energy need to be highlighted when both

turbulence models are assessed. Consequently, flow around an elastically mounted cylinder is modelled and the numerical results are compared with previously published experimental data obtained by Govardhan and Williamson (2000). Furthermore, the theoretical power coefficient of VIV power for a single cylinder is presented based on four dimensionless parameters.

## 2. Mathematical formulation

With the aim of harnessing VIV energy from currents and shallow rivers, in this section, the equations of incompressible flow are presented followed by the structural model.

### 2.1. Flow model

In order to predict the response of the circular cylinder under the effect of the flow, Reynolds Average Navier-Stokes equations for 2D flow comprising conservation of mass and momentum for incompressible flow are employed and can be written as follows:

$$\frac{\partial u_i}{\partial x_i} = 0, \quad (1)$$

$$\frac{\partial u_i}{\partial t} + u_j \frac{\partial u_i}{\partial x_j} = -\frac{1}{\rho} \left( \frac{\partial P}{\partial x_i} \right) + \vartheta \frac{\partial^2 u_i}{\partial x_j^2} - \frac{\overline{u'_i u'_j}}{\partial x_j}, \quad (2)$$

where,  $x$  represents the direction,  $u$  is the mean velocity component in  $x$  and  $y$  directions,  $u'$  is the fluctuating part of the free stream velocity,  $\rho$  is the density of the fluid and  $P$  denotes the dynamic pressure. The term  $\overline{u'_i u'_j}$  presents the Reynolds stress component, which is defined in terms of a turbulent viscosity  $\vartheta_t$  as

$$-\frac{\overline{u'_i u'_j}}{\partial x_j} = \vartheta_t \left( \frac{\partial u_i}{\partial x_j} + \frac{\partial u_j}{\partial x_i} \right) - \frac{2}{3} k \delta_{ij}, \quad (3)$$

where,  $k$  is the turbulent kinetic energy and  $\delta_{ij}$  is the Kronecker delta function.

The SST model is an Unsteady Reynolds-Averaged Navier-Stokes (URANS) model, which was developed by Menter (1994). It accounts for the transport of the turbulent shear stress inside the boundary layers. SST comprises a combination of the  $k-\omega$  and  $k-\varepsilon$  turbulence models to overcome the problems associated with the prediction of length scales, not only close to the walls for the  $k-\omega$  model, but also free stream dependency of the  $k-\varepsilon$  model (Menter 1994). It has been shown that the prediction of flow structure over a circular cylinder with SST is more accurate compared to both  $k-\omega$  and  $k-\varepsilon$  models (Liaw 2005). The values of  $k$  and  $\omega$  can be calculated from the transport equations for the turbulence kinetic energy ( $k$ ) and the turbulence eddy frequency ( $\omega$ ), respectively, which are written as follows

$$\begin{aligned} \frac{\partial(\rho k)}{\partial t} + \frac{\partial(\rho u_j k)}{\partial x_j} &= P_t - \beta^*(\rho \omega k) \\ &+ \frac{\partial}{\partial x_j} \left[ (\mu + \sigma_k \mu_t) \frac{\partial k}{\partial x_j} \right] \end{aligned} \quad (4)$$

$$\begin{aligned} \frac{\partial(\rho \omega)}{\partial t} + \frac{\partial(\rho u_j \omega)}{\partial x_j} &= \frac{\gamma}{\vartheta_t} P_t - \beta \rho \omega^2 + \frac{\partial}{\partial x_j} \left[ (\mu + \sigma_\omega \mu_t) \frac{\partial \omega}{\partial x_j} \right] \\ &+ 2(1 - F_1) \frac{\rho \sigma \omega^2}{\omega} \frac{\partial k}{\partial x_j} \frac{\partial \omega}{\partial x_j}. \end{aligned} \quad (5)$$

In the above equations,  $\mu$  and  $\mu_t$  are the laminar and turbulent viscosity, respectively,  $\beta$  and  $\beta^*$  are constant coefficients,  $\vartheta_t$  is the eddy viscosity,  $\gamma$

---

represents turbulence intermittency factor. Here,  $P$  is the turbulence production rate and is a function of turbulence viscosity. The turbulence viscosity can be calculated via

$$\mu_t = \frac{\alpha \rho k}{\max(\alpha \omega, SF_2)}, \quad (6)$$

where,  $\alpha$  is a constant,  $S$  is the magnitude of the shear strain rate,  $F_1$  and  $F_2$  are blending functions. These functions switch smoothly between two turbulence models based on values of the local solution and the distance from the wall.

Despite the advantages of the SST model compared with  $k-\omega$  and  $k-\varepsilon$ , it behaves similarly to the  $k-\varepsilon$  model away from the wall (Fletcher and Langrish 2009). When the SST model is utilised in transient simulations, it generates large length-scales and consequently turbulence viscosities are too high. Hence, this does not allow a spectrum of length scales to be determined appropriately (Menter and Egorov 2005). In the SAS turbulence model, the incapability of resolving the turbulence length-scale is overcome by considering the definition of Von Karman length scale, which is given by

$$L_{vk} = k \left| \frac{\partial U / \partial y}{\partial^2 U / \partial y^2} \right|. \quad (7)$$

Here,  $k$  represents the turbulent kinetic energy. Using the von Karman length scale enables the model to adapt its behaviour to Scale Resolving Simulation (SRS) according to the stability parameters of the flow (Egorov *et al.* 2010). This allows the model to provide a balance between the contributions of the simulated and resolved parts of the turbulence stresses. Hence, the model can effectively and automatically switch from the Large



Eddy Simulation (LES) mode to the Reynolds Average Navier Stokes (RANS) mode (Menter and Egorov 2010).

## 2.2. Structural model

Figure 1 shows the schematic of the system under investigation, comprising an elastically mounted circular cylinder with one degree of freedom in the  $y$ -direction perpendicular to the free stream velocity of a cross flow. The response of the cylinder can be approximated by a mass-spring-damper model (Bearman 1984). Therefore, the equation of motion based on a linear mass-spring-damper can be written as

$$m\ddot{y}(t) + c\dot{y}(t) + ky(t) = F_y(t), \quad (8)$$

where,  $m$  is the mass of the cylinder,  $\dot{y}$  and  $\ddot{y}$  are the velocity and acceleration of the cylinder, respectively,  $c$  is the viscous damping constant and  $k$  is the spring stiffness. Here,  $F_y$  represents the force exerted on the cylinder by the fluid perpendicular to the direction of flow.

In the VIV phenomenon, the natural frequency of oscillation can be influenced considerably by the additional mass of fluid that is accelerated with the bluff body, and is particularly prevalent in bluff bodies immersed in water, as opposed to air. For this reason, the mass ratio is defined as the non-dimensional parameter based on the specific mass of the fluid in which the cylinder is immersed (Assi 2009). Therefore, the structural parameters, including the mass ratio and structural damping ratio, are generally expressed by  $m^* = 4m/\rho\pi D^2L$  and  $\zeta = c/2\sqrt{km}$ , respectively (Khalak and Williamson 1996). Here,  $L$  is the length of the cylinder.

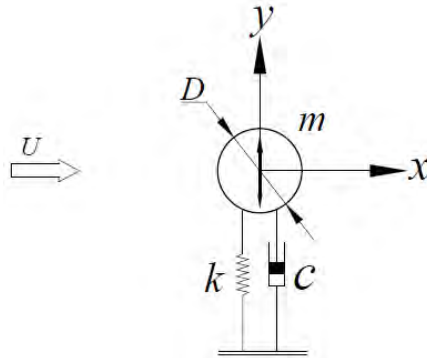


Figure 1: Schematic of an elastically mounted cylinder with 1DOF in a cross flow.

The dynamic response of the cylinder needs to be interpreted instantaneously during the modelling using ANSYS Fluent package. Therefore, in a User Defined Function (UDF) the dynamic response of the cylinder was defined. The UDF file is a C++ code comprising the equation of motion of the cylinder, which was loaded in ANSYS Fluent. Consequently, the oscillation of the cylinder was estimated in Fluent along the unconstrained direction ( $y$ -axis) at every time step. This is obtained by defining instantaneous changes in the velocity of the elastically mounted cylinder, which can be obtained by manipulating Equation (8) to give the expression for the velocity of the cylinder

$$d\dot{y} = \frac{F_y - c\dot{y} - ky}{m} dt. \quad (9)$$

Equation (9) was utilized along with dynamic mesh model in ANSYS Fluent. The dynamic mesh model operates an *Arbitrary Lagrangian Eulerian (ALE)* algorithm and a local remeshing approach for the adaption of the mesh in Fluid Structure Interaction problems. Of the three types of meshing methods available in ANSYS (smoothing, layering and remeshing), the diffusion smoothing mesh method was selected to model the dynamic response of the cylinder and the mesh was updated at each time

---

step. This allows the nodes to follow the motion of the cylinder as rigidly as possible without any interference between mesh and cylinder. Therefore, a consistent  $y$ -plus (non-dimensional wall distance for a wall-bounded flow), is achievable regardless of the motion of the cylinder.

### 2.3. Domain and mesh structure

The 2D, time-dependent, incompressible Navier-Stokes equations were solved using a symmetry preserving Finite-Volume scheme of second order spatial and temporal accuracy. The cylinder was mounted on an elastic support and was allowed to move in the  $y$ -direction only. Figure 2 shows a schematic of the boundary domain and the position of the cylinder. The cylinder was mounted in a large boundary domain to eliminate the effects of the blockage and outlet pressure. The streamwise spacing of  $25D$  was chosen behind the cylinder to eliminate the effect of outlet pressure. Furthermore,  $9D$  spacing was created on each side of the cylinder to remove the blockage effects when the cylinder oscillates. Consequently, the blockage ratio was approximately 5%, which is smaller than the blockage ratio of 8% used by Wanderley *et al.* (2008), who demonstrated that this blockage is adequate. The blockage ratio is calculated based on the projected area of the cylinder and cross-section area. The diameter of the cylinder was  $D = 50$  mm and the Reynolds number was varied from 2,000 to 25,000. It was assumed that cylinder's surface was smooth.

The structural parameters such as diameter, mass, stiffness and damping constant used in the current work have been chosen based on the experimental data of Govardhan and Williamson (2000). Therefore, the mass ratio and damping ratio of the system were set up at  $m^* = 2.4$  and  $m^* \zeta = 0.01$ , respectively.

### Chapter 3: Harnessing hydropower energy using a single cylinder

---

In order to ensure a grid-independent solution, three sets of structured meshes were generated and the models were simulated at the maximum Reynolds number considered in this study ( $Re = 25,000$ ). This selection ensures that all the lower Reynolds number cases have a high quality mesh.

The density of the mesh elements around the cylinder is shown in Figure 3 and the results including the Strouhal number, the drag and lift coefficients are summarized in Table 1. The grid convergence results reveal that the refined and highly refined meshes provide similar outcomes in terms of the Strouhal number and time averaged drag and lift coefficients (refer to Table 1). Therefore, the refined mesh (Test case 2) is considered to give sufficient grid resolution for the remaining numerical models.

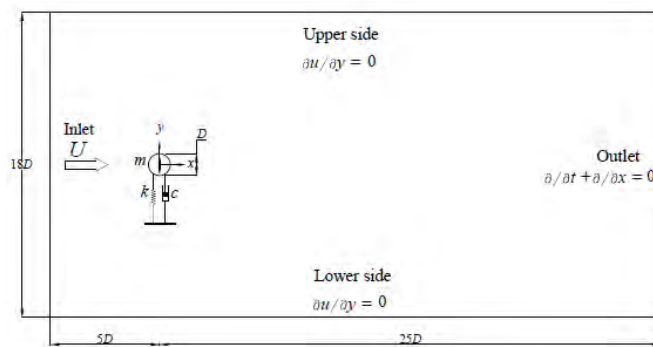
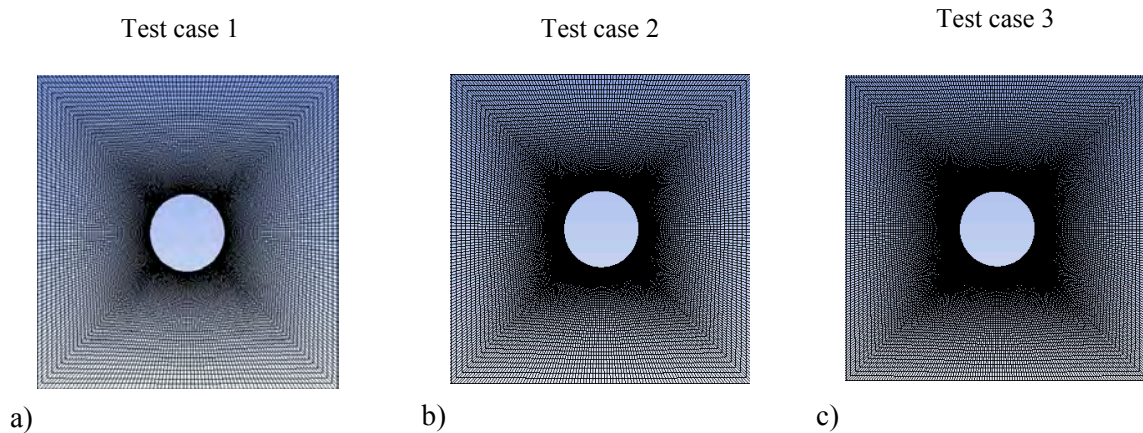


Figure 2: Schematic of computational domain for the elastically mounted circular cylinder comprising boundary conditions.



## Chapter 3: Harnessing hydropower energy using a single cylinder

---

Figure 3: Computational mesh, and the density of mesh in proximity of the circular cylinder. The detail of each test case is explained in Table 1.

Table 1: Mesh refinement sensitivity, including the Strouhal number and time-averaged drag and lift coefficients.

Test case	Mesh quality	Mesh elements	Strouhal number	$\bar{C}_D$	$\bar{C}_L$
1	Coarse	38520	0.210	1.15	0.17
2	Refined	51668	0.200	1.05	0.15
3	Highly refined	60628	0.200	1.05	0.15

### 3. Results and discussion

Numerical simulations were initially validated using previous experimental studies conducted on flow around a single cylinder. With this approach, the flow around a *stationary* and *elastically* mounted cylinder was modelled.

#### 3.1. Validation of models

In order to ensure the validity of the numerical simulation and the mesh in the current study, the flow around the stationary cylinder was modelled utilizing both SAS and SST models. Transient flow around the cylinder was modelled at  $Re = 3,900$ , which is similar to Lourenco and Shih (1993), Ong and Wallace (1996) and Lia (2005). This facilitates the comparison of the numerical results with experimental and numerical data reported in the literature. In order to achieve solution convergence on the effect of the residual level on the numerical results, a maximum residual target of  $10^{-5}$  was applied. Furthermore, the lift and drag coefficients of the cylinder were monitored during the solution process and the stability of these coefficients was taken into account to accompany the convergence criterion. The time step was set to  $\Delta t = 0.025$  s, which is small enough to satisfy the Courant–

Friedrichs–Lewy (CFL) condition ( $CFL < 1$ ), and is essential for convergence of the simulations.

Figure 4 shows the profiles of the dimensionless mean streamwise velocity in the wake region of the cylinder at  $x/D = 1, 3$  and  $5$ . Here,  $\bar{u}$  represents the average of the  $x$ -component of the velocity, which was calculated over the total running time. At the  $x/D = 1$  region, which is very close to the cylinder, the velocity profile drops to below zero, representing a recirculation region. Further away in the wake of the cylinder, at  $x/D = 3$  and  $x/D = 5$ , the velocity profiles show positive values. For all selected regions in the wake of the cylinder, the behaviour of the velocity profiles shows an identical trend. In addition, it is observed that for both turbulence models, the size of the recirculation region in the wake of the cylinder is very similar to the experimental and numerical data of Lourenco and Shih (1993), Ong and Wallace (1996) and Kiaw (2005). For instance, at  $x/D = 1$ , the recirculation region shows negative values for both turbulence models and further in the wake, at  $x/D = 3$  and  $x/D = 5$ , positive values are estimated.

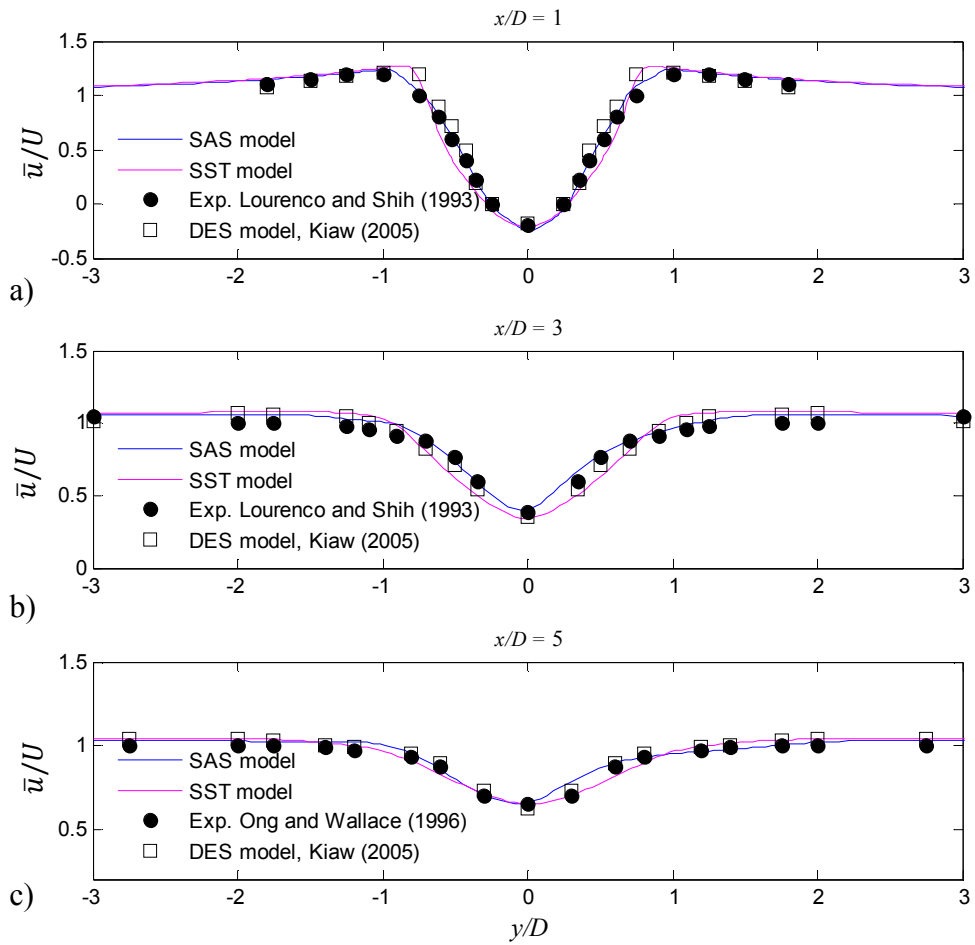


Figure 4: Non-dimensional mean streamwise velocity at different regions in the wake of the stationary cylinder at  $Re = 3,900$ , a)  $x/D = 1$ , b)  $x/D = 3$  and c)  $x/D = 5$ .

In order to evaluate the power coefficient of the VIV, the dynamic response of the cylinder is also considered. Figure 5 summarizes the results of the dynamic behaviour of the elastically mounted cylinder in terms of the dimensionless amplitude,  $Y^*$ , and the force-displacement phase angle,  $\Phi$ , as a function of the reduced velocity. The amplitude of the oscillation is compared with the experimental data of Govardhan and Williamson (2000) and numerical results of the  $k-\omega$  model reported by Guilmineau and Queutey (2003). The amplitude of oscillation using  $k-\omega$  shows that although this model captures the salient dynamics of the *initial* and *lower branches* of

the displacement, at *the upper branch* the results do not match the experimental data or the results from SST and SAS models. In spite of the limitations of the  $k-\omega$  model, the SST and SAS models reveal that these two models are able to reproduce all three branches of oscillation. On the other hand, at  $U_r \geq 10$  (lower branch of oscillation), the results of SST model shows a better agreement compared to SAS model. It is also worth noting that even at *the lower branch* of oscillation, the SST model shows better agreement compared with the SAS model. In addition, it can be seen that by increasing the reduced velocity the phase angle jumps to the upper curve with approximately  $175^\circ$  with the transition in the vortex formation mode. Therefore, to evaluate the theoretical power coefficient of the cylinder, the SST model is chosen for the rest of study.



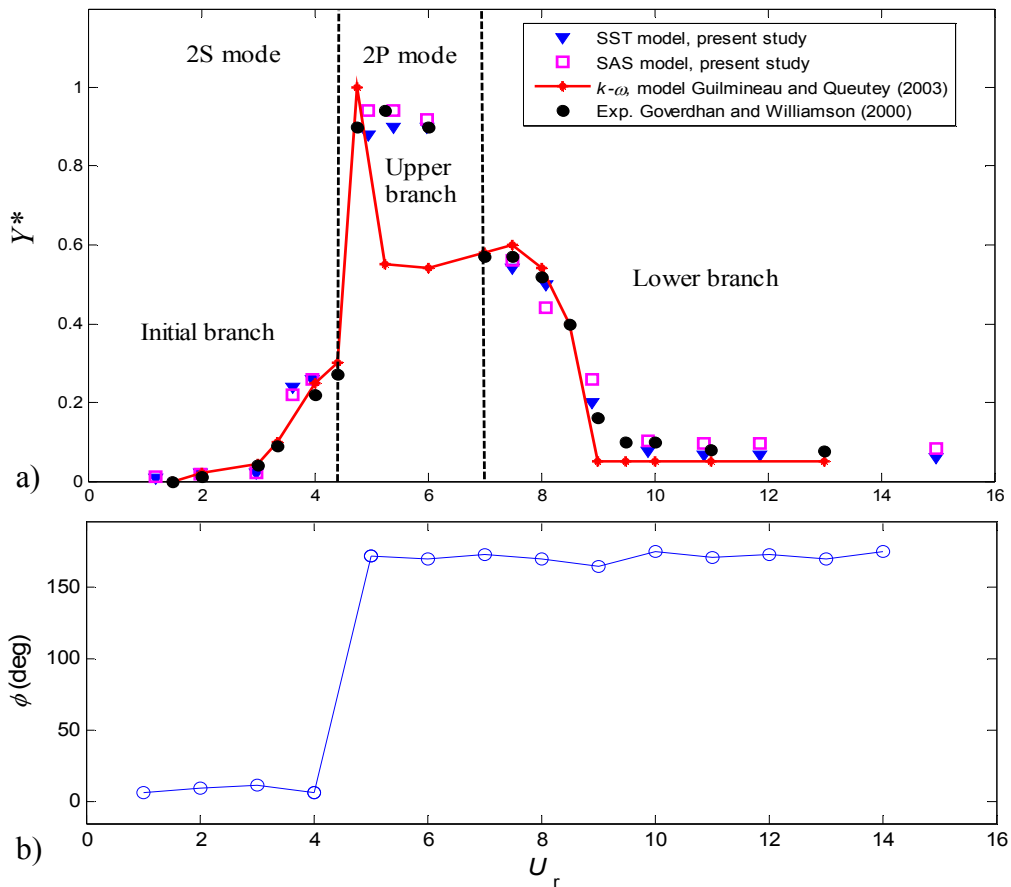


Figure 5: Dynamic response of the cylinder, a) comparison of the displacement amplitude of the circular cylinder for both SST and SAS models as a function of the reduced velocity, b) phase angle between force and displacement as a function of reduced velocity.

### 3.2. Vortex dynamics

The cylinder in this system is constrained to oscillate in  $y$ -direction only and the transverse oscillation depends upon the strength of the vortex shed. The dynamic response of the cylinder alters as the reduced velocity increases due to a growth of the free stream velocity. Therefore, to calculate the power coefficient of the cylinder, both the vortex structure and the key parameters of the VIV energy need to be considered, where the fluid and structure interaction problems are solved. As mentioned earlier, the response

of the cylinder can be categorised into three groups named as initial, upper and lower (Govardhan and Williamson 2000) as a function of reduced velocity. Therefore, to study the dynamic response of the cylinder in each category, a typical reduced velocity (or equivalent Reynolds number) was chosen and the results of the numerical studies for SST model is analysed.

The oscillation of the cylinder depends on the strength of the vortices, and vortex structure would highlight the features of vortices in the wake of the cylinder. Figure 6 compares the instantaneous vorticity contours at four Reynolds numbers for SST model. The Reynolds numbers are chosen based on the three branches of oscillation. In addition, the figure shows instantaneous vorticity contours at  $Re = 8,000$  ( $U_r = 4.8$ ), where the cylinder jumps to the upper branch. Herein, to aid in the comparison, the minimum and maximum vorticity magnitude are defined with the same range between 0 and 20. The range of vorticity magnitude was set in ANSYS Fluent.

The vortex shed in the wake of the circular cylinder depends on the reduced velocity. The pattern can involve a single vortex (S) and/or pair of vortices (P) generating patterns such as 2S, 2P modes or a combination of them. The term 2S is defined as two single vortices produced during each oscillation cycle, while the 2P mode is characterised by two pairs of vortices per cycle, which are the principal modes of vortices in the synchronisation region (Williamson and Roshko 1988). It can be seen that at the initial branch, the 2S mode pattern is formed. By increasing the reduced velocity to  $U_r = 4.8$ , the mode of vortices changes to 2P mode.

An explanation for this trend is offered here. At the initial branch, the vortices originate from each surface of the cylinder with 2S mode. As the reduced velocity increases, the generated vortices which are closer to the cylinder form a little earlier, relative to the new half period. This allows the

generation of two pairs of vortices by rolling up the developed vortices, resulting in stronger vortices in the 2P mode. The significance of the transition from 2S to 2P mode (or from lower to the upper branches of oscillation) is in the sharp increment of the shear forces acting on the cylinder, which was reported by Bishop and Hassan (1964). As a consequence, the maximum amplitude of oscillation for the cylinder under the effect of the sharp increment of the shear forces is acceptable at the upper branch of oscillation. It can be seen that the major vortex pattern of 2P is captured by both SST and SAS models at the upper branch of oscillation and accordingly the cylinder is under the effect of the principal vortices.

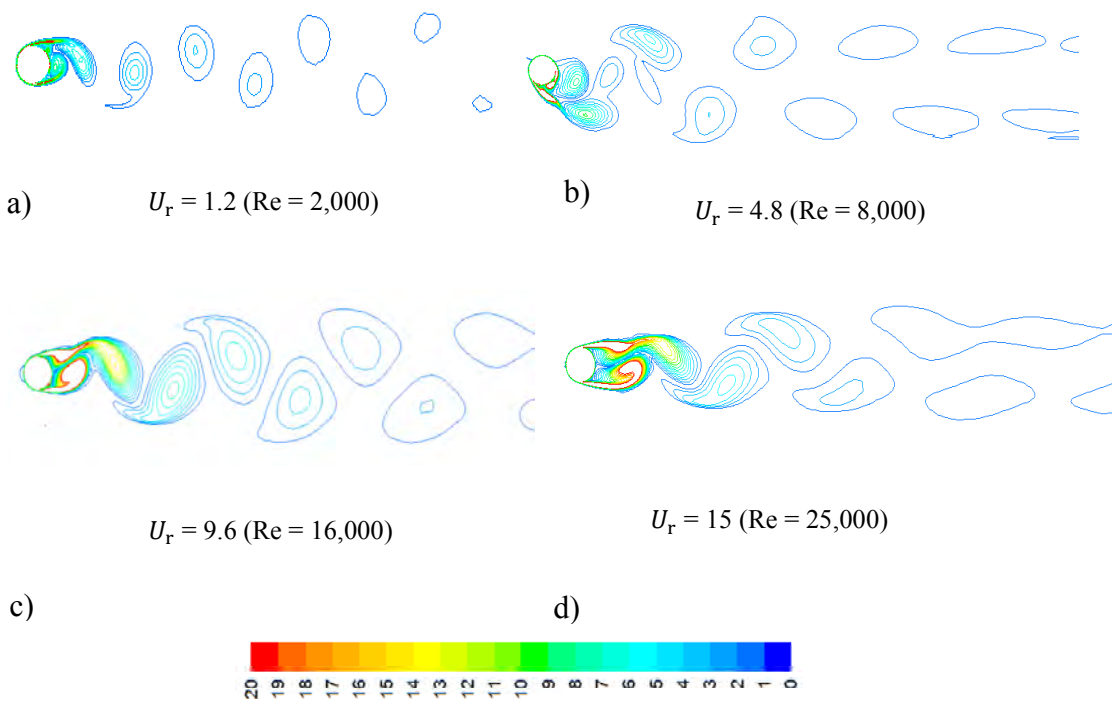


Figure 6: Instantaneous vorticity contours ( $s^{-1}$ ) at the initial, upper and lower branches of oscillation. Reduced velocities are  $U_r = 1.2, 4.8, 9.6$  and  $15$ , or  $Re = 2,000, 8,000, 16,000$  and  $25,000$ , respectively.

The resulting time histories of the lift and drag coefficients are plotted in Figure 7. The lift and drag coefficients are presented at selected reduced velocities;  $U_r = 1.2, 3.6, 4.8, 6.0, 9.6$  and  $15.0$  (or equivalent Reynolds numbers  $Re = 2,000, 6,000, 8,000, 10,000, 16,000$  and  $25,000$ , respectively). It is observed that at a low reduced velocity ( $Re = 2,000$ ) or initial category of the VIV response, the SST model estimates the regular fluctuations for drag and lift coefficients (Figure 7-a). By increasing the reduced velocity to  $U_r = 3.6$ , the shear force fluctuations increase. Although this trend arises for both lift and drag forces, the results reveal that the fluctuation of the drag is weaker compared with the fluctuation of the lift coefficient. The shear forces significantly increase as the Reynolds number increases to  $Re = 8,000$  or ( $U_r = 4.8$ ). The larger lift force here is generated by the vortex shedding process, in which the frequency of vortices is very close to the natural frequency of the cylinder. The induced drag force is generated and As a consequence, the maximum amplitude of the drag coefficient increases (Figures 7-e). It can be seen that by increasing the Reynolds number from 2,000 to 8,000 in the initial branch of oscillation, the magnitude of the drag coefficient increases. At this range of Reynolds numbers, the lift coefficient of the cylinder gradually increases. It is also observed that the frequency of the shear forces gradually increases when the Reynolds number rises. The maximum lift and drag coefficient can be observed when the cylinder starts to jump to the upper branch of oscillation at  $Re = 8,000$ .

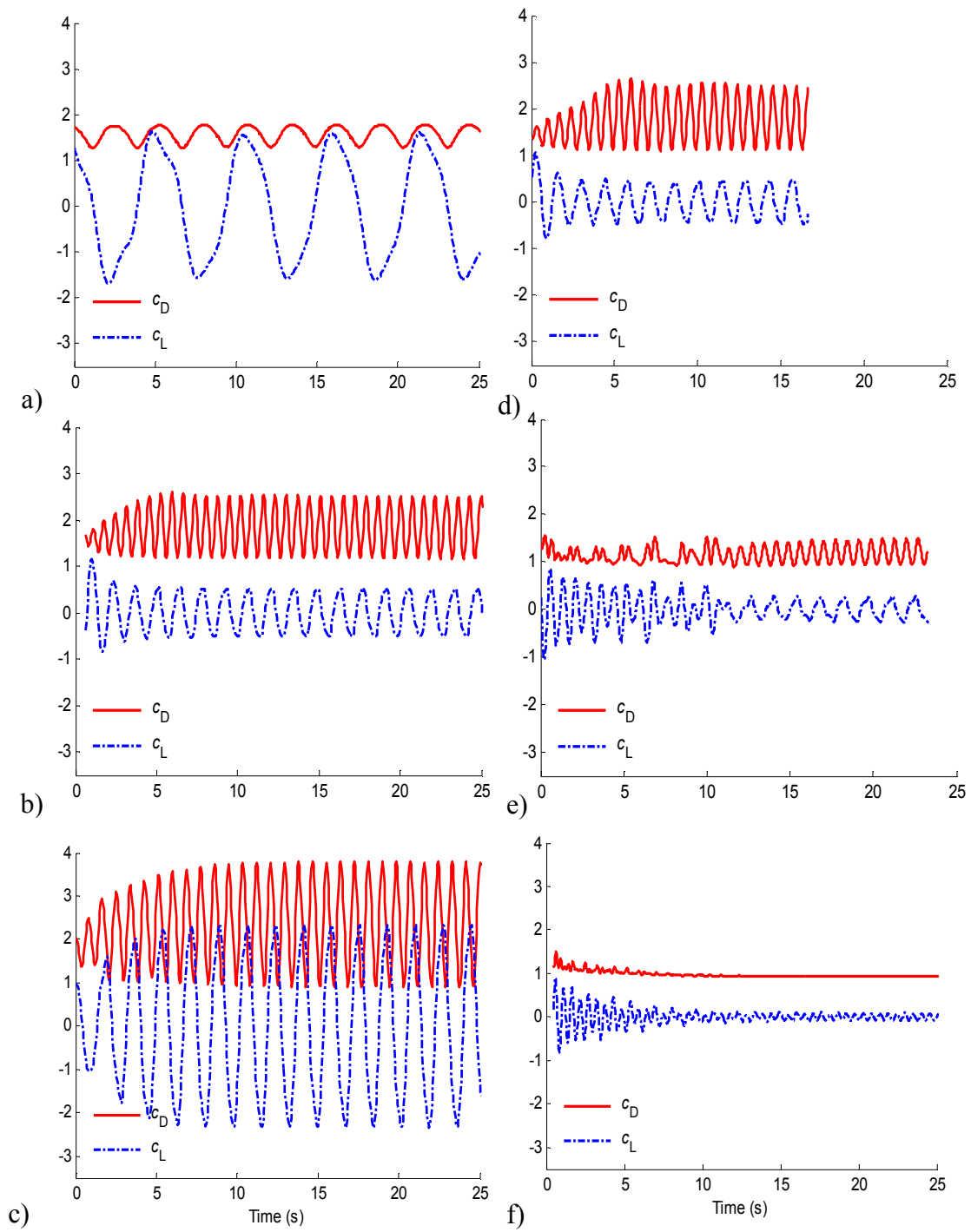


Figure 7: Time history of the lift and drag coefficients of the elastically mounted cylinder as a function of the Reynolds number (reduced velocity). a)  $Re = 2,000$ , b)  $Re = 6,000$ , c)  $Re = 8,000$ , d)  $Re = 10,000$ , e)  $Re = 16,000$ , f)  $Re = 25,000$ .

Further increase in the Reynolds number results in a reduction in the drag coefficient. This is due to the reduction of turbulent viscosity at higher Reynolds numbers. In a turbulent flow, the effective viscosity is the sum of the laminar and turbulent viscosity. For higher Reynolds numbers, the drag coefficients of the cylinder exhibits a similar trend with the same average amplitude, in particular at the maximum Reynolds number,  $Re = 25,000$ .

The time history of the displacement of the cylinder is also analysed and the results are plotted in the left hand column of Figure 8 as a function of the Reynolds number. The instantaneous displacement of the cylinder was calculated in ANSYS Fluent at each Reynolds number. In addition, spectral analysis using the Fast Fourier Transform of the displacement of the cylinder was carried out to gain more insight. The right column in Figure 8 represents the amplitude spectrum of the vertical displacement of the cylinder, plotted as a function of the dimensionless frequency (defined as the frequency of oscillation normalised by the natural frequency of the cylinder). The amplitude spectrum was obtained using a FFT, with the data sampled at 40 Hz based on the selected time step ( $\Delta t = 0.025$  s) over a total length.

In Figure 8-a, the first time series of the displacement ( $Re = 2,000$ ) shows the minimum amplitude of oscillation since it is in the initial branch of the VIV response. Furthermore, the magnitude of the FFT plot at this Reynolds number (Figure 8-b) exhibits two peaks, in which the lower frequency with higher magnitude belongs to the vortex shedding frequency and the higher frequency with lower magnitude reflects the natural frequency of the cylinder. By increasing the Reynolds number, these two peaks appear to merge into one peak and lock-in occurs with maximum amplitude of oscillation. The maximum amplitude of  $Y^* = y/D = 0.95$  occurs when the Reynolds number is  $Re = 8,000$  (Figure 8-e). This amplitude is in good

quantitative agreement with published data of Govardhan and Williamson (2000). Further increase in Reynolds number leads to a regular reduction of the amplitude of oscillation. This can be also observed from the magnitude of FFT of the cylinder displacement (comparing the magnitude of the oscillation frequencies in Figures 8-h and 8-j).

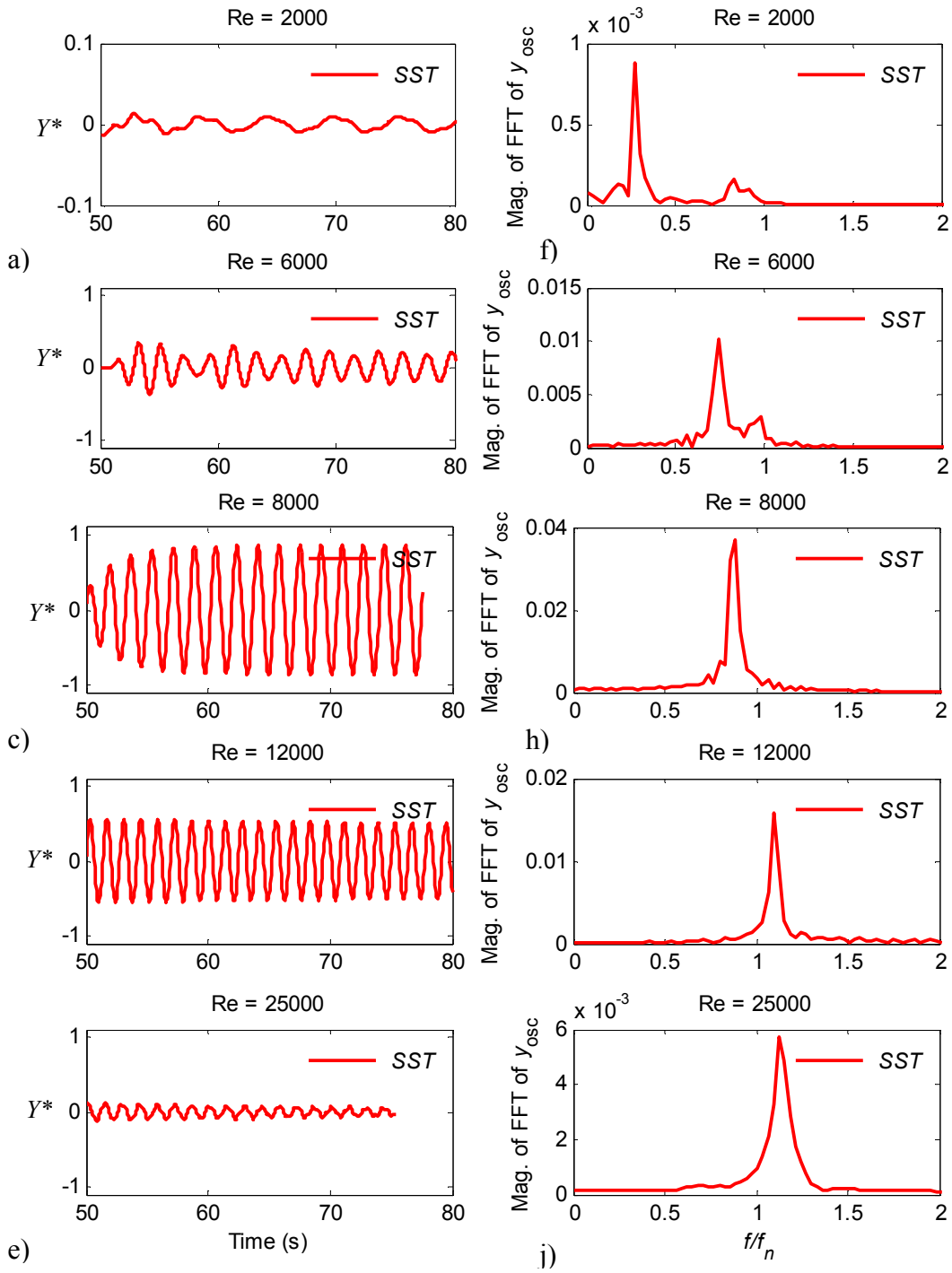


Figure 8: Comparison of the time history of the cylinder displacement as a function of the Reynolds number (left column) for SST model and the frequency response of the cylinder (right column), a) and b) Re = 2,000, a) and c) Re = 6,000, e) and f) Re = 8,000, g) and h) Re = 12,000, and i) and j) Re = 25,000.



### 3.3. Power coefficient of VIV for a single cylinder

By assuming linear behaviour and sinusoidal response of the cylinder, the time dependent displacement, velocity and lift coefficient of the cylinder can be obtained from the following equations respectively,

$$y(t) = y \sin(2\pi f_s t), \quad (10)$$

$$\dot{y}(t) = (2\pi f_s) y \cos(2\pi f_s t), \quad (11)$$

$$c_L(t) = C_L \cdot \sin(2\pi f_s t + \Phi), \quad (12)$$

where,  $y$  is the maximum amplitude of the displacement,  $f_s$  represents the frequency at which vortices are shed,  $\dot{y}$  and  $c_L$  are the time dependent velocity and lift coefficient of the cylinder,  $C_L$  is the lift coefficient amplitude, and  $\Phi$  is the phase angle of the displacement with respect to the exciting lift force.

The work done by the fluid force during one cycle of oscillation,  $T_{cyl}$ , can be calculated as (Bernitsas *et al.* 2008)

$$W_{VIV} = \int_0^{T_{cyl}} C_L \cdot \dot{y} \cdot dt. \quad (13)$$

The mean power delivered by the cylinder is given by

$$P_{VIV} = \frac{W_{VIV}}{T_{cyl}}. \quad (14)$$

It can be seen that by integrating the right hand term of Equation (13) and averaging over the cycle period, the power due to VIV for a circular cylinder can be obtained

$$P_{\text{VIV}} = \frac{1}{2} \pi \rho U^2 C_L f_{\text{osc}} y_{\text{max}} DL \sin(\Phi). \quad (15)$$

The detailed derivation of Equation (15) has been reported in Bernitsas and Raghavan (2004). Hence, the power coefficient of VIV can be written as

$$\eta_{\text{VIV}} = \frac{P_{\text{VIV}}}{P_{\text{fluid}}}, \quad (16)$$

where,  $P_{\text{fluid}}$  is the power of the fluid, which is the product of the acting force on the cylinder ( $\frac{1}{2} \rho U^2 DL$ ) and the velocity in the same direction of force ( $U$ ); thus, the available power in the fluid can be formulated as

$$P_{\text{fluid}} = \frac{1}{2} \rho U^3 DL. \quad (17)$$

The power coefficient of VIV can be summarized as

$$\eta_{\text{VIV}} = \frac{\frac{1}{2} \pi \rho U^2 C_L f_{\text{osc}} y_{\text{max}} DL \sin(\Phi)}{\frac{1}{2} \rho U^3 DL} \quad (18)$$

$$\eta_{\text{VIV}} = \pi C_L \text{St} (y_{\text{max}}/D) \sin(\Phi) \quad (19)$$

Equation (19) shows that the theoretical power coefficient of VIV of the single cylinder depends on four non-dimensional parameters; the lift coefficient, the Strouhal number, St, the maximum dimensionless amplitude of oscillation, and the phase angle between acting force on the cylinder and the displacement of the cylinder.

In VIV of a single cylinder, the fluidic parameters such as Reynolds number or reduced velocity are significant to analyse the dynamic response of the

---

cylinder. Furthermore, the structural parameters such as the mass and damping ratios are vital. To evaluate the amount of energy, which can be captured by the cylinder, as a function of the Reynolds number, the variation of the reduced velocity can be considered. In addition, another relative parameter to VIV problems such as vortex shedding frequency or Strouhal number is important. Nevertheless, the vortex shedding frequency is implicit, while the Reynolds number varies and cannot be explicitly specified. Furthermore, the Reynolds number is related once the diameter of the cylinder and fluid properties are fixed. Thus, the vortex shedding frequency cannot be recognized a priori for the VIV of a single cylinder. On the other hand, the structural parameters of the cylinder as an elastic structure such as mass and damping ratios were kept constant and consequently, only the free stream velocity was changed which deliver a series of the numerical models. As a consequence, all dimensionless parameters available in Equation (19) can be explained as a function of the free stream velocity.

In order to evaluate the power coefficient of the VIV, the key parameters of the VIV explained in Equation (19) need to be addressed. These parameters characterise the power coefficient of VIV and comprising the lift coefficients, the vortex shedding frequency and maximum displacement of the cylinder. The calculated dimensionless parameters of the power coefficient including the average magnitude of the lift coefficient, the Strouhal number, and the maximum amplitude of oscillation have been summarized in Table 2. Accordingly, the theoretical efficiency of the VIV power can be evaluated using Equation (19). For the cases investigated, the table shows that the maximum amplitude displacement was obtained when  $Re = 8,000$  and the maximum efficiency of the VIV power calculated within the upper branch of oscillation is found to be approximately 10%.

### Chapter 3: Harnessing hydropower energy using a single cylinder

---

Table 2: Dimensionless parameters of the VIV response of a single elastically mounted cylinder as a function of the Reynolds number including the reduced velocity, the lift coefficient, the Strouhal number, the maximum amplitude and efficiency of the VIV power.

Re	$U_r$	$C_L$	St	$y_{\max}/D$	$\eta_{\text{VIV}}\%$
2,000	1.2	1.50	0.210	0.02	0.1
4,000	2.4	1.65	0.210	0.11	1.2
6,000	3.6	1.92	0.200	0.40	6.7
8,000	4.8	2.05	0.190	0.95	<b>10.1</b>
10,000	6.0	0.69	0.190	0.65	4.1
12,000	7.3	0.69	0.185	0.42	0.5
14,000	8.5	0.67	0.185	0.35	0.3
16,000	9.6	0.65	0.184	0.12	0.2
20,000	12.1	0.58	0.181	0.12	0.2

Derakhshandeh *et al.* (2014) have experimentally shown that employing two circular cylinders can significantly increase the power coefficient of the device. In their experiments the wake energy of vortices were captured using a downstream circular cylinder. It was shown that the power coefficient of the Wake-Induced Vibration (WIV) is calculated to be 28% when the cylinders were arranged in a staggered arrangement, which is approximately three times higher than the power coefficient of the single cylinder. In addition, along with the power coefficient, the maximum theoretical power and the power density of the WIV was evaluated as important parameters of the device. It was shown that the power density of the WIV was evaluated based on the volume of the optimum staggered arrangement of the cylinders, with longitudinal and lateral distances of  $x_0/D = 4.5$  and  $y_0/D = 1.5$ , respectively.

It is worth noting that the efficiency of VIV power is comparable with the efficiency of the other converters such as turbine systems. It has been shown that the maximum theoretical efficiency of a turbine is limited to the Betz limit, which is approximately 59.3%. On the other hand, the efficiency of

mechanical or electrical processes reduces the overall output with a total actual efficiency of the system ranging between 20% and 55% (Vries, 1983).

A brief comparison between the power density of the VIV converter and hydro turbines, which is utilized as a convectional converter, can provide a better perception of the mechanisms. The output power density of VIV can be calculated using an average efficiency of generator, which is expected to be  $\eta_{\text{gen}} = 75\text{-}85\%$  depending on the structure of the generator (Meng *et al.* 2012). Therefore, considering the average of efficiency of  $\eta_{\text{gen}} = 80\%$  for the generator, the output power of VIV can be calculated as follow:

$$P_{\text{VIV}} = \eta_{\text{VIV}} \eta_{\text{gen}} P_{\text{fluid}} = \eta_{\text{VIV}} \eta_{\text{gen}} \left( \frac{1}{2} \rho U^3 DL \right) \quad (21)$$

The power density of the VIV power can then be obtained as a function of free stream velocity based on the projected area of the cylinder ( $\text{W}/\text{m}^2$ ). Figure 9 compares the power density of the VIV converter of single cylinder with the power density of a river turbine and maximum obtainable power which is defined as Betz limit. It is observed that the power density of the river turbine is three times higher than the power density of the single cylinder considering to the VIV efficiency of the single cylinder (10.1%). It is worth noting that the efficiency of the VIV power can be optimized and increased to 28% when a staggered arrangement of the cylinder is utilized (Derakhshandeh *et al.* 2014). Considering to the optimized efficiency of the VIV power, the figure indicates that the power density of the optimized efficiency is comparable to the power density of the river turbines.

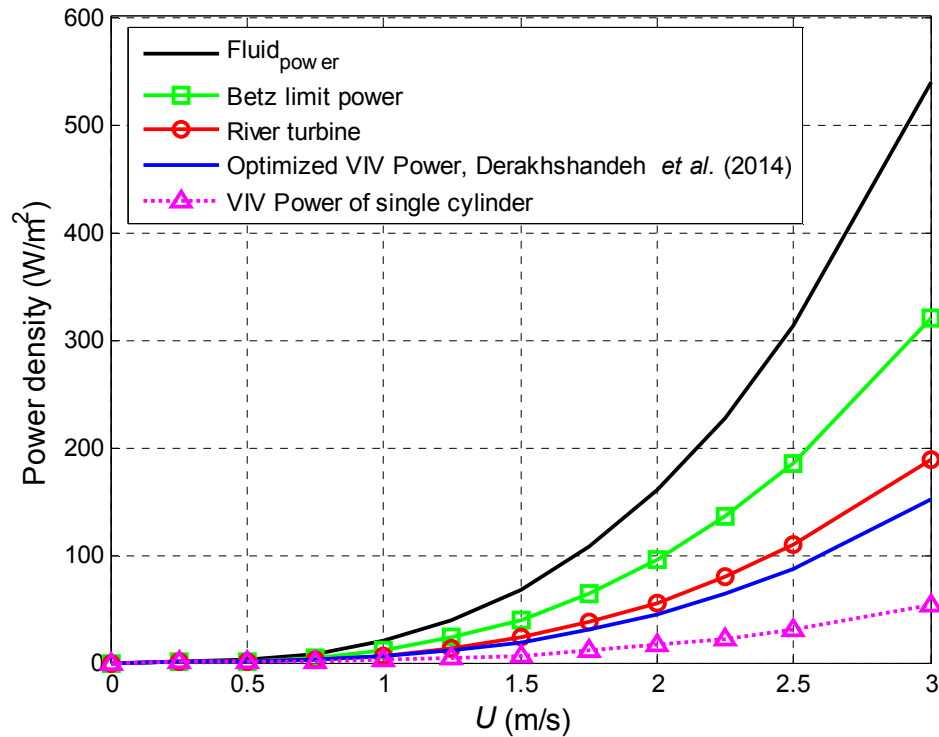


Figure 9: Comparison of power density of VIV converter with river turbine.

Further comparison between generated power of two types of turbines, including high and low speeds turbines, and VIV converter would provide a better insight into the capacities of these converters. Turbine selection is generally based on the water head. For instance, impulse turbines are mostly employed for high water heads, and reaction turbines are utilized for low water heads. It has been reported that reaction or river turbines are usually designed and built to operate with rated free stream velocity of 1.75-2.25 m/s or even higher (Khan *et al.* 2008). However, the impulse turbines can be used with 10 to 15 times higher flow speed compared with the reaction turbines. Therefore, it is meaningful to compare the produced power density of the reaction turbine with the VIV converter, whereas both of them can be operated at similar conditions with low speed flow.

The power density of the VIV converter is based on the optimised efficiency of the VIV with the staggered arrangement ( $\eta_{VIV} = 28\%$ ), which is shown in Figure 10. In order to calculate the power density ( $W/m^2$ ), it can be seen that  $\frac{1}{2}$  cylinder is included in the area of  $4.5D*1D$ . These longitudinal and lateral distances have been chosen based on the optimum arrangements of the cylinder with the maximum efficiency of VIV power which has been previously reported by Derakhshandeh *et al.* (2014). Therefore, the power density can be calculated as:

$$P_{\text{power density}} = \left( \frac{0.75P_{WIV}}{13.5D^2L} \right) \quad (22)$$

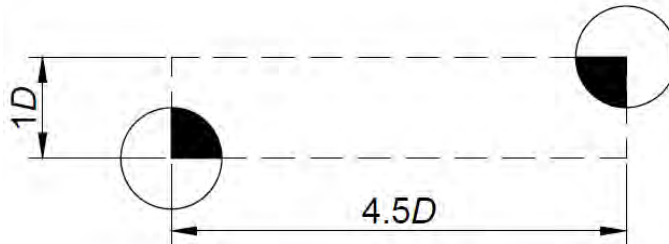


Figure 10: Configuration of the cylinders to calculate the area density

Substituting  $P_{VIV}$  from Equation (21) into Equation (22), the power density of VIV can be calculated. The results for both reaction turbine and VIV converter are summarized in Table 3. Interestingly, it can be seen that the power density of the VIV converter follows the power density of the reaction turbine with 20% lower value.

### Chapter 3: Harnessing hydropower energy using a single cylinder

---

Table 3: Comparison between the power density of a river turbine and power density of a VIV converter under an identical free stream velocity.

System	Size (m)	Flow speed (m/s)	Power (KW)	Area (m <sup>2</sup> )	Power density (KW/ m <sup>2</sup> )
River turbine (Extracted from EPA 2013)	$D_{\text{turbine}} = 0.144$	3	2.40	$\pi D_{\text{turbine}} = 0.144 \pi$	5.3
VIV converter	$D_{\text{cylinder}} = 0.04$	3	0.06	$4.5D * 1D = 0.0072$	4.2

#### 4. Conclusions

The current study evaluates the maximum theoretical power coefficient of the VIV of a single circular cylinder, which can be harnessed from an oscillating cylinder at a range of reduced velocity of  $U_r = 1.0$  to  $15.0$ . The shear forces, displacement amplitude and frequency of oscillation were calculated and consequent analysis supports the following conclusions:

1. It was observed that the theoretical power coefficient of VIV can be explained as a function of four dimensionless parameters, which are the key parameters of the VIV response. However, all these parameters are implicit, while the reduced velocity varies and cannot be explicitly specified. Therefore, the power coefficient of VIV for a single cylinder can be formulated only as a function of the reduced velocity.
2. Unlike the previous numerical results of Guilmineau and Queutey (2003), in which the  $k-\omega$  turbulence model was unsuccessful when simulating the upper branch of displacement, in the present study, it was shown that SST and the hybrid model of SAS can cover all three categories of oscillation properly. However, the numerical results of the SST model showed better agreement at the *lower branch* of oscillation.



3. It was shown that the maximum power coefficient of the VIV power can be calculated at upper branch with 2P mode and it is calculated to be approximately 10% for a single elastically mounted cylinder.
  
4. It is also shown that there is a great potential to utilize this approach for low velocity shallow water channels and rivers with 80% of the power density of a river turbine.

## References

Assi, G., Mechanisms for flow-induced vibration of interfering bluff bodies. PhD thesis, Imperial College London, UK, (2009).

Bearman, P.W., Vortex shedding from oscillating bluff bodies. *Journal of Fluid Mechanics*, 16, 195-222, (1984).

Bishop R. E. D. and Hassan A. Y., The lift and drag forces on a circular cylinder oscillating in a flowing fluid. Proceeding of the Royal society (London), series A 277, 51-75, (1964).

EPA, Renewable Energy Fact Sheet: Low-Head Hydropower from Wastewater, United States Environmental Protection Agency, (2013).

Derakhshandeh J. F., Arjomandi., M., Cazzolato, B., and Dally, B., Harnessing hydro-kinetic energy from wake-induced vibration using virtual mass spring damper system, *Journal of Ocean Engineering*, submitted (2014).

Egorov, Y., Menter, F., Lechner, R. and Cokljat, D., The scale-adaptive simulation method for unsteady turbulent flow predictions. Part 2: Application to complex flows. *Flow, Turbulence and Combustion*, 85 (1), 139-165, (2010).

Feng, C., The measurement of vortex induced effects in flow past stationary and oscillating circular and D-section cylinders, Master thesis, National Taiwan University, (1968).

Fletcher, D. and Langrish, T., Scale-adaptive simulation (SAS) modelling of a pilot-scale spray dryer. *Chemical Engineering Research and Design*, 87(10), 1371-1378, (2009).

Govardhan, R. and Williamson, C., Modes of vortex formation and frequency response of a freely vibrating cylinder. *Journal of Fluid Mechanics*, 420, 85-130, (2000).

Govardhan, R. and Williamson, C., Critical mass in vortex-induced vibration of a cylinder. *European Journal of Mechanics-B/Fluids*, 23 (1), 17-27, (2004).

Guilmineau, E. and Queutey, P., Numerical simulation of vortex-induced vibration of a circular cylinder with low mass-damping in a turbulent flow, *Journal of Fluids and Structures*, 19 (4), 449-466, (2003).

Khalak, A. and Williamson, C., Dynamics of a hydroelastic cylinder with very low mass and damping, *Journal of Fluids and Structures*, 10 (5), 455-472, (1996).

Liaw, K., Simulation of flow around bluff bodies and bridge deck sections using CFD, PhD thesis, University of Nottingham, (2005).

Lourenco, L. and Shih, C., Characteristics of the plane turbulent near wake of a circular cylinder, a particle image velocimetry study (Data published in Liaw, K., (2005)).

Meng, F., Chen, L., Sun, F., Effects of temperature dependence of thermoelectric properties on the power and efficiency of a multi element thermoelectric generator, *International Journal of Energy and Environment*, 137-150, (2012).

Menter, F.R., Two-equation eddy-viscosity turbulence models for engineering applications, *Journal of American Institute of Aeronautics and Astronautics*, 32(8), 1598-1605, (1994).

Menter, F. and Egorov, Y., A scale-adaptive simulation model using two-equation models, 43<sup>rd</sup> *Journal of American Institute of Aeronautics and Astronautics*, 1-13, (2005).

Menter, F. and Egorov, Y., The scale-adaptive simulation method for unsteady turbulent flow predictions. Part 1: Theory and model description, *Flow, Turbulence and Combustion*, 85 (1), 113-138, (2010).

Ong, L. and Wallace, J., The velocity field of the turbulent very near wake of a circular cylinder. *Experiments in Fluids*, 20(6), 441-453, (1996).

Parkinson, G., Phenomena and modelling of flow-induced vibrations of bluff bodies. *Progress in Aerospace Sciences*, 26, 169-224, (1989).

Wanderley, J. B. V., Souza, G. H. B., Sphaier, S. H., Levi, C., Vortex-induced vibration of an elastically mounted circular cylinder using an upwind TVD two-dimensional numerical scheme, *Ocean Engineering*, 35(14), 1533-1544, (2008).

## Chapter 4

### Harnessing hydro power using wake energy

#### 4.1. Chapter overview

When employing a tandem body in a cross flow, vortices shed from the upstream cylinder will not only pass by the downstream cylinder, but also interfere with its own generated vortices. This interference between flow patterns becomes more complex compared to a single cylinder which is under the effect of a Vortex Induced Vibration (VIV) phenomenon and requires more investigation that is affected by the wake coming from the first cylinder. Hence, this chapter is concerned with the flow interference between two circular cylinders as a tandem, comprising a numerical study and experimental investigations. In the numerical study, a SAS model is used to model the dynamic response of the downstream cylinder. For the experimental investigations, a virtual mass-spring damper is designed and employed in a water channel in the transient flow regime.

In this chapter two articles have been embedded. The first one has been published as

“The effect of arrangement of two circular cylinders on the maximum efficiency of Vortex-Induced Vibration power using a Scale-Adaptive

---

#### Chapter 4: Effect of arrangement of the cylinders

---

Simulation model”, by Derakhshandeh J. F., Arjomandi, M., Dally, B., Cazzolato B., *Journal of Fluids and Structures*, 49, 654-666, (2014).

The second one has been submitted to the “*Journal of Ocean Engineering*” as:

“A harnessing hydro-kinetic energy from wake induced vibration using virtual mass spring damper system”, by Derakhshandeh, J. F., Arjomandi, M., Dally, B., Cazzolato, B., *Journal of Ocean Engineering*, No: OE-D-14-00232, 2014.



## Statement of Authorship

Title of Paper	The effect of arrangement of two circular cylinders on the maximum efficiency of Vortex-Induced Vibration power
Publication Status	<input checked="" type="radio"/> Published, <input type="radio"/> Accepted for Publication, <input type="radio"/> Submitted for Publication, <input type="radio"/> Publication style
Publication Details	Derakhshandeh, J. F., Arjomandi, M., Dally, B., Cazzolato, B., The effect of arrangements of two circular cylinders on the maximum efficiency of Vortex-Induced Vibration power using a Scale-Adaptive Simulation model, Journal of Fluids and Structures, Vol. 49, Pages 654–666, 2014.

### Author Contributions

By signing the Statement of Authorship, each author certifies that their stated contribution to the publication is accurate and that permission is granted for the publication to be included in the candidate's thesis.

Name of Principal Author (Candidate)	Javad Farrokhi Derakhshandeh		
Contribution to the Paper	Investigation of the effect of the arrangement of the cylinder on the power coefficient of the converter employing tandem, side-by-side and staggered arrangements of the cylinders.		
Signature		Date	18/03/2015

Name of Co-Author	Maziar Arjomandi		
Contribution to the Paper	Supervised the work, assisted in developing ideas and manuscript evaluation.		
Signature		Date	18.03.2015

Name of Co-Author	Bassam Dally		
Contribution to the Paper	Supervised the work, assisted in developing ideas and manuscript evaluation.		
Signature		Date	18-03-15

Name of Co-Author	Benjamin Cazzolato		
Contribution to the Paper	Supervised the work, assisted in developing ideas and manuscript evaluation.		
Signature		Date	18/3/15



## Statement of Authorship

Title of Paper	Harnessing hydro-kinetic energy from wake-induced vibration using virtual mass spring damper
Publication Status	<input type="radio"/> Published, <input type="radio"/> Accepted for Publication, <input checked="" type="radio"/> Submitted for Publication, <input type="radio"/> Publication style
Publication Details	Derakhshandeh, J. F., Arjomandi, M., Dally, B., Cazzolato, B., Harnessing hydro-kinetic energy from wake induced vibration using virtual mass spring damper system, Journal of Ocean Engineering, No: OE-D-14-00232, 2014.

### Author Contributions

By signing the Statement of Authorship, each author certifies that their stated contribution to the publication is accurate and that permission is granted for the publication to be included in the candidate's thesis.

Name of Principal Author (Candidate)	Javad Farrokhi Derakhshandeh
Contribution to the Paper	Develop a virtual mass spring damper to investigate the effect of the arrangement of the cylinders in harnessing kinetic energy of the vortices
Signature	Date 18/03/2015

Name of Co-Author	Maziar Arjomandi
Contribution to the Paper	Supervised the work, assisted in developing ideas and manuscript evaluation.
Signature	Date 18.03.2015

Name of Co-Author	Bassam Dally
Contribution to the Paper	Supervised the work, assisted in developing ideas and manuscript evaluation.
Signature	Date 18.03.2015

Name of Co-Author	Benjamin Cazzolato
Contribution to the Paper	Supervised the work, assisted in developing ideas and manuscript evaluation.
Signature	Date 19/3/15

### 4.2. Article



Contents lists available at [ScienceDirect](#)

Journal of Fluids and Structures

journal homepage: [www.elsevier.com/locate/jfs](http://www.elsevier.com/locate/jfs)



## The effect of arrangement of two circular cylinders on the maximum efficiency of Vortex-Induced Vibration power using a Scale-Adaptive Simulation model

Javad Farrokhi Derakhshandeh\*, Maziar Arjomandi, Bassam Dally, Benjamin Cazzolato

School of Mechanical Engineering, University of Adelaide, Adelaide, South Australia 5005, Australia

### ARTICLE INFO

Article history:  
Received 18 August 2013  
Accepted 1 June 2014

Keywords:  
VIV  
Vortex shedding  
Scale Adaptive Simulation  
Shear Stress Transport  
Two tandem cylinders

### ABSTRACT

The complex behaviour of an unsteady flow around two circular cylinders in tandem is of interest for many civil engineering applications across a wide range of aerospace, mechanical and marine applications. The present paper analyses Vortex-Induced Vibration (VIV) for the flow around two circular cylinders. It has been shown that the amount of kinetic energy which can be captured by VIV is a function of the arrangement of the two cylinders. The upstream cylinder is fixed while the downstream is mounted elastically with one degree of freedom normal to the mean flow direction. The efficiency of the VIV power obtained from downstream cylinder is compared for different arrangement of the cylinders. For this purpose, the longitudinal and lateral distances between the cylinders were varied and the Reynolds number was kept constant. Scale-Adaptive Simulation (SAS) and Shear Stress Transport (SST) CFD models are utilized to analyse the validity of the SAS turbulence model. The results indicate that both turbulence models predict the flow characteristics around the cylinders with reasonable precision; however, the predictions from SAS were more accurate compared to the SST. Based on this comparison, SAS model was chosen as a tool to analyse the VIV response of the downstream cylinder. The location of the downstream cylinder has been altered in the wake of upstream one in order to obtain the optimum efficiency of the VIV power. The results reveal that the arrangement of the cylinders can significantly change the efficiency. It is also observed that cylinders offset from one another show a higher efficiency compared to cylinders with their centres aligned.

© 2014 Elsevier Ltd. All rights reserved.

### 1. Introduction

In regards to the abundance of water sources in the world, it is obvious that harnessing hydrokinetic energy can be a considerable source of energy for future generations. Hydropower energy can be extracted from different sources such as rivers, waves, tides, thermal and salinity gradients (Bernitsas et al., 2008). Güney and Kaygusuz (2010) compared different hydropower energy sources and predicted the global increasing demand on hydrokinetic energy generation in the near future. They expected that hydropower energy production, including ocean sources, will provide 200 GW of installed production capacity by 2025 (Fig. 1). Therefore, hydropower energy can be recognized as a significant source of electricity

\* Corresponding author.

E-mail address: [javad.farrokhideerakhshandeh@adelaide.edu.au](mailto:javad.farrokhideerakhshandeh@adelaide.edu.au) (J.F. Derakhshandeh).

<http://dx.doi.org/10.1016/j.jfluidstructs.2014.06.005>  
0889-9746/© 2014 Elsevier Ltd. All rights reserved.

Please cite this article as: Derakhshandeh, J.F., et al., The effect of arrangement of two circular cylinders on the maximum efficiency of Vortex-Induced Vibration power using a Scale-Adaptive Simulation model. Journal of Fluids and Structures (2014), <http://dx.doi.org/10.1016/j.jfluidstructs.2014.06.005>

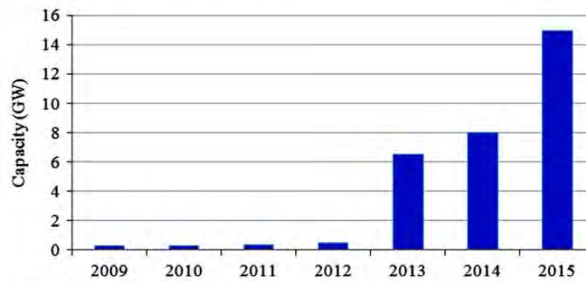


Fig. 1. Prediction of global hydrokinetic energy capacity between 2009 and 2015 (based on Güney and Kaygusuz (2010)).

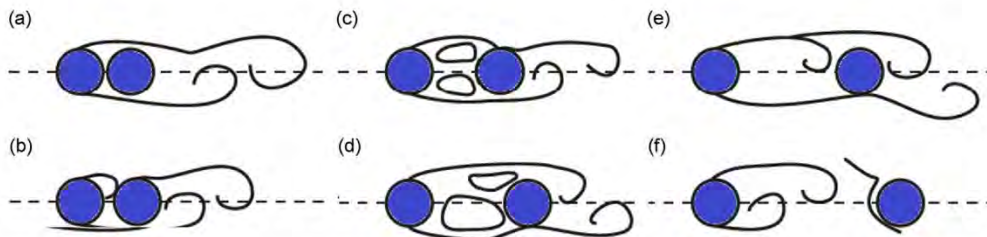


Fig. 2. Flow patterns around two stationary circular cylinders as a function of streamwise separation (a-f) (based on Igarashi (1981)).

production. This objective has encouraged the scientists and engineers to develop refined methods to harness the maximum available energy from the oceans and other source of water using different methods such as wave energy (Khan et al., 2009).

Vortex Induced Vibration (VIV) arises from the interaction of a moving fluid with an elastic structure. The number of publications on VIV is extensive (Bearman, 1984; Blevins, 1990; Khalak and Williamson, 1996, 1997; Zdravkovich, 1997; Govardhan and Williamson, 2000). Khalak and Williamson (1997) investigated the dynamic response of a circular cylinder and the effect of the mass ratio on the VIV mechanism. In their research, the displacement amplitude of a circular cylinder for very low mass and damping ratios has been categorized into three types; known as *initial*, *upper* and *lower* branches. In the initial category, the oscillation of the cylinder begins to build up and in the upper one resonance occurs with the maximum obtainable amplitude ratio. Finally, at the lower amplitude response, the oscillation of the cylinder is damped. Williamson (1996) also conducted a series of experimental studies to define the instability of the Strouhal number at low Reynolds numbers flows,  $120 \leq Re \leq 260$ . In addition, a comprehensive review of the flow around a circular cylinder has been undertaken by Williamson (1996), comparing previous numerical and experimental work which had focused on the wake of a circular cylinder.

Recently, it has been shown that the VIV mechanism has the potential to produce renewable energy and a great deal of attention has been devoted to research in this field (Bernitsas and Raghavan, 2004; Bernitsas et al., 2008, 2009; Chang et al., 2011; Lee et al., 2011; Raghavan and Bernitsas, 2011). In contrast to the more common turbine systems, the VIV mechanism can be categorized into a non-turbine system (Khan et al., 2009). For a turbine system the maximum theoretical efficiency is defined by the Betz limit which is equal to  $16/27$  or approximately 59.3% for a single and open free blade (Van Kuik, 2007). However, the efficiency of mechanical or electrical processes reduces the overall output with a total actual efficiency of the system ranging between 20% and 55% (Vries, 1983). In contrast to the turbine system, the theoretical efficiency of a VIV as a non-turbine system was calculated 37%, while the efficiency from experiments has been measured 22% (Bernitsas et al., 2008). The efficiency achievements of researchers investigating energy production from VIV suggest that further study is warranted.

For two aligned cylinders in tandem, the wake of the upstream cylinder is highly dependent on the streamwise separation between the cylinders and the resulting flow may be categorized into six different patterns (Igarashi, 1981). This tandem configuration has been studied experimentally and numerically by Zdravkovich (1987) and Carmo (2005), respectively. Fig. 2 illustrates the flow patterns of the unstable shear layers as a function of the distance between two cylinders (patterns A to F). In the case where the distance between cylinders is less than  $1.5D$ , where  $D$  is the diameter of the cylinder, the vortices have no interaction in the wake area (patterns A and B). By increasing the separation of the cylinders to  $1.5 < x/D < 3$ , (patterns C and D), two recirculation regions appear in the wake of the upstream cylinder. Initially, the vortices are symmetric and later they alternate to the asymmetric reattachment of shear layers. Therefore, it can be concluded that a mean value of the sinusoidal lift force of the upstream cylinder is equal to zero (Assi, 2009). For larger spacings between the cylinders, the shear layers begin to roll up in the wake and finally a fully developed vortex street is formed behind the upstream cylinder.

Almost all previous studies confirmed that vortex formation behind the upstream cylinder requires the minimum wake spacing between two similar cylinders to be greater than  $1.5D$ . The critical measured wake spacing by Igarashi (1981) is between  $1.5D$  and  $3.53D$ , while a critical range of  $1.5D$  to  $4D$  was recorded by Kuo et al. (2008). Ljungkrona et al. (1991) showed that for two similar cylinders the critical wake spacing is  $4.5D$  for a Reynolds number of 1400 and decreased to  $3.0D$  for a Reynolds number of 42 000. Further studies analysed the effect of the cylinder's diameter. Alam and Zhou (2007) investigated the effect of Reynolds number and the diameter of the cylinders on the flow pattern of two circular cylinders. In this arrangement the diameter of the upstream cylinder ( $d$ ) was gradually increased from 6 mm to 25 mm, while the diameter of the downstream cylinder ( $D$ ) was kept constant at 25 mm. They concluded that a decrease in the diameter ratio ( $d/D$ ) causes a reduction in the Strouhal number at a specific longitudinal distance between cylinders.

Even though previous studies have highlighted the influence of different parameters on VIV response, particularly the longitudinal distance, in an attempt to gain further insight into the capturing VIV energy, a numerical analysis of flow around two circular cylinders with different arrangement is considered. In this work, the upstream cylinder is stationary while the downstream one is elastically mounted at different longitudinal and lateral distances. The newly developed Scale-Adaptive Simulation (SAS) model (Langtry and Menter, 2009; Menter et al., 2010) was employed to investigate the behaviour of the flow around two cylinders in tandem in order to obtain the downstream response. Based on the behaviour of the downstream cylinder, the maximum efficiency of the VIV power has been calculated for different arrangements.

## 2. Methodology

For the purpose of VIV modelling the behaviour of the elastically mounted cylinder with one degree of freedom can be approximated as a simple mass–damper–spring (Bearman, 1984). Fig. 3 shows a simple schematic of the arrangement of two circular cylinders. The downstream rigid cylinder is elastically coupled to a rigid base is allowed to move in one degree of freedom along the  $y$ -direction.

The equation of motion for an elastically mounted cylinder of mass  $m$  can be defined as

$$m\ddot{y} + c\dot{y} + ky = F_y(t), \quad (1)$$

where

$$F_y(t) = F_{\text{viscous}} + F_{\text{pressure}}. \quad (2)$$

In these equations,  $y$  is the direction normal to the flow,  $\dot{y}$  and  $\ddot{y}$  are the velocity and acceleration of the cylinder, respectively,  $c$  is the viscous damping coefficient,  $k$  is the spring stiffness, and  $F_y$  is the sum of the viscous and pressure forces which are exerted on the downstream cylinder perpendicular to the flow direction (Fig. 3).

Assuming linear behaviour and a sinusoidal response of the cylinder, the fluctuating transverse amplitude and force coefficient can then be obtained from

$$y = y_{\text{max}} \sin(2\pi f_{\text{osc}} t), \quad (3)$$

$$c_L(t) = C_L \sin(2\pi f_{\text{osc}} t + \Phi), \quad (4)$$

where  $y_{\text{max}}$  and  $f_{\text{osc}}$  represent the harmonic amplitude and frequency of the cylinder, respectively,  $c_L$  is the time dependent lift coefficient,  $C_L$  is the lift coefficient amplitude,  $\Phi$  is the phase angle of the displacement with respect to the exciting fluid force, which for a linear system, at resonance, is close to  $\pi/2$  (Bernitsas et al., 2008) acting on the downstream cylinder. The work done by the fluid force during one cycle of oscillation,  $T_{\text{cyl}}$ , can be calculated as (Bernitsas et al., 2008)

$$W_{\text{VIV}} = \int_0^{T_{\text{cyl}}} F_y \dot{y} dt. \quad (5)$$

The mean power delivered by the cylinder is given by

$$P_{\text{VIV}} = \frac{W_{\text{VIV}}}{T_{\text{cyl}}}. \quad (6)$$

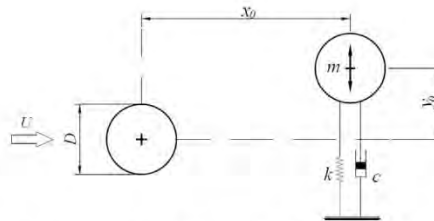


Fig. 3. Schematic of two cylinders in a cross flow. The upstream is rigidly mounted; the downstream is free to move along the  $y$ -axis.  $[x_0, y_0]$  represents the offset of the downstream cylinder from the upstream cylinder.

## Chapter 4: Effect of arrangement of the cylinders

It can be seen that by integrating the right hand term of Eq. (5) and averaging over the cycle period, the power due to VIV for a circular cylinder can be obtained

$$P_{VIV} = \frac{1}{2} \pi \rho U^2 C_{Lf} f_{osc} y_{max} DL \sin(\Phi), \quad (7)$$

where  $\rho$  is the density of the fluid,  $U$  is the free stream velocity,  $C_L$  is the lift coefficient amplitude,  $y_{max}$  represents the harmonic amplitude of cylinder,  $D$  is the cylinder diameter, and  $L$  is the length of the cylinder. The detailed derivation of Eq. (7) can be found in [Bernitsas and Raghavan \(2004\)](#). Therefore, the efficiency of VIV can be written as

$$\eta_{VIV} = \frac{P_{VIV}}{P_{fluid}} \quad (8)$$

where  $P_{fluid}$  is the power of the fluid which is the product of the acting force on the cylinder ( $(1/2)\rho U^2 DL$ ) and the velocity in the same direction of force ( $U$ ); hence, the power in the fluid can be calculated as

$$P_{fluid} = \frac{1}{2} \rho U^3 DL. \quad (9)$$

The efficiency of VIV can be summarized as

$$\eta_{VIV} = \frac{(1/2)\pi \rho U^2 C_{Lf} f_{osc} y_{max} DL \sin(\Phi)}{(1/2)\rho U^3 DL} = \frac{\pi C_{Lf} f_{osc} y_{max} \sin(\Phi)}{U} \quad (10)$$

In the current study, Computational Fluid Dynamics (CFD) was used to analyse the behaviour of the flow around two cylinders, from which the lift force, the frequency of vortices and the maximum displacement of downstream cylinder may be determined. The CFD package of choice was ANSYS Fluent. Therefore, selecting an accurate and suitable turbulent model for external flow around a bluff body is essential to investigate the flow behaviour in the wake of the upstream cylinder and is discussed in [Section 2.1](#).

The displacement and velocity of the downstream cylinder can be interpreted by a User Defined Function (UDF) file which can be loaded in ANSYS Fluent. Using the UDF file one can calculate the displacement of the cylinder with an elastic support in response to the fluid force in the normal direction of the mean flow at every time step  $\Delta t$ . The instantaneous change in the velocity of the downstream cylinder can be extracted from Eq. (1) as

$$\Delta \dot{y} = \frac{F_y - c\dot{y} - ky}{m} \Delta t. \quad (11)$$

For numerical validation purposes, the values of damping constant ( $c$ ), mass ( $m$ ) and stiffness ( $k$ ) used in the current study were chosen based on the previous experiment by [Assi \(2009\)](#). Therefore, in this study, the mass and damping ratios of the system were set at 2.6% and 0.7%, respectively, where the mass ratio is defined as  $m^* = 4m/\rho\pi D^2 L$ , while the damping ratio is generally defined based on the structural damping  $\zeta = c/2\sqrt{km}$ . It should be noted that to achieve an effective VIV response, the stiffness of the system has to be selectively chosen based on the mass ratio and the frequency of the vortices, which can be obtained from the numerical simulation in ANSYS Fluent.

### 2.1. Numerical methods

Two turbulence models, namely SST and SAS, were employed to investigate the flow behaviour around the cylinders. The SST model developed by [Menter \(1994\)](#) is a combination of  $k-\omega$  and  $k-\epsilon$  turbulence models, enhanced to overcome the problems associated with the prediction of length scales close to the walls for the  $k-\omega$  and free stream dependency of the  $k-\epsilon$  model ([Menter, 1994](#)). For flow around two cylinders, the SST model can be utilized for the transport of the turbulence shear stress inside the boundary layers. In this turbulence model, the aim is to increase the accuracy of predictions of flow with strong adverse pressure gradients. It has been shown that SST can better predict flow separation compared with either the  $k-\omega$  or  $k-\epsilon$  ([Liaw, 2005](#)). Although, the SST model for flow around two cylinders provides a good compromise between accuracy and complexity amongst RANS models, it tends to predict a turbulence field with an excessively large length scale ([Menter and Egorov, 2005](#)). Hence, seeking a solution to investigate the flow behaviour around a pair of cylinders can provide both computational efficiency and accurate flow predictions.

Another common CFD technique is Large Eddy Simulation (LES), which solves the filtered Navier–Stokes equations by directly computing the large scale turbulence structures and modelling the smaller scale of dissipative eddies ([Sagaut, 2001](#)). The LES analysis of the flow around two circular cylinders in tandem can reasonably predict the flow pattern behaviour and vortex shedding pattern between the cylinders ([Palau-Salvador et al., 2008](#)). However, the computational cost associated with LES is almost 640 times greater than the  $k-\epsilon$  model ([Cheng et al., 2003](#)). The recently developed model of SAS provides an Unsteady Reynolds Average Navier Stokes (URANS) model with an LES concept in an unsteady domain ([Menter et al., 2010](#)).

URANS models are not capable of accurately predicting the turbulent structures in separated flow regions. A classic example of such a limitation is the unsteady flow past a cylinder, where URANS models result in excessively large scale, unsteady structures. On the other hand the SAS model utilizes the von Karman length scale which allows the model to adjust its behaviour using Scale Resolving Simulation (SRS) based on the stability characteristics of the flow ([Egorov et al., 2010](#)). The advantage that SAS offers is in balancing the contributions of modelled and resolved parts of the turbulence

## Chapter 4: Effect of arrangement of the cylinders

stresses. Therefore, in unsteady flows, the model has the ability to effectively switch automatically from an LES model to a RANS model (Menter and Egorov, 2010). Furthermore, SAS models are less dependent on the mesh resolution compared to LES models (Menter et al., 2010). These capabilities make SAS an attractive model for unsteady flow, with lower computational cost than current alternatives whilst still maintaining reasonable accuracy.

### 2.2. Problem definition

In this study, flow around two identical circular cylinders was modelled using 2D unsteady turbulence models. The downstream cylinder was located at a number of different nominal positions in the wake of the upstream cylinder in order to capture the energy from the vortices. In this arrangement, the diameters of both cylinders were equal ( $D=50$  mm) and the Reynolds number based on the diameter of the cylinders was kept constant at  $Re=65\,000$ . This Reynolds number corresponds to  $U=1.306$  m/s. As mentioned earlier, the structural parameters including the mass and damping ratios were set at  $m^*=2.6\%$  and  $\zeta=0.7\%$ , respectively, to reflect Assi (2009).

The selected arrangements of the cylinders are shown in Fig. 4. The centre of the downstream cylinder is indicated by the (+) symbols in Fig. 4, with a total of thirty five test cases. The maximum longitudinal and lateral distances of  $x_0/D=4.5$  and  $y_0/D=2$  were chosen based on the literature and the known size of the wake behind the first cylinder.

Fig. 5 shows the computational domain as well as the generated grid for Test Case 35. The size of the computational domain for this typical model was  $30D \times 14D$ . In this case the blockage ratio was calculated to be approximately 7%, which is the recommended limit for water channel experiments. This value also is smaller than the blockage ratio of 8% used by Wanderley et al. (2008), who demonstrated that this blockage is adequate. In this work, the blockage ratio was kept constant for all 35 test cases.

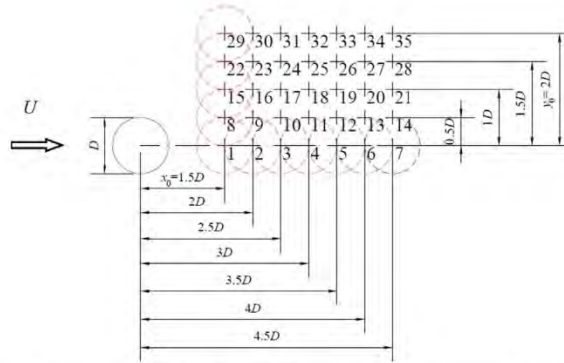


Fig. 4. Configurations of the cylinders investigated in this study (with 35 locations for the downstream cylinder in the wake of the upstream one).

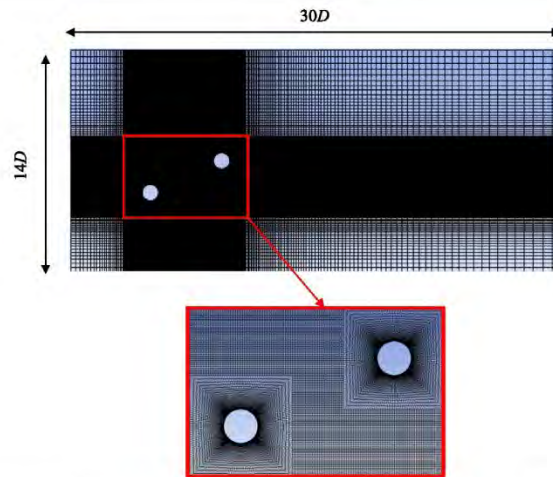


Fig. 5. Two-dimensional grid of two identical cylinders with staggered arrangement (Test Case 35,  $x_0/D=4.5$  and  $y_0/D=2$ ).

## Chapter 4: Effect of arrangement of the cylinders

6

J.F. Derakhshandeh et al. / Journal of Fluids and Structures ■ (■■■■) ■■■–■■■

**Table 1**  
Mesh refinement sensitivity of Test Case 6.

Mesh case	Mesh quality	Number of elements	Strouhal number
(1)	Coarse	20 000	0.165
(2)	Refined	40 000	0.170
(3)	Highly refined	90 000	0.170

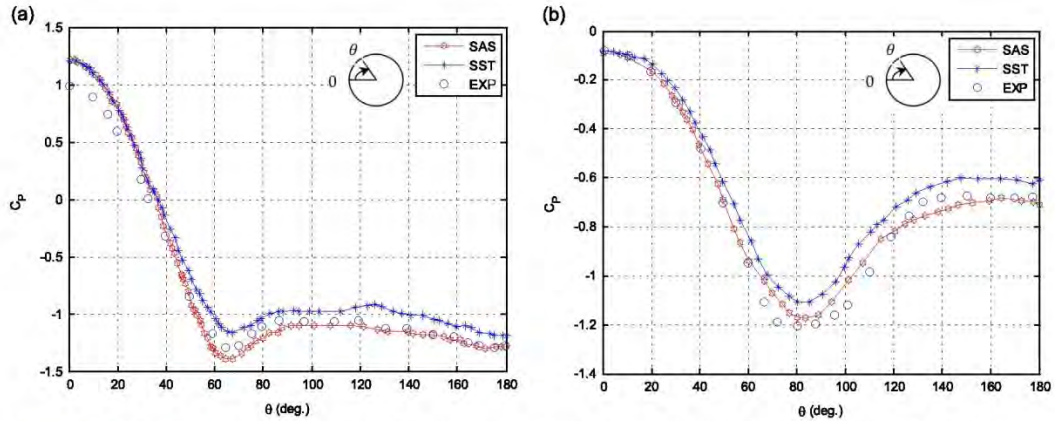


**Fig. 6.** Comparison the time averaged pressure coefficients distribution around two stationary cylinders at  $Re=65\,000$ , Test Case 7, with the experimental data of Alam et al. (2003). (a)  $C_p$  around the upstream cylinder and (b)  $C_p$  around the downstream cylinder.

The same initial conditions and boundary conditions were used for all numerical simulations. The number and type of mesh elements have been selected in an iterative solution with a minimal time step to obtain an accurate solution. With such a time step the maximum number of iterations for each time step was 30. The convergence criteria required the residuals to reach the value of  $10^{-5}$ . In addition, the lift and drag coefficients on the cylinders were monitored during the computational process and a sinusoidal behaviour of these coefficients was taken into account to accompany the convergence criterion. A grid independent study was conducted with three quadrilateral mesh models on Test Case 6 whose results are given in Table 1. Therefore, the refined mesh case 2 was chosen for the remaining simulations, and the SST and SAS turbulence models were used to investigate the turbulent flow behaviour around the two cylinders.

The dynamic mesh model in ANSYS Fluent employs an Arbitrary Lagrangian Eulerian (ALE) algorithm and a local remeshing approach for the adaption of the mesh in Fluid Structure Interaction (FSI) problems. The behaviour of the downstream cylinder is then described as a rigid body in the setup menu linked to the UDF file. Of the three types of meshing methods available in ANSYS (smoothing, layering and remeshing), the diffusion smoothing mesh method was chosen to simulate the oscillation of the downstream cylinder and the mesh was updated at each time step. This approach achieved a consistent  $y$ -plus (non-dimensional wall distance for a wall-bounded flow), regardless of the motion. Considering the chosen number and type of mesh elements, the diffusion parameter was set at 0.09 which inturns makes the nodes follow the motion of the cylinder as rigidly as possible without any interference between mesh and cylinder.

### 2.3. Validation results

The numerical schemes have been performed at high Reynolds numbers which are consistent with previous experimental conditions in order to evaluate the applicability of the turbulence model. To achieve this, the flow around a pair of stationary aligned cylinders was initially modelled at a Reynolds number of 65 000. The Reynolds number was chosen based on the experiments of Alam et al. (2003). To enhance the validity of the numerical results, further simulations were conducted for a single elastically mounted cylinder with the same conditions as the previously published data by Assi (2009).

### 2.4. Pressure coefficients and shear forces of the cylinders

The distribution of the pressure coefficient of the stationary upstream and downstream cylinders at a Reynolds number of 65 000 is plotted in Fig. 6. The figure compares the numerical results with the experiments of Alam et al. (2003). It is clear that the magnitude of the pressure coefficient of the upstream cylinder becomes zero at  $34^\circ$  in the experiment, while for the SAS and SST predictions this occurs approximately at  $36^\circ$  and  $37^\circ$ , respectively (Fig. 6a). The maximum negative pressure for

## Chapter 4: Effect of arrangement of the cylinders

the experimental data, the SAS and SST occur at angles of between  $66^\circ$  and  $70^\circ$ . However, the magnitude of the pressure coefficient for the SST differs significantly from the experimental data ( $-1.1^\circ$  versus  $-1.65^\circ$ ). Furthermore, it can be seen that in the wake of the upstream cylinder ( $\theta > 100^\circ$ ), the pressure magnitude of the rear part of the curve for the SAS model is closer to the experimental data compared to the SST. Based on this it is reasonable to conclude that the SAS model shows better agreement with the experimental data for the pressure distribution around the upstream cylinder.

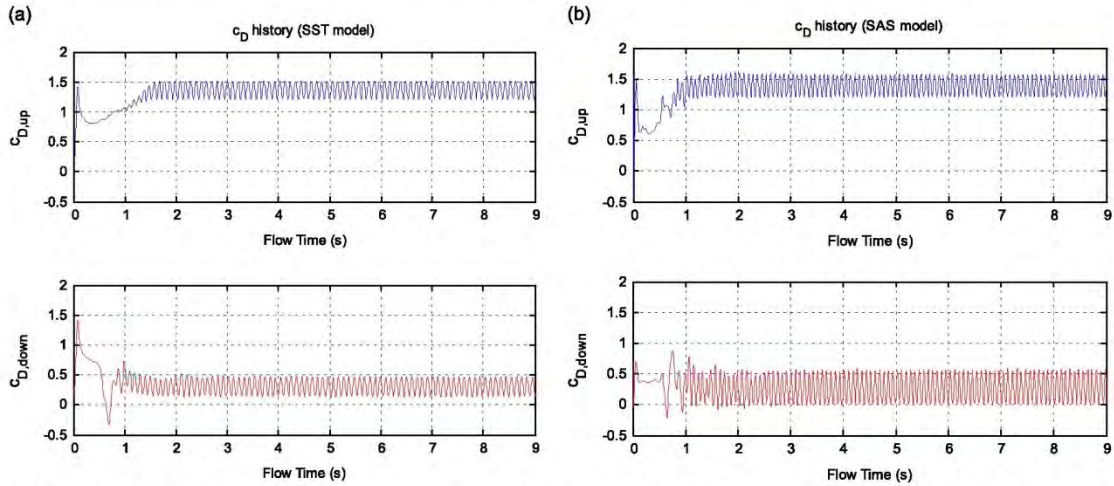


Fig. 7. Time history of the drag coefficients of the stationary upstream (top) and the stationary downstream (bottom) cylinders for Test Case 7. (a) SST model and (b) SAS model.

Table 2

Comparison of the mean drag coefficients ( $\overline{C_D}$ ), the lift coefficient amplitude ( $C_L$ ) and the Strouhal number with experimental data at  $Re=65,000$ , for  $x_0/D=4.5$  with both cylinders stationary.

Method	$\overline{C_{D,up}}$	Error	$\overline{C_{D,down}}$	Error	$C_{L,up}$	Error	$C_{L,down}$	Error	St	Error
SST	1.35	3.8%	0.29	6.4%	0.40	13.0%	0.64	12.3%	0.192	4.0%
SAS	1.36	4.6%	0.32	3.2%	0.50	8.6%	0.75	2.7%	0.205	2.5%
Exp. data (Alam et al., 2003)	1.30	–	0.31	–	0.46	–	0.73	–	0.2	–

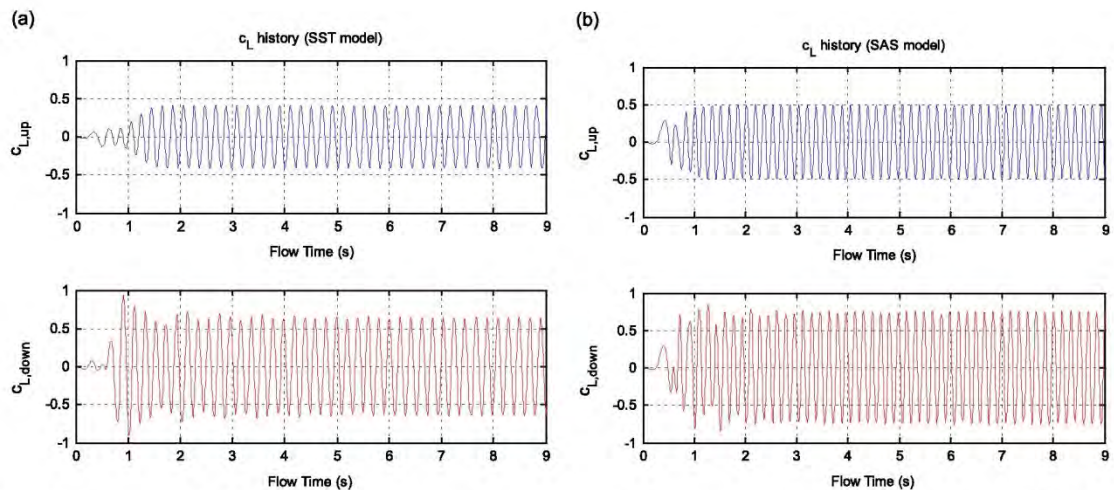


Fig. 8. Time history of the lift coefficients values of the stationary upstream (top) and the stationary downstream (bottom) cylinders obtained for the Test Case 7. (a) SST model and (b) SAS model.



Similarly, the time averaged pressure distribution around the downstream cylinder is plotted in Fig. 6b. The figure shows a similar trend between experimental and numerical data in terms of the angle corresponding to the minimum magnitude of pressure. The minimum magnitude of pressure occurs at an angle of approximately  $82^\circ$  for all three cases. Further, the pressure coefficient distribution for SAS shows a very good agreement with experimental data up to an angle of approximately  $60^\circ$ ; whereas for SST an acceptable agreement can be seen up to an angle of  $40^\circ$ , above which the numerical results depart from the experimental data. Another significant trend in the pressure coefficient distribution is demonstrated by the SAS results, where above an angle of approximately  $120^\circ$  it closely approximates the results from Alam et al. (2003). Therefore, although both numerical techniques are used for modelling an external flow around bluff bodies, it can be concluded that the pressure distributions on both cylinders obtained using the SAS model demonstrates a better agreement with the experimental results as compared to the SST model. Nevertheless, the figures reveal some differences in pressure distribution for both upstream and downstream cylinders. The type of mesh, the number of elements and structural parameters were also kept constant throughout the analysis. The time history of the drag coefficients have been plotted for both the SAS and SST models in Fig. 7, from which the mean drag coefficients of the cylinders have been calculated. In order to ensure the accuracy of the results, the mean drag and lift coefficients of each turbulence model for both upstream and downstream cylinders, as well as Strouhal numbers, have been compared with data reported by Alam et al. (2003). The findings have been summarized in Table 2, in which the numerical results are compared with experimental data, and the differences between each parameter are quantified. The percentage errors were calculated with respect to the SAS and SST results obtained through the simulations. It can be seen from the percentage errors that differences between the experimental and numerical values in the mean drag coefficients and Strouhal number associated with both models are in an acceptable range (less than 10% difference), revealing that all numerical findings sufficiently agree with the experimental data. However, the error of the mean drag coefficient of the upstream cylinder in SAS model is larger compared to the SST model.

The time history of the lift coefficient for the upstream and downstream cylinders have been plotted for both SAS and SST models (Fig. 8a and b). It can be seen that the magnitude of the lift coefficient values using SST model are approximately  $C_L=0.40$  and  $C_L=0.64$  for the upstream and downstream cylinders, respectively (Fig. 8a). The lift coefficient values for the upstream and downstream cylinders obtained with the SAS model show higher values of  $C_L=0.5$  and  $C_L=0.75$ , respectively (Fig. 8b). This means that both models exhibit an increase in lift of approximately 50% compared to the single cylinder. This increase of the lift coefficient of the downstream cylinder has been reported by others (Zdravkovich and Pridden, 1977; Alam et al., 2003). However, the results reveal that the SAS model achieves better quantitative agreement with the results of Alam et al. (2003). The measured lift coefficient of the upstream and have been measured 0.46 and 0.73, respectively by Alam et al. (2003). Therefore, the comparison between numerical findings and experimental data shows that the numerical

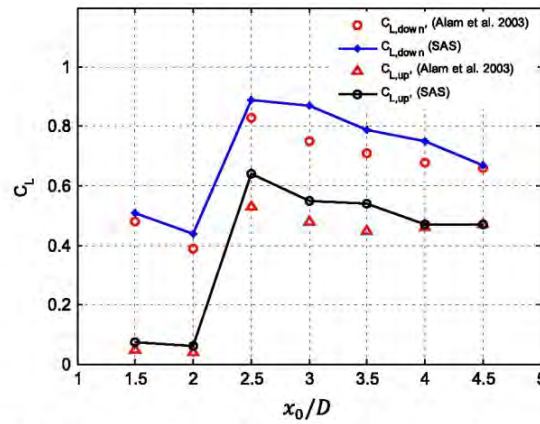


Fig. 9. Variation in the fluctuating lift coefficient of two stationary cylinders as a function of spacing ratio,  $x_0/D$ .

Table 3

Comparison of the lift coefficient, the maximum amplitude of oscillation, and the non-dimensional frequency of the oscillation of a cylinder based on the natural frequency ( $f_n$ ) at  $V_r = 4.0$ ;  $m^*\zeta \approx 0.01$  for the numerical simulations and experiments.

Method	$C_{L-single\ cyl.}$	Max. error <sup>a</sup> $C_L$	$(y/D)_{max}$	Max error <sup>a</sup> $(y/D)_{max}$	$f_{osc}/f_n$	Max error <sup>a</sup> $f_{osc}/f_n$
Numerical data (SAS model)	1.4	5.5%	0.74	9.7%	1.00	5.2%
Exp. data (Khalak and Williamson, 1996)	NA <sup>b</sup>	–	0.80	–	1.03	–
Exp. data (Assi, 2009)	1.5	–	0.82	–	0.95	–

<sup>a</sup> Maximum errors have been calculated based on the maximum differences between numerical and experimental data.

<sup>b</sup> NA: not available.

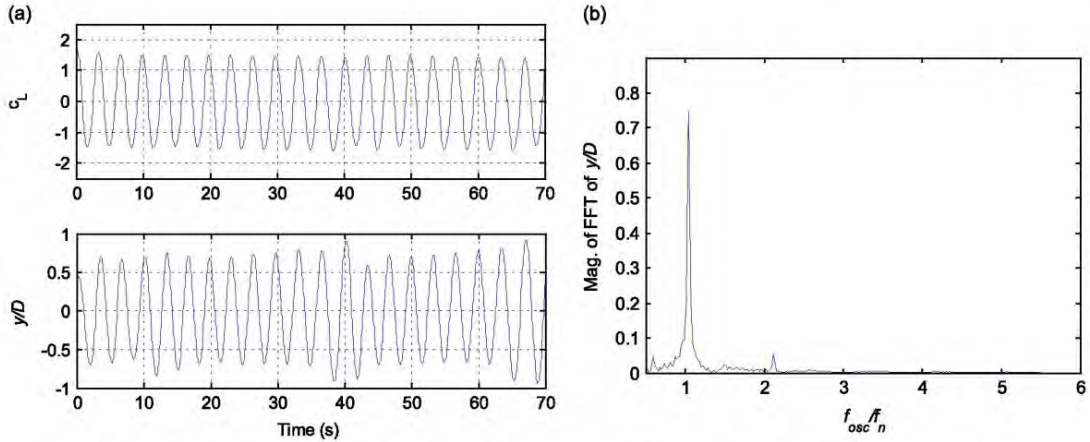


Fig. 10. VIV response of a circular cylinder at  $V_r=4.0$ . (a) Time history of the  $c_l$  and  $y/D$  and (b) magnitude of the FFT of  $y/D$ .

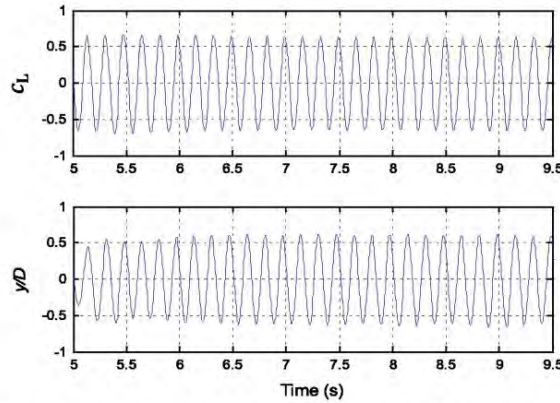


Fig. 11. Time history of the lift coefficient and displacement amplitude of a single cylinder at  $Re=65\ 000$ .

results using SAS model are more accurate (with less than 10% error) compared to the results achieved by the SST model. Table 2 lists the drag and lift coefficients of both cylinders as well as Strouhal number for both models and the experiments.

The fluctuating lift coefficient of the downstream cylinder has major impact on the efficiency of VIV power. A comparison of the calculated fluctuating lift coefficient with the published data of Alam et al. (2003) is shown in Fig. 9. As mentioned earlier, it can be seen that the lift coefficient of the upstream cylinder is lower than the lift coefficient of the downstream cylinder. It is also observed that the lift coefficient of both cylinders is very sensitive to the streamwise separation between the cylinders, particularly when the downstream cylinder was mounted sufficiently far from the upstream cylinder  $x_0/D \geq 2.0$ . With sufficient longitudinal distance, a vortex street generates (Igarashi, 1981) and the pressure field around the downstream cylinder alters which can generate higher value of shear forces.

A further simulation was conducted for the flow around a single elastically mounted cylinder in a turbulent flow using SAS model to further validate the numerical approach. The structural conditions were chosen based on published experimental data (Khalak and Williamson, 1996; Assi, 2009) and a similar reduced velocity of  $V_r=U/(f_{osc}D)=4.0$  was selected.

It is clear from the results presented above (Tables 2 and 3) that the SAS model is more suitable for modelling the turbulent flow around the cylinders and hence will be utilized for the rest of the study.

The VIV response of a single cylinder obtained from the numerical model is plotted in Fig. 10. The figure shows the time history of the lift coefficient, and the non-dimensional displacement of the cylinder (Fig. 10a). The Fast Fourier Transform (FFT) function of the displacement of the cylinder over the total time of the signal is plotted in (Fig. 10b) with the sampling time 0.01 s (with the sampling frequency of 100 Hz) using 512 points FFT. The FFT may be used to obtain both the frequency of oscillation as well as the dynamic magnitude of the signal. The comparison between the numerical results and the available experimental data (Khalak and Williamson, 1996; Assi, 2009) is summarized in Table 3. The numerical data is in good quantitative agreement with experimental data which gives us confidence to use this model for further investigation.

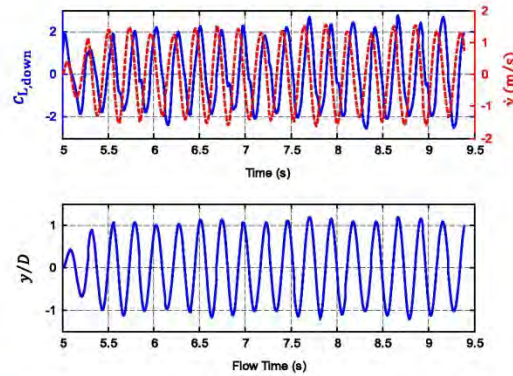


Fig. 12. Lift coefficient (—), velocity (---) and non-dimensional displacement of the downstream cylinder for Test Case 20 ( $x_0/D=4$ ,  $y_0/D=1$ ) at  $Re=65\ 000$ .

### 2.5. Power efficiency of the VIV response

The VIV response of the cylinder was interpreted in ANSYS Fluent using a UDF file. For cases involving two circular cylinders, Eq. (10) was only applied to the elastically mounted downstream mounted cylinder.

Fig. 11 shows the time history of the lift coefficient and displacement of the elastically single cylinder. The numerical results show that the efficiency of the single cylinder is  $\eta_{VIV} = 22.4\%$ . It should be noted that the time average lift coefficient has been chosen to calculate the efficiency of the VIV power.

The efficiency of VIV power for the two-cylinder cases was also calculated. For all simulations with two cylinders, the VIV efficiency was calculated as a function of the position of the downstream cylinder and other conditions were kept constant. Fig. 12 reveals a typical response of the elastically mounted cylinder at  $x_0/D=4$ ,  $y_0/D=1$  (Test Case 20). Included in this plot are the time series of the lift coefficient, the velocity, and the displacement of the downstream cylinder. Based on the average amplitude of the key parameters in this plot, the VIV response of all test cases as a function of the arrangement of the cylinders is calculated.

The numerical results including Strouhal number, the average magnitude of the lift coefficient, the non-dimensional amplitude  $y_{max}/D$ , and finally the efficiency of VIV power are summarized in Table 4. For the cases investigated, the table shows five groups of data which have been categorized based on  $y_0/D$ . According to the obtained results for the key parameters in Eq. (10), which affect the efficiency of the VIV power in Table 4, it can be argued that the best location to capture VIV energy is related to Group 4. Furthermore, it is clear that efficiency of the VIV power is strongly dependent on the lift coefficient, the displacement of downstream cylinder and vortex shedding frequency.

Fig. 13 presents the isoline contours of the lift coefficient and displacement amplitude of the downstream cylinder. The isoline contours plots can facilitate a better understanding of the effect of the arrangement of the cylinders on the key parameters that control VIV power. The figures show that both the lift coefficient and the displacement amplitude are functions of the longitudinal and lateral distances. It is also observed that with the staggered arrangement, the maximum values for these parameters can be achieved to improve energy harnessing potential.

The effect of all key parameters of the efficiency explained in Eq. (10) is summarized in Fig. 14 as a contour plot of the VIV efficiency. The contours of efficiency are plotted as a function of longitudinal distance,  $x_0/D$ , and lateral distance,  $y_0/D$ . The contours clearly show that in all the arrangements modelled in this study, the VIV efficiency is a function of the position of the downstream cylinder. The results illustrate that among the five simulated groups of constant  $y_0/D$  the Group 4 with  $y_0/D = 1.5$  gives the maximum observed values of VIV efficiency,  $\eta_{VIV} = 48.4\%$  which is much higher than the efficiency of a single cylinder. Among the cases investigated, the staggered arrangements show more potential to capture the vortices energy compared with the cylinders having aligned centre. It is observed that at the range of  $3.5 \leq x_0/D \leq 4.5$  and  $1 \leq y_0/D \leq 2$  the maximum efficiency can be achieved. Furthermore, it is worth noting that the obtained efficiency of VIV is comparable to that of the turbine system (Betz limit  $\approx 59.3\%$ ). These results should encourage researchers to further develop the VIV concept to optimize this technology for the production of hydropower energy. An extensive experimental study is about to commence in order to demonstrate the relative change in VIV efficiency for the above configurations and to determine the maximum actual efficiency achievable.

### 3. Conclusions

Vortex Induced Vibration in the wake of a single cylinder is a relatively new concept for the production of hydropower energy from oceans and shallow rivers. The availability of ocean current flow and shallow rivers in the world, even at low

## Chapter 4: Effect of arrangement of the cylinders

**Table 4**

Results of the 35 test cases including Strouhal number, the lift coefficient amplitude,  $C_L$ , the non-dimensional displacement,  $y_{max}/D$ , and the VIV efficiency,  $\eta_{VIV}$  (%).

Groups	Test case	$x_0/D$	$y_0/D$	St	$C_L$	$y_{max}/D$	$\eta_{VIV}$ (%)
1	1	1.5	0	0.195	1.21	0.40	9.4
	2	2	0	0.165	0.81	0.60	8.0
	3	2.5	0	0.171	0.75	0.90	11.5
	4	3	0	0.187	1.07	0.65	13.1
	5	3.5	0	0.191	1.10	0.90	18.8
	6	4	0	0.170	1.82	0.92	28.5
	7	4.5	0	0.164	1.76	0.82	23.7
2	8	1.5	0.5	0.172	0.8	0.70	9.6
	9	2	0.5	0.183	0.55	0.70	7.03
	10	2.5	0.5	0.185	0.85	0.90	14.1
	11	3	0.5	0.183	0.98	0.94	16.8
	12	3.5	0.5	0.202	1.35	0.90	24.5
	13	4	0.5	0.204	1.40	0.85	24.2
	14	4.5	0.5	0.214	1.70	0.70	25.4
3	15	1.5	1	0.197	1.60	0.85	26.8
	16	2	1	0.168	2.05	0.60	20.7
	17	2.5	1	0.216	2.40	0.70	36.2
	18	3	1	0.176	2.40	0.81	34.2
	19	3.5	1	0.200	2.00	0.90	35.9
	20	4	1	0.168	1.90	0.97	31.0
	21	4.5	1	0.214	2.00	0.80	34.1
4	22	1.5	1.5	0.233	2.00	0.40	18.6
	23	2	1.5	0.220	2.80	0.60	36.9
	24	2.5	1.5	0.202	2.50	0.90	45.3
	25	3	1.5	0.220	2.10	0.90	41.5
	26	3.5	1.5	0.198	2.00	0.90	35.6
	27	4	1.5	0.233	2.60	0.80	<b>48.4</b>
	28	4.5	1.5	0.233	2.60	0.65	39.3
5	29	1.5	2	0.189	2.10	0.50	19.9
	30	2	2	0.183	2.30	1.00	42.2
	31	2.5	2	0.222	2.85	0.70	44.2
	32	3	2	0.183	1.08	0.85	16.8
	33	3.5	2	0.225	2.50	0.80	44.9
	34	4	2	0.222	2.10	0.72	33.5
	35	4.5	2	0.220	2.30	0.70	35.3

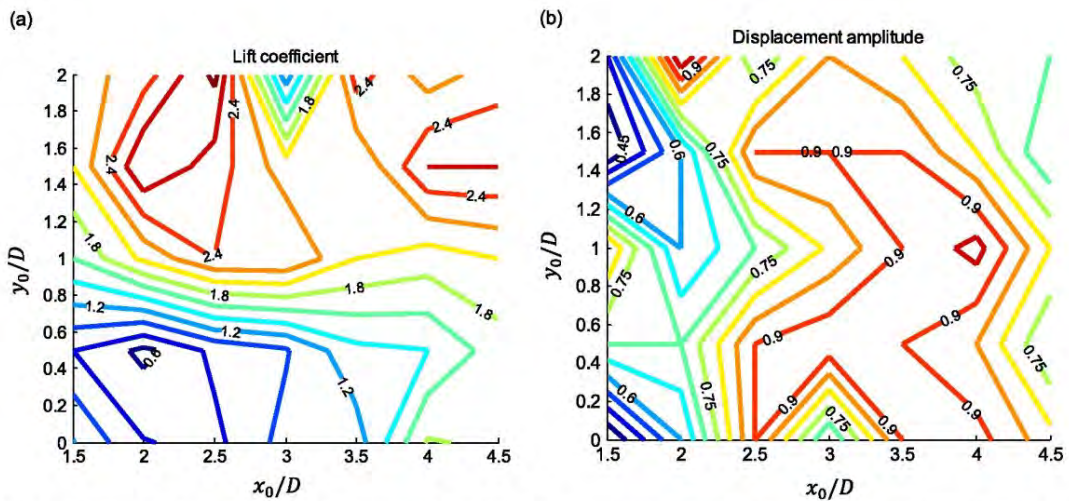


**Fig. 13.** Isoline contours of the lift coefficient and displacement amplitude of the downstream cylinder as a function of its position. (a) Lift coefficient and (b) displacement amplitude.

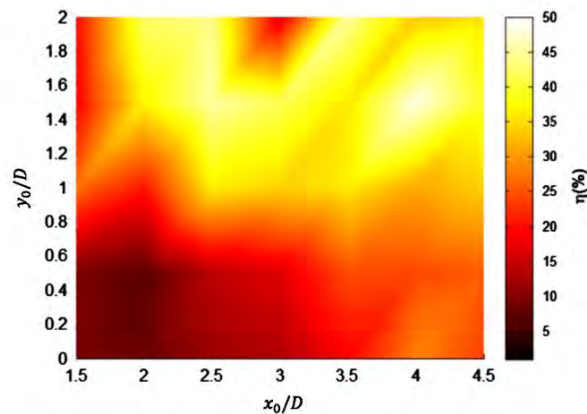


Fig. 14. Contour plot of the efficiency of the VIV power (percentage) as a function of the location of the downstream cylinder.

speeds, provide an opportunity for a new viable method for hydropower generation. The arrangement of the bluff bodies is one outstanding feature which can significantly affect the VIV response. In this study, two numerical models (SAS and SST) were utilized and compared to one another to investigate the external turbulent flow around two circular cylinders with different arrangements. In these models, the upstream cylinder was stationary while the downstream one was supported by an elastic structure. The SST and SAS turbulence models have been compared by investigating the flow behaviour around the two tandem cylinders. The Reynolds number of the flow was chosen based on previously published experiments (Khalak and Williamson, 1996; Alam et al., 2003; Assi, 2009) to validate the numerical data. Validation of the numerical study was conducted by comparison of the pressure coefficients of two stationary cylinders. Both turbulence models were observed to show a good agreement with the experimental findings. However, in comparison with the SST model, the SAS model shows better agreement with the experimental data. Additionally, to ensure the accuracy of simulation other parameters such as drag and lift coefficients and Strouhal number were also compared with the recorded experimental data (Khalak and Williamson, 1996; Assi, 2009) for a single elastically mounted cylinder.

In the models for which the upstream cylinder was stationary and the downstream cylinder was elastically mounted, simulations reveal that the VIV efficiency is very sensitive to the geometric arrangement. It was shown that the lift coefficient and displacement of the downstream cylinder are function of the longitudinal and lateral distances and can significantly influence the efficiency of the VIV power. The maximum efficiency of 48.4% was obtained when the downstream cylinder was located at  $3.5 \leq x_0/D \leq 4.5$ ,  $1.0 \leq y_0/D \leq 2.0$  in respect to the upstream cylinder which is much higher than a single elastically mounted cylinder with the efficiency of the 24.5%.

### References

- Alam, M.M., Moriya, M., Takai, K., Sakamoto, H., 2003. Fluctuating fluid forces acting on two circular cylinders in a tandem arrangement at a subcritical Reynolds number. *Journal of Wind Engineering and Industrial Aerodynamics* 91 (1), 139–154.
- Alam, M.M., Zhou, Y., 2007. Dependence of Strouhal number, drag and lift on the ratio of cylinder diameters in a two-tandem cylinder wake. In: *Proceedings of 16th Australasian Fluid Mechanics Conference*, pp. 750–757.
- Assi, G., 2009. Mechanisms for Flow-induced Vibration of Interfering Bluff Bodies (Ph.D. thesis), Imperial College London, London, UK.
- Bearman, P.W., 1984. Vortex shedding from oscillating bluff bodies. *Fluid Mechanics* 16, 195–222.
- Bernitsas, M., Raghavan, K., 2004. Converter of Current/Tide/Wave Energy. Provisional Patent Application. United States Patent and Trademark Office Serial no. 60/628,252.
- Bernitsas, M.M., Ben-Simon, Y., Raghavan, K., Garcia, E., 2009. The VIVACE converter: model tests at high damping and Reynolds number around 10. *Journal of Offshore Mechanics and Arctic Engineering* 131, 1–12.
- Bernitsas, M.M., Raghavan, K., Ben-Simon, Y., Garcia, E., 2008. VIVACE (Vortex Induced Vibration Aquatic Clean Energy): a new concept in generation of clean and renewable energy from fluid flow. *Journal of Offshore Mechanics and Arctic Engineering* 130, 1–15.
- Blevins, R.D., 1990. *Flow-induced Vibration*. Krieger Publishing Company, Malabar, Florida, USA.
- Carmo, B.S., 2005. Estudo numerico do escoamento ao redor de cilindros alinhados (Master's thesis). University of Sao Paulo, Brazil.
- Chang, C.C.J., Ajith Kumar, R., Bernitsas, M.M., 2011. VIV and galloping of single circular cylinder with surface roughness at  $3.0 \times 10^4 \leq Re \leq 1.2 \times 10^5$ . *Ocean Engineering* 38, 1713–1732.
- Cheng, Y., Lien, F., Yee, E., Sinclair, R., 2003. A comparison of large eddy simulations with a standard k– $\omega$  Reynolds-averaged Navier–Stokes model for the prediction of a fully developed turbulent flow over a matrix of cubes. *Journal of Wind Engineering and Industrial Aerodynamics* 91 (11), 1301–1328.
- Egorov, Y., Menter, F., Lechner, R., Cokljat, D., 2010. The scale-adaptive simulation method for unsteady turbulent flow predictions. Part 2: application to complex flows. *Flow, Turbulence and Combustion* 85 (1), 139–165.
- Govardhan, R., Williamson, C., 2000. Modes of vortex formation and frequency response of a freely vibrating cylinder. *Journal of Fluid Mechanics* 420, 85–130.
- Güney, M., Kaygusuz, K., 2010. Hydrokinetic energy conversion systems: a technology status review. *Renewable and Sustainable Energy Reviews* 14 (9), 2996–3004.
- Igarashi, T., 1981. Characteristics of the flow around two circular cylinders arranged in tandem. *JSME International Journal Series B* 24, 323–331.
- Khalak, A., Williamson, C., 1996. Dynamics of a hydroelastic cylinder with very low mass and damping. *Journal of Fluids and Structures* 10 (5), 455–472.
- Khalak, A., Williamson, C.H.K., 1997. Fluid forces and dynamics of a hydroelastic structure with very low mass and damping. *Journal of Fluids and Structures* 11 (8), 973–982.

## Chapter 4: Effect of arrangement of the cylinders

---

- Khan, M., Bhuyan, G., Iqbal, M., Quaicoe, J., 2009. Hydrokinetic energy conversion systems and assessment of horizontal and vertical axis turbines for river and tidal applications: a technology status review. *Applied Energy* 86 (10), 1823–1835.
- Kuo, C., Chein, S., Hsieh, H., 2008. Self-sustained oscillations between two tandem cylinders at Reynolds number 1,000. *Experiments in Fluids* 44 (4), 503–517.
- Langtry, R.B., Menter, F.R., 2009. Correlation-based transition modeling for unstructured parallelized computational fluid dynamics codes. *AIAA journal* 47 (12), 2894–2906.
- Lee, J.H., Xiros, N., Bernitsas, M.M., 2011. Virtual damper–spring system for VIV experiments and hydrokinetic energy conversion. *Ocean Engineering* 38 (5–6), 732–747.
- Liaw, K., 2005. Simulation of Flow Around Bluff Bodies and Bridge Deck Sections Using CFD (Ph.D. thesis). University of Nottingham.
- Ljungkrona, L., Norberg, C., Sunden, B., 1991. Free-stream turbulence and tube spacing effects on surface pressure fluctuations for two tubes in an in-line arrangement. *Journal of Fluids and Structures* 5 (6), 701–727.
- Menter, F., Egorov, Y., 2005. A Scale-adaptive Simulation Model Using Two-equation Modeled. American Institute of Aeronautics and Astronautics, 43rd AIAA Aerospace Sciences Meeting and Exhibit 1–13.
- Menter, F., Egorov, Y., 2010. The scale-adaptive simulation method for unsteady turbulent flow predictions. Part 1: theory and model description. *Flow, Turbulence and Combustion* 85 (1), 113–138.
- Menter, F., Garbaruk, A., Smirnov, P., Cokljat, D., Mathey, F., 2010. Scale-adaptive simulation with artificial forcing. *Progress in Hybrid RANS-LES Modelling*, 235–246.
- Menter, F.R., 1994. Two-equation eddy-viscosity turbulence models for engineering applications. *AIAA Journal* 32 (8), 1598–1605.
- Palau-Salvador, G., Stoesser, T., Rodi, W., 2008. LES of the flow around two cylinders in tandem. *Journal of Fluids and Structures* 24 (8), 1304–1312.
- Raghavan, K., Bernitsas, M., 2011. Experimental investigation of Reynolds number effect on vortex induced vibration of rigid circular cylinder on elastic supports. *Ocean Engineering* 38 (5), 719–731.
- Sagaut, P., 2001. *Large Eddy Simulation for Incompressible Flows*. Springer, Berlin.
- Van Kuik, G.A.M., 2007. The Lanchester–Betz–Joukowski limit. *Wind Energy* 10 (3), 289–291.
- Vries, O., 1983. On the theory of the horizontal-axis wind turbine. *Annual Review of Fluid Mechanics* 15 (1), 77–96.
- Wanderley, J.B., Souza, G.H., Sphaier, S.H., Levi, C., 2008. Vortex-induced vibration of an elastically mounted circular cylinder using an upwind TVD two-dimensional numerical scheme. *Ocean Engineering* 35 (14), 1533–1544.
- Williamson, C.H.K., 1996. Three-dimensional vortex dynamics in bluff body wakes. *Journal of Experimental Thermal and Fluid Science* 12, 150–168.
- Zdravkovich, M., 1987. The effects of interference between circular cylinders in cross flow. *Journal of Fluids and Structures* 1 (2), 239–261.
- Zdravkovich, M., 1997. 1st edition, *Flow Around Circular Cylinders*, vol. 1. Oxford University Press Inc., New York.
- Zdravkovich, M., Pridden, D., 1977. Interference between two circular cylinders; series of unexpected discontinuities. *Journal of Wind Engineering and Industrial Aerodynamics* 2 (3), 255–270.

### 4.3. Manuscript

#### **Harnessing hydro-kinetic energy from wake-induced vibration using virtual mass spring damper system**

Derakhshandeh J. F., Arjomandi M., Cazzolato B. S. and Dally B.  
School of Mechanical Engineering  
University of Adelaide, Adelaide, Australia

#### **Abstract**

Wake-Induced Vibration (WIV) has been considered as a potential candidate to capture hydrokinetic energy. This paper reports the experimental results of the WIV of a circular cylinder, positioned in the wake of an upstream circular cylinder. Investigations were carried out to determine the effects of the arrangement of the cylinders, with respect to each other, and the Reynolds number on the amount of energy. The upstream cylinder was kept stationary during the experiment, while the downstream cylinder was mounted on a virtual elastic base. The virtual elastic mechanism consists of a motor and a controller, a belt-pulley transmission system. In comparison with the more traditional mechanical impedance mechanisms, comprising of a real spring and damper system, the virtual mechanism utilized in this work, provided greater flexibility and robustness. The Reynolds number based on the diameter of the upstream cylinder was varied between 2,000 and 15,000. The tests revealed that the power coefficient of WIV power is a function of the Reynolds number and the phase shift between the fluidic force and displacement of the downstream cylinder. The results indicated that the amount of WIV energy, that can be captured, increases in a staggered arrangement, in comparison with an aligned arrangement.

*Keyword: Wake-Induced Vibration, vortex shedding, hydropower energy, PID control, and circular cylinders.*

#### **1. Introduction**

Environmental concerns and global warming have motivated scientists to investigate new and alternative methods to produce clean energy. Hydrokinetic

---

energy is one such renewable source and can be captured by turbine or non-turbine converters (Khan *et al.* 2009). In contrast to conventional methods (turbine systems), such as dams, where a water head is created, there is a growing trend to produce hydroelectric energy without extensively altering the natural conditions of the water stream. One such relatively new technology is Vortex-Induced Vibration (VIV), typically considered as a non-turbine system. VIV arises from the interaction of a moving fluid with an elastic structure. The method has the potential to harness hydrokinetic energy from the oceans, currents and shallow rivers (Bernitsas and Raghavan 2004). For a turbine system the maximum power coefficient is defined by Betz's limit, which is equal to  $16/27$  for a single and open free blade (Jamieson and Hassan 2008). On the other hand, the actual efficiency of the system reduces due to the efficiency of electrical and mechanical processes and it is limited between 20% and 55% (Vries, 1983).

The VIV converter is a relatively new concept in hydropower generation and its scalability and flexibility make it suitable for a wide variety of applications. It was reported that the VIV converter can be scaled between microwatt and megawatt sizes based on the dimensions of the cylinders, the number of the cylinders and the flow speed (Bernitsas *et al.* 2008). Table I classifies some non-exhaustive VIV converters and highlights the capacity of the produced power extracted from Bernitsas *et al.* (2008). Here,  $D$  and  $L$  represent the diameter and length of the cylinder and  $U$  is the flow speed.

Table I: Scaled classification of the vortex induced vibration converters (extracted from Bernitsas *et al.* 2008).

Scale	Power (MW)	Number of cylinders	$D$ (m)	$L$ (m)	$U$ (knots)
Large	10	1,314	1	20	11.4
Medium	1	526	0.5	10	1.1
Small	0.1	328	0.2	4	0.1

VIV of an elastically mounted circular cylinder in cross-flow has been well-studied in the literature (Sarpkaya 1978, Sarpkaya 1979, Bearman 1984, Williamson and

---



Roshko 1988, Govardhan and Williamson 2000, Govardhan and Williamson 2004). Bearman (1984) studied the oscillation of a cylinder, due to vortices, in a cross-flow and found that the maximum amplitude of oscillation is achievable over a range of the reduced velocities  $U_r = U/(f_n D)$ , where,  $f_n$  is the natural frequency of the elastically suspended cylinder and  $D$  is the diameter of the cylinder. Simultaneous measurements of force and displacement of an elastically mounted circular cylinder was conducted by Govardhan and Williamson (2000). They utilised Digital Particle Image Velocimetry (DPIV) to determine the response of the cylinder with both high and low mass damping ratios ( $m^*\zeta$ ), where the mass ratio is defined as  $m^* = 4m/\rho\pi D^2L$ , based on the mass ( $m$ ) of the cylinder, and the diameter ( $D$ ) and length ( $L$ ) of the cylinder, respectively. Here,  $\zeta$  is the damping ratio of the elastically mounted cylinder. With a low mass damping ratio, the authors observed three different types of responses for the amplitude of oscillation, known as *initial*, *upper* and *lower* branches; compared to only the *initial* and *lower* amplitudes observed with high mass damping ratios. As a consequence, the maximum displacement amplitude of the cylinder was achieved at the upper branch of oscillation using a low mass damping ratio.

The complexity of the dynamic response of the cylinder increases considerably by having two cylinders arranged in tandem. Since the longitudinal distance between two cylinders affects the dynamic behaviour of the vortices, even for stationary cylinders (Igarashi 1981), tandem arrangements of cylinders comprising a stationary and elastically mounted cylinder would alter the response of the downstream cylinder. Brika and Laneville (1999) conducted a series of wind tunnel experiments for flow around two cylinders, with the longitudinal distance of  $7 \leq x_0/D \leq 25$  and Reynolds numbers ranging from 5,000 to 27,000 (where  $x_0$  is the longitudinal distance between the centre of the cylinders). They reported that smaller longitudinal distances cause larger displacement amplitudes of the downstream cylinder. Similarly, Assi (2009) conducted water channel tests for  $4 \leq x_0/D \leq 20$ , in order to study the effects of  $x_0/D$  on the WIV of the downstream cylinder. It was observed that the displacement amplitude of the cylinder at low Reynolds number,  $Re < 6,000$ , (or  $U_r \leq 5$ ) is independent of the longitudinal

distance between the cylinders. While at higher Reynolds numbers,  $Re > 6,000$ , it was found that the amplitude of the oscillation is inversely proportional to  $x_0/D$  and that it decreases with increasing longitudinal separation. Although the influence of longitudinal distance was thoroughly investigated by Assi (2009), the effect of the lateral separation between the cylinders was not discussed for the WIV mechanism.

Bernitsas and Raghavan (2004) and Bernitsas *et al.* (2008) conducted a series of water channel experiments on an array of cylinders and determined an empirical expression for the efficiency of VIV power. They showed that the phase lag of the lift force on the cylinder, with respect to the displacement of the cylinder, would cause a reduction in the overall work production, since work is the product of the force and displacement. Inspired by the initial results, Cheng *et al.* (2011) carried out further water channel tests to investigate the effect of the Reynolds number on the VIV of a circular cylinder with surface roughness. The significance of this study was the identification of the influence of the roughness and high Reynolds numbers,  $3 \times 10^4 \leq Re \leq 1.2 \times 10^5$  on the flow induced vibration, including galloping and VIV of the cylinder. Surface roughness was changed by placing a strip (one inch wide) on the surface of the cylinder at a different angle relative to the stagnation point of the cylinder. The results indicated that at different strip locations on the surface of the cylinder ( $20-64^\circ$ ), the VIV is suppressed by the roughness for  $U_r < 10$ , while it induced galloping for  $U_r > 10$ .

Bearman (1984) was the first to postulate that the response of an elastically mounted circular cylinder can be modelled as a Mass Spring Damper (MSD). Following the proposed model by Bearman (1984), Hover *et al.* (1997), a pioneer of the computer model of Virtual Mass Spring Damper (VMSD), designed and employed a force-feedback controller in real time. The VMSD system allowed the operator to electronically set the desired impedance of the MSD. The advantage of the VMSD is that it allows a wide range of tests to be conducted rapidly compared to the real physical MSD, which requires changes in the physical elements in order to change the impedance. The ease of application of the VMSD allowed Hover *et al.* (1997) to analyse the effect of damping ratio and the Reynolds number on the

VIV response of a cylinder from 60 experiments. Although it was shown that the VMSD is able to record reliable results, such as lift coefficient and the amplitude of oscillation, the system was observed to produce an additional phase lag of 12 degrees. The phase lag between lift and displacement was due to the Chebyshev third-order digital filter (Hover *et al.* 1997), which can cause a reduction in energy conversion.

The use of VMSD also opened the way for optimisation and further development of energy extraction from VIV. In particular, it was used to explore many unresolved issues including the force-displacement phase lag, the power coefficient of energy harnessing, etc. For example, Lee *et al.* 2011 developed a VMSD of a VIV converter including a circular cylinder, a timing belt-pulley, a motor, and a controller. They used VMSD to perform a wide range of experiments, in which the spring stiffness was kept constant at 800 N/m and the viscous damping was varied from 0 to 0.16 in increments of 0.04. In this model, they reduced the phase lag between the force and displacement to zero, which could significantly improve the harnessed energy. Although significant improvements were made in this model, the mass of the cylinder was imposed on the motor and generated significant frictional force due to the static weight of the cylinder (Lee *et al.* 2011).

Despite the considerable published studies on the VIV phenomenon, WIV has not received much attention in the literature, particularly as an application for the extraction of energy. In general, the WIV of the downstream cylinder can be thought of as the unsteady vortex-structure interaction that occurs between the cylinder and the upstream wake (Assi *et al.* 2010). Hence, the WIV response of a circular cylinder is distinctively different from the VIV response. In the WIV mechanism, when the downstream cylinder is displaced sideways, a lift force acts to move the cylinder towards the centreline (Zdravkovich 1977) and it can occur outside of the resonance frequency (Assi *et al.* 2010). A series of experimental investigations of the WIV of an elastically mounted circular cylinder were conducted by Assi in 2009, in the range of  $1,000 \leq Re \leq 30,000$ . It was demonstrated that in the WIV mechanism, and at high reduced velocity,  $U_r > 17$ , the amplitude of oscillation is much higher than the VIV response of a single

cylinder. Therefore, it is possible to achieve higher displacement amplitudes, outside of the resonance frequency, in the WIV mechanism.

In this article, the WIV response of a downstream elastic cylinder is investigated, to capture the hydrokinetic energy of vortices from an upstream cylinder for a range of the Reynolds numbers, and different lateral and longitudinal distances between cylinders. The paper also compares the VIV response of a single cylinder for the same range of Reynolds numbers and structural parameters with the WIV response of the downstream cylinder. To achieve this, a new structural design of the VMSD system was designed and employed. In this new approach, a vertically mounted cylinder in a cross-flow was utilized, as opposed to previous designs, which employed horizontally mounted cylinders. The advantage of this approach is that the static weight (minus the buoyancy force) is no longer applied to the motor. In addition, the gravitational force is not in the same direction as the lift force acting on the cylinder and, therefore, it does not affect the dynamic response of the cylinder. Hence, it is not necessary to ignore the gravitational force, as was done in the previous study (Lee *et al.* 2011). In the current system, a Proportional Integral Derivative (PID) control system was utilized to control the instantaneous displacement of the downstream cylinder.

## 2. Methodology

This section outlines the apparatus and techniques used to conduct the experimental tests.

### 2.1. Experimental Setup

A series of tests were conducted in the closed-loop water channel at the University of Adelaide Thebarton Research Facility. The water channel test section had a 2,000 mm length, 500 mm width, and 600 mm depth. Figure 1 shows the schematic arrangement of the cylinders and the different test cases, examined in this study, are listed in Table II. In the table, the sixteen different combinations of longitudinal and lateral distances between cylinders are listed, along with the resulting angle from the horizontal plane  $\theta$ . The selected test cases have been chosen with

## Chapter 4: Effect of arrangement of the cylinders

sufficient longitudinal ( $x_0$ ) and lateral ( $y_0$ ) distances, based on the literature (Igarashi 1984 and Assi 2009), to allow the formation of coherent vortices from the upstream cylinder. The upstream cylinder, with a diameter ( $D_1$ ) of 40 mm and a length of 600 mm, was fixed on the stationary support; whereas, the downstream cylinder, with a diameter ( $D_2$ ) of 30 mm and a length 400 mm, was fixed on an elastic base.

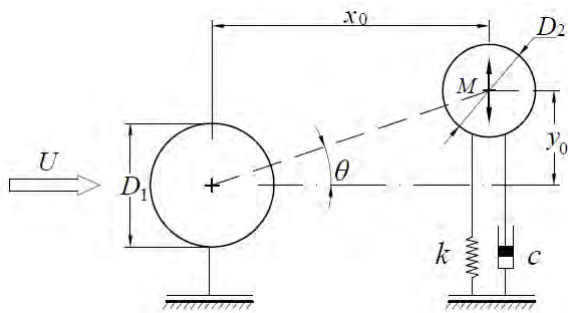


Figure 1: Schematic illustration of two circular cylinders with different diameters under the action of the free stream velocity.

Table II: List of longitudinal and lateral distances of the cylinders as seen in Figure 1.

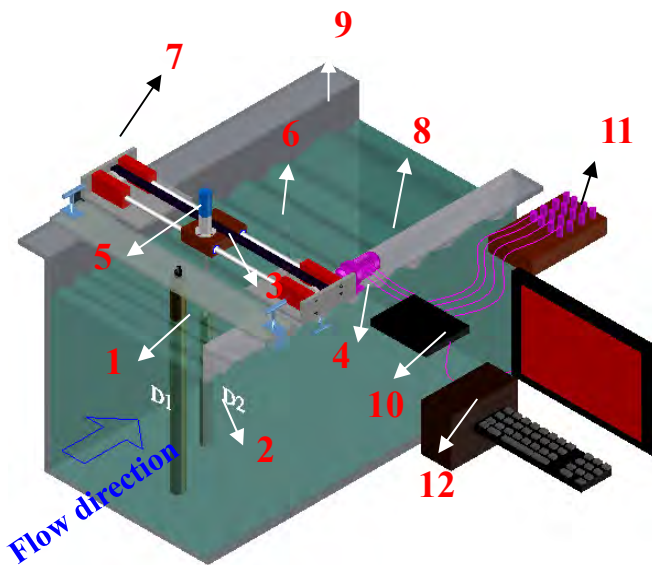
Test Case	$x_0/D_1$	$y_0/D_1$	$\theta$ (deg.)
1	2.5	0	0
2	3	0	0
3	4	0	0
4	5	0	0
5	2.5	1	21.8
6	3	1	18.4
7	4	1	14.0
8	5	1	11.3
9	2.5	2	38.6
10	3	2	33.7
11	4	2	26.5
12	5	2	21.8
13	2.5	3	50.2
14	3	3	45.0
15	4	3	36.8
16	5	3	30.9

During the experiments the longitudinal ( $x_0$ ) and lateral ( $y_0$ ) distances between the cylinders were varied by altering the position of the upstream cylinder. Consequently, the downstream cylinder always remained at a fixed location and oscillated around the centreline of the test section. The blockage ratio caused by the upstream cylinder was 8% and the highest achievable free stream velocity through the test section of the water channel was 0.374 m/s, which was set using a frequency controller that drove the channel centrifugal pump. Therefore, the Reynolds number can be varied between 0 and 15,000. It was shown that at this range of Reynolds number, the Strouhal number is approximately constant at  $St \approx 0.2$  (Blevins 1990), which assists to estimate the vortex shedding frequency.

The water density at the measured temperature of 20°C was 1000 kg/m<sup>3</sup>. A photograph of the corresponding equipment is shown in Figure 2. In addition, a 3D model of the system including the water channel, and the VMSD associated controller is shown in this figure and it reflects how the components of the test rig and vertical cylinders were mounted in the water channel. Descriptions of the main parts of the VMSD system are shown in Table III. Finally, the dSPACE system was employed for the real time data acquisition. dSPACE is an interface software package for the controller development process and facilitates the capture of data in a real time.



a) Water channel and VMSD model



b) A 3D model of test rig

Table III: Descriptions of the experimental parts associated with Figure 2-b.

Part number	Description
1	Upstream cylinder
2	Downstream cylinder
3	Strain gauges
4	Frame
5	Carriage with linear bearings
6	Timing belt
7	Pulley 2
8	Motor, gearbox and encoder (model EC-max 30)
9	Test section
10	Maxon ESCON 50/5 servo controller
11	dSPACE board (DS 1104)
12	Computer control (dSPACE and Simulink)

Figure 2: a) The experimental setup with VMSD model for force and displacement measurements, b) A 3D model of the water channel setup including the test rig, the controller, the dSPACE board and the computer.

2.2. Details of VMSSD

The VMSSD system comprised of a vertically mounted cylinder, attached to a carriage, running on two pairs of linear bearings. The carriage is driven by a toothed belt, which is coupled to two toothed pulleys; one free acting as an idler, the other coupled to a Maxon brushless EC-Max 30 (with a 2000 quad-count encoder) servo-motor via a gearbox of 51/1 ratio. The servo-motor is controlled by a Maxon ESCON 50/5 servo controller in current-operation mode. The force applied to the downstream cylinder in the lateral direction (normal to the mean flow) is estimated using two strain gauges in a half-bridge arrangement. The bridge directly measures the moment at the root of the cantilevered column, and by assuming 2D flow conditions the lateral force may be estimated. The control of the VMSSD was achieved using Matlab/Simulink, then using the Real Time Workshop and the model was compiled to target a dSPACE-DS1104 rapid prototyping control board. The real-time controller was manipulated in dSPACE Control Desk. The Simulink model, used to create the VMSSD, is illustrated in Figure 3, where the voltage signal from the load cell (Strain gauge) is read by a 16 bit A/D converter. The position of the motor is obtained from reading the signals from the incremental encoder and the Maxon servo-controller is commanded using an analog voltage sent via a 16 bit D/A converter.

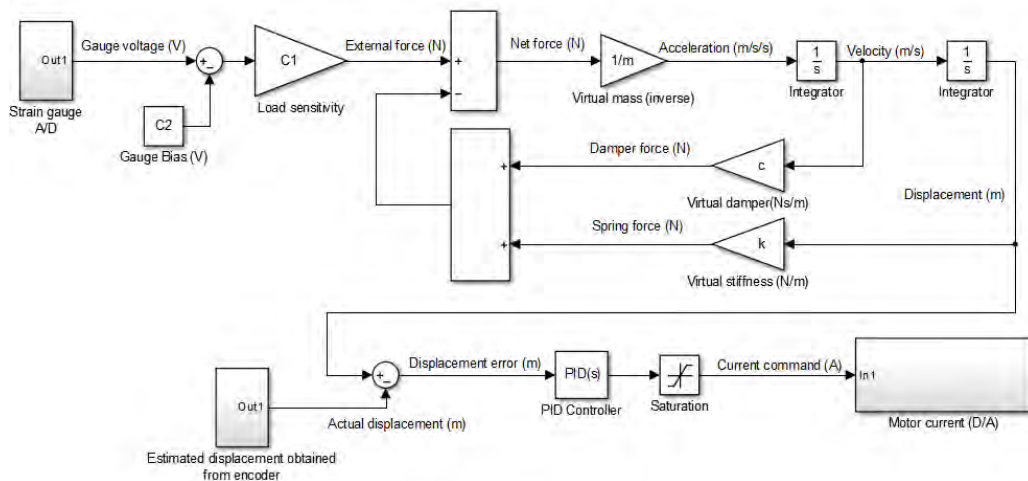


Figure 3: Simulink block diagram of the VMSSD model using PID control system.



### 2.3. PID Controller and parameter tuning

A Proportional-Integral-Derivative (PID) controller was designed to control the instantaneous displacement of the cylinder. The incremental encoder embedded inside the motor delivers square wave signals whose pulses can be counted for positioning (angle) and/or speed (angular velocity) measurement. The position signal of the motor was used for feedback control. A gain coefficient, which represents the load, allows for conversion of the motor rotation to the linear displacement of the cylinder. The difference between the measured displacements of the cylinder to those obtained from the virtual model was used as the input (error) signal to the PID controller. The PID controller was initially tuned using Ziegler Nichols method (Astrom and Hagglund 2006) and then manually optimised. The proportional, integral and derivative gains of the PID controller were set to minimize the displacement error to less than 1 mm. Such accuracy, as compared with the dynamic amplitude of the cylinder, was sufficient to provide meaningful analysis of the amplitude of the elastically mounted cylinder. The mass and damping ratios were kept constant in order to study the influence of the geometry and the Reynolds number on the power coefficient of the WIV converter. This also helped in the comparison between results presented here and those published previously by Assi (2009).

The mass and damping ratios were kept constant at 2.4 and 0.01, respectively, while the Reynolds numbers was changed to the maximum of 15,000. It is important to note that the selected damping ratio is likely to vary when the arrangement of the cylinders changes. Therefore, the chosen damping ratio is unlikely to be optimal in this investigation. The mass and damping ratios in the current paper have been chosen to be consistent with the previous studies for validation purposes of the VMSD system. In addition, the dynamic response of the downstream cylinder under the WIV mechanism is compared with the VIV of a single cylinder. Hence, it is essential to ensure that the initial conditions are identical for these two mechanisms in order to obtain a meaningful comparison.

#### 2.4. Mathematical modelling

The vibration of the elastically mounted cylinder due to the flow, known as forced vibration, has been modelled by Bearman (1984) as:

$$\ddot{y}(t) + 2\zeta\omega_n\dot{y}(t) + \omega_n^2y(t) = F_y(t)/M, \quad (1)$$

Here,  $y$ ,  $\dot{y}$  and  $\ddot{y}$  are the transverse displacement, velocity and acceleration of the cylinder, respectively,  $\zeta$  is the damping ratio of the second order system, and  $\omega_n = 2\pi f_n$ , where  $f_n$  is the natural frequency in Hz. On the right hand side of Equation (1),  $F_y$  and  $M$  are the fluid force exerted on the cylinder perpendicular to the flow direction and the effective mass of the system, comprised of only the cylinder, respectively.

The structural parameters and the response of the cylinder due to the flow can be set by the non-dimensional parameters defined in Table IV. Here,  $c$  is the damping constant,  $k$  is the spring stiffness, and  $\mu$  is the dynamic viscosity of water.

The time dependent displacement and the lift coefficient can be obtained from the following equations, respectively, by assuming linear behaviour and sinusoidal response of the cylinder:

$$y(t) = y_{\max}\sin(2\pi f_s t), \quad (2)$$

$$c_L(t) = C_L\sin(2\pi f_s t + \Phi), \quad (3)$$

In Equation (2),  $y_{\max}$  is the harmonic displacement amplitude and  $f_s$  represents the vortex shedding frequency. In Equation (3),  $c_L$  is the time dependent lift coefficient,  $C_L$  is the lift coefficient amplitude and  $\Phi$  is the force-displacement phase angle, which is vitally important in the WIV response of the cylinder (Sarpkaya 1978, Khalak and Williamson 1999), particularly for energy conversion (Bernitsas and Raghavan 2004 and Bernitsas *et al.* 2008).

Table IV: Non-dimensional parameters.

---

Mass ratio	$m^*$	$4M/\rho\pi D_2^2 L$
Damping ratio	$\zeta$	$c/2\sqrt{kM}$
Lift coefficient	$C_L$	$F_y/0.5 \rho U^2 D_2 L$
Amplitude ratio	$Y^*$	$y_{\max}/D_2$
Frequency ratio	$f^*$	$f/f_n$
Reynolds number	Re	$\rho U D_1/\mu$

Considering Equations (2) and (3) and the schematic of the structural design of the experimental model shown in Figure 4, the equations of motion for the VMSD can be written as follows:

$$(I_m + I_{p1}).\ddot{\theta}_1(t) = T_m(t) - t_m(t) + r_p(F_3(t) - F_1(t)), \quad (4)$$

$$I_p.\ddot{\theta}_2(t) = r_p(F_2(t) - F_3(t)) - t_p, \quad (5)$$

$$M.\ddot{y}(t) = (F_1(t) - F_2(t)) - F_{\text{bearings}}(t), \quad (6)$$

where,  $I_m$  and  $I_p$  are the mass moment of inertia of the motor and pulley, respectively,  $\ddot{\theta}_1$  and  $\ddot{\theta}_2$  represent the angular acceleration of the rotor and/or pulleys,  $T_m$  is the torque of the motor,  $t_m$  is the damping torque of the motor,  $r_p$  is the radius of the pulleys,  $t_p$  is the damping torque of pulleys,  $F_1$ ,  $F_2$  and  $F_3$  are the timing-belt tension and  $F_{\text{bearings}}$  is the friction force of the linear bearings. The lower side of the timing belt was connected to the bottom surface of the carriage. This causes a tension difference on the lower side of the timing belt ( $F_1$  and  $F_2$  in Figure 4). By assuming that there is no slip between the timing-belt and pulleys, one can deduce that the angles of rotation for both pulleys are equal to,  $\theta_1(t) = \theta_2(t) = \theta(t)$ , which then leads to  $y(t)$  being evaluated as  $y(t) = r_p \theta(t)$ . Therefore, Equations (4), (5), and (6) can be simplified as

## Chapter 4: Effect of arrangement of the cylinders

$$(I_m + 2 I_p + M \cdot r_p^2) \ddot{\theta}(t) = T_m(t) - (t_{p2}(t) + t_m(t)) + r_p \cdot F_{\text{bearings}}(t). \quad (7)$$

This equation can be expressed as follows:

$$\left( \frac{I_m}{r_p^2} + \frac{2 I_p}{r_p^2} + M \right) \ddot{y}(t) = F_m(t) - \left[ \frac{T_m(t)}{r_p} + \frac{t_{p2}(t)}{r_p} + F_{\text{bearings}}(t) \right] \quad (8)$$

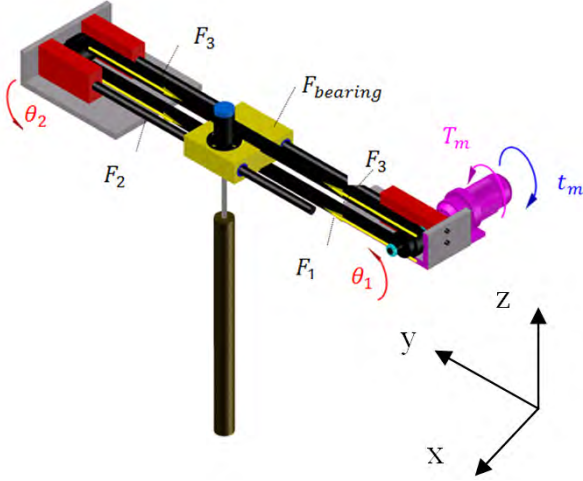


Figure 4: A 3D model of the VMSSD illustrating loads and kinematic variables.

Table V: Identification of components of VMSSD.

$I_m$	Mass moment of inertia of the rotor
$I_{p,i}$	Mass moment of inertia of the pulleys 1 and 2
$T_m$	Torque of motor
$t_m$	Damping torque of motor
$t_{p,i}$	Damping torque of pulleys 1 and 2
$r_p$	Radius of the pulley
$\theta_i, i: 1,2$	Angle of rotor and/or pulley 1 and 2
$F_i, i: 1,2,3$	Timing belt tension
$F_{\text{bearings}}$	Bearing's friction
$M$	Mass of the system

where,  $F_m = T_m/r_p$  and represents the tension in the belt from the motor torque.

Thus, for designing the controller, Equation (8) can be written as

$$(m_{\text{eff}} + M) \ddot{y}(t) = F_m(t) - F(t). \quad (9)$$

where,

$$\left( \frac{I_m}{r_p^2} + \frac{2 I_p}{r_p^2} \right) = m_{\text{eff}}, \quad (10)$$

$$F(t) = \frac{t_m(t)}{r_p} + \frac{t_{p2}(t)}{r_p} + F_{\text{bearings}}(t). \quad (11)$$

A brief description of each component of Figure 4 and Equations (4) to (11) is summarized in Table V.

One of the biggest advantages of the VMSD mechanism compared to the physical mass-spring damper is its capability to be implemented as a frictionless mechanism. This is feasible when measuring the friction of each part separately. In this study, the friction associated with each part of the mechanism, including servomotor, pulley, and bearings of carriage has been measured separately and the overall friction was estimated. As has been mentioned, in Equations (9) and (11), the dynamic response of the cylinder is defined based on the total measured friction or  $F(t)$ .

The dynamic response of the cylinder has been formulated based on Equation (9). In this equation,  $F(t)$  represents the total mechanical losses and it is modelled as the sum of the static friction ( $F_s$ ) and the viscous damping ( $c_{\text{eff}}$ ). Furthermore, considering the VMSD force, generated in the normal direction of the flow, with a spring constant of  $k$ , the mathematical model of the system for the motor-pulley-belt (VMSD) can be written as:

$$(m_{\text{eff}} + M)\ddot{y}(t) + (c_{\text{eff}})\dot{y} + ky(t) + F_s \frac{|\dot{y}|}{\dot{y}} = 0. \quad (12)$$

It is worth noting that in Equation (12),  $F_s$  is a function of displacement and has a negative and positive sign depending on the sign of the velocity of the cylinder. In addition, it can be seen that Equations (12) is second order differential equation and the general solution of these equations for a linear system can be written as  $Ae^{\zeta\omega_n t} \cos(\omega_d t + \Phi) + B$ . Therefore, it is observed that the static friction does not influence the damped natural frequency. In addition, in this study, the viscous damping is reasonably small due to the selected damping ratio ( $\zeta = 0.01$ ). Consequently, the damped natural frequency can be approximated as:

$$\omega_d = \frac{2\pi}{T_d} = \omega_n \sqrt{1 - \zeta^2} \approx \omega_n = \sqrt{\frac{k}{m_{\text{eff}}}}. \quad (13)$$

where,  $T_d$  represents the damping period. The servo-motor produces a virtual spring and damping torque utilising the angle and angular velocity measurements, and hence the rotation of the shaft is converted into the vibration of the cylinder. The acting virtual torque of the affects the angle and angular velocity, while the shear forces due to vortices are exerted on the surface of the cylinder. The rotary movement of the shaft is then converted to a linear displacement via the pulleys, the timing belt, the carriage and finally the cylinder, which is connected to the carriage.

Thus, integrating the inner product of the force and the instantaneous velocity, the total generated work can be calculated over a complete cycle of oscillation ( $T$ ),

$$W_{\text{WIV}} = \int_0^T F_y \dot{y} dt. \quad (14)$$

The average power is given by

$$P_{\text{WIV}} = \frac{W_{\text{WIV}}}{T}. \quad (15)$$

The fluid power given by  $P_{\text{fluid}} = FU = (\frac{1}{2})\rho U^3 D_2 L$  (Bernitsas and Raghavan 2004), was used to calculate the power coefficient

$$\eta_{\text{WIV}} = \frac{P_{\text{WIV}}}{P_{\text{fluid}}}. \quad (16)$$

### 3. Results and Discussion

The VMSD results have been validated for a single elastically mounted cylinder (VIV mechanism) as well as the dynamic response of the downstream cylinder (WIV mechanism) in the presence of the stationary upstream cylinder.

### 3.1. Validation

A series of displacement and force measurements were carried out in order to investigate the dynamic response of the downstream cylinder, as a function of the cylinders' arrangement and the Reynolds number. In practice, the dynamic response of the downstream cylinder is extremely sensitive to parasitic modes within the structure (Blevins 1990). Consequently, extra attention was given to measure the natural frequency of the fundamental bending mode of the cantilevered cylinder using the free-decay tests, which were performed in the water channel at zero free stream velocity. The natural frequency of the cantilevered cylinder was found to be  $f_n = 9.7$  Hz (also seen later in Figure 9-c), which is close to the oscillation frequency and amplifies noise around the vibration of the cylinder. Therefore, a filter can be designed and utilized to attenuate the generated noise.

Figure 5 shows the typical time series of the VIV responses of the single elastically mounted cylinder at upper and lower branches of oscillation. For the purpose of validation, the amplitude of oscillation of the cylinder was compared against the available experimental data (Assi 2009), which was collected under the same fluidic conditions ( $Re = 4,000$  and  $8,000$ ) and structural settings ( $m^* = 2.4$  and  $\zeta = 0.01$ ). The results include the lift coefficient and dimensionless displacement of the cylinder. In general, it is observed that the variation of the maximum amplitude with respect to the amplitude of the cylinder is insignificant. In addition, it can be observed that both the lift force and displacement of the cylinder, at the upper branch of oscillation, are in phase. This leads to an increase of the oscillation of the cylinder towards the maximum magnitude at this branch. Once the Reynolds number increases to the lower branch, a phase shift between the signals occurs and the magnitude of the oscillation of the cylinder shows a considerable reduction at  $Re = 12,000$ . At the lower branch of oscillation, the lift force-displacement phase angle shows approximately a  $180^\circ$  phase shift. Figure 6 summarizes the dimensionless amplitude of oscillation of the single cylinder under the VIV mechanism as a function of the Reynolds number. The experimental results of the VMSD are also compared with real physical MSD mechanism, presented by Assi

---

(2009) for the VIV response of a single cylinder, for which there is good agreement.

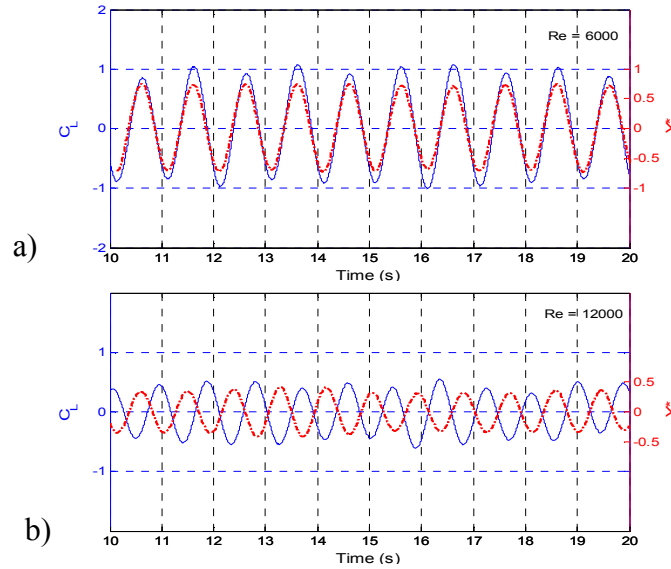


Figure 5: Typical time series of the lift coefficient,  $c_L$ , and the dimensionless displacement of the cylinder,  $Y^*$ , at a)  $Re = 6,000$  and b)  $Re = 12,000$ .

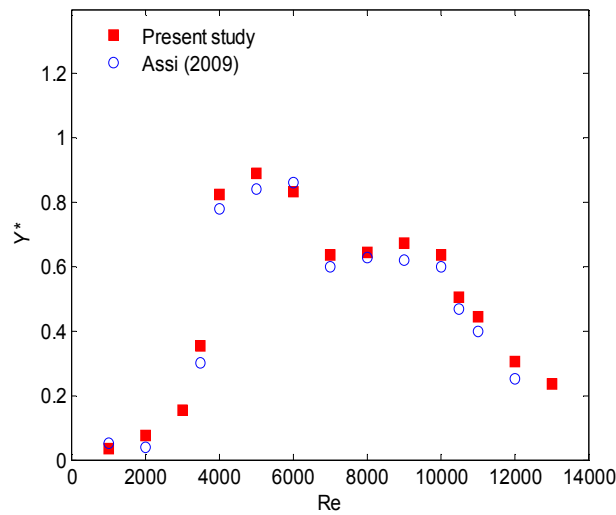


Figure 6: Comparison of the dimensionless displacement of the single cylinder,  $Y^*$ , under the VIV mechanism using the VMSD with the real physical MSD system (Assi 2009) as a function of the Reynolds number.



Along with the previous comparison, in order to further validate the current VMSD system, a similar arrangement (Test Case 3) was chosen and, the displacement amplitude of oscillation of the downstream cylinder was compared with the previous investigation of Assi (2009). A typical time series of the displacement amplitude of the downstream cylinder is plotted in Figure 7 for Test Case 3 (Table II), where  $x_0/D = 4$  and  $y_0/D = 0$ . It can be seen that the displacement of the downstream cylinder becomes irregular with increasing Reynolds number (or reduced velocity); however, the displacement amplitude of the cylinder increases at higher Reynolds number and plays an important role in increasing the power coefficient of the WIV mechanism. The dimensionless displacement amplitudes are in a good quantitative agreement with the ones produced by Assi (2009), which were 0.6 and 0.9, respectively.

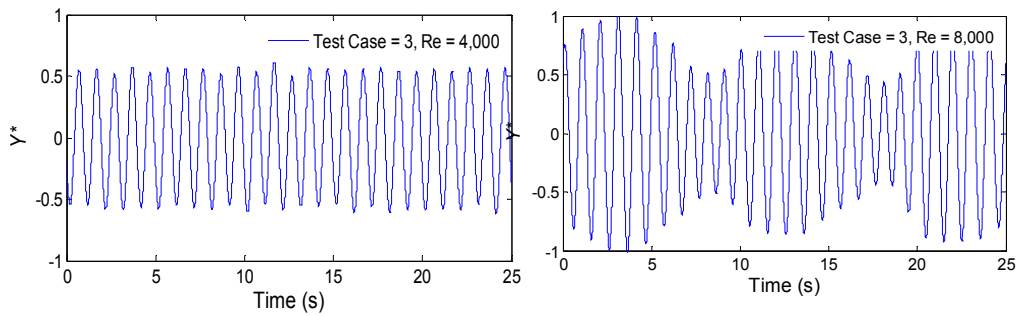


Figure 7: Measured time history of displacement for Test Case 3 (see Table I) at two different Reynolds numbers.

The displacement time series has been measured by the encoder of the motor. It was found that the frequency of oscillation is approximately  $f_{osc} = 0.9$  Hz. The oscillation frequency is an order of magnitude lower than the natural frequency of the cantilever bending mode of the structure, which makes system identification unreliable. Accordingly, due to the proximity of these two frequencies, a notch filter was designed and used to attenuate noise associated with the cantilever bending mode. The transfer function of notch filter can be written as follows and the effect of the frequency response of notch filter is shown in the Bode diagram in Figure 8.

$$G(s) = \frac{s^2 + 0.2774s + 2410}{s^2 + 27.74s + 2410} \quad (17)$$

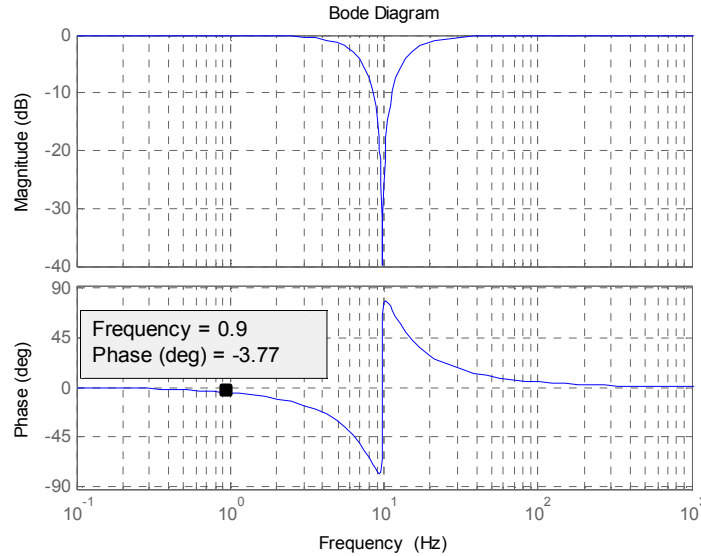


Figure 8: Frequency response of the notch filter used to filter the lift force signal in an attempt to remove the fundamental bending mode of the cylinder which has a natural frequency of 9.7Hz.

In the phase part of the diagram, in Figure 8, it is observed that close to the frequency of oscillation,  $f_{osc} = 0.9\text{Hz}$ , a small phase lag of  $3.7^\circ$  is produced. It is obvious that the generated phase lag influences the total work produced by the downstream cylinder. However, in this paper, all test cases were conducted utilizing the same phase lag, and, therefore, the test cases have an equivalent phase lag and a direct comparison between results is possible. This implies that the generated phase lag causes a similar and very small reduction in the power coefficient (less than 0.3%) of the WIV in all studied test cases.

The effect of the notch filter on the lift force signals is shown in Figure 9. The figure presents the time series of the lift force, for Test Case 1 at  $Re = 6,000$ , for about 10 cycles of oscillation. It can be observed from the figure that the designed notch filter sufficiently filters out the parasitic vibration, which is close to the

desired natural frequency of the cylinder VMSD. The power spectral density has been used to highlight the effect of notch filter. In the Fast Fourier Transform plots, the sampling time was 0.001s, utilizing 1024 points, and a Hanning window. The power spectral densities shown in Figures 9-c and 9-d reveal that the attenuation from the filtering occurs at the parasitic resonance frequency ( $f_n = 9.7$  Hz) and the notch filter assists in attenuating the noise.

The results of VMSD are compared in Figure 10 ( $x_0/D = 4.0$  and  $y_0/D = 0$ ). From Figure 10, it is clear that with increasing longitudinal distance, between cylinders, for  $Re > 6,000$ , the amplitude of oscillation of the downstream cylinder reduces. For this reason, the displacement of the downstream cylinder, as a function of longitudinal ( $x_0$ ) and lateral ( $y_0$ ) distances, was measured for different Reynolds numbers and sixteen test cases.

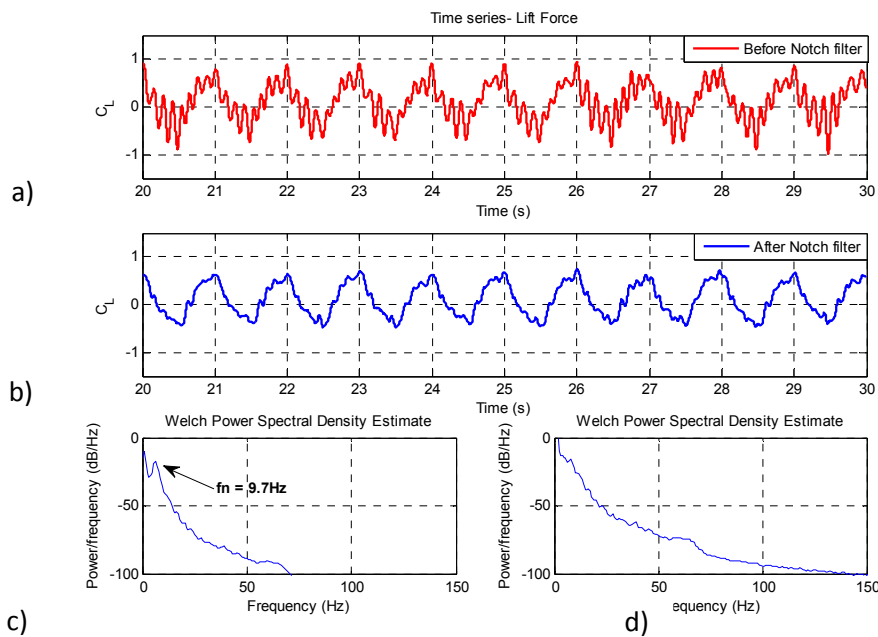


Figure 9: Measured lift coefficient signals before a) and after b) notch filter for Test Cases 1,  $Re = 6,000$ . Welch power spectral density utilised a Hanning window with sampling frequency of 1,000 Hz before c) and after d) filtering.

The displacement of the cylinder for Test case 3 is in good agreement with Assi (2009). It can be seen that at higher Reynolds numbers ( $Re > 12,000$ ), there is a small discrepancy, of less than 10%, between this study and the previous work. The small discrepancy between the data is likely due to different experimental methods, and is within acceptable bounds for experimental reproducibility.

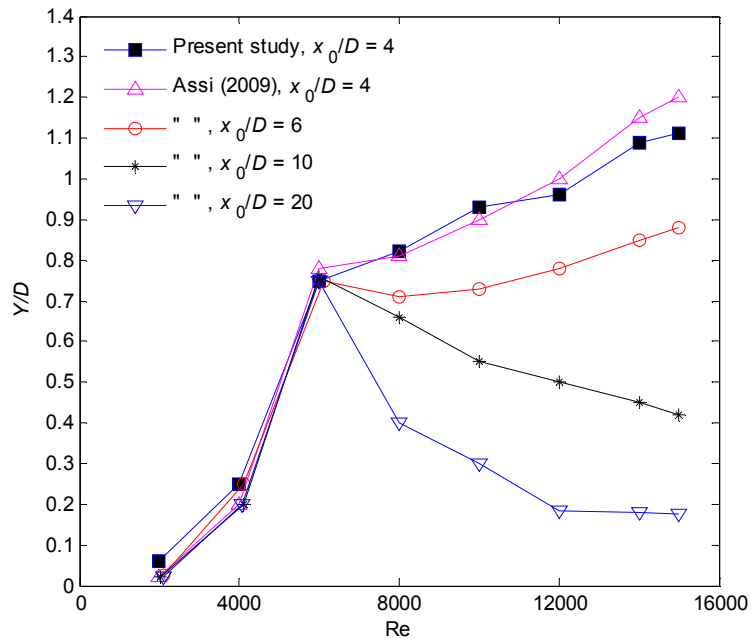


Figure 10: WIV response of the downstream cylinder as a function of the Reynolds number and a comparison of the data for  $x_0/D = 4$  with previous work (Assi 2009) (Test Case 3).

### 3.2. Effects of cylinder configuration and Reynolds number

Figure 11 demonstrates that both the longitudinal and lateral distances between the cylinders affect the amplitude of oscillation. In this figure, the effect of the arrangement of the cylinders is shown with circular symbols for all studied test cases. The minimum and maximum displacement amplitudes belong to Test Cases 1 and 11, respectively, and are marked by the lower ( $-\nabla-$ ) and upper ( $-\Delta-$ ) bounds. As the dynamic response of the downstream cylinder under the WIV mechanism is irregular compared with the VIV response of the single cylinder (compare the time history of the displacements under VIV and WIV mechanism in Figures 5 and 7), the variation of the displacement is also included in this figure. The amplitude of

oscillation of the other fourteen test cases is limited within these two bounds. It can be seen that for  $Re \leq 6,000$  the lateral distance between cylinders changes the dimensionless displacement of the downstream cylinder (compare Test Cases 1 and 11). This property was not studied in the previous work by Assi (2009) (see Figure 10). It is also observed that the displacement amplitude of the downstream cylinder increases when the longitudinal distance between cylinders increases from  $x_0/D = 2.5$  to 4 (Test Case 1 and 11, respectively). As mentioned earlier, Assi (2009) showed that among those test cases with  $4 \leq x_0/D \leq 20$ , the maximum displacement amplitude of the cylinder is achievable for  $x_0/D = 4$ . Figure 10 also shows that based on the studied test cases, the maximum displacement amplitude occurs at  $x_0/D = 4$ , which is the critical longitudinal distance between cylinder with a maximum amplitude of oscillation.

The response of the WIV mechanism in terms of the displacement amplitude of the cylinder was compared with the VIV response of a single cylinder in Figure 12. The figure shows the displacement amplitude of the VIV of a single cylinder, for which there are three distinct regimes, known as the initial, upper and lower branches in the literature. Here, these responses are categorised into three zones, as Zone 1, Zone 2 and Zone 3. In the Zone 1, the displacement amplitude of WIV shows higher values for the staggered arrangement of the cylinders, in comparison of the VIV response of a single cylinder; however, in the second zone the maximum achievable amplitude of the WIV displays lower values for the same range of the Reynolds numbers. It is also observed that for the staggered arrangement of the cylinders (for instance Test case 11); Zone 3 again shows higher displacement amplitude compared with the VIV response of a single cylinder. It is also worth noting that in the Zone 3 the amplitude of displacement is higher than the upper branch of the VIV response of a single cylinder in Zone 2. Therefore, in contrast to the VIV of a single cylinder, the results illustrate that in the WIV mechanism, the maximum amplitude of oscillation is not limited to the natural frequency of the cylinder and by increasing the Reynolds number the amplitude of oscillation increases. This assists to design and employ structures with

fewer limitations when capturing the hydrokinetic energy of streams using the WIV mechanism.

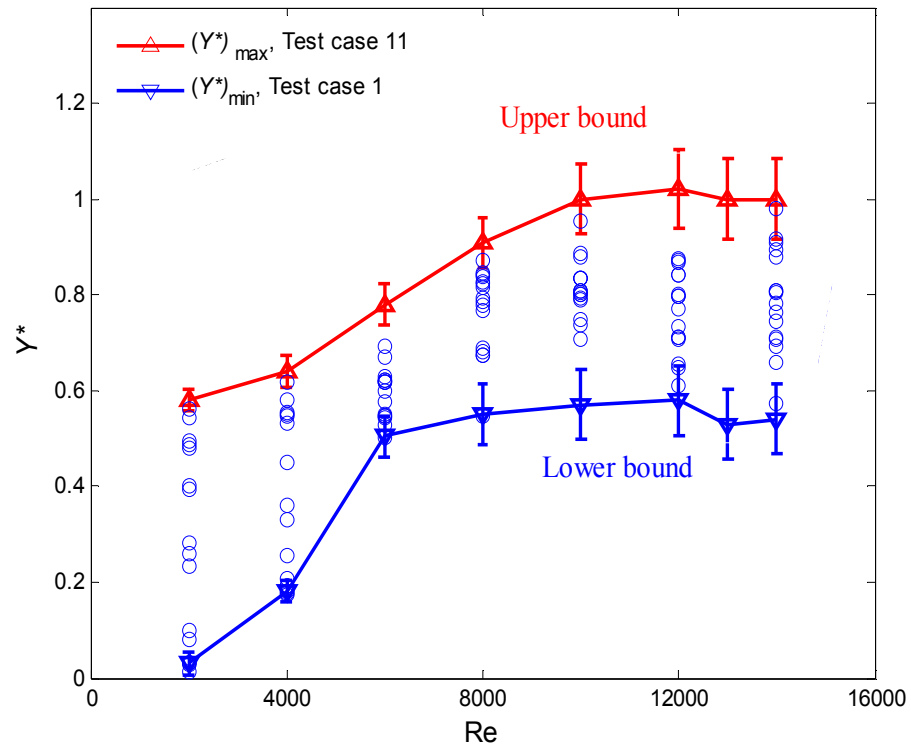


Figure 11: Scatter plot of all test cases comprising the lower and upper bounds Test case 1 and 11, respectively, as a function of the Reynolds number, and the lateral and the longitudinal distances between cylinders. The O symbols refer to other test cases included in Table II and error bars indicate the variation of the WIV response of the cylinder at each Reynolds number.

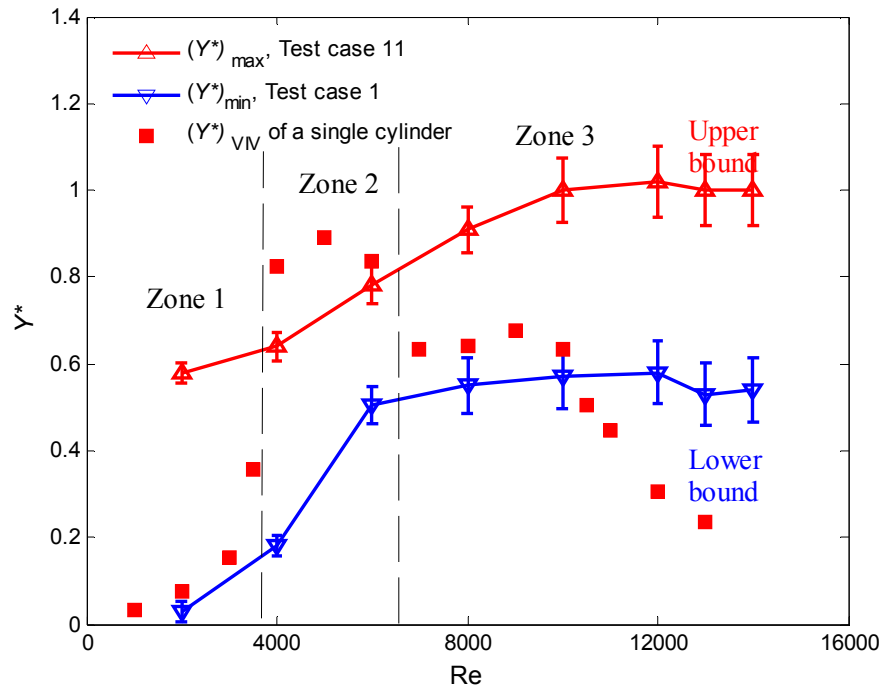


Figure 12: Comparison of the WIV response of the downstream cylinder and the VIV of a single cylinder. Error bars indicate the variation of the WIV response of the cylinder at each Reynolds number.

Considering Equations (14) to (16), it is observed that the amplitude of oscillation, the lift coefficient of the cylinder, the vortex shedding frequency, and the phase angle between the lift force and displacement can influence the power coefficient of the WIV converter. Therefore, the effect of these parameters on the WIV power coefficient is discussed in detail next.

Typical time series of  $c_L$  and  $y_0/D$  of the downstream cylinder are shown in Figures 13 and 14. The selected WIV response of the downstream cylinder is for Test Cases 3 and 7, in which the longitudinal distance is kept at  $x_0/D = 4$  (the critical distance) and lateral distances are  $y_0/D = 0$  and 1, respectively. These test cases have been chosen to compare the effect of lateral distance between the cylinders at the critical longitudinal distance,  $x_0/D = 4$ . Comparison between two different Reynolds numbers for each test case reveals that by increasing the Reynolds number, from 4,000 to 10,000, the amplitude of oscillation increases. The

larger amplitude of oscillation is also observed for Test Case 7, which has a comparable lateral distance to that of Test Case 3. This is due to the flow interference between the cylinders and the exerted lift force on the downstream cylinder which can affect the downstream cylinder because of a smaller phase difference between the lift force and displacement.

Previous numerical analyses (Derakhshandeh *et al.*, 2014a and 2014b) also showed that the phase difference between lift force and displacement of the cylinder can significantly change the extracted energy harnessed from the vortices. Similar correlations were also found in the current study. The estimated phase difference between force and displacement signals in this study was obtained using Transfer Function Estimate in Matlab, with a sampling time of 0.001s using a 1024 point FFT and Hanning window.

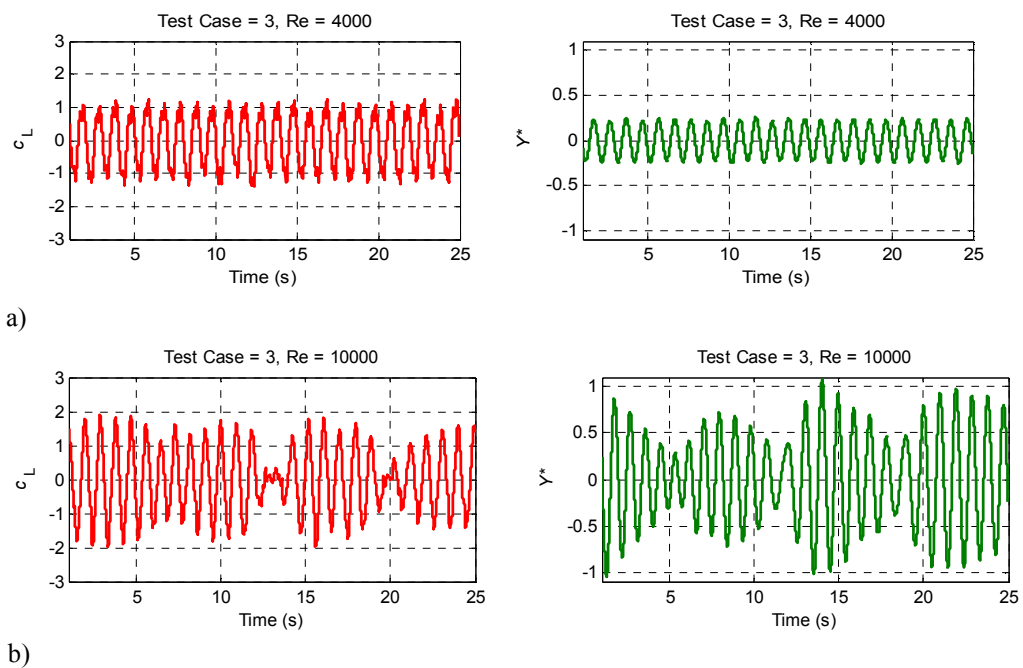


Figure 13: Time histories of the lift coefficient and displacement of the downstream cylinder for Test Case 3 at two different Reynolds numbers; a)  $Re = 4,000$ , b)  $Re = 10,000$ .



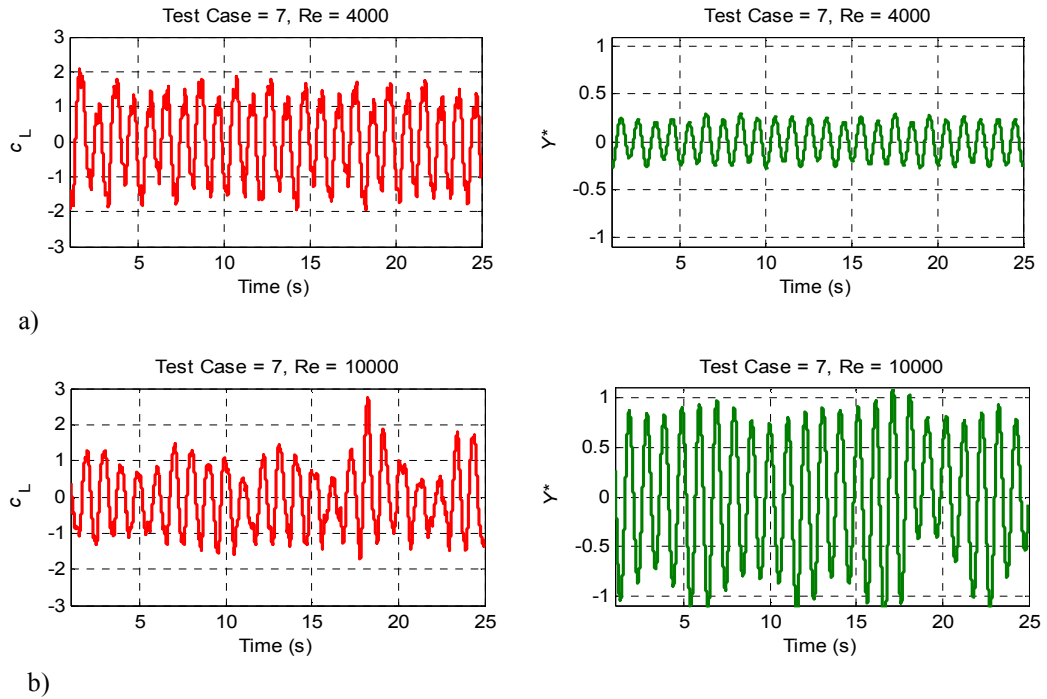


Figure 14: Time histories of the lift coefficient and displacement of the downstream cylinder Test case 7 at two different Reynolds numbers; a)  $Re = 4,000$ , b)  $Re = 10,000$ .

The results of phase differences are shown, using isolines contours, in Figure 15 for different Reynolds numbers ( $Re = 4,000, 6,000, 10,000$  and  $14,000$ ), as a function of longitudinal and lateral distances. The significance of phase difference in capturing the vortex energy is an important finding of this study. Two important outcomes can be extracted from these plots. Firstly, the results indicate that at the lower Reynolds number cases, the phase difference between force and displacement is smaller compared to the higher Reynolds number cases, which means that both signals are approximately in phase. For lower Reynolds number cases, a dominant frequency can be observed and the response of the downstream cylinder is more regular; while, for higher Reynolds number cases the response appears irregular (see Figures 13 and 14). Secondly, of all test cases studied, the results demonstrate that the minimum phase difference between the two signals occurs for test cases with  $3.5 \leq x_0/D \leq 4.5$  and  $1 \leq y_0/D \leq 2$ .

## Chapter 4: Effect of arrangement of the cylinders

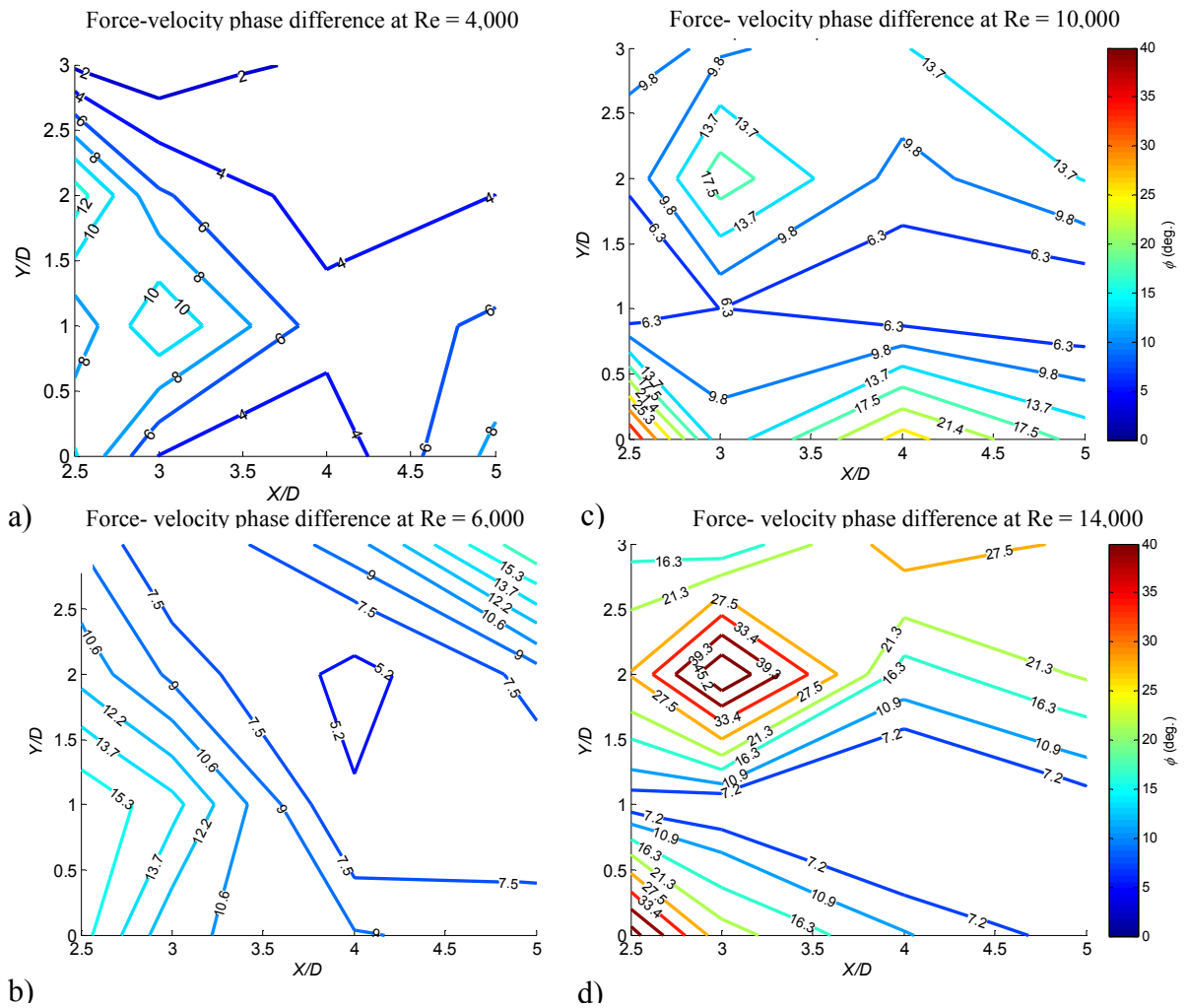


Figure 15: Isolines contours of the phase shift between force and velocity as a function of the arrangement of the cylinders and Reynolds numbers, a) Re = 4,000, b) Re = 6,000, c) Re = 10,000 and d) Re = 14,000.

In order to calculate the WIV power coefficient, the lift coefficient of the elastically mounted cylinder was calculated for all arrangements of the cylinders at different Reynolds numbers. The correlation between the lift coefficient and the Reynolds number, for all test cases, is approximately similar. The average lift coefficients have been calculated for each Reynolds number and plotted along with the respective Standard Error of Measurement (SEM) in Figure 16. The SEM is the deviation of the sampling distribution over all measurement sample tests. It can be seen that the most significant change in the lift coefficient occurs when the

Reynolds number increases from 4,000 to 6,000 due to the small phase shift. The main reason for this increment can be explained here. In the WIV mechanism, the total lift acting on the downstream cylinder can be divided into two components (Williamson and Govardhan 2004): (1) a *potential-force* component ( $F_{potential}$ ) due to the ideal flow inertia force and (2) a *vortex-force* ( $F_{vortex}$ ), which is only produced by the dynamics of the vorticity field around the downstream cylinder. Here, the *potential-force* is a function of the cylinder's acceleration and its magnitude is proportional to the product of the displaced fluid mass and the acceleration of the cylinder. Meanwhile, the *vortex-force* is dependent on the dynamics of generated vortices (Assi 2009). Consequently, in the WIV mechanism, the maximum lift coefficient acting on the downstream cylinder is accessible when both the potential lift coefficient and vortex lift coefficient become a maximum and the phase angle remains very close to zero. It was shown that, in the WIV mechanism, the total phase angle is approximately zero when the reduced velocity is roughly 4.6 and both potential and vortex forces are approximately equal (Assi 2009). In the current study, the maximum lift coefficient is obtained at  $Re = 6,000$ , which in terms of the reduced velocity is  $U_r = 4.1$ , and it is similar to the previous study (Assi 2009). With the obtained maximum lift for vortex-force and potential force, therefore, the total force can be obtained.

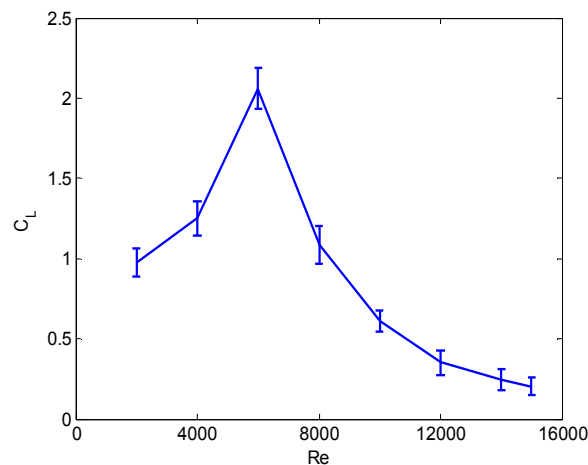


Figure 16: Effect of the Reynolds number on the lift coefficient of the downstream elastically mounted cylinder for all test cases with SEM.

---

In order to demonstrate the significance of the key parameters influencing the power coefficient of WIV, discussed above, coloured contour plots of the WIV power coefficient are plotted in Figure 17. The plotted color bar of each figure shows the range of power coefficient, in percent, within a range of 0 to 30%. The contours of the power coefficient are plotted as a function of  $(x_0/D$  and  $y_0/D)$  at different Reynolds numbers to highlight the effect of both arrangements of the cylinders and the Reynolds number. From Figure 17, it is observed that for cases with Reynolds numbers close to 6,000, maximum WIV power coefficient is obtained particularly for test cases with a staggered arrangement. Also observed is that the highest WIV power coefficient, of 28%, is obtained for the cases with  $3.5 \leq x_0/D \leq 4.5$  and  $1 \leq y_0/D \leq 2$  and a  $Re = 6,000$ . However, it is clear that the staggered arrangement above gives the highest power coefficient for all Reynolds numbers and this is due to the small phase difference between the force and velocity of the downstream cylinder.

## Chapter 4: Effect of arrangement of the cylinders

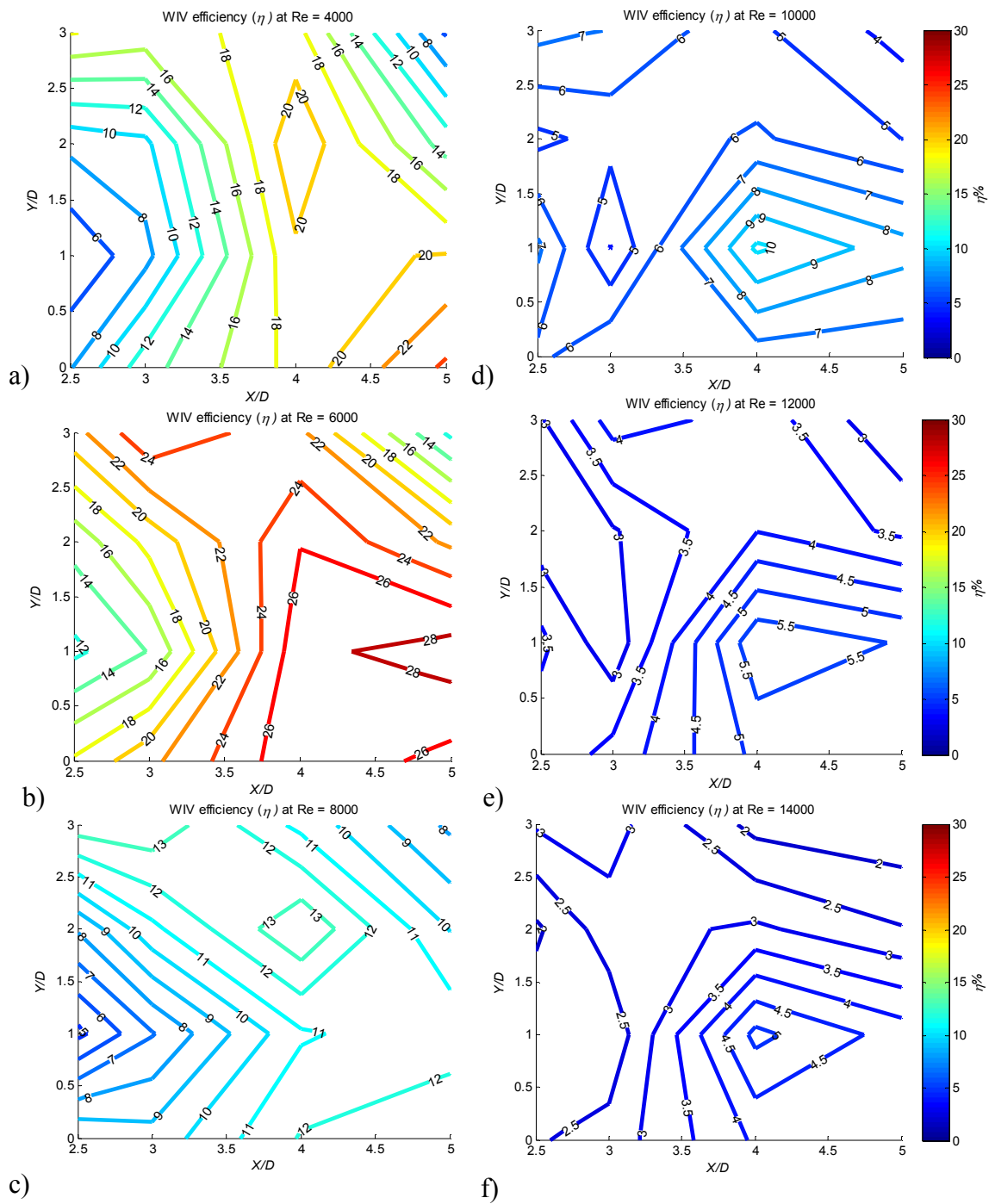


Figure 17: Effect of arrangement of the cylinders and Reynolds numbers on the power coefficient ( $\eta_{WIV}$ %) of WIV power; a) Re = 4,000, b) Re = 6,000, c) Re = 8,000, d) Re = 10,000, e) Re = 12,000 and f) Re = 14,000.

### 3.3. Maximum power content of WIV

It is worth noting that the power coefficient of the WIV converter can be calculated as a function of Betz's limit and water channel dimensions. Assuming  $U_1$  and  $U_2$  are the upstream and downstream flow velocities, respectively, the average free stream velocity is calculated to be  $\bar{U} = (U_1 + U_2)/2$ . Consequently, the mass flow rate is:

$$\dot{m} = \rho W T \bar{U} = \rho W T (U_1 + U_2)/2, \quad (18)$$

where,  $\rho$  is the density of the fluid, and  $W$  and  $T$  represent the width and depth of the channel, respectively. Based on the flow rate, the kinetic power in the channel can be calculated as

$$P_{\text{channel}} = \frac{\rho}{2} W T \bar{U}^3. \quad (19)$$

The maximum obtainable theoretical power, then, can be calculated as the difference between the hydrokinetic energy of the upstream and downstream flow, which can be written as:

$$P = \left(\frac{1}{2}\right) \dot{m}(U_1^2 - U_2^2) = \left(\frac{1}{2}\right) \rho W T U^3 \left(1 + \frac{U_2}{U_1}\right) \left[1 - \left(\frac{U_2}{U_1}\right)^2\right]. \quad (20)$$

According to Betz's limit, it was shown that the maximum theoretical power can be captured when  $U_2/U_1 = 1/3$  (Vries 1983). Hence, the maximum power for WIV can be written as follows:

$$P_{\text{theory}} = (16/27) \frac{\rho}{2} W T U^3. \quad (21)$$

The wake of the upstream cylinder can be divided into three regions based on the lateral and longitudinal distances between the cylinders. Zdravkovich (1988) categorized these regions as a) proximity interference, b) wake interference and c)

---

## Chapter 4: Effect of arrangement of the cylinders

---

no interference regions. It was shown that when the downstream cylinder is mounted at  $x/D > 4$  and  $y/D > 1$ , there is no significant interference between oncoming vortices and the downstream cylinder.

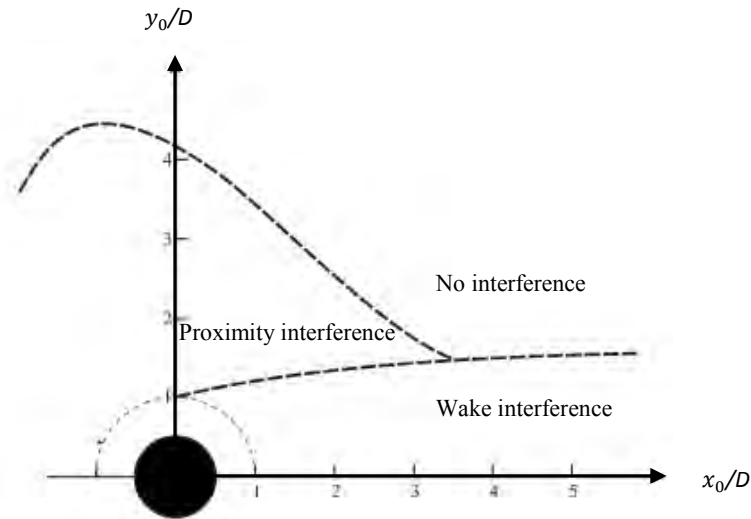


Figure 18: A map of wake interference regions when the upstream cylinder is mounted stationary (Zdravkovich 1988).

Along with the power coefficient,  $P_{WIV}$ , and the maximum theoretical power,  $P_{max}$ , the power density of the WIV can be considered as an important parameter of the device. Accordingly, the power density ( $P.D.$ ) of the WIV can be calculated based on the volume of the optimum staggered arrangement of the cylinders, where the wake region appears ineffective. The optimum longitudinal distance among those test cases examined in this study is found to be calculated  $x_0/D = 4.5D$  and  $y_0/D = 1.5 D$ . Considering the symmetric wake interference region, a staggered configuration with  $4.5D$  longitudinal distance and  $3D$  lateral distance is chosen. Figure 19 shows the volume control of this arrangement with the length of the unit. It is observed that in the selected control volume 2.5 cylinders are immersed in a volume of  $4.5D \times 3D \times L$ . Therefore, the power density can be calculated as follows:

$$P_{\text{power density}} = \left( \frac{2.5P_{\text{WIV}}}{13.5D^2L} \right) \quad (22)$$

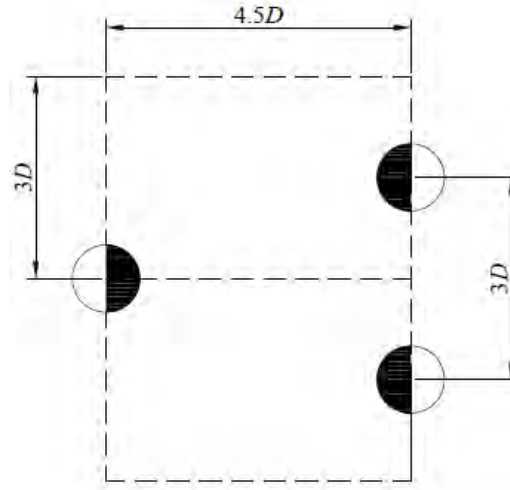


Figure 19: Configuration of the cylinders to calculate the control volume.

A brief comparison between the power coefficient of the WIV converter, the total power of the channel, and the power density can provide a better insight into the WIV converter. Table VI summarises the power generated by the WIV converter at different Reynolds numbers for the staggered arrangement shown in Figure 18. It can be seen that the generated power based on the conditions of the test cases in this study is not considerable due to the laboratory scale of the equipment. Nevertheless, the flexibility, modularity and scalability of the WIV convertor allow to access to a wide range of the Reynolds number only by altering the diameter of the cylinder. This allows enables to set a desirable Reynolds number, even at very low free stream velocities without significant changes in mechanical parameters of the convertor.



## Chapter 4: Effect of arrangement of the cylinders

---

Table VI: Power content of WIV convertor as a function of free stream velocity including the maximum theoretical power, the power of the water channel, the fluid power, the power density and the power coefficient.

$U$ (m/s)	$P_{\text{theory}}$ (mW)	$P_{\text{WIV}}$ (mW)	$P_{\text{WIV}}/P_{\text{theory}}$ (%)	$P_{\text{channel}}$ (mW)	$P_{\text{fluid}}$ (mW)	$P.D.$ (W/m <sup>3</sup> )	$\eta_{\text{WIV}}$ (%)
0.05	9.2	0.03	0.40	150	1.87	0.006	1.6
0.10	74.1	1.26	1.70	125	15.0	0.218	8.4
0.15	250.0	14.1	7.04	421	50.6	3.055	28.0
0.20	593.0	17.0	2.87	1000	120.0	2.960	14.1
0.25	1111.0	16.5	1.48	1953	230.0	2.864	7.1
0.30	2001.0	16.0	0.80	3375	400.0	2.777	4.0
0.35	3170.0	11.0	0.34	5359	643.0	1.909	1.7

### 4. Conclusions

In the present article, the effects of the arrangement of cylinders and the Reynolds number on the power coefficient of the Wake-Induced Vibration, of a two cylinder system, were studied. A Virtual Mass Spring Damper (VMSSD) system was designed, built and employed to harness the WIV energy using a PID control system. Force, displacement and frequency measurements were conducted in a closed-loop water channel and the following outcomes were observed:

1. A successful structural mechanism was designed and built to investigate the WIV response of the cylinder using a VMSSD, instead of real spring damper. In this virtual mechanism, the cylinder was installed vertically in the water channel. This assisted in avoiding the static loads on the motor arising from the cylinder, thus reducing friction and improving the response of the cylinders. Therefore, the test rig was designed to operate at a low free stream velocity (or low Reynolds number, such as  $Re = 2,000$ ) without the nonlinearities observed in previous works.
2. It is clear that in the VIV mechanism, the upper branch of amplitude occurs at a limited range of frequencies (or reduced velocities) in which the shedding frequency is very close to the resonance frequency of the mass-spring-damper. However, for the staggered arrangement of the cylinders,

the results show that WIV responses can occur at frequencies outside the range in which VIV is observed.

3. The staggered arrangement of the cylinders results in increased WIV power coefficient, as compared to the aligned arrangement of the cylinders. The results of water channel tests of sixteen different arrangements revealed that staggered arrangement with  $3.5 \leq x_0/D \leq 4.5$  and  $1 \leq y_0/D \leq 2$  showed the highest power coefficient of the WIV.
4. The present experimental work using VMSD system also showed that the Reynolds number plays an important role on the power coefficient of the WIV. The alteration of the Reynolds number changes the upstream vortex shedding frequency which affects the phase difference of the lift and displacement of the downstream cylinder, subsequently impacting on the WIV power coefficient.
5. WIV mechanism can be considered as an alternative source of energy, which is able to capture hydro-kinetic energy of the ocean currents and shallow rivers, in particular compared with VIV. Most importantly, there is possibility for improvement of the WIV converter such as optimising mass and damping ratios.

**References**

Assi, G., 2005, Experimental study of the flow interference effect around aligned cylinders, Master thesis, University of Sao Paulo, Brazil.

Assi, G., 2009, Mechanisms for flow-induced vibration of interfering bluff bodies. PhD thesis, Imperial College London, UK.

Assi, G., Bearman, P. and Meneghini, J., 2010, On the wake-induced vibration of tandem circular cylinders: The vortex interaction excitation mechanism. *Journal of Fluid Mechanics*, 61, 365-401.

Astrom, K. J. and Hagglund, T., 2006, *Advanced PID Control*, ISA.

Bearman, P. W., 1984, Vortex shedding from oscillating bluff bodies. *Journal of Fluid Mechanics*, 16, 195-222.

Bernitsas, M. M. and Raghavan, K., 2004, Converter of current/tide/wave energy. *Provisional Patent Application, United States Patent and Trademark Office Serial No. 60/628,252*.

Bernitsas, M. M., Raghavan, K., Ben-Simon, Y. and Garcia, E., 2008, VIVACE (Vortex Induced Vibration Aquatic Clean Energy): A new concept in generation of clean and renewable energy from fluid flow, *Journal of Offshore Mechanics and Arctic Engineering*, 130, 1-15.

Blevins, R. D., 1990, Flow-induced vibration. *Krieger publishing company, Malabar, Florida, USA*.

Brika, D. and Laneville, A., 1999, The flow interaction between a stationary cylinder and a downstream flexible cylinder. *Journal of Fluids and Structures*, 13, 579-606.

Chang, C. C. J., Ajith Kumar, R. and Bernitsas, M. M., 2011, VIV and galloping of single circular cylinder with surface roughness at  $3.0 \times 10^4 \leq Re \leq 1.2 \times 10^5$ . *Journal of Ocean Engineering*, 38, 1713-1732.

Derakhshandeh, J. F., Arjomandi, M., Dally, B. and Cazzolato, B., 2014-a, The effect of arrangements of two circular cylinders on the maximum

efficiency of vortex- induced vibration power using a scale-adaptive simulation model. *Journal of Fluids and Structures*, 49, 654-666.

Derakhshandeh J. F., Arjomandi, M., Dally, B. and Cazzolato, B., 2014-b, Effect of a rigid wall on the vortex induced vibration of two staggered cylinders. *Journal of Renewable and Sustainable Energy Reviews*, 6, 033114.

Govardhan, R. and Williamson, C., 2000, Modes of vortex formation and frequency response of a freely vibrating cylinder. *Journal of Fluid Mechanics*, 420, 85-130.

Govardhan, R. and Williamson, C., 2004, Critical mass in vortex-induced vibration of a cylinder. *European Journal of Mechanics-B/Fluids*, 23, 17-27.

Hover, F., Miller, S. and Triantafyllou, M., 1997, Vortex-induced vibration of marine cables: Experiments using force feedback. *Journal of Fluids and Structures*, 11 (3), 307-326.

Igarashi, T., 1981, Characteristics of the flow around two circular cylinders arranged in tandem. I. *JSME International Journal Series B*, 24, 323-331.

Khalak, A. and Williamson, C., 1999, Motions, forces and mode transitions in vortex-induced vibrations at low mass-damping. *Journal of Fluids and Structures*, 13 (7-8), 813-851.

Khan, M., Bhuyan, G., Iqbal, M. and Quaicoe, J., 2009, Hydrokinetic energy conversion systems and assessment of horizontal and vertical axis turbines for river and tidal applications: A technology status review. *Journal of Applied Energy*, 86 (10), 1823-1835.

Lee, J. H., Xiros, N. and Bernitsas, M. M., 2011, Virtual damper–spring system for VIV experiments and hydrokinetic energy conversion, *Journal of Ocean Engineering*, 38 (5-6), 732-747.

Sarpkaya, T., 1978, Fluid forces on oscillating cylinders. *NASA STI/Recon Technical Report A*, 78, 46523.

Sarpkaya, T., 1979, Vortex-induced oscillations, a selective review. *Journal of Applied Mechanics*, 46, 241-258.

#### Chapter 4: Effect of arrangement of the cylinders

---

Williamson, C. and Roshko, A., 1988, Vortex formation in the wake of an oscillating cylinder. *Journal of Fluids and Structures*, 2, 355-381.

Zdravkovich, M., 1977, Review of flow interference between two circular cylinders in various arrangements. *ASME Transactions Journal of Fluids Engineering*, 99, 618-633.

## Chapter 5

### Effect of a rigid wall

#### 5.1. Chapter overview

The arrangement of the cylinder on capturing the energy of the wake has been presented in the previous chapter. Along with the arrangement of the cylinders, in this section, it is shown how a rigid wall can influence the dynamic response of the downstream cylinder.

To analyse the effect of the wall on the WIV response of the downstream cylinder, numerical analyses have been conducted for transient flow regime over a pair of cylinders using the SAS turbulence model. As a consequence, the key parameters such as the lift coefficient, the maximum amplitude of oscillation, the Strouhal number, and the phase angle between the exerted lift force on the cylinder and the displacement of the cylinder on the efficiency of the WIV were analysed. This chapter has been published as

“Effect of a rigid wall on the vortex induced vibration of two staggered cylinders”, by Derakhshandeh, J. F., Arjomandi, M., Dally, B., Cazzolato, B., American Society of Physics (AIP), *Journal of Renewable and Sustainable Energy*, 6, 033114, 2014.

## Statement of Authorship

Title of Paper	The effect of arrangement of two circular cylinders on the maximum efficiency of Vortex-Induced Vibration power
Publication Status	<input checked="" type="radio"/> Published, <input type="radio"/> Accepted for Publication, <input type="radio"/> Submitted for Publication, <input type="radio"/> Publication style
Publication Details	Derakhshandeh, J. F., Arjomandi, M., Dally, B., Cazzolato, B., The effect of arrangements of two circular cylinders on the maximum efficiency of Vortex-Induced Vibration power using a Scale-Adaptive Simulation model, Journal of Fluids and Structures, Vol. 49, Pages 654–666, 2014.

### Author Contributions

By signing the Statement of Authorship, each author certifies that their stated contribution to the publication is accurate and that permission is granted for the publication to be included in the candidate's thesis.

Name of Principal Author (Candidate)	Javad Farrokhi Derakhshandeh		
Contribution to the Paper	Investigation of the effect of the arrangement of the cylinder on the power coefficient of the converter employing tandem, side-by-side and staggered arrangements of the cylinders.		
Signature		Date	18/03, 2015

Name of Co-Author	Maziar Arjomandi		
Contribution to the Paper	Supervised the work, assisted in developing ideas and manuscript evaluation.		
Signature		Date	18.03.2015

Name of Co-Author	Bassam Dally		
Contribution to the Paper	Supervised the work, assisted in developing ideas and manuscript evaluation.		
Signature		Date	18.03.2015

Name of Co-Author	Benjamin Cazzolato		
Contribution to the Paper	Supervised the work, assisted in developing ideas and manuscript evaluation.		
Signature		Date	19/3/15

#

## 5.2. Article

JOURNAL OF RENEWABLE AND SUSTAINABLE ENERGY 6, 033114 (2014)



### Effect of a rigid wall on the vortex induced vibration of two staggered circular cylinders

Javad Farrokhi Derakhshandeh,<sup>a)</sup> Maziar Arjomandi, Benjamin S. Cazzolato, and Bassam Dally  
*School of Mechanical Engineering, University of Adelaide, Adelaide, South Australia 5005, Australia*

(Received 4 December 2013; accepted 8 May 2014; published online 23 May 2014)

Vortex Induced Vibrations (VIVs) play a key role in a wide range of engineering applications including the extraction of renewable energy. In this paper, numerical studies of the phenomenon of VIV were conducted to investigate the flow behaviour around two identical circular cylinders. The upstream cylinder was located in the vicinity of a rigid wall and downstream one was mounted on an elastic support with one degree of freedom. The Reynolds number based on the cylinder's diameter was kept constant at 8700, while the separation between the upstream cylinder and the wall was varied. The results show that this separation distance known as the gap ratio has a significant effect on the dynamic behaviour of the upstream and downstream cylinders. Accordingly, the interaction of shear layers between the upstream cylinder and the rigid wall has a strong influence on the vortex dynamics of both cylinders, in particular, when the upstream cylinder was mounted close to the wall. In this arrangement, a jet flow produced in the wake of the upstream cylinder significantly affects the vortex shedding frequency, and the lift and drag coefficients of both cylinders. This can alter the dynamic response of the downstream cylinder and theoretical efficiency of the VIV power. © 2014 AIP Publishing LLC.  
[\[http://dx.doi.org/10.1063/1.4879275\]](http://dx.doi.org/10.1063/1.4879275)

#### I. INTRODUCTION

The conventional sources of energy, such as fossil fuels, are environmental pollutants and rapidly depleting. Therefore, it is necessary to seek alternative sources of energy, preferably those available freely in nature, such as renewable energies. The increasing need for renewable energy has motivated the harness of energy from the ocean and water resources such as currents and shallow rivers. Considering that almost two third of the earth's surface is covered with water and water resources are accessible, it is obvious that harnessing hydrokinetic energy can be a substantial source of renewable energy in the near. Guney and Kaygusuz<sup>1</sup> in their report expected that hydropower energy production, including ocean power, provides up to 200 GW of installed production capacity by 2025. Hence, hydropower energy can be recognised as an emerging source of electricity production.

Recently, the Vortex Induced Vibration (VIV) converter has been invented to harness the kinetic energy of ocean currents to produce electricity.<sup>2</sup> In general, VIV is a destructive phenomenon and related to the response of bluff bodies immersed in a fluid flow. VIV can be characterised by both fluidic parameters, such as dynamic forces, and structural parameters including the mass and damping ratios. Due to the interaction of these parameters, extensive studies have been dedicated to investigate the VIV response of a circular cylinder.

From the literature, it has become clear that VIV can be considered as a cost effective source of energy.<sup>3</sup> Although using hydropower as a source of energy has its own challenging, such as structural corrosion, employing a new technology to harness the abundance clean

---

<sup>a)</sup>Email: javad.farrokhideerakhshandeh@adelaide.edu.au



energy from currents and oceans with high density, low maintenance, sensible efficiency, and long life is always desirable.<sup>4</sup> Among different hydropower sources of energy, VIV appears the most advantageous in terms of production cost and volumetric power density. The comparison between conventional sources of energy and VIV energy generation indicates that the cost of VIV is comparable with those sources of energy.<sup>3</sup> In a benchmarking study, VIV energy converter was compared to three types of wave energy converters including Pelamis, the Opt power buoy, and Energetech. Pelamis is a floating ocean wave converter; Opt power buoy is another floating wave converter which is moored to the sea bed, and Energetech is located on the sea bed or moored at a low depth which has been developed in Australia in 1992. Figure 1 shows that the volume density of VIV ( $\text{kW}/\text{m}^3$ ) is much higher than other types of wave converters.<sup>3</sup>

Vortex formation of an oscillating bluff body has been studied by Bearman.<sup>5</sup> This study modelled the behaviour of an elastically mounted cylinder as a simple mass-spring-damper. Khalak and Williamson<sup>6</sup> measured shear forces on a circular cylinder in a water channel. They classified the amplitude response of a circular cylinder for a very low mass and damping system into three categories: initial, upper, and lower. In the initial category, the oscillation of the cylinder begins to build up and in the upper one the resonance occurs with the maximum obtainable amplitude ratio. Finally, at the lower amplitude response, the oscillation of the cylinder is damped.

Govardhan and Williamson<sup>7</sup> showed that the maximum amplitude of oscillation is a function of reduced velocity which is defined as  $V_r = U/(fD)$ , where  $U$  is the free stream velocity,  $f$  is the frequency of oscillation, and  $D$  is the diameter of the cylinder. They demonstrated that at reduced velocity between  $V_r = 5$  and 10, the upper category of oscillation ( $y/D = 1$ ) is achievable using the low product of mass and damping ratios ( $m^* \zeta = 0.01$ ). The mass and damping ratios can be defined as  $m^* = 4m/\rho\pi D^2 L$  and  $\zeta = c/2\sqrt{km}$ , respectively, where  $m$  is the mass of the system,  $L$  is the length of the cylinder,  $c$  is the viscous damping coefficient, and  $k$  is the spring stiffness.

Scholars also have determined the efficiency of the VIV power both theoretically and experimentally for different scenarios. Bernitsas and Raghavan<sup>3</sup> invented a converter to capture the VIV energy of ocean currents and developed a mathematical model to calculate the theoretical efficiency of VIV power. In their investigations, the experimental and theoretical VIV efficiencies were estimated to be 22% and 37%, respectively. Furthermore, Raghavan and Bernitsas<sup>8</sup> showed that the Reynolds number has a significant effect on the amplitude ratio of the cylinder and plays an important role than the mass and damping ratios'. Their experiments in the Transition Shear Layer (TrSL3) regime ( $2 \times 10^4 - 4 \times 10^4 < \text{Re} < 3.5 \times 10^5 - 6 \times 10^6$ ) were found to produce a maximum amplitude ratio of  $y/D = 1.8$  with a mass damping ratio 20 times higher than that of Govardhan and Williamson.<sup>7</sup> It is shown that the maximum amplitude of the oscillation can considerably affect the efficiency of the VIV power.

Derakhshandeh<sup>9</sup> investigated the effect of arrangements of two staggered circular cylinders on the efficiency of the VIV power at high Reynolds number. They modelled 35 arrangements

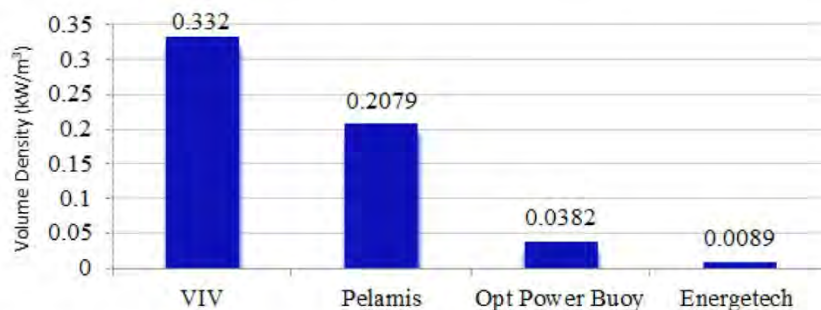


FIG. 1. Comparison of volume energy density of VIV with three types of wave converters, based on Bernitsas *et al.*<sup>3</sup>

of the identical cylinders based on longitudinal ( $x/D$ ) and lateral ( $y/D$ ) distances between cylinders. According to their studies, the best location for the downstream cylinder to achieve the maximum efficiency of VIV was  $3.5 \leq x/D \leq 4.5$  and  $1 \leq y/D \leq 2$  with approximately 48% of theoretical efficiency.

All previous studies were generally conducted to analyse the response of VIV for cylinders which were mounted without any blockage effects. Apart from the flow around unbounded cylinders, there are several studies of a flow over a single cylinder with different cross sections near the wall. The studies of flow around a single cylinder in the vicinity of a rigid wall have shown that the form of the dynamics of vortex formation differs noticeably with changes of the gap ratio ( $G/D$ ), where  $G$  is the separation between the cylinder and the wall.

The effect of a wall on the cylinder generates a non-uniform velocity profile in the wake of the cylinder. Consequently, asymmetric shear forces affect the cylinder, and a jet flow behind the cylinder is generated. This fact has been highlighted by previous researchers experimentally and numerically.<sup>10–13</sup> In these studies, the critical gap ratio ( $G/D$ ) in which the suppression of vortex shedding occur was found to be approximately in the range of  $0.3 \leq G/D \leq 0.45$ .

Although the previous studies have highlighted the influence of different parameters on VIV for unbounded and bounded cylinders, the authors are not aware of any investigation which analyse the flow around bounded cylinders to extract VIV energy. Hence, in the current paper, the response of the elastically mounted downstream cylinder in the wake of the stationary upstream cylinder is considered. In this staggered arrangement, the gap ratio of the upstream cylinder differs from 0.25 to 1.5. This study aims to calculate the theoretical efficiency of the VIV energy that can be harnessed by a downstream elastically mounted cylinder, as a function of the gap ratio of the upstream cylinder.

## II. METHODS

In this paper, Computational Fluid Dynamics (CFD) analysis was implemented using ANSYS Fluent package to determine the shear forces, the maximum amplitude of the downstream cylinder and the phase lag between the force and displacement of the downstream cylinder, which is necessary to determine the amount of power generated by the device.

The displacement of the downstream cylinder was modelled using the dynamic mesh of ANSYS Fluent. Of the three types of dynamic mesh methods (namely, smoothing, layering, or remeshing) available in Fluent, the remeshing method is the most suitable for unstructured meshes and the layering approach is employed for the case where the entire mesh moves up and down. The diffusion smoothing is the most suitable for quadrilateral mesh types employed in this study. By setting up the diffusion method as a "boundary distance," the diffusion mainly influences the interior cells and to a lesser extent the cells adjacent to the moving wall. This approach assists in achieving a consistent  $y$ -plus (non-dimensional wall distance for a wall-bounded flow) value, regardless of the motion at each time step.

To study the characteristics of the flow around the cylinders, the Scale Adaptive Simulation (SAS) turbulence model of ANSYS Fluent was used based on the Finite Volume Method (FVM) with a pressure based algorithm. In comparison to the other turbulence models, the SAS model is a relatively new model and was developed by Menter and Egorov.<sup>14</sup> This model uses the von Karman length scale which is defined as

$$L_{vk} = k_t \left| \frac{\partial U / \partial y}{\partial^2 U / \partial y^2} \right|. \quad (1)$$

Here,  $k_t$  is the turbulent kinetic energy. Using the von Karman length scale enables the model to adapt its behaviour to Scale Resolving Simulation (SRS) according to the stability parameters of the flow.<sup>15</sup> This allows the model to provide a balance between the contributions of the simulated and resolved parts of the turbulence stresses. Hence, the model can effectively and automatically switch from the Large Eddy Simulation (LES) mode to the Reynolds Average Navier Stokes (RANS) mode.<sup>16</sup>

Although the SAS model is not as accurate as the LES model, it is less dependent on the mesh element resolution compared with the LES models and can capture the turbulence length scales more accurately than  $k-\omega$ ,  $k-\varepsilon$  or even Shear Stress Transport (SST) models.<sup>17</sup> Furthermore, Guilmineau and Queutey<sup>18</sup> showed that SST model cannot predict the maximum amplitude of oscillation in the upper category of oscillation. Therefore, compared to the LES model, the SAS model can be utilized with a coarser mesh while still keeping its accuracy. This advantage of the SAS model reduces the computational cost without compromising the model accuracy. A detailed explanation of the SAS model has been reported elsewhere.<sup>14,16,17</sup>

### A. Mathematical model

The response of an elastically mounted cylinder with one degree of freedom (1-DOF) (here, the degree of freedom is in  $y$ -direction perpendicular to the free stream velocity) can be approximated by a mass-spring-damper model (Bearman, 1984). Therefore, the equation of motion can be written as

$$m\ddot{y}(t) + c\dot{y}(t) + ky(t) = F_y(t), \quad (2)$$

where  $\dot{y}$  and  $\ddot{y}$  are the velocity and acceleration of the cylinder, respectively, and  $F_y$  is the force exerted on the cylinder by the fluid perpendicular to the direction of flow.

In the VIV phenomenon, the natural frequency of oscillation is considerably influenced by the additional mass of fluid that is accelerated with the bluff body. For instance, the added mass of bluff body immersed in air is often negligible, however a bluff body immersed in water can have significant additional mass. For this reason, the mass ratio is defined as non-dimensional parameters based on the specific mass of the fluid in which the cylinder is immersed.<sup>19</sup> Therefore, the structural parameters including the mass ratio and structural damping are generally expressed by  $m^* = 4m/\rho\pi D^2 L$  and  $\zeta = c/2\sqrt{km}$ , respectively.<sup>20</sup> Here,  $\rho$  presents the fluid density.

By assuming linear behaviour and sinusoidal response of the cylinder, the time dependent fluctuation amplitude, the velocity, and lift coefficient of the cylinder can be obtained from the following equations, respectively:

$$y(t) = y_{\max} \sin(2\pi f_s t), \quad (3)$$

$$\dot{y}(t) = (2\pi f_s) y_{\max} \cos(2\pi f_s t), \quad (4)$$

$$c_L(t) = C_L \cdot \sin(2\pi f_s t + \Phi), \quad (5)$$

where  $y_{\max}$  is the maximum amplitude,  $f_s$  represents the frequency at which vortices shed,  $\dot{y}$  and  $c_L$  are the time dependent velocity and lift coefficient of the cylinder,  $C_L$  is the lift coefficient amplitude, and  $\Phi$  is the phase angle of the displacement with respect to the exciting lift force, which for a linear system at resonance is close to  $\pi/2$ .<sup>3</sup>

The total work produced by the downstream cylinder may be obtained using the vertical force, comprising the pressure and viscous forces on the cylinder. Hence, the work acting on the downstream cylinder can be calculated as the inner product of the total vertical force by the displacement of the cylinder in a one complete cycle of oscillation ( $T$ ),

$$W_{\text{VIV}} = \int_0^T F_y \dot{y} dt. \quad (6)$$

By integrating the right hand side of Eq. (6), the power of VIV can be written as follows:

$$P_{\text{VIV}} = \frac{W_{\text{VIV}}}{T}, \quad (7)$$

$$P_{\text{VIV}} = \frac{1}{2} \pi \rho U^2 C_L f_s y_{\max} D L \sin(\Phi). \quad (8)$$

The detailed derivation of Eq. (8) can be found in Bernitsas and Raghavan.<sup>3</sup>

Finally, the fluid power can be used to calculate the efficiency of the VIV power over a complete cycle as follows:

$$\eta_{\text{VIV}} = \frac{P_{\text{VIV}}}{P_{\text{fluid}}}, \quad (9)$$

where  $P_{\text{fluid}}$  is the fluid power based on the dynamic pressure which is extracted from the Bernoulli's equation  $\frac{1}{2}\rho U^2$ . Therefore, correlating the wetted area of the cylinder,  $DL$ , and dynamic pressure results in the force over the projected area. Hence, the power in the fluid can be written as  $P_{\text{fluid}} = 0.5\rho U^3 DL$  and the efficiency of VIV can be defined as

$$\eta_{\text{VIV}} = \frac{\frac{1}{2}\pi\rho U^2 C_L f_s y_{\text{max}} DL \sin(\Phi)}{\frac{1}{2}\rho U^3 DL} = \frac{\pi C_L f_s y_{\text{max}} \sin(\Phi)}{U},$$

which in terms of the Strouhal number,  $St$ , is

$$\eta_{\text{VIV}} = \pi C_L \left(\frac{y_{\text{max}}}{D}\right) St \sin(\Phi). \quad (10)$$

Equation (10) shows that the theoretical efficiency of VIV power depends on four non-dimensional parameters, namely, the lift coefficient, the maximum amplitude of oscillation normalized by the cylinder diameter, the Strouhal number ( $St$ ), and the phase angle between the exerted lift force on the cylinder and the displacement of the cylinder. In the current study, the impact of the key parameters of Eq. (10) on the VIV efficiency is analysed.

### B. Problem definition

A two-dimensional schematic of two staggered cylinders is shown in Figure 2. In this arrangement, the diameters of the cylinders were kept equal to  $D = 50$  mm. To facilitate the comparison, the Reynolds numbers and structural parameters were chosen based on the previous studies by Yang and Gao.<sup>21</sup> The Reynolds number based on the diameter of the cylinders was kept constant at  $Re = 8700$ . This Reynolds number corresponds to  $U = 0.174$  m/s. The structural parameters including the mass and damping ratios were set at  $m^* = 3.87$  and  $\zeta = 0.0152$ , respectively. Therefore, the mass of the cylinder was defined in the user defined function (UDF) file as  $m = 1.97$  kg. In addition, the natural frequency of the structure was set at  $f = 1.27$  Hz. The fluid density was constant and close to the density of water at  $998.2$  kg/m<sup>3</sup>. The upstream cylinder was located at  $10D$  from the inlet boundary. The turbulent boundary layer thickness over a flat plate can be estimated by  $\delta \approx 0.382x/Re^{1/5}$ .<sup>22</sup> For the chosen Reynolds number at this

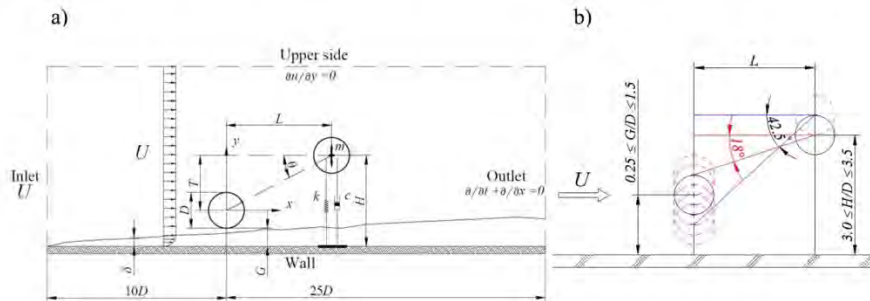


FIG. 2. (a) Schematic of the computational domain including the cylinders arrangement and boundary conditions. (b) schematic of the arrangements of cylinders; 6 positions for the upstream cylinder and 2 for the downstream cylinder.

location, the thickness of the boundary layer was approximately  $\delta = 31.1$  mm or  $\delta/D = 0.622$ . In the numerical model, the gap ratio between the upstream cylinder and the wall was varied from 0.25 to 1.5 with an increment of 0.25, which means that for Test cases 1 and 2, the upstream cylinder was partially submerged in the boundary layer (Table I). For instance, at  $G/D = 0.25$ , the distance between the wall and the upstream cylinder is  $G = 12.5$  mm which means the upstream cylinder was submerged in the boundary layer by 18.6 mm. Due to the blockage and tripping effects, the downstream cylinder was found to be affected by the jet and wake of the upstream cylinder. Six gap ratios of the upstream cylinder and two longitudinal locations, ( $H/D$ ), of the downstream cylinders (in total twelve arrangements) were analysed. By increasing the gap ratio from  $G/D = 0.25$  to 1.5, the angle between the cylinders ( $\theta$ ) was reduced from  $42.5^\circ$  to  $18.4^\circ$  (Figure 2(b)). The effect of the position of the downstream cylinder on VIV response is analysed using two longitudinal locations. Table I summarises the geometrical dimensions of the twelve test cases modelled in this study.

Considering these features, two main case studies were defined and analysed based on the structural support of the downstream cylinder.

**Case Study I** includes twelve test cases in which both cylinders were mounted on the stationary supports to investigate the fluid flow (Table I). This assists to analyse the key parameters of the flow, such as shear forces and the frequency of vortices.

**Case Study II** considers the effect of the stationary upstream cylinder on the downstream elastically mounted cylinder, with the same geometrical parameters are summarised in Table I, to analyse the efficiency of the VIV power.

The quadrilateral mesh element was utilized for all numerical models. The mesh created was approximately 45 000 elements. Derakhshandeh *et al.*<sup>9</sup> previously showed that this number of mesh elements is sufficient to accurately capture the flow pattern around two cylinders in a turbulent flow. Considering the minimum mesh size and free stream velocity, the selected time step was set at 0.05 s to achieve a converging solution. A typical structured mesh is shown in Figure 3.

### III. RESULTS

Numerical simulations first were validated using experimental studies conducted on flow around a single stationary cylinder under the effect of a rigid wall.<sup>23,24</sup> Following the validation, the results of numerical analyses for both case studies (Case studies I and II) are presented in this section.

#### A. Validation of the model

For the ease of comparison, the Reynolds numbers were chosen similar to the ones used in the experiments of Price and Sumner<sup>23</sup> and Khabbouchi and Guellouz<sup>24</sup> ( $Re = 1400, 3900, \text{ and } 8700$ ). Typical results of dimensionless mean velocity ( $\bar{u}/U$ ) at  $G/D = 1.0$  are compared with experimental data of Khabbouchi and Guellouz<sup>24</sup> at six sections behind the cylinder (Figure 4). Here,  $\bar{u}$  is the average of the  $x$ -velocity, which was calculated over the total running time. The trend of the velocities curve can be seen in the wake of the cylinder at different sections. The results show that the behaviour of the velocity profile and size of the recirculation region of the numerical findings well matches to the recorded experimental results. However, some

TABLE I. Geometrical dimensions of twelve test cases including the gap ratios,  $G/D$ ,  $H/D$ , and angle between the cylinders ( $\theta$ ).

Test case	1 <sup>a</sup>	2 <sup>a</sup>	3	4	5	6	7	8	9	10	11	12
$G/D$	0.25	0.5	0.75	1	1.25	1.5	0.25	0.5	0.75	1.0	1.25	1.5
$H/D$	3.5	3.5	3.5	3.5	3.5	3.5	3.0	3.0	3.0	3.0	3.0	3.0
$\theta$ (deg)	42.5	39.8	36.8	33.7	30.2	26.5	36.8	33.7	30.2	26.5	22.6	18.4

<sup>a</sup>First cylinder is partially submerged in the boundary layer.

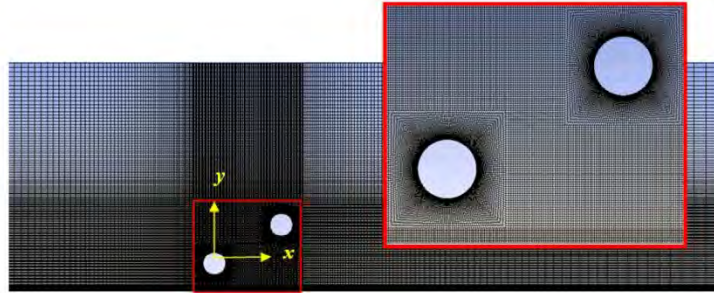


FIG. 3. Typical mesh grid around two circular cylinders for the Test case 3 (see Table I).

differences occur at  $x/D = 1$  and  $x/D = 1.5$  close to the cylinder where the numerical results show a V-shape profile compared to the U-shape of experimental results. The V-shape profiles of the numerical findings are due to the finer meshes around the cylinder where the meshes have been created by bias factor compared to the coarse meshes far from the cylinder (see Figure 3). Therefore, the mean streamwise velocity profile of finer meshes retains the V shape at lower wake sections. It is obvious that both characteristics of the size and form of the recirculation region are directly related to the length of the vortex formation region.<sup>25</sup>

The Strouhal number is an important parameter in determining the VIV efficiency (Eq. (10)) which has been obtained from the numerical simulations and is plotted in Figure 5(a) as a function of the gap ratio along with the experimental results of Price and Sumner.<sup>23</sup> This figure shows that when the cylinder was positioned close to the wall, the Strouhal number increases due to the suppression of vortices between the cylinder and the wall. This is primarily because of the jet flow behaviour experienced by the generated vortices as they are quickly expunged from the cylinder vicinity. When the cylinder was located very close to the wall,  $G/D = 0.25$ , the Strouhal frequency profile shows two peaks at different ranges of Reynolds numbers. Figure 5(b) demonstrates these two peaks at  $Re = 1400$ . These two peaks occur due to the interaction of the boundary layers between the cylinder and wall which can lead to non-linearities.

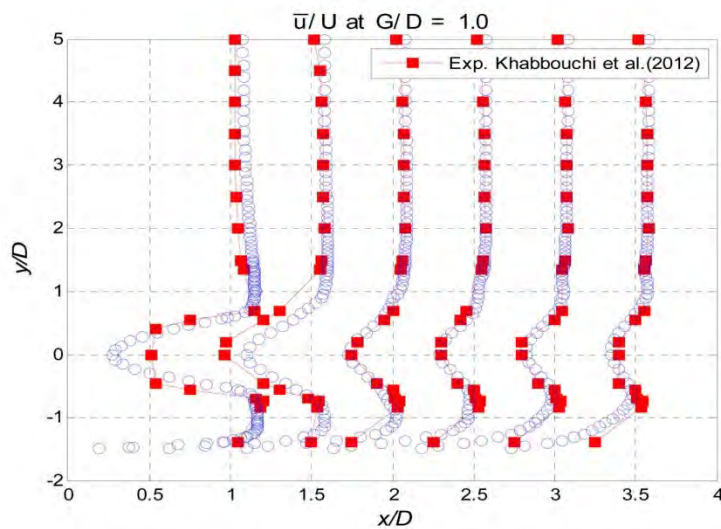


FIG. 4. Comparison of the mean streamwise ( $\bar{u}/U$ ) profiles in the near wake of the cylinder at gap ratio  $G/D = 1.0$  and  $Re = 8700$  for a single cylinder. The experimental results extracted from Khabbouchi *et al.*<sup>24</sup> and are shown as red squares. The simulations are the blue circles.

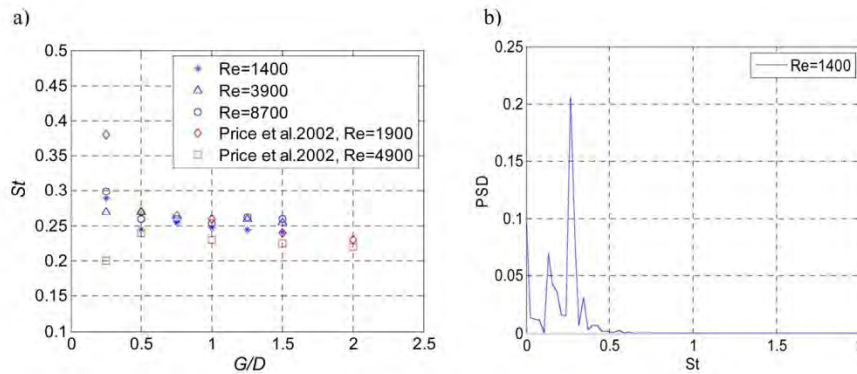


FIG. 5. Strouhal frequency of a single cylinder; (a) comparison of the Strouhal numbers at different gap ratios with the experimental data of Price *et al.*,<sup>23</sup> (b) power spectral density of the lift coefficient at  $G/D = 0.25$  and  $Re = 1400$ .

**B. Case study I**

Figures 6 and 7 depict the mean drag and fluctuating lift coefficients of the upstream and downstream cylinders, respectively. When the upstream cylinder is located in the vicinity of the wall, larger shear forces are produced due to the boundary layer effects. This increases the mean drag and fluctuating lift coefficients of the upstream cylinder. It can be seen that when the cylinder is located under the boundary layer, the drag coefficient increases at  $G/D = 0.5$ . At a lower gap ratio,  $G/D = 0.25$ , the upstream drag and fluctuating lift coefficients are lower due to the suppression of the vortices (Figures 6(a) and 7(a)). Increasing the gap ratio to  $G/D \geq 0.75$  has minor impact on the drag and fluctuating lift coefficients. The sensitivity of these coefficients to the longitudinal distance of the downstream cylinder ( $H/D$ ) is insignificant on both cylinders. Hence, when considering the VIV power of the downstream cylinder, it is deemed more appropriate to analyse only one group of the Test cases where the  $H/D$  is equal to 3.5.

The mean drag and fluctuating lift coefficients of the downstream cylinder are shown in Figures 6(b) and 7(b) as a function of the gap ratio. It is observed that the mean drag coefficient of the downstream cylinder shows an *OPPOSITE* trend compared to the mean drag coefficient of the upstream cylinder at low gap ratios. However, the variation of the fluctuating lift coefficient of the downstream cylinder is limited to a narrow range approximated to be between 0.6 and 0.7. Since the downstream cylinder is placed in the outside of the boundary layer and can be only influenced by the jet flow of the produced vortices of the upstream cylinder, the drag coefficient of the downstream cylinder decreases to 0.5 at  $G/D = 0.5$ . The trend of the fluctuating lift coefficient of the upstream cylinder reveals that this parameter is more dependent

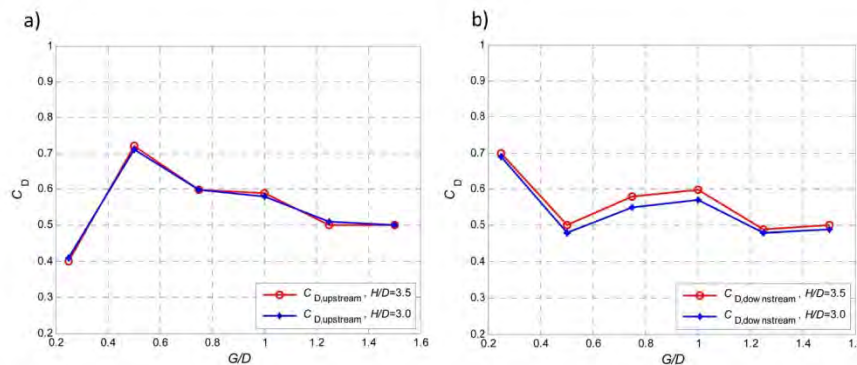


FIG. 6. Effect of the gap ratio and location of the downstream cylinder on the mean drag coefficients of the (a) upstream cylinder and (b) downstream cylinder at  $Re = 8700$ .

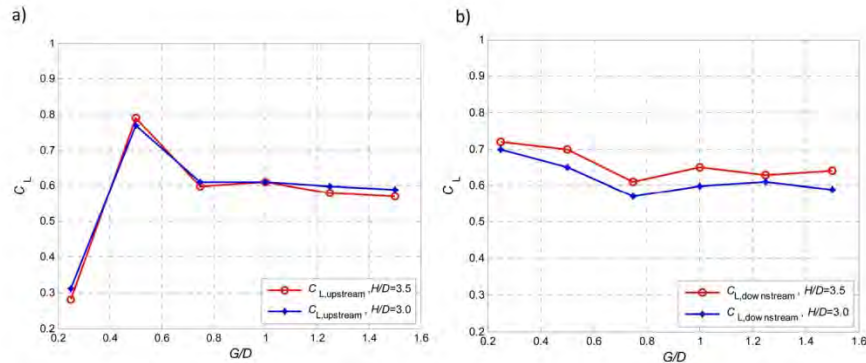


FIG. 7. Effect of the gap ratio and location of the downstream cylinder on the fluctuating lift coefficients of the (a) upstream cylinder and (b) downstream cylinder at  $Re = 8700$ .

and sensitive to the boundary layer (Figure 7(a)). It can be seen that the variation of the fluctuating lift coefficient is between 0.3 and 0.8 at lower gap ratios and by increasing the gap ratio to  $G/D = 0.75$ , this factor decreases noticeably. This reduction can also be seen for the downstream cylinder.

As mentioned earlier in Eq. (10), the lift coefficient is one of the parameters that can affect the extracted power of the VIV efficiency. However, Figure 7(b) illustrates that the range of variation of the lift coefficient with respect to the gap ratio of the upstream cylinder is relatively small.

### C. Dynamics of vorticity

To analyse the effect of wall and jet flow, in the wake of the upstream cylinder, the typical profiles of the mean streamwise velocity for two gap ratios,  $G/D = 0.25$  and 1.0, are depicted in Figure 8. The data were normalized against the free stream velocity and the diameter of the cylinder. The streamwise velocity profile is shown in blue circles at  $X/D = 3$  at which the downstream cylinder was positioned. It is observed that due to the wall effect, the mean streamwise velocity profiles are not symmetric and tend to be inclined towards one side. In addition, comparison between the streamwise velocity profiles at the same sections reveals that at lower gap ratio,  $G/D = 0.25$ , the streamwise velocity is higher than at the larger gap ratio  $G/D = 1.0$ , which means a larger jet flow in the gap is generated. This interaction alters the pressure coefficient of the downstream cylinder and it is expected to change the VIV response of the cylinder when the second cylinder was mounted elastically.

Vorticity contours of the Test cases 2 and 5 over 0.8 s after convergence are shown in Figures 9 and 10, respectively. These test cases have been selected due to the critical values of the shear forces. The time period is sufficiently large to capture a complete cycle of vortex formation.

The vortices generated from upper and lower surfaces of the upstream cylinder have been identified in Figure 9. The positive vortices are generated from the lower surface, while the negative ones arise from the upper surface. The pattern of vortex shedding in the wake of the upstream cylinder is referred to as two single vortex-modes, "2S," and indicating two single vortices in the wake of the upstream cylinder generated per cycle.<sup>26</sup> The presence of the rigid wall forces the positive vortex to move forward. (Figure 9, at  $t = 17.6$  s). The motion direction of the generated vortex depends on the gap ratio of the upstream cylinder. Figure 9 ( $G/D = 0.5$ ) shows that these two vortices grow gradually and the negative vortex eventually rolls up over the positive vortex and covers the lower vortex. For the 2S mode, the transverse amplitude of vortices is small and it increases very slowly with increasing the Reynolds number or reduced velocity.<sup>27</sup> Consequently, during a complete cycle of the vortex formation, the produced upstream vortices pass the downstream cylinder without any contact and the space of  $S$  is



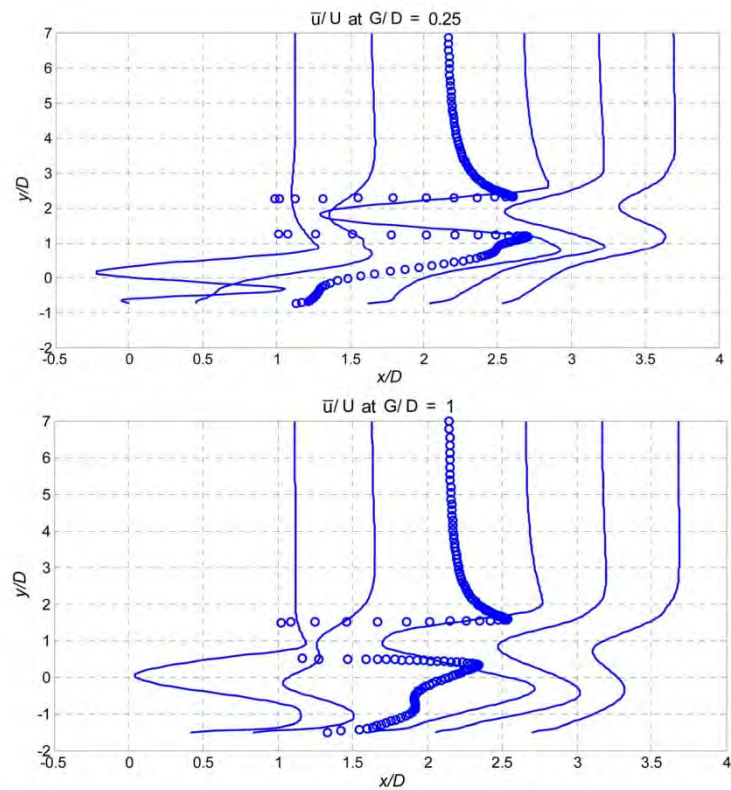


FIG. 8. Mean streamwise ( $\bar{u}/U$ ) profiles in the near wake of the two cylinders at gap ratios  $G/D=0.25$  and  $1$ , at  $Re=8700$ . Blue circles depict the mean streamwise velocity at  $x/D=3$  which is the position of the second cylinder.

generated between the vortices and downstream cylinder (see Figures 9 and 10, at  $t=17.6$  s). The reason for this behaviour is related to the transverse amplitude of the single vortex mode. By increasing the gap ratio to  $G/D=1.25$ , the positive vortices can still translate upward from the wall and  $S$  space gradually decreases to a minimum and finally at  $t=17.6$  s the positive vortex connects to the lower surface of the downstream cylinder (Figure 10,  $t=17.6$  s). The brackets around the vortices show that the maximum transverse amplitude of 2S vortex mode.

Govardhan and Williamson<sup>26</sup> showed that at low mass damping ratios, three types of behaviour of VIV response occur. These are known as initial, upper, and lower branches, in which the 2S mode corresponds to the initial branch of VIV response. With formation of the 2S mode in the initial branch, the intense strain region occurs outside the developing vortices; therefore, the vortices cannot be split and consequently, a high strain rate region can exist between the two generated vortices.<sup>26</sup>

With 2S vortex mode, the maximum transverse force can arise from the initial to the upper transmission branches due to the effect of phase between force and displacement of the cylinder. Therefore, to enhance the influence of the positive vortices with limited transverse amplitude, not only the position of the downstream cylinder is important but also the force-displacement phase angle plays a vital role in harnessing the energy of vortices. Equation (10) demonstrates that the phase angle between force and displacement can considerably affect the generated work by the downstream cylinder. It is assumed that for a linear system at resonance, the phase angle between force and displacement for unbounded cylinders is  $\pi/2$ ;<sup>3</sup> however, in reality and particularly due to the effect of the wall, the phase angle can change and affect the maximum amplitude of oscillation ( $y_{\max}$ ). In reference to Eq. (10), the maximum amplitude of oscillation is also an important factor which can directly influence the efficiency of VIV power.

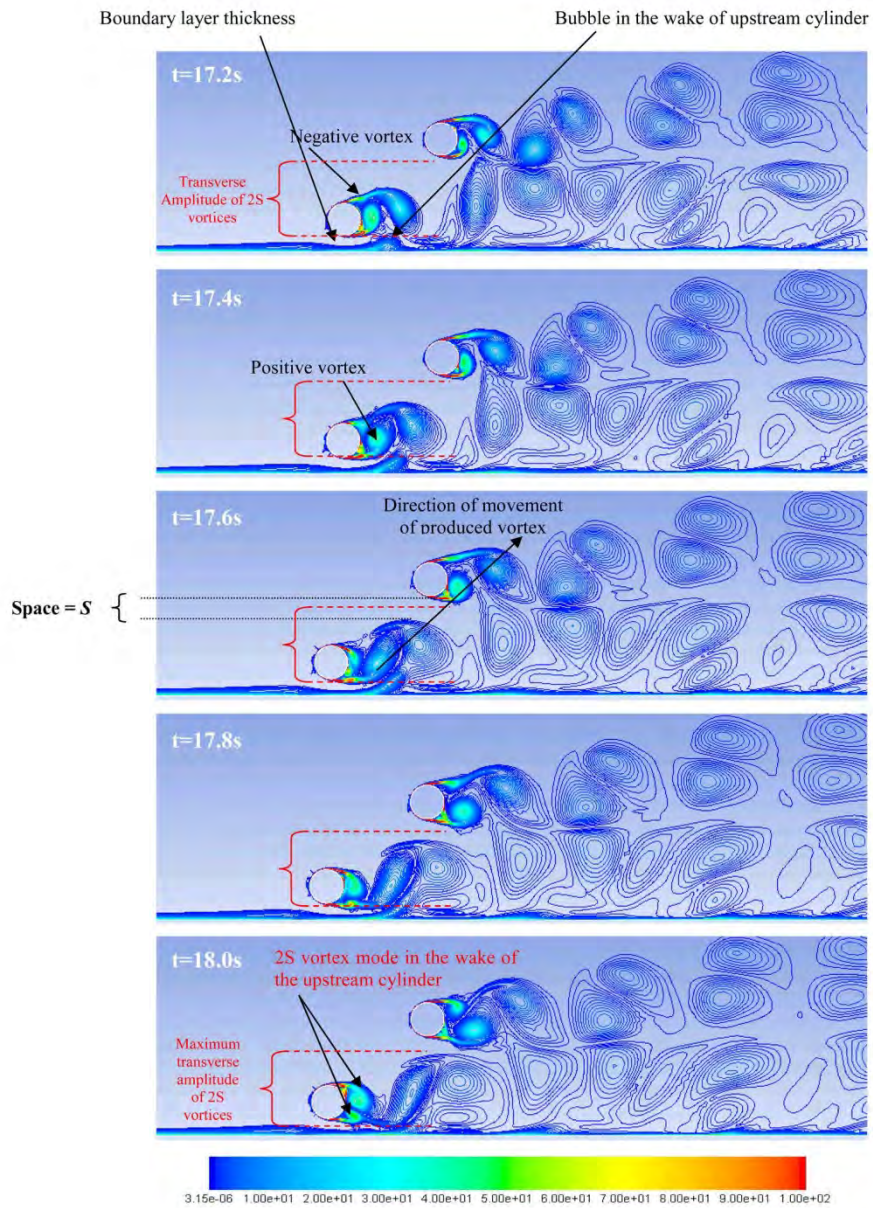


FIG. 9. Instantaneous vorticity contours ( $s^{-1}$ ) at  $G/D = 0.5$ ,  $H/D = 3.5$ , and  $Re = 8700$ .

Hence, in Sec. III D the importance of the lift coefficient, displacement amplitude, and force-displacement phase lag on efficiency is studied.

#### D. Case study II

The efficiency of the VIV power for each test case can be calculated based on the obtainable parameters from the CFD model and using Eq. (10).

The typical response of the downstream elastically supported cylinder under the produced jet flow of the upstream stationary cylinder is plotted in Figure 11. Included in this plot are the time series of the lift coefficient, the velocity, and the displacement of the cylinder

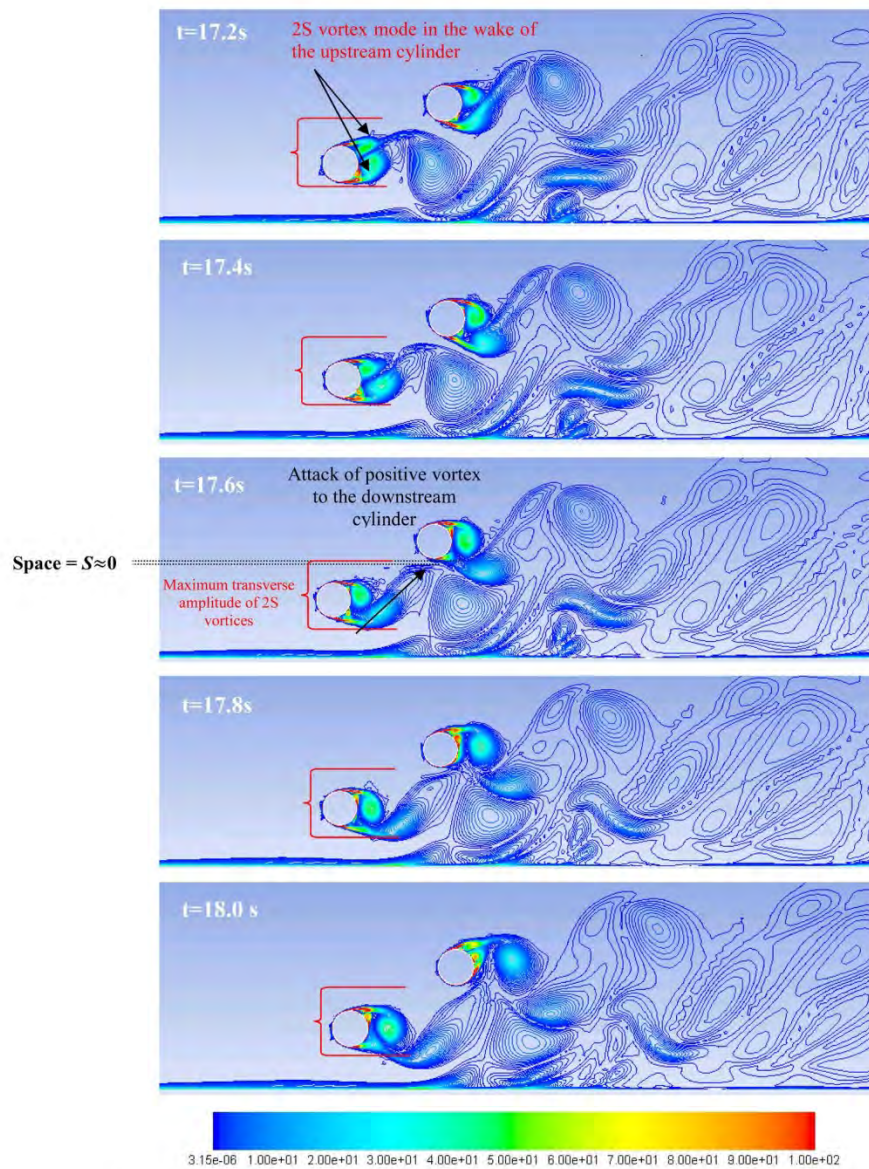


FIG. 10. Instantaneous vorticity contours ( $s^{-1}$ ) at  $G/D = 1.25$ ,  $H/D = 3.5$ , and  $Re = 8700$ .

(Test case 2). Based on the maximum amplitude and the phase angle between force and displacement, the VIV response of all test cases as a function of the gap ratio has been summarized in Figure 12. The variation of the lift coefficient demonstrates that when the upstream cylinder is submerged in the boundary layer, the maximum lift coefficient of the downstream cylinder is achieved. Despite the maximum lift coefficient of the downstream cylinder at lower gap ratios,  $G/D \leq 0.5$ , the amplitude of oscillations,  $y/D$ , remains at minimum. Outside of the critical gap ratio,  $0.5 \leq G/D \leq 1.0$ , the amplitude of oscillation almost doubles and reaches a maximum. The reason for this is related to the phase angle between the lift force and the displacement of the downstream cylinder. It can be seen that the optimum phase angle is achieved at  $G/D = 1$  in which  $\Phi = 90^\circ$ . It is observed that the phase angle can significantly affect the

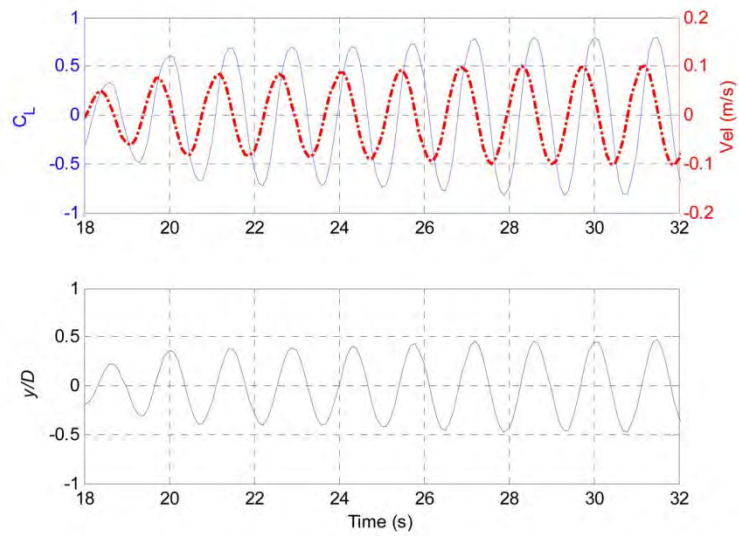


FIG. 11. Time history of the lift coefficient, velocity, and displacement of the downstream cylinder at  $G/D = 0.5$ , Test case 2.

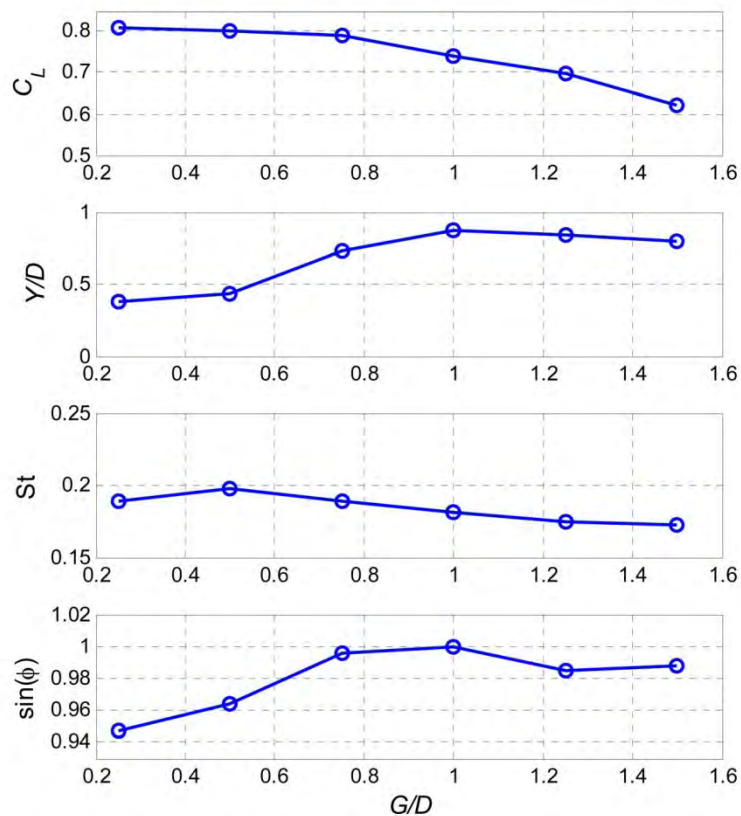


FIG. 12. Non-dimensional displacement, the lift coefficient and force-displacement phase shift of the downstream cylinder as a function of the gap ratio of the upstream cylinder at  $Re = 8700$ .

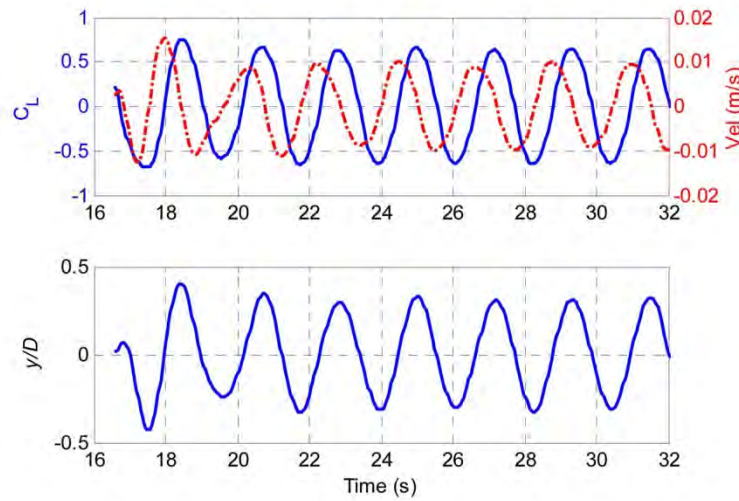


FIG. 13. VIV response of a single unbounded cylinder including time history of the lift coefficient, the velocity, and the displacement of the cylinder at  $Re = 8700$ .

total generated work of the downstream cylinder. Hence, the force-displacement phase angle plays a more significant role in reducing the efficiency of the VIV power.

To compare the efficiency of the VIV power from two cylinders under the effect of the boundary layer in vicinity of the wall, additional calculations were performed to analyse the efficiency of the VIV power for a single flexible mounted cylinder in a free stream flow. The numerical modelling was conducted with the same conditions as the bounded cylinders. Therefore, the fluid and structural parameters such as the Reynolds number and the density of fluid, the mass and damping ratios remain unchanged.

Time series of the lift coefficient, velocity and displacement of the cylinder are plotted in Figure 13 and the results have been added in the last row of Table II. The numerical outcomes of a single circular cylinder, such as the lift coefficient, and the displacement of the cylinder are in reasonable agreement with those of the experiments (Assi, 2009). The numerical data show that for the unbounded cylinder, the efficiency of VIV power is limited to 11.1% which is much lower than the efficiency of the bounded cylinders.

As shown in Eq. (10), the lift force and the displacement of the cylinder as well as the Strouhal number can alter the total efficiency of VIV power. The effect of all key parameters is summarised and plotted in Figure 14 as the efficiency of the VIV power. It is clear from this figure that the efficiency increases with an increase in the gap ratio, from  $G/D \leq 0.25$  to  $G/D \leq 1$ . Consequently, the maximum efficiency of the VIV power among the test cases is

TABLE II. Effect of gap ratio on the frequency of oscillation, the Strouhal number, the displacement, the velocity of the downstream cylinder, and the efficiency of VIV power.

$G/D$	$f$ (Hz)	St	$y/D$	$C_L$	$\sin(\Phi)$	$\eta_{VIV}$ (%)
0.25	0.65	0.189	0.385	0.81	0.947	18.3
0.50	0.69	0.198	0.430	0.80	0.963	20.6
0.75	0.66	0.189	0.733	0.79	0.996	34.4
1.00	0.63	0.181	0.875	0.74	0.999	37.2
1.25	0.61	0.175	0.845	0.70	0.984	31.0
1.50	0.60	0.172	0.802	0.62	0.998	25.8
Unbounded cylinder (Num. results)		0.201	0.28	0.63	1.0	11.1
Unbounded cylinder <sup>a</sup> (Exp. results)		0.205	0.25	0.60	1.0	9.6

<sup>a</sup>Calculation of VIV efficiency based on the fluidic parameters of Assi<sup>19</sup> at  $Re = 8700$ .

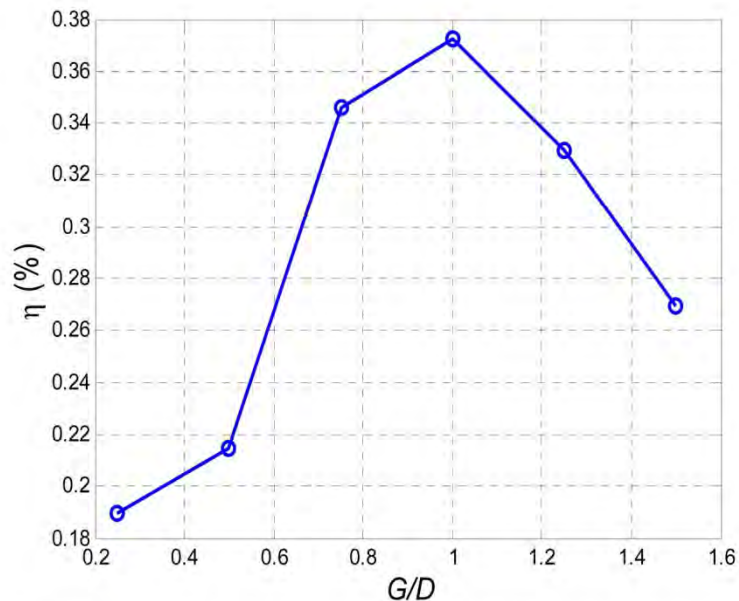


FIG. 14. Efficiency of VIV power as a function of the gap ratio of the upstream cylinder.

found at the gap ratio of  $G/D = 1$  ( $\eta_{VIV} = 37.2\%$ ). This efficiency is considerably higher compared to the efficiency of VIV power for an unbounded single cylinder. In addition, in comparison to a turbine based system the overall efficiency is comparable. A developed numerical model reported by Li and Calisal<sup>28,29</sup> has shown an advantage of mounting a twin turbine system with an increase of 25% over the two standalone turbines. Further development of these systems will better enhance their power output and competitiveness with our energy converters.

#### IV. CONCLUSIONS

Numerical analyses have been conducted to investigate the VIV response of two staggered circular cylinders using SAS turbulence model. The downstream elastically mounted circular cylinder was affected by the “jet flow” of the upstream stationary cylinder mounted next to a rigid wall. Fluidic parameters such as shear forces and the vortex shedding frequency of the cylinders were analysed. It was shown that the arrangements of the cylinders based on the gap ratio of the upstream cylinder can affect the lift and drag coefficients. Furthermore, the VIV response of the downstream cylinder was influenced by the jet flow of the upstream cylinder. At gap ratios  $0.25 \leq G/D \leq 0.5$  the drag and fluctuating lift coefficients change dramatically due to the effects of the boundary layer. Furthermore, key parameters such as; the lift coefficient, the maximum amplitude of oscillation, the Strouhal number, and the phase angle between the exerted lift force on the cylinder and the displacement of the cylinder on the efficiency of the VIV power were analysed. Despite the maximum lift coefficient of downstream cylinder at lower gap ratios, the maximum oscillation of the downstream cylinder occurs at higher gap ratios ( $G/D \geq 1$ ). This is due to the phase angle between the exerted lift force and displacement of the cylinder. It was observed that the maximum achievable theoretical efficiency of VIV power for the current test cases is approximately 37% at  $G/D = 1$  and it is much higher than the VIV efficiency of a single unbounded cylinder. Such findings have important implications on harnessing hydropower energy from VIV phenomenon.

<sup>1</sup>M. Güney and K. Kaygusuz, “Hydrokinetic energy conversion systems: A technology status review,” *Renewable Sustainable Energy Rev.* **14**(9), 2996–3004 (2010).

<sup>2</sup>M. Bernitsas and K. Raghavan, “Converter of current/tide/wave energy,” Provisional patent application 7493759 B2, United States Patent and Trademark Office Serial (2004).

- <sup>3</sup>M. M. Bernitsas, K. Raghavan, Y. Ben-Simon, and E. Garcia, "VIVACE (Vortex Induced Vibration Aquatic Clean Energy): A new concept in generation of clean and renewable energy from fluid flow," *J. Offshore Mech. Arctic Eng.* **130**, 1–15 (2008), see <http://www.vortexhydroenergy.com/>.
- <sup>4</sup>M. M. Bernitsas, Y. Ben-Simon, K. Raghavan, and E. Garcia, "The vivace converter: Model tests at high damping and Reynolds number around  $10^5$ ," *J. Offshore Mech. Arctic Eng.* **131**, 011102 (2009).
- <sup>5</sup>P. W. Bearman, "Vortex shedding from oscillating bluff bodies," *Annu. Rev. Fluid Mech.* **16**, 195–222 (1984).
- <sup>6</sup>A. Khalak and C. H. K. Williamson, "Fluid forces and dynamics of a hydroelastic structure with very low mass and damping," *J. Fluids Struct.* **11**(8), 973–982 (1997).
- <sup>7</sup>R. Govardhan and C. Williamson, "Critical mass in vortex-induced vibration of a cylinder," *Eur. J. Mech.-B/Fluids* **23**(1), 17–27 (2004).
- <sup>8</sup>K. Raghavan and M. M. Bernitsas, "Experimental investigation of Reynolds number effect on vortex induced vibration of rigid circular cylinder on elastic supports," *Ocean Eng.* **38**(5–6), 719–731 (2011).
- <sup>9</sup>J. F. Derakhshandeh, M. Arjomandi, B. Dally, and B. Cazzolato, "The effect of arrangements of two circular cylinders on the maximum efficiency of vortex-induced vibration power using a scale-adaptive simulation model," *J. Fluids Struct.* (unpublished).
- <sup>10</sup>P. Bearman and M. Zdravkovich, "Flow around a circular cylinder near a plane boundary," *J. Fluid Mech.* **89**(1), 33–47 (1978).
- <sup>11</sup>S. Taniguchi and K. Miyakoshi, "Fluctuating fluid forces acting on a circular cylinder and interference with a plane wall," *Exp. Fluids* **9**(4), 197–204 (1990).
- <sup>12</sup>N. Mahir and D. Rockwell, "Vortex formation from a forced system of two cylinders. Part I: Tandem arrangement," *J. Fluids Struct.* **10**(5), 473–489 (1996).
- <sup>13</sup>S. Sarkar and S. Sarkar, "Vortex dynamics of a cylinder wake in proximity to a wall," *J. Fluids Struct.* **26**(1), 19–40 (2010).
- <sup>14</sup>F. Menter and Y. Egorov, "A scale-adaptive simulation model using two-equation models," in *Proceedings of the American Institute of Aeronautics and Astronautics* (2005), pp. 1–13.
- <sup>15</sup>Y. Egorov, F. Menter, R. Lechner, and D. Cokljat, "The scale-adaptive simulation method for unsteady turbulent flow predictions. Part 2: Application to complex flows," *Flow, Turbul. Combust.* **85**(1), 139–165 (2010).
- <sup>16</sup>F. Menter and Y. Egorov, "The scale-adaptive simulation method for unsteady turbulent flow predictions. Part 1: Theory and model description," *Flow, Turbul. Combust.* **85**(1), 113–138 (2010).
- <sup>17</sup>F. Menter, A. Garbaruk, P. Smirnov, D. Cokljat, and F. Mathey, "Scale-adaptive simulation with artificial forcing," in *Progress in Hybrid RANS-LES Modelling* (2010), pp. 235–246.
- <sup>18</sup>E. Guilmineau and P. Queutey, "Numerical simulation of vortex-induced vibration of a circular cylinder with low mass-damping in a turbulent flow," *J. Fluids Struct.* **19**(4), 449–466 (2004).
- <sup>19</sup>G. Assi, "Mechanisms for flow-induced vibration of interfering bluff bodies," Ph.D. dissertation (Imperial College London, London, UK, 2009).
- <sup>20</sup>A. Khalak and C. Williamson, "Dynamics of a hydroelastic cylinder with very low mass and damping," *J. Fluids Struct.* **10**(5), 455–472 (1996).
- <sup>21</sup>B. Yang, F. Gao, D.-S. Jeng, and Y. Wu, "Experimental study of vortex-induced vibrations of a cylinder near a rigid plane boundary in steady flow," *Acta Mech. Sin.* **25**(1), 51–63 (2009).
- <sup>22</sup>H. Schlichting and K. Gersten, *Boundary-Layer Theory* (Springer Verlag, 2000).
- <sup>23</sup>S. Price, D. Sumner, J. Smith, K. Leong, and M. Paidoussis, "Flow visualization around a circular cylinder near to a plane wall," *J. Fluids Struct.* **16**(2), 175–191 (2002).
- <sup>24</sup>I. Khabbouchi, M. Guellouz, and S. B. Nasrallah, "A study of the effect of the jet-like flow on the near wake behind a circular cylinder close to a plane wall," *Exp. Therm. Fluid Sci.* **44**, 285–300 (2012).
- <sup>25</sup>A. G. Kravchenko and P. Moin, "Numerical studies of flow over a circular cylinder at  $Re = 3900$ ," *Phys. Fluids* **12**, 403–417 (2000).
- <sup>26</sup>R. Govardhan and C. Williamson, "Modes of vortex formation and frequency response of a freely vibrating cylinder," *J. Fluid Mech.* **420**, 85–130 (2000).
- <sup>27</sup>M. Zhao and L. Cheng, "Numerical simulation of two-degree-of-freedom vortex induced vibration of a circular cylinder close to a plane boundary," *J. Fluids Struct.* **27**(7), 1097–1110 (2011).
- <sup>28</sup>Y. Li and S. M. Calisal, "Modeling of twin-turbine systems with vertical axis tidal current turbines: Part I—Power output," *Ocean Eng.* **37**(7), 627–637 (2010).
- <sup>29</sup>Y. Li and S. M. Calisal, "Modeling of twin-turbine systems with vertical axis tidal current turbine: Part II—Torque fluctuation," *Ocean Eng.* **38**(4), 550–558 (2011).

## Chapter 6

### Effect of Airfoil

#### 6.1. Chapter overview

The current chapter presents a detailed discussion of the dynamic response of a symmetric airfoil with two degrees of freedom, which was mounted in the wake of upstream stationary cylinder. In this chapter, the behaviour of several parameters of the fluid flow such as vortex structure, vortex length scale, circulation, and variation of the Strouhal number as a function of the longitudinal and lateral distances are presented. The discussions are based on a series of numerical models, which are combined with the water channel tests. In addition, it is shown that the flutter of airfoil is a function of the angle of attack. This chapter has been submitted for publication as

“Flow-induced vibration of an elastically mounted airfoil under the influence of the wake of a circular cylinder”, by Javad Farrokhi Derakhshandeh, Maziar Arjomandi, Bassam Dally and Benjamin Cazzolato, *Journal of Experimental Thermal and Fluid Science*, under review.



## Statement of Authorship

Title of Paper	Flow-induced vibration of an elastically mounted airfoil under the influence of the wake of a circular cylinder.
Publication Status	<input type="radio"/> Published, <input type="radio"/> Accepted for Publication, <input checked="" type="radio"/> Submitted for Publication, <input type="radio"/> Publication style
Publication Details	Derakhshandeh, J. F., Arjomandi, M., Dally, B., Cazzolato, B., Flow induced vibration of an elastically mounted airfoil under the influence of oncoming vortices, under review, 2014.

### Author Contributions

By signing the Statement of Authorship, each author certifies that their stated contribution to the publication is accurate and that permission is granted for the publication to be included in the candidate's thesis.

Name of Principal Author (Candidate)	Javad Farrokhi Derakhshandeh
Contribution to the Paper	To investigate the effect of non-circular cylinder to capture the wake energy of an upstream stationary circular cylinder.
Signature	Date 18/03/2015

Name of Co-Author	Maziar Arjomandi
Contribution to the Paper	Supervised the work, assisted in developing ideas and manuscript evaluation.
Signature	Date 18.03.2015

Name of Co-Author	Bassam Dally
Contribution to the Paper	Supervised the work, assisted in developing ideas and manuscript evaluation.
Signature	Date 18.03.2015

Name of Co-Author	Benjamin Cazzolato
Contribution to the Paper	Supervised the work, assisted in developing ideas and manuscript evaluation.
Signature	Date 19/3/15

## 6.2. Manuscript

### **Flow-induced vibration of an elastically mounted airfoil under the influence of the wake of a circular cylinder**

Derakhshandeh J. F., Arjomandi M., Dally B. and Cazzolato B.  
School of Mechanical Engineering  
University of Adelaide, Adelaide, South Australia 5005, Australia

#### **Abstract**

The effect of vortices generated by a rigidly mounted cylinder on the dynamic response of an airfoil is investigated in this study. This work extends previous investigation of vortex interaction with a second cylinder to capture the wake energy (Derakhshandeh *et al.* 2014-c). Accordingly, the Flow-Induced Vibration (FIV) of a symmetric NACA 0012 airfoil positioned in the wake of the rigidly-mounted upstream cylinder is studied. The airfoil mount allows it to move in two degrees-of-freedom; pitch and heave. The pitching axis is kinematically driven using a brushless permanent-magnet DC servo motor. The heave axis of the airfoil is coupled with a Virtual Elastic Mechanism (VEM), which is an electro-mechanical device designed to create any desired impedance. The VEM system replaces the physical damper and spring systems and allows the airfoil to oscillate due to the lift force in the normal direction of the flow. The airfoil is set at different positions in the wake of the upstream cylinder in order to characterise the impact of the arrangement of a coupled cylinder-airfoil on energy extraction. Special attention was paid to the angle of attack of the airfoil to explore the optimal performance of the system. Force and displacement measurements of the airfoil were conducted in a closed loop water channel. The experimental work was complimented by a Computational Fluid Dynamics (CFD) modelling study which was aimed at calculating the vortex frequency shedding and visualise the vortex structure. It is observed that the vortex shedding frequency, the length scale and transverse spacing of the vortices are function of the longitudinal and lateral distances between the cylinder the airfoil. The results also demonstrate that there is a correlation between the configuration of cylinder and airfoil and vortex structure. Due to this correlation, the shear forces acting on the airfoil alters the fluttering response of the airfoil depending on the angle of attack, which in turn influences the obtained power coefficient of the device. The

maximum power coefficient of FIV is obtained for cases with  $3.5 \leq x_0/D \leq 4.5$  and  $1 \leq y_0/D \leq 1.5$  arrangements, which is limited to the narrower lateral distances as compared to the previous study ( $1 \leq y_0/D \leq 2$ ) by the authors (Derakhshandeh *et al.* 2014-c) employing a pair of cylinders.

*Keywords: Flow-induced vibration, vortex shedding frequency, circulation, airfoil, circular cylinder.*

## **Introduction**

It has been predicted that the growth rate in energy consumption over the next 20 years is much higher than the growth rate of population due to the incremental increase in demand for electricity in developing countries (Trevor 2013). Consequently, the production of electricity would increase from 20 Petawatt hours in 2010 to 31.2 Petawatt hours in 2030 (Trevor 2013). Considering that electricity production using fossil fuel is responsible for producing the largest amount of carbon dioxide emission (26%) (Trevor 2013), it is essential that alternative sources of energy to be sought to cater for the increased demand of electricity around the world. One such renewable source is ocean energy which can be harnessed using turbine and non-turbine convertors (Khan *et al.* 2009).

Vortex-Induced Vibration (VIV) phenomenon, known as a non-turbine convertor (Khan *et al.* 2009), has been extensively studied in the past (Sarpkaya 1978, Williamson and Roshko 1988, Zdravkovich 1979, Bearman 1984, Khalak and Williamson 1996, Govardhan and Williamson 2004, Sarpkaya 2004). In this phenomenon, the fluid-structure interaction occurs due to the synchronization between structure and vortex shedding. A previous investigation by Bernitsas *et al.* (2008) has shown that the VIV convertor is feasible both technically and economically. It has been found that the theoretical and experimental efficiencies of the VIV convertor were estimated to be 37% and 22%, respectively (Bernitsas and Raghavan 2004). In addition, it was shown that the Reynolds number plays a more important role than the mass damping ratio. In addition, Bernitsas *et al.* (2008) have noted that VIV convertors are easily scalable and can operate under different Reynolds number, which makes them applicable for a wide variety of applications.

An oscillating airfoil might be considered as a non-turbine convertor. This convertor has drawn the attention of scholars to avoid the problems of rotary turbines. Although the rotary river turbines can be employed in shallow waters, the wake interference reduces the performance of an array of the turbines (Chamorro *et al.* 2013). In addition, the river turbines generally suffer from drawbacks such as starting torque and low efficiencies, particularly at low flow speeds (Khan *et al.* 2009). Consequently, employing airfoils with oscillating behaviour, known as flutter, was proposed (McKinney and DeLaurier 1981) to capture kinetic energy of the fluid.

Harnessing the available kinetic energy from wind using an oscillating airfoil was initially suggested by McKinney and DeLaurier (1981). It has been shown that the measured efficiency of a fluttering airfoil is approximately 28%, which is comparable to the experimental efficiencies of the rotary devices which range from 20% to 55% depending on the efficiency of the convertors (Vries 1983). The efficiency of oscillation-based converters using an airfoil is shown to be higher than the measured efficiency of the VIV with 22% when employing a circular cylinder (Bernitsas *et al.* 2008). Along with the experimental tests of a fluttering airfoil mechanism, the numerical analysis of Zhu and Peng (2009) showed unexpectedly that the efficiency of 34% was achievable when the normalized oscillation frequency was around 0.15 (the frequency was normalized by the chord length of the airfoil and the free stream velocity). Further investigations have been conducted by Zhu and Peng (2009) and Zhu (2011) using numerical modelling to capture kinetic energy from flapping foils in a uniform flow. Zhu and Peng (2009) have found that the behaviour of the airfoil is dependent on the stiffness of the system. It has also been shown that the location of the pitching axis plays an important role in the dynamic response of the airfoil. Depending on the location of the pitching axis and the rotational spring stiffness, four distinguishable responses have been offered by the authors, namely: static, periodic, irregular and oscillation motions. Among these responses, they postulated that the periodic motion of the airfoil has the highest feasibility of energy harvesting.

While a few numerical studies have shown the potential of a fluttering airfoil to generate useful power, the lack of examination of the fluttering response of an airfoil in capturing hydrokinetic energy has motivated the current experiments. In practice, two types of flutter response for an airfoil

can be considered: purely passive and semi-active mechanisms. In the purely passive fluttering, the airfoil will be entirely excited by Flow-Induced Vibration (FIV) such as those reported by Sváček *et al.* (2007). On the other hand, in the semi-activated system only one of the dynamic modes, such as heave or pitch response can be excited by the cyclic acting forces due to the vortices, while the other mode can be applied to the airfoil. In the latter case, the semi-actuated design requires an activator system to make the specified pitching motion, for instance, virtually. The semi-actuated mechanism enables the optimization of desirable displacement amplitude of the airfoil using a control system, which is suitable for the energy harvester.

In this study, a Semi-Active Virtual Elastic Mechanism (SAVEM) system is employed instead of a real physical spring damper. The use of SAVEM system can rapidly open the way for optimisation and further development of energy utilization from FIV. The SAVEM system consists of two motors and two controllers, a belt-pulley transmission, a carriage and an airfoil, which allows the movement of the airfoil in two degrees of freedom. In order to identify stable conditions in the wake of the cylinder in current study, the effect of longitudinal and lateral distances between the cylinder and the airfoil are analysed. In addition, with combination of heaving and pitching motions of the airfoil to capture hydrokinetic energy of oncoming vortices, the effect of wake instability and the arrangement of the coupled cylinder-airfoil are also investigated.

## 1. Dynamic model

This section outlines the mathematical model used for an elastically mounted airfoil with two degrees of freedom.

### 1.1. Mathematical model

To study the oscillation of an airfoil under the effect of oncoming vortices, the flutter behaviour of an aero-elastic airfoil is analysed based on the schematic model shown in Figure 1. Point ' $p$ ' is of interest in this model and refers to the aerodynamic centre of the system. This point also represents the reference point, where the heave of the airfoil ' $h$ ' is measured and it is located at the quarter-chord of the airfoil  $x_p$ . By choosing this point, the effect of torque is eliminated and the airfoil is only under the influence of

the lift force. The heaving and pitching of the airfoil are restrained by two springs with the constants of  $k_h$  and  $k_\alpha$ , respectively, and damped with dampers with damping constants  $b_h$  and  $b_\alpha$ .

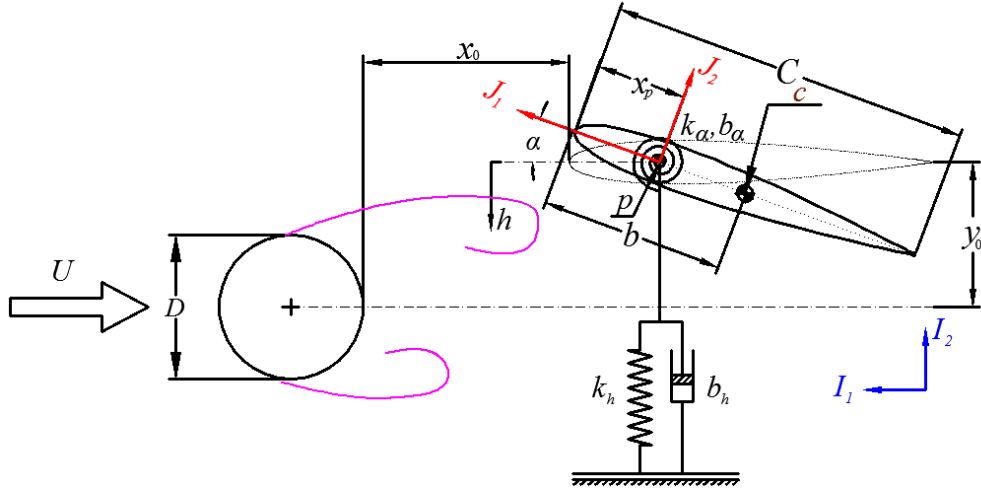


Figure 1: Schematic section of a coupled circular cylinder and elastic airfoil with two degrees of freedom including pitch and heave.

In order to find the total virtual work of the airfoil, initially, the equations of motion for an airfoil with two degrees of freedom and with large displacement are formulated as (Sváček *et al.* 2006)

$$m\ddot{h} + k_h \cdot h + S_\alpha \ddot{\alpha} \cdot \cos\alpha - S_\alpha \cdot \dot{\alpha}^2 \sin\alpha + d_h \dot{h} = -F_L(t), \quad (1)$$

$$S_\alpha \dot{h} \cos\alpha + I_\alpha \ddot{\alpha} + k_\alpha \cdot \alpha + d_\alpha \cdot \dot{\alpha} = M(t), \quad (2)$$

where,  $h$ ,  $\dot{h}$  and  $\ddot{h}$  are the transverse displacement, velocity and acceleration of the airfoil (m, m/s and m/s<sup>2</sup>), respectively,  $\alpha$  is the angle of attack of the airfoil (rad),  $\dot{\alpha}$  and  $\ddot{\alpha}$  represent the angular velocity and acceleration of the airfoil (rad/s and rad/s<sup>2</sup>),  $m$  represents the mass of the airfoil (kg),  $k_h$  is the spring stiffness (N/m),  $S_\alpha$  is the static moment (kg m),  $d_h$  denotes the structural damping in bending (kg/s),  $d_\alpha$  is the structural damping in torsion (kgm<sup>2</sup>/s rad),  $I_\alpha$  represents the mass moment (kg m<sup>2</sup>),  $k_\alpha$  is the spring stiffness (Nm/rad),  $F_L$  is the fluid force acting on the airfoil perpendicular to the flow speed (N), and  $M$  represents the moment of the system (Nm).

To achieve the total virtual work, both the kinetic and potential energies as well as the resulting aerodynamic forces acting on the surface of the airfoil are considered. The potential and kinetic energies of the airfoil can be written as follow (Hodges and Pierce 2011):

$$P = \frac{1}{2} k_h h^2 + \frac{1}{2} k_\alpha \alpha^2, \quad (3)$$

$$K = \frac{1}{2} m V_c^2 + \frac{1}{2} I_c \dot{\alpha}^2, \quad (4)$$

where,  $I_c$  is the moment of inertia about  $C$  and  $V_c$  is the velocity of the centre of gravity ' $c$ ' (refer to Figure 1), which can be found by

$$V_c = V_p + \dot{\alpha} \hat{j}_3 \times b \hat{j}_1. \quad (5)$$

In Equation (5),  $\hat{j}$  axes represent coordinate system mounted on the reference point ' $p$ ' and  $V_p$  is the initial velocity of the reference point ' $p$ ' and it can be calculated as  $V_p = -\dot{h} \hat{l}_2$ ; hence, the velocity of the centre of mass is

$$V_c = -\dot{h} \hat{l}_2 + b \dot{\alpha} \hat{j}_2. \quad (6)$$

where,  $\hat{l}$  axes are the fixed unit vectors (refer to Figure 1). By substituting the velocity of the mass into Equation (4), the kinetic energy is summarised as

$$K = \frac{1}{2} m (\dot{h}^2 + b^2 x_\alpha^2 \dot{\alpha}^2 + 2b x_\alpha \dot{h} \dot{\alpha}) + \frac{1}{2} I_c \dot{\alpha}^2. \quad (7)$$

The displacement of the airfoil can be obtained by integrating the velocity at point ' $p$ ' e.g. ( $V_p = -\dot{h} \hat{l}_2$ ); Thus,

$$\Delta d_p = -\Delta h \hat{l}_2, \quad (8)$$

where,  $h$  presents heave of the airfoil based on point ' $p$ ' (refer to Figure 1).

In the next step, to calculate the work done by the aerodynamic lift, the displacement of the airfoil for point ' $p$ ' is considered. As mentioned earlier, the aerodynamic centre of the airfoil is adapted by the elastic axis (point ' $p$ ')

---

at the quarter of the chord length of the airfoil. As a consequence, the generated moment at this point is zero ( $M_{1/4} = 0$ ). Therefore, the virtual work of the lift force during one cycle of oscillation can be written as

$$W = F_L(-d_p), \quad (9)$$

Here, the aerodynamic lift force  $F_L$  acting in the normal direction to the flow with two degrees of freedom can be formulated as

$$F_L = \rho U^2 b l c_{l\alpha} \left[ \alpha + \dot{h}/U + (b/2) \left( \frac{\dot{\alpha}}{U} \right) \right]. \quad (10)$$

By integrating the right hand side of Equation (10) and averaging it over a complete cycle of oscillation, the mean generated power during one cycle of vibration ( $T_{cyl}$ ) can be found as

$$\bar{P}_{FIV} = \frac{W}{T_{cyl}}. \quad (11)$$

The power coefficient of FIV can be calculated based on the power of the fluid  $P_{fluid}$ , which is the product of the acting force on the airfoil ( $\frac{1}{2} \rho U^2 A C_L = \rho U^2 b l C_L$ ) and the velocity in the same direction of the force ( $U$ ). Here,  $l$  is the length or span of the airfoil;  $A$  is the area and  $C_L$  is the lift coefficient. Therefore, the power of the fluid can be written as  $P_{fluid} = \rho U^3 b l$  and the power coefficient can be written as

$$\eta_{FIV} = \frac{\bar{P}_{FIV}}{P_{fluid}}. \quad (12)$$

## 2. Wake regimes

In order to analyse the vortex structure in the wake area of the cylinder, a numerical analysis can be employed. Therefore, with the purpose of visualizing the flow pattern and studying the effect of critical parameters that influence FIV, such as the vortex length scale, the transverse spacing of the vortices and the vortex frequency shedding, preliminary numerical analyses were conducted with a single cylinder and a coupled cylinder-airfoil.



Flow around a *stationary single* cylinder at  $Re = 10,000$ , was initially modelled using ANSYS Fluent Workbench. At this Reynolds number, the flow is classified in intermediate Transition in Shear Layers (TrSL) (Zdravkovich 1997). At TrSL flow regime, in which all numerical models and experiments were performed in this paper, the discrete periodic vortices are formed and accordingly the Strouhal number remains approximately constant (Blevins 1990). This facilitates the harnessing of the energy from the vortices, which are generated at a constant frequency which is close to lock-in. In order to predict the wake regimes, a Scale Adaptive Simulation (SAS) turbulence model was used based on the Finite Volume Method (FVM) with a pressure based algorithm. In comparison to other turbulence models, the SAS model is a relatively new model and was developed by Menter and Egorov (2010). This model uses the Von Karman length scale, which allows it to adapt its behaviour to Scale Resolving Simulation (SRS) according to the stability parameters of the flow. This also allows the model to provide a balance between the contributions of the simulated and resolved parts of the turbulence stresses. Hence, the model can effectively and automatically switch from the Large Eddy Simulation (LES) mode to the Reynolds Average Navier Stokes (RANS) mode (Menter and Egorov 2010). In previous studies, the author have shown that this model is suitable for predicting the VIV response of a cylinder mounted in a transient flow regime (Derakhshandeh *et al.* 2014-a, and 2014-b). A quadrilateral mesh with 51,668 elements was utilized for all numerical models and details of numerical simulations can be found in (Derakhshandeh *et al.* 2014-a).

Figure 2 presents the vorticity contours of a single cylinder at  $Re = 10,000$  obtained from the CFD model along with the experimental results of Lau (2003). It can be seen from the figure that the calculated vorticity distribution in the wake of the cylinder is quite similar to that reported experimentally. Consistent with the previous investigations (Roshko (1955), Unal and Rockwell (1988) and Lau (2003)), three regimes in the wake of cylinder are identified: pre-vortex-formation regime ( $X_1$ ), primary-vortex-formation regime ( $X_2$ ), and fully developed-vortex formation regime ( $X_3$ ). It is observed that at  $X_1$ , the shear layers merge and the initial vortex starts to shed. As the longitudinal distance is increased to  $X_2$  and  $X_3$  regimes, the vortices are formed and become fully developed. This means that at  $X_2$  and  $X_3$ , fully developed vortices with larger length scale and higher circulations of the vortices are observed.

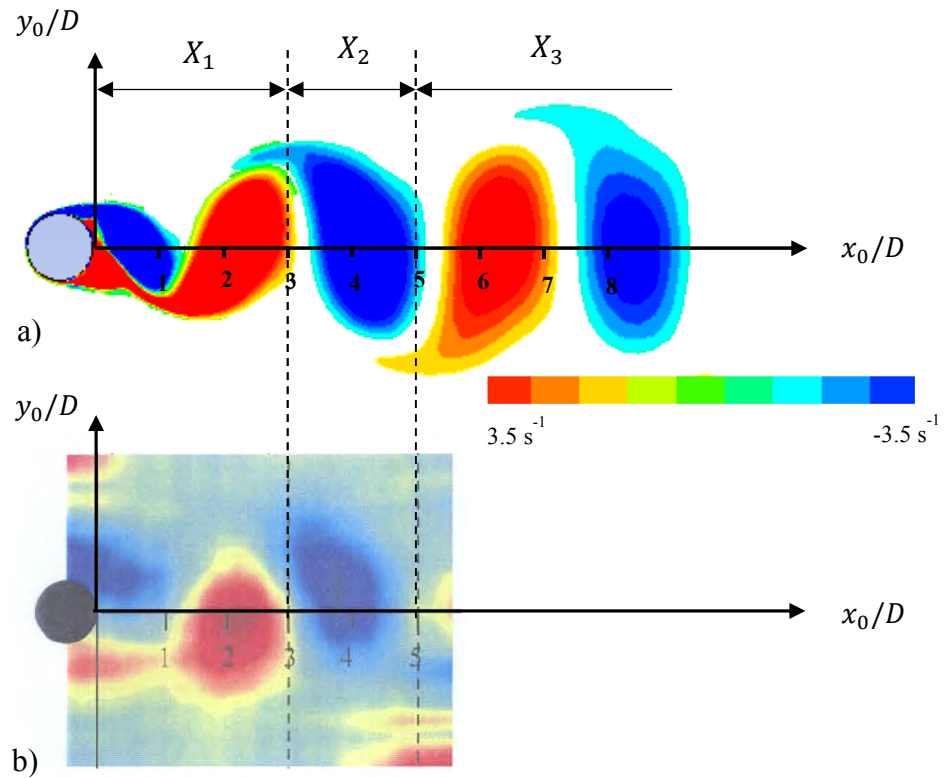


Figure 2: Vorticity contour ( $\text{s}^{-1}$ ) in the wake of the circular cylinder at  $\text{Re} = 10,000$ , a) numerical modelling of the present study, b) experimental result of Lau (2003).

Since the length scale and circulation of the developed vortices are directly proportional to the shear forces, e.g. lift force acting on the cylinder, it is predicted that the primary-vortex-formation ( $X_2$ ) and fully developed-vortex-formation ( $X_3$ ) regimes are more suitable for kinetic energy harnessing by a downstream body. Analysing the power density generated in the wake of the cylinder including  $X_2$  and  $X_3$  can provide further insight for this prediction.

## 2.1. Power density

Figure 3 shows the non-dimensionalised power density of the fluid in the symmetric plane. For 2D model, the power density is defined as the force acting on the wetted area of the cylinder in the same direction of the flow. Therefore, the fluid power equation can be written as  $\frac{1}{2} \rho U^3 A$ . The locations with higher power density can be observed as a zigzag pattern in the wake

of the cylinder. It is seen that although at  $X_3$  the vortices are fully developed (refer to Figure 2), due to the dissipation of the kinetic energy, the power density of the fluid gradually reduces. Consequently, with the aim of capturing the wake energy of the upstream cylinder both visual patterns of vorticity contours and the power density contours provide an initial estimation for the optimum location of the downstream body. Therefore, for the rest of the current investigation the primary-vortex-formation regime ( $X_2$ ) is considered as an ideal longitudinal distance between the cylinder and airfoil.

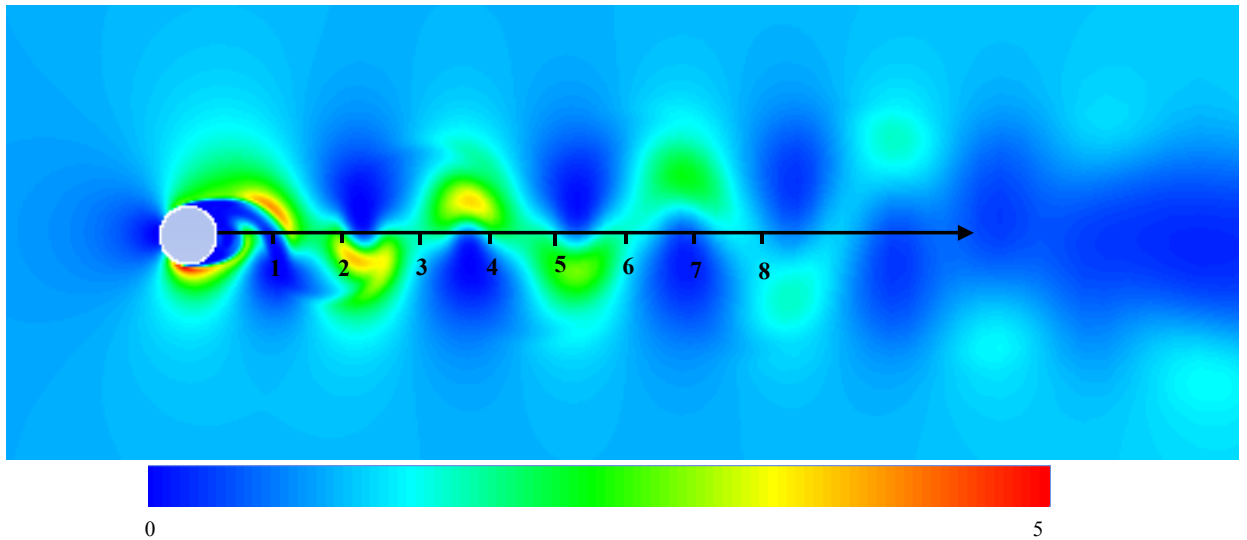


Figure 3: Non-dimensionalised power density in the wake of a stationary circular cylinder ( $P_f/P_{f\infty}$ ) at  $Re = 10,000$ .

## 2.2. Strouhal number

Vortex length scale and vortex shedding frequency (or Strouhal number) was studied for the cylinder-airfoil case. Models were developed for different longitudinal and lateral distances between the cylinder and the airfoil. Two arrangements were modelled, at  $y_0/D = 0$  and  $y_0/D = 1$ , and the airfoil was positioned at all three wake regimes ( $X_1, X_2$  and  $X_3$ ) at zero angle of attack.

Typical vorticity contours around the coupled cylinder-airfoil at three wake regimes are shown in Figure 4. In this figure the longitudinal distance,  $x_0/D$ , was increased to cover  $X_1$  to  $X_3$  regimes with the airfoil mounted along the centre line of the cylinder ( $y_0/D = 0$ ). The vorticity contours have been

plotted at the same time for all numerical models ( $t = 15$  s). This facilitates the comparison between the vortex structures. It is observed that due to the small evolution of the vortices at  $X_1$ , the wake appears to be affected by the airfoil. As a consequence, at smaller  $x_0/D$  such as pre-vortex formation regime ( $X_1$ ), the vortices split before they fully develop (Figure 3-a). The splitting of the vortices alters the shear forces acting on the airfoil and the frequency of the vortex shedding. At higher longitudinal distances, e.g. at  $X_2$  and  $X_3$  regimes (Figure 3-b, and 3-c), the airfoil is alternately under the effect of either the primary or the fully developed vortices regimes.

The spectral analysis of the lift force acting on the airfoil was also carried out. The right column of Figure 4 shows the magnitude of the lift force versus Strouhal number at three wake regimes from  $X_1$  and  $X_3$  (Figure 3-ed, 3-e and 3-f, respectively) obtained using the Fast Fourier Transform (FFT). In the FFT profile, the sampling time was 0.01 s, which is equal to the selected time step used in the numerical simulations.

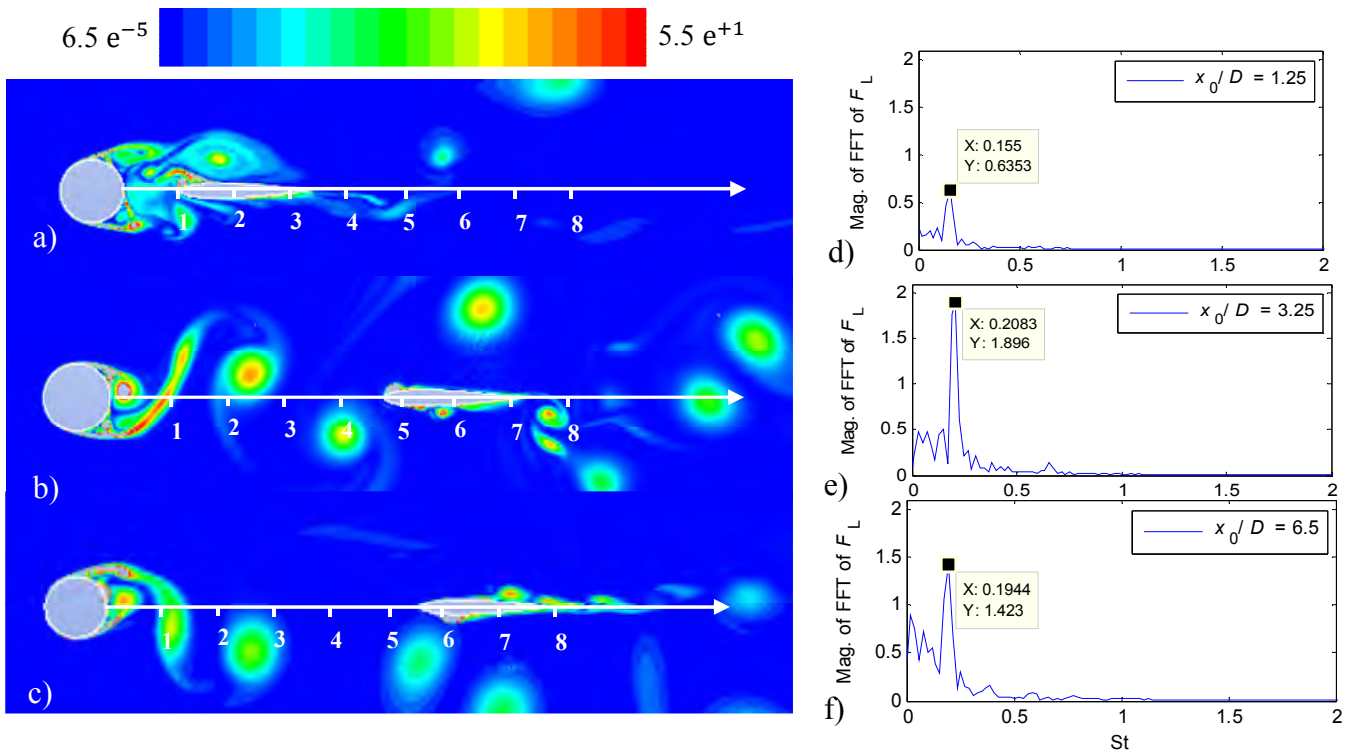


Figure 4: Vorticity contours including positive and negative eddies around a coupled cylinder-airfoil as a function of longitudinal distance at  $y_0/D = 0$ ,  $\alpha = 0$  and  $Re = 10,000$ , a)  $X_1$  regime, b)  $X_2$  regime, c)  $X_3$  regimes. d), e) and f) in the right column present the FFT plot of the lift force at each wake regime, respectively.

When comparing the FFT plots it becomes readily apparent that when the airfoil is located at  $X_1$ , the minimum Strouhal number is obtained. The Strouhal number becomes close to the vortex shedding frequency of a single cylinder ( $St \approx 0.2$ ) at higher longitudinal distances (at  $X_2$  and  $X_3$ ). It is interesting to note that although the Strouhal number reaches  $\sim 0.2$  at  $X_3$  regime, the maximum magnitude of the lift force is obtained at the  $X_2$  regime, which is almost 3 times the magnitude of the lift force at  $X_1$  regime (compare the magnitudes of the lift force in Figures 3-d and 3-e).

Figure 5 also shows instantaneous vorticity contours of the flow in the wake of the cylinder at  $t = 15$  s, when the airfoil is offset by the lateral distance of  $y_0/D = 1$ . It is seen that similar to the centrally aligned arrangements, the transverse spacing of the vortices gradually increases when the longitudinal distance between cylinder and airfoil increases; however, at the lateral distance of  $y_0/D = 1$ , there is no splitting occurs for the vortices.

It is observed that at the  $X_1$  regime, the vortices smoothly pass from the upper surface of the airfoil and they approach the leading edge of the airfoil at higher  $x_0/D$  ( $X_2$  and  $X_3$  regimes). This can be more highlighted at  $X_3$  regime, where the oncoming vortex is attached to the leading edge of the airfoil (Figure 5-c). The effect of longitudinal distance on vortex shedding frequency was evaluated from the time history of the lift coefficient of the airfoil when the airfoil was mounted at  $y_0/D = 0$ . FFT plot of the lift force demonstrates that the magnitude of the lift force is approximately similar at three regimes and the discrepancy of the Strouhal number is insignificant (compare Figures 4-d, 4-e and 4-f).

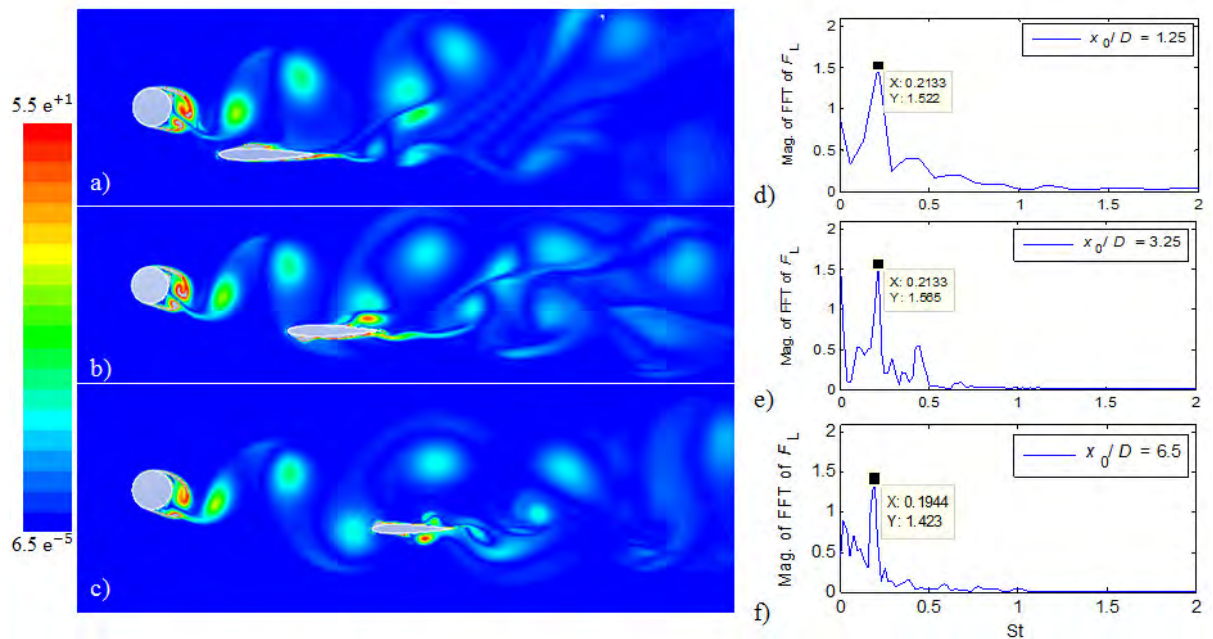


Figure 5: Vorticity magnitude contours ( $s^{-1}$ ) around a coupled cylinder-airfoil as a function of longitudinal distance at  $y_0/D = 1$ ,  $\alpha = 0$  and  $Re = 10,000$ . d), e) and f) in the right column present the FFT plot of the lift force at each wake regime, respectively.

Figure 6 summarises the trend of the Strouhal number as a function of  $x_0/D$  and  $y_0/D$ , at  $Re = 10,000$ . For the centrally aligned arrangements, it is observed that when the airfoil was mounted at  $X_1$ , the Strouhal number is far away from the vortex frequency of a single cylinder and by minimizing the gap between the cylinder and airfoil, the vortices are split causing a reduction in the length scale. Since the Strouhal number is inversely proportional to the length scale of the vortices (Unal and Rockwell 1988), a reduction in the gap size between cylinder and airfoil would increase the Strouhal number. However, the Strouhal number still shows smaller values at  $X_1$ , compared with the obtained values at  $X_2$  and  $X_3$ . The variations of obtained Strouhal number show similar trend with results of wind tunnel tests conducted by Ozono (1999) for the flow around a coupled cylinder-plate at  $Re = 6,700$  and  $y_0/D = 0$ . When the airfoil was mounted at  $X_2$  and  $X_3$ , the results demonstrated the Strouhal number approximately converges to the vortex shedding frequency of a single cylinder.

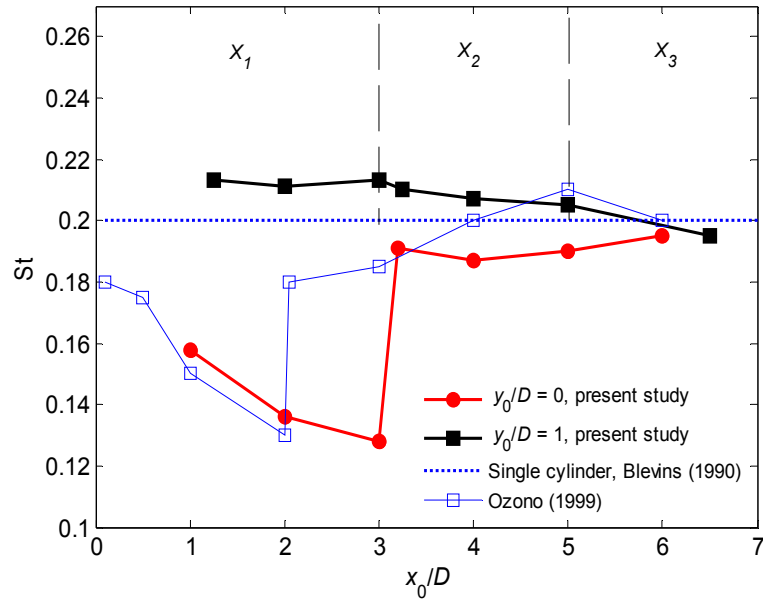


Figure 6: Variation of the Strouhal number as a function of longitudinal distance between a coupled cylinder-airfoil at  $Re = 10,000$ . The symbol ( $\square$ ) reflects the results of a coupled cylinder-plate at  $Re = 6,700$  and  $y_0/D = 0$ , Ozono (1999).

### 2.3. Transverse spacing of vortices

The Transverse Spacing (TS) of oncoming vortices can be also considered when the coupled cylinder and airfoil is analysed. The TS of a vortex is measured from the centre of the vortex to maximum transverse movement of the vortex over the airfoil using vorticity contours and it is normalised by the diameter of the cylinder. The variation in the TS is extracted from Figures 4 and 5 and the results are summarized in Figure 7, for both centrally aligned and staggered arrangements. It can be seen that the TS becomes larger when the airfoil was positioned at higher longitudinal distances for both centre aligned and staggered arrangements of cylinder and airfoil. The smallest transverse spacing is obtained with minimal longitudinal distance between the cylinder and the airfoil (at  $X_1$  regime). The TS then gradually increases at  $X_2$  and there is no significant change can be seen at  $X_3$ .

The effect of lateral distance is to increase the TS when the airfoil was positioned at  $y_0/D = 1$ . As a consequence, it is expected that larger transverse spacing for the oncoming vortices yield stronger circulation of vortices,  $\Gamma$ . However, it is worth noting that by increasing the gap size

between the cylinder and the airfoil, in both directions ( $x/D$  and  $y/D$ ), the dissipation of vortices needs to be considered. Therefore, extra attention is needed to estimate the circulation of vortices,  $\Gamma$ , for each test case.

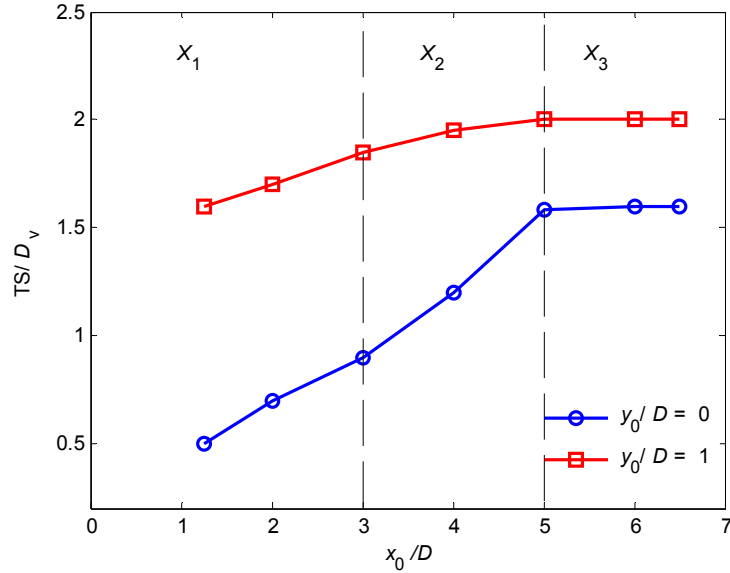


Figure 7: Dimensionless transverse spacing of the vortices as a function of longitudinal and lateral distances of upstream cylinder and downstream airfoil at  $\alpha = 0^\circ$  and  $Re = 10,000$ .

#### 2.4. Circulation of vortices

The circulation of vortices,  $\Gamma$ , can be estimated by the integral around a closed area of the vorticity field as shown in Figure 8; hence:

$$\Gamma = \iint \omega \, ds = \sum_{i=1}^n \omega_i \Delta x_i \Delta y_i. \quad (11)$$

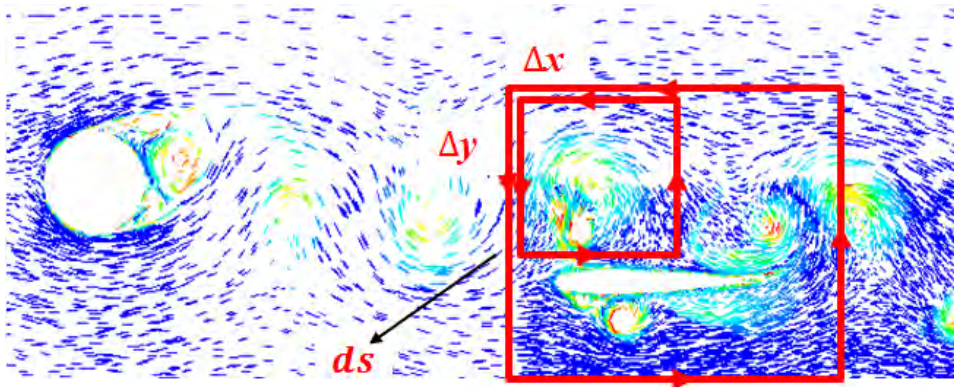


Figure 8: Circulation contours around a coupled cylinder and airfoil surrounded by two areas ( $ds$ ).



In order to ensure that the circulation is independent from the area of the vorticity, further analyses is required to obtain independent circulation values from the selected area. The independent solution for circulation has been chosen for a typical model when the airfoil is mounted at  $X_3$  due to the maximum obtainable TS at this regime. The independent results for  $\Gamma$  are shown in Figure 9 as a function of the chord length of the airfoil. Here, circulation is normalised by free stream velocity and the chord length of the airfoil. It is observed that the selected area ( $ds$ ) with approximately  $2C$  ( $C$  is the chord length of the airfoil) length yields insignificant changes of results in terms of the circulation. Therefore, this length is chosen to calculate the circulation around the airfoil for all test cases.

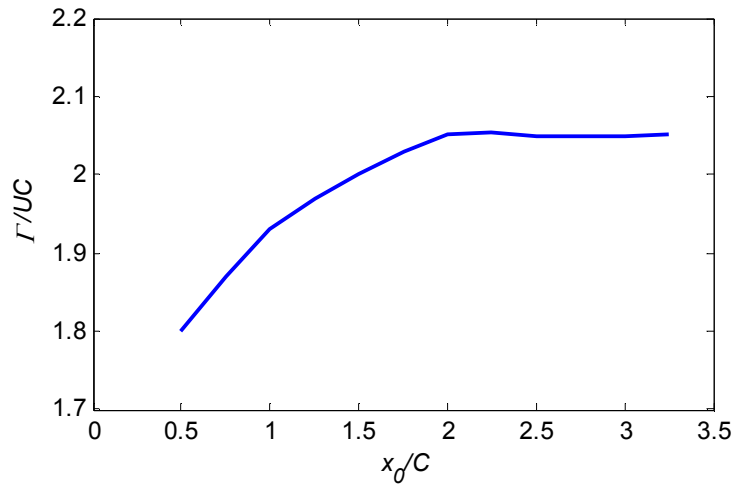


Figure 9: Independent variation of the dimensionless circulation as a function of area for a typical arrangement of cylinder and airfoil located at the  $X_3$  regime.

Figure 10 shows the variation of the dimensionless circulation as a function of the longitudinal and lateral distances. In general, it can be seen that the vortex circulation is higher when the airfoil is arranged at  $y_0/D = 1$ . The results also demonstrate that for the centre aligned cylinder-airfoil, the maximum circulation can be obtained for the studied model with  $x_0/D = 4$ . Although it was expected to achieve the highest circulation at fully develop regime ( $X_3$ ), it can be seen that due to dissipation, the vortex circulation shows a significant drop for both centre aligned and staggered arrangements. Since an increase in circulation of incident vortices acts to increase the lift force on the airfoil and all fluidic and structural conditions

of the cylinder and airfoil are constant, the heave performance of the airfoil can be affected by the generated vortices or shear forces.

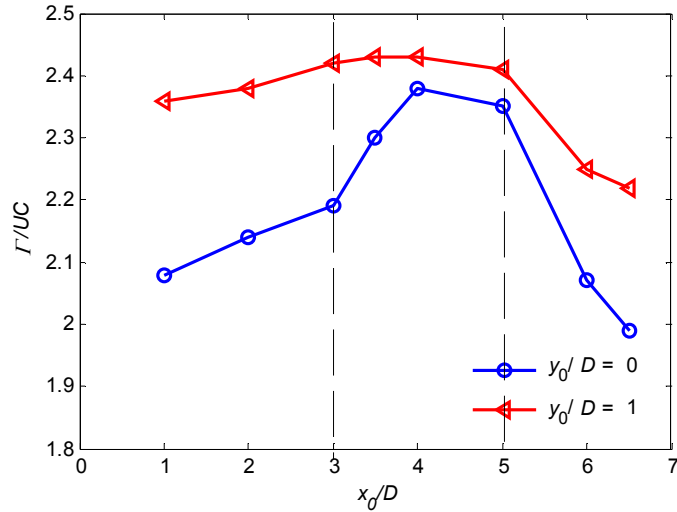


Figure 10: Effect of longitudinal and lateral distances on the vortex circulation at  $Re = 10,000$ .

## 2.6. System configuration

Analysing different aspects of flow pattern using numerical models was helpful in providing insight into the vortical structure and the optimum configuration of the cylinder and airfoil with higher potential to harness the kinetic energy in the flow. Therefore, the longitudinal and lateral distances between the cylinder and the airfoil along with the angle of attack of the airfoil were altered in the experiments.

Sixteen physical arrangements were tested in a water channel. The downstream airfoil was kept at the centre of the water channel to avoid any blockage effects, while the upstream cylinder was moved to different positions. The different arrangements of the cylinder and airfoil are shown in Figure 11. For each test case, ten angles of attack of the airfoil were considered leading to a total of 160 test cases.

Due to the extensive number of test cases, the SAVEM system is used to run the experiments rapidly by setting the angle of attack for each arrangement of the coupled cylinder-airfoil. In Section 3, the details of experimental test



linear bearings. The advantage of this model with a vertically mounted airfoil is that the static weight (minus the buoyancy force) is no longer applied to the motor which provides the linear movement of the airfoil. This approach eliminates the effect of the weight and buoyancy forces on the drive mechanism. The carriage is driven by a toothed belt. The timing belt is coupled to two toothed pulleys; one free acting as an idler, the other coupled to a Maxon brushless EC-Max 30 (with a 2000 quad-count encoder) servo-motor via a gearbox of 51:1 ratio. The servo-motor is controlled by a Maxon ESCON 50/5 servo controller. The force applied to the airfoil is measured using a pair of strain gauges in a half bridge arrangement. The bridge directly measures the bending moment at the root of the cantilevered column and consequently by assuming 2D flow conditions, the lateral force normal to the mean flow direction was measured.

Control of the SAVEM was activated using Matlab/Simulink and its Real Time Workshop; the model was compiled to target a dSPACE-DS1104 rapid prototyping control board. The real-time controller was manipulated in dSPACE Control Desk. A Proportional-Integral-Derivative (PID) controller was designed to measure the instantaneous aerodynamic forces exerted on the airfoil and the displacement of the oscillation. The incremental encoder embedded inside the motor delivers square wave signals whose pulses can be counted for positioning (angle) and/or speed (angular velocity) measurement. The position signal of the motor was used for feedback control. A gain coefficient which represents the load allows for conversion of the motor rotation to the linear displacement of the cylinder. The difference between the measured displacements of the cylinder and those obtained from the virtual model was used as the input signal to the PID controller. The proportional, integral and derivative gains of the PID controller were set to minimize the output error of displacement to less than 0.5 mm, which was tuned using Ziegler Nichols method (Astrom and Hagglund 2006). The assembled equipment and main parts of the SAVEM system are shown in Figure 13. More detailed explanation of the VEM system can be found in the previous study of the authors (Derakhshandeh *et al.* 2014-c).

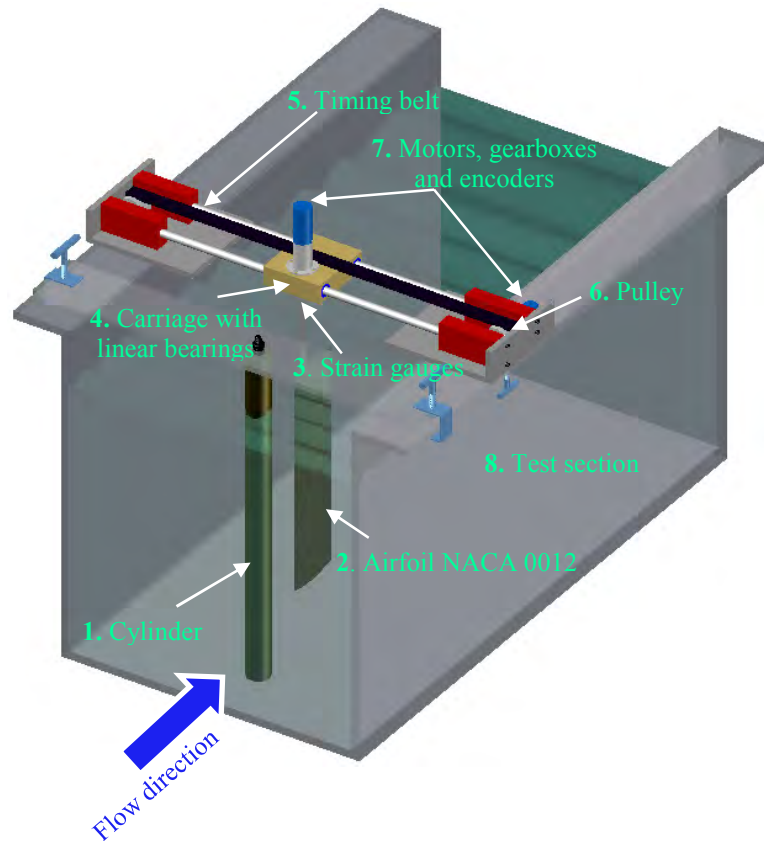


Figure 12: Schematic of 3D model of the test rig including the upstream circular cylinder, the downstream airfoil, the SAVEM system and the test section of water channel.

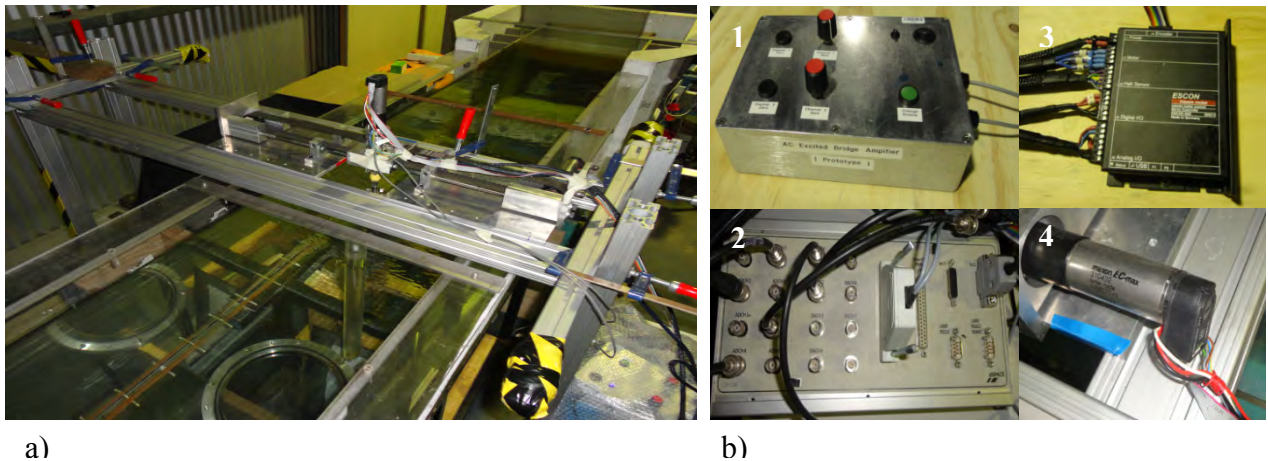


Figure 13: a) A photograph of the assembled equipment including the test section, b) main electric elements of the SAVEM system including 1: AC excited bridge amplifier with two channels, 2: A dSPACE Board (DS 1104) with 16 bit D/A converter, 3: A Maxon ESCON 50/5 servo controller, and 4: A Maxon servo motor (model EC-max 30) via a gearbox of 51:1 ratio comprising embedded encoder.

---

In FIV, the Reynolds number, the mass and damping ratios play a significant role in the dynamic response of the airfoil. The mass ratio is defined as  $m^* = 4m/\rho\pi C^2 l$ , based on the mass ( $m$ ) of the airfoil, the density ( $\rho$ ) of the fluid, the chord length ( $C$ ), and the length ( $l$ ) of the airfoil. The mass damping ratio is ( $m^*\zeta$ ) where,  $\zeta$  represents the damping ratio of the elastically mounted airfoil. In the current study, with the intention of study of the effect of the arrangement between the cylinder and airfoil, the mass and damping ratios were kept constant at 2.4 and 0.01, respectively, while the angle of attack was varied between  $0 < \alpha < 45^\circ$  degrees with an increment step of  $5^\circ$ . The reduced frequency was also kept constant at  $k_r = 0.75$  Hz. The reduced frequency is defined as  $k_r = \omega C/U$ , where  $\omega$  represents the circular frequency of rotation of the airfoil.

### 3.6. Lift measurement using SAVEM system

In order to utilize work conducted by the lift force acting on the airfoil, initially it is essential to measure and compare the exerted shear force in the normal direction to the flow as a function of angle of attack. The lift forces on the mounted airfoil were measured and the results were validated against the available published data. The angle of attack of the airfoil can be fixed at any desired value relative to the direction of the free stream (refer to  $\alpha$  in Figure 1) by changing the angle of the rotor using a real-time Simulink model. The lift coefficient acting on the airfoil can be quantified as follows

$$C_L = \frac{F_L}{\frac{1}{2}\rho U^2 CL} \quad (13)$$

where  $F_L$  is the lift force measured by strain gauges in the normal direction to the flow stream line.

Figure 14 shows the dependence of the lift coefficient on the angle of attack of the airfoil along with the previously measured data of Alam *et al.* (2010). It is observed that the lift coefficient initially drops at  $\alpha = 10^\circ$ , where the static stall occurs. The static stall is generally associated with separation of fluid flow at the suction side of the airfoil (Larsen *et al.* 2007). However, in another scenario Laitone (1997) reported that due to the transition from laminar to turbulence static stall can occur. Consequently, it is seen that when the flow around the airfoil is about half of the Reynolds number used

in this study (e.g.  $Re = 5,300$ ), the lift coefficient monotonically increases until the second stall appears around  $\alpha = 45^\circ$ . At this range of Reynolds numbers, it is assumed that the flow regimes are laminar (Alam *et al.* 2010). Therefore, the lift coefficient around  $\alpha = 10^\circ$  is far from those found by Alam *et al.* (2010) at the lower Reynolds number. In addition, it is observed that at  $Re = 10,000$  the trend of the measured data of  $C_L$  is very close to the previously published data, which is required for the study of the dynamic response of the elastically mounted airfoil. A small discrepancy between measured data with those reported by Alam *et al.* (2010) can be seen at a higher angle of attack  $\alpha > 60^\circ$ . This discrepancy might be a result of the blockage effects when the angle of attack of the airfoil increases. Accordingly, for the rest of this study, a safe range of angle of attack of  $\alpha \leq 45^\circ$  was chosen to investigate the dynamic response of the airfoil.

To avoid resonance, it is necessary that the natural frequency of the cantilevered airfoil occurs outside of the frequency of oscillation due to vortices. Therefore, the stiffness and mass of system was kept constant during the experiments and were defined to be  $k = 50$  N/m and  $m = 2$  kg, respectively. This provided the system with a frequency of oscillation of  $f_{osc} = 0.79$  Hz. The natural frequency of the fundamental bending mode of the cantilevered airfoil was measured using the free-decay tests. Free-decay tests for the cantilevered airfoil were performed in the water channel within a stagnant fluid when both motors and controllers were disabled. Based on the dynamic response of the airfoil, the fundamental natural frequency of the cantilevered airfoil was found to be  $f_n = 4.70$  Hz, which is outside of the frequency of oscillation.

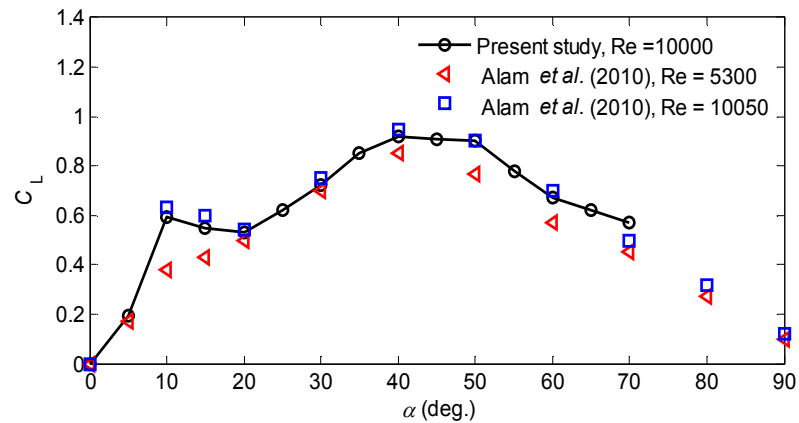


Figure 14: Comparison of the lift coefficient as a function of angle of attack of airfoil with published experimental data (Alam *et al.* 2010).

### 3.7. Dynamic response of the Airfoil

Typical time series of the lift coefficient for all Test Cases (TC) are plotted in Figure 15, when the angle of airfoil was set at  $\alpha = 0^\circ$  and  $Re = 10,000$ . It is clear that the behaviour of the lift coefficient varies with both longitudinal and lateral distances. The amplitude of the lift coefficient is approximately similar for Test Cases 1 and 2 and the trend of the signal is very regular. However, by increasing the longitudinal distance to  $x_0/D = 4$  and 5 (for Test Cases 3 and Test Cases 4), the behaviour of the lift coefficient becomes more irregular and its amplitude increases. As the position of airfoil shifts to larger longitudinal distances, the fully developed vortices are generated. As a consequence, the lift force acting on the airfoil can originate from two components known as *potential-force* due to the ideal flow inertia force and *vortex-force* due to the dynamics of vorticity field around the airfoil (Williamson and Govardhan 2004). Based on the numerical-analysis in Section 2, the higher amplitude of the lift coefficient was expected at primary vortex formation regime ( $X_2$ ) and this expectation is now confirmed for Test cases 3 and 4.



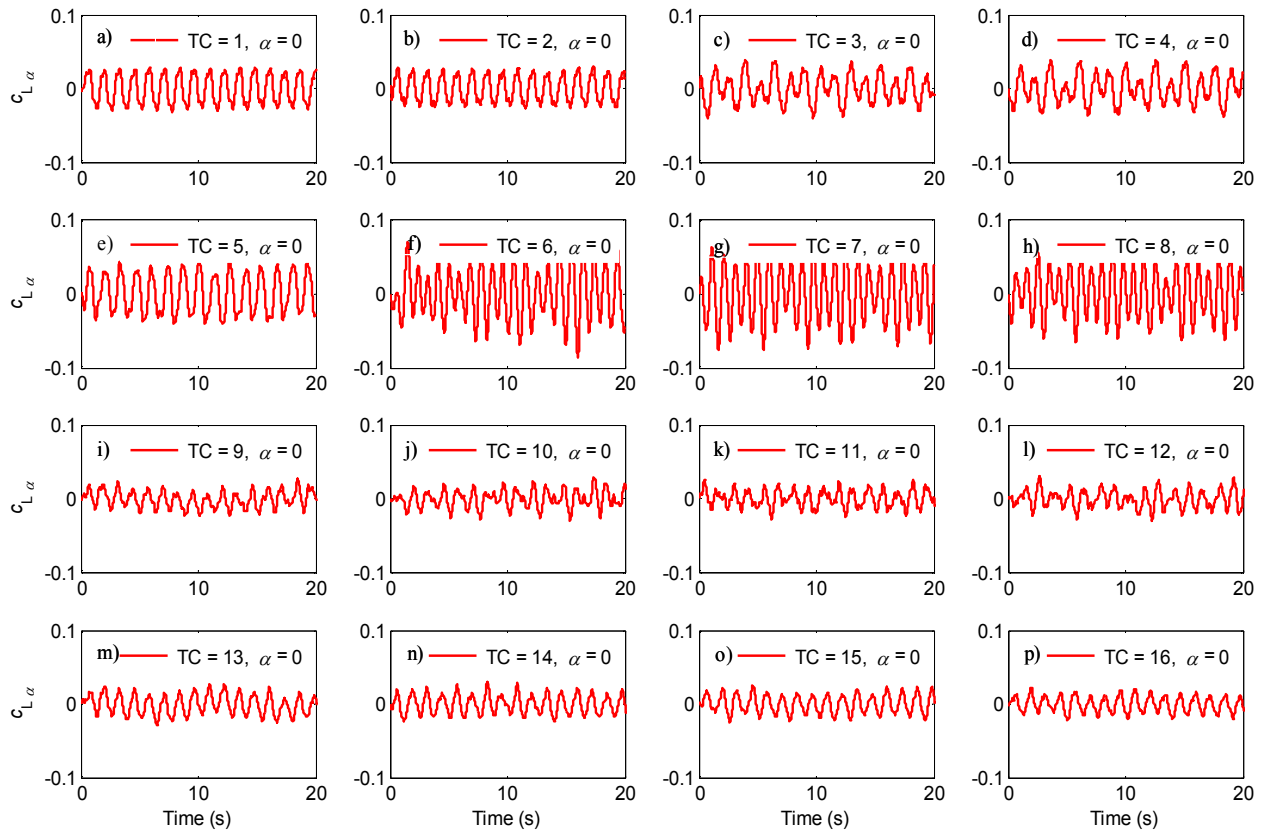


Figure 15: Typical time series of the lift coefficient for sixteen arrangements of the coupled cylinder-airfoil (or four groups) at  $\alpha = 0^\circ$  and  $Re = 10,000$ , a)  $TC = 1$ , b)  $TC = 2$ , c)  $TC = 3$ , d)  $TC = 4$ , e)  $TC = 5$ , f)  $TC = 6$ , g)  $TC = 7$ , h)  $TC = 8$ , i)  $TC = 9$ , j)  $TC = 10$ , k)  $TC = 11$ , l)  $TC = 12$ , m)  $TC = 13$ , n)  $TC = 14$ , o)  $TC = 15$ , p)  $TC = 16$ .

For the test cases with lateral distance  $y_0/D = 1$ , a higher amplitude of the lift coefficient is observed as compared to the centre aligned arrangements. It can be also seen that among all staggered arrangements, a coupled cylinder-airfoil with  $y_0/D = 1$  provides the maximum amplitude of the lift coefficient, which is due to the higher circulation of oncoming vortices to the downstream airfoil. Numerical analysis of the staggered arrangements revealed that, the maximum transverse spacing of the vortices, for staggered models with  $y_0/D = 1$ , is limited to  $\sim 2$ . Therefore, it is expected that outside of this range (such as  $y_0/D \geq 2$ ), the downstream airfoil is less influenced by the generated vortices. This hypothesis is now confirmed by the experimental results, where the airfoil was positioned at  $y_0/D = 2$  or higher lateral distances (refer to Figures 15-i to 15-p).

The importance of the staggered arrangement of a coupled cylinder and airfoil in capturing kinetic energy of vortices can be observed by comparing the heave response of the airfoil for centre aligned and staggered arrangements. Figure 16 shows the time history of the dimensionless (using chord length of airfoil) heave response of all examined test cases at a typical angle of attack  $\alpha = 10^\circ$ . The time history of the airfoil undergoes a smaller range of oscillation when the airfoil is positioned at the centre line of the upstream cylinder as compared to the staggered arrangements. Furthermore, it can be seen that the maximum time series of the heave response belongs to the staggered arrangements of  $y_0/D = 1$ . It is also observed that further increasing at the lateral distance has no significant effect on the amplitude of the heave (refer to Figures 16-i to 16-p).

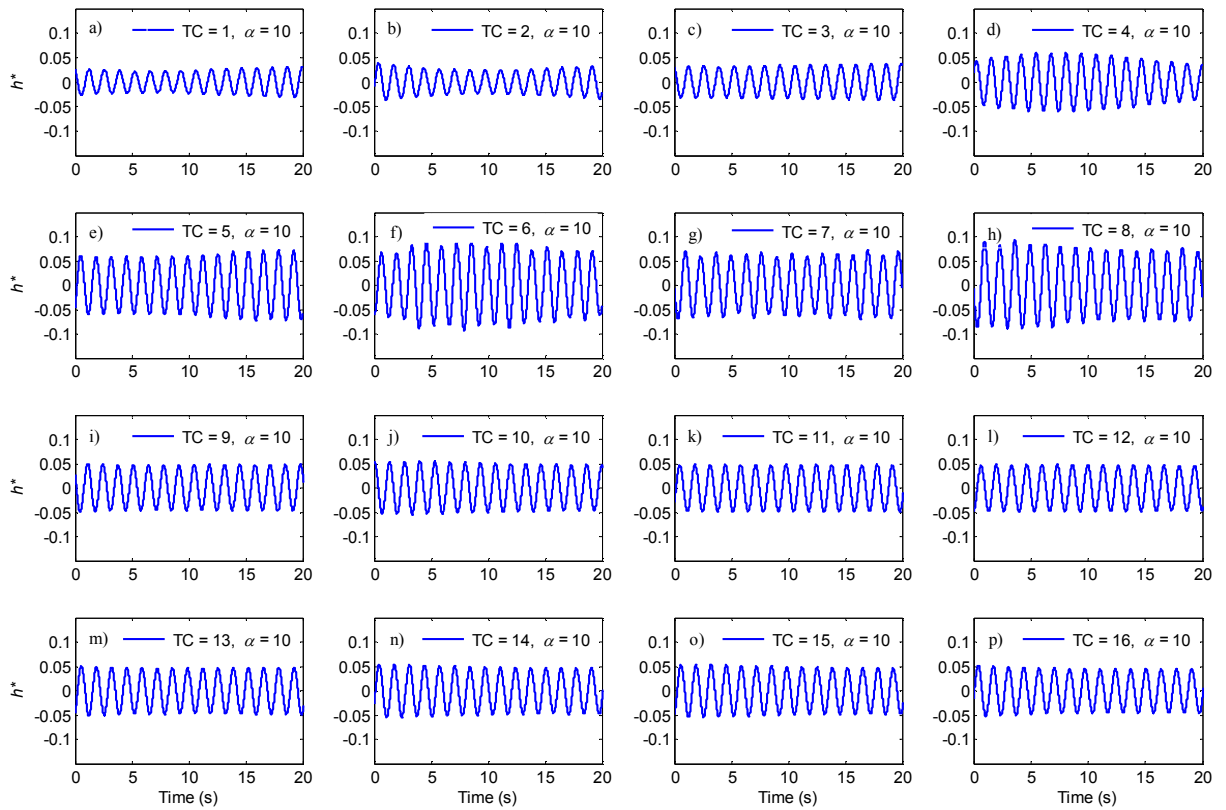


Figure 16: Typical time series of the heave response for sixteen arrangements of the coupled cylinder-airfoil (or four groups) at  $\alpha = 10^\circ$  and  $Re = 10,000$ , a) TC 1, b) TC 2, c) TC 3, d) TC 4, e) TC 5, f) TC 6, g) TC 7, h) TC 8, i) TC 9, j) TC 10, k) TC 11, l) TC 12, m) TC 13, n) TC 14, o) TC 15, p) TC 16.

An explanation for this trend in the heave response of the airfoil can be offered here using the spectral analysis of the lift force. The spectra of the measured force applied on the airfoil is plotted in Figure 17 when the airfoil angle was set to  $\alpha = 10^\circ$ . Herein, the frequency of the lift force is normalised by the natural frequency of the structure. For all test cases a dominant peak is observed in the spectrum. This peak corresponds to the frequency of the oscillation. When the airfoil was positioned at  $y_0/D = 1$ , particularly for TC 6, 7 and 8, another frequency appears in the signals, which is close to the frequency of the oncoming vortices. Compared with the numerical results for staggered arrangement of  $y_0/D = 1$ , there is evidence that the measured frequency of the vortices is approximately  $St = 0.2$  or the frequency of generated vortices in the wake of the cylinder. Based on the measured frequency ( $f/f_{osc} = 1.30$ ), the Strouhal number is calculated to be  $St \approx 0.19$ . It can be seen that for all test cases, the magnitude of the force signal is a maximum for the second group of test cases with  $y_0/D = 1$ , and in particular Test Cases 5 to 10 (Figures 17-e to 17-h). Further increasing the lateral distance between the cylinder and airfoil causes a reduction in the magnitude of the signal and indicates that the second peak disappears; however, the frequency of oscillation still remains at  $f/f_{osc} = 1$ . As a consequence, it is expected that the heave amplitude of the airfoil increases for staggered arrangements with  $y_0/D = 1$ .

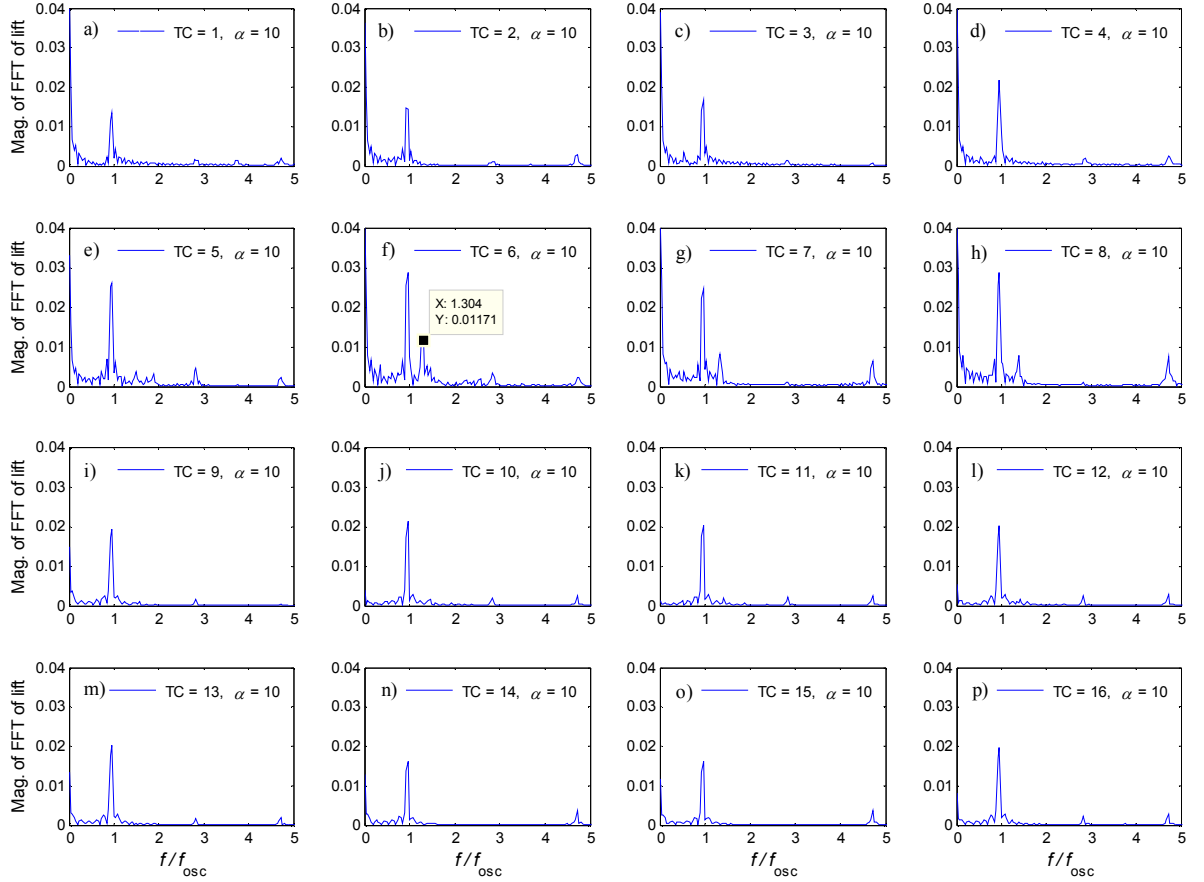


Figure 17: Magnitude of FFT of the lift force acting on the airfoil for sixteen arrangements of the coupled cylinder-airfoil at  $\alpha = 10^\circ$  and  $Re = 10,000$ , a) TC 1, b) TC 2, c) TC 3, d) TC 4, e) TC 5, f) TC 6, g) TC 7, h) TC 8, i) TC 9, j) TC 10, k) TC 11, l) TC 12, m) TC 13, n) TC 14, o) TC 15, p) TC 16.

### 3.8. Effect of angle of attack

The effect of angle of attack on the heave of the airfoil is examined in this section. The difference between the average of maximum and minimum of the heave amplitude  $\Delta h^*$ , is calculated as a percentage of discrepancy among all test cases at each angle of attack. This highlights the role of angle of attack in the heave response of the airfoil against the arrangement of the coupled cylinder-airfoil. Figure 18 shows the percentage of this discrepancy as a function of the angle of attack. It can be seen that at lower angles of attack such as  $\alpha = 0^\circ$  or  $5^\circ$ , the difference between the average of maximum and minimum of the heave amplitude,  $\Delta h^*$ , is approximately similar. Herein, the heave is normalized by the chord length of the airfoil. Figure 18

indicates a significant growth at  $\alpha = 10^\circ$ , in which  $\Delta h^*$  is approximately 130%. There is a significant drop for  $\Delta h^*$  when the angle of attack increases to  $15^\circ$ . Further increasing in the angle of attack causes a consequent reduction between the maximum and minimum amplitude of the heave. This means that the effect of the angle of attack at larger angles is weaker and by increasing the angle of attack, the arrangements of the cylinder and airfoil could not influence the heave response of the airfoil. The reason for this relates to the correlation of the selected reduced frequency and angle of attack of the airfoil. Zhu (2011) found that the dynamic response of the airfoil at different angle of attacks is a function of the reduced frequency. Therefore, it is found that under the defined condition for reduced frequency of the airfoil, the lower angle of attack,  $\alpha \leq 20^\circ$ , has the strongest effects on the dynamic response of the airfoil, whereas the large angles  $\alpha \geq 25^\circ$  plays a secondary role.

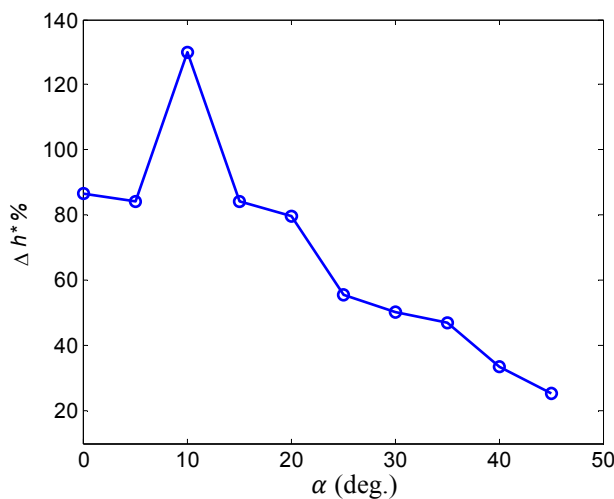


Figure 18: The percentage of variation of heave of airfoil obtained from difference between the average of the maximum and minimum of the heave at each set of arrangements as a function of angle of attack at  $Re = 10,000$ .

### 3.9. Effects of the longitudinal and lateral distances and angle of attack

In order to highlight the combined effect of the longitudinal and lateral distances along with the angle of attack of the airfoil, a contour plot diagram is utilized, which summarizes the effect of all the above parameters. With the aim of visualization and quantification of the arrangement on the heave amplitude of the airfoil, the interpolation of the measured values is

developed to the studied test cases. Furthermore, to aid in the interpretation of the heave values, isolines are added to the contour plot. The maximum dimensionless heave of the airfoil as a function of  $x_0/D$ ,  $y_0/D$ , and  $\alpha$  is presented in Figure 19. In general, it is observed that the maximum heave occurs for the staggered arrangements. Most significantly, it is observed that the highest heave of the airfoil appears when the airfoil was mounted at the primary vortex-formation regime ( $X_2$ ). In addition, it can be seen that the minimum and maximum bounds of the primary vortex-formation regime, (e.g.  $x_0/D = 3-5$ ), are very critical at the heave response of the airfoil. When the airfoil was set at smaller angle of attack of  $\alpha < 25^\circ$ , the heave response of the airfoil shifts to the lower bound of  $X_2$  or  $x_0/D = 3$ . By increasing the angle of attack to  $\alpha \geq 25^\circ$ , the higher heave amplitude of the airfoil moves to the higher value of the longitudinal distance of  $x_0/D = 4$  or even more (Figures 19-e to 19-h). As an effect of the lateral distance, in general, it can be noted that the maximum heave occur at the staggered arrangements when the airfoil was mounted at  $1 \leq y_0/D \leq 1.5$  and  $3.5 \leq x_0/D \leq 4.5$ .

Chapter 6: Effect of non-circular cylinder

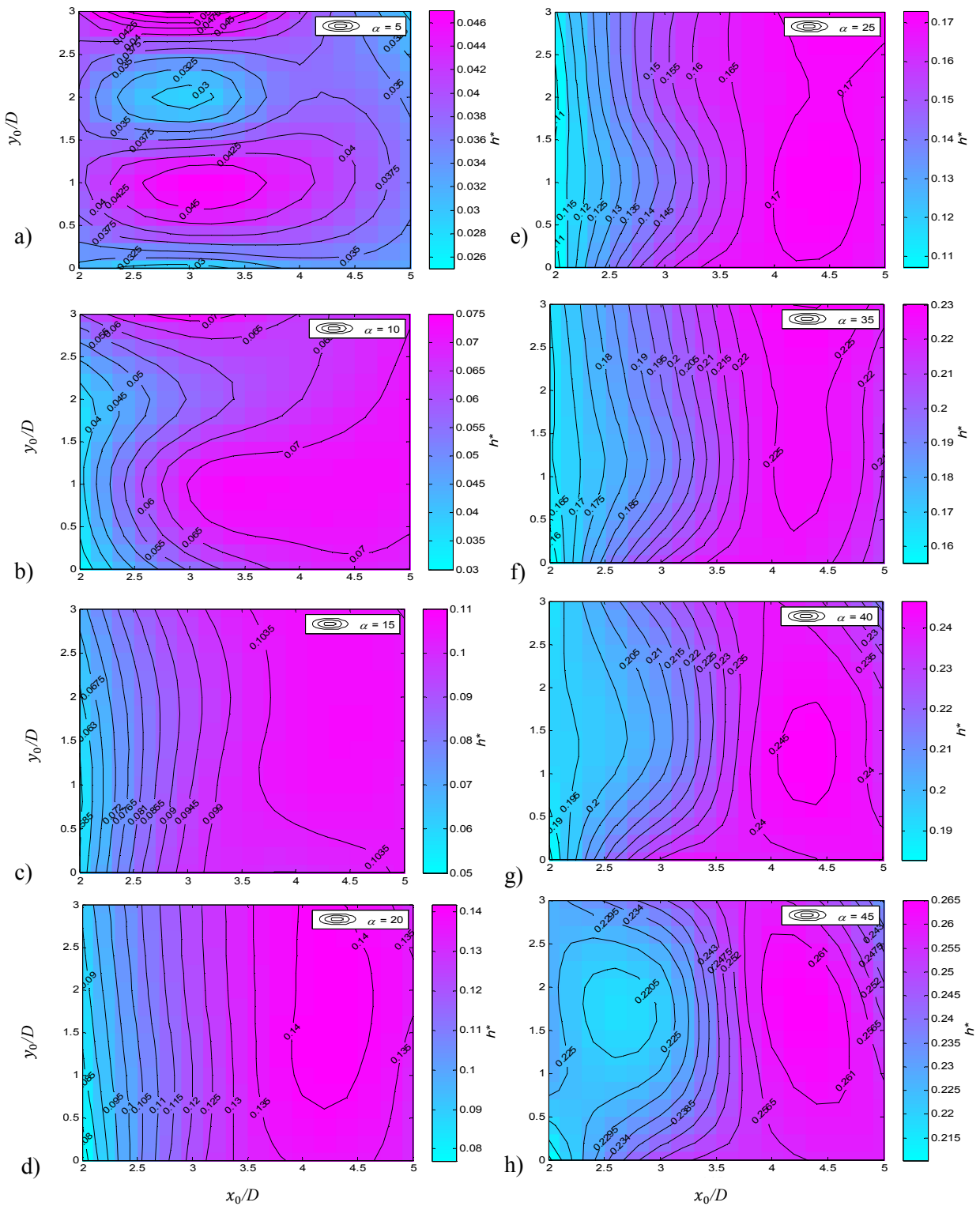


Figure 19: Isoline contours of the heave of the airfoil as a function of longitudinal and lateral distances at different angle of attack at  $Re=10,000$ . a)  $\alpha = 5^\circ$ , b)  $\alpha = 10^\circ$ , c)  $\alpha = 15^\circ$ , d)  $\alpha = 20^\circ$ , e)  $\alpha = 25^\circ$ , f)  $\alpha = 35^\circ$ , g)  $\alpha = 40^\circ$ , h)  $\alpha = 45^\circ$ .

### 3.4. Power coefficient of the FIV

The effect of the arrangements of the coupled cylinder-airfoil and angle of attack of the airfoil impacting on the power coefficient can be considered. In Figure 20 the contour plot of the power coefficient is shown. The contour plot has been chosen for the maximum  $\Delta h^*$  when the airfoil was at  $\alpha = 10^\circ$ . The plotted color bar of the figure shows the range of efficiency within a range of 0 to 30%. The contour of the efficiency is plotted as a function of longitudinal and lateral distance ( $x_0/D$  and  $y_0/D$ , respectively). It is observed that the maximum FIV efficiency of 30% is obtained for cases with  $3.5 \leq x_0/D \leq 4.5$  and  $1 \leq y_0/D \leq 1.5$ . It is seen that the increment of the lateral distance has no considerable influence on the power coefficient of the FIV as compared to the increase of the longitudinal distance.

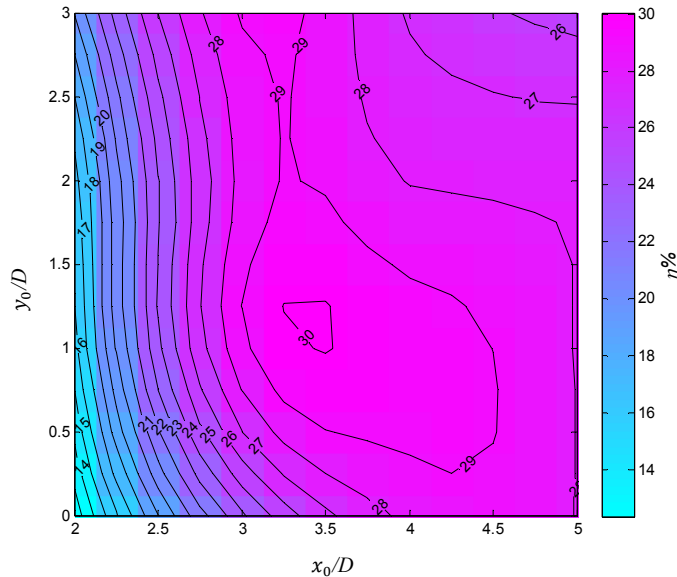


Figure 20: Variation of the power coefficient as a function of the longitudinal and lateral distances between the coupled cylinder-airfoil at  $\alpha = 10^\circ$  and  $Re = 10,000$ .

## 4. Conclusions

The wake flow patterns around the cylinder and airfoil was studied using CFD along with the water channel tests at a transient flow regime ( $Re = 10,000$ ). The results of the numerical modelling and experimental tests support the following observations accordingly:



- The locations with higher power density were determined as a zigzag pattern in the wake of the cylinder. It is found that although at  $X_3$  the vortices are fully developed, due to the dissipation of vortices, the power density of the fluid gradually reduces. As a consequence, the primary-vortex-formation regime ( $X_2$ ), is identified as an ideal longitudinal distance between the cylinder and airfoil;
- The vortex shedding frequency of the wake is a function of the longitudinal distance and lateral distances between coupled cylinder and airfoil and it was varied from  $X_1$  to  $X_2$  and it ultimately converged to the Strouhal number of a single cylinder at  $X_3$ . Consequently,  $X_1$  is not appropriate for harnessing the vortices energy with irregular frequency of vortex shedding;
- The length scale of vortices behind a cylinder becomes larger at  $X_2$  and  $X_3$  as well as the transverse spacing of the vortices. This provides a stronger circulation of vortices and consequently increases the lift force on the downstream airfoil. The variation of the length scale of vortices and transverse spacing of the vortices can be seen in both centre aligned and staggered arrangements when the longitudinal distance increases. However, this variation was higher for the centre aligned arrangements;
- The effect of the arrangements of the coupled cylinder-airfoil on the aerodynamic force and the heave response of the airfoil were examined. It was shown that both longitudinal and lateral distances play an important role in the heave response of the airfoil to capture the energy of the vortices;
- In regard to the angle of attack in capturing vortices energy it was observed that the optimum angle of attack was found to be  $\alpha = 10^\circ$ . For this angle of attack, the maximum FIV efficiency of 30% is obtained for cases with  $3.5 \leq x_0/D \leq 4.5$  and  $1 \leq y_0/D \leq 1.5$  arrangements, which is limited to the narrower lateral distances as compare to the previous study of the authors (Derakhshandeh *et al.* 2014-c) employing a pair of cylinders.

## References

Alam, M.M., Zhou, Y., Yang, H., Guo, H. and Mi, J., 2010, The ultra-low Reynolds number airfoil wake. *Journal of Experiments in Fluids*, 48 (1), 81-103.

Astrom, K. J. and Hagglund T., 2006, Advanced PID control, ISA.

Bearman, P.W., 1984, Vortex shedding from oscillating bluff bodies. *Journal of Fluid Mechanics*, 16, 195-222.

Bernitsas, M. M., and Raghavan K., 2004, Converter of Current/Tide/Wave Energy, Provisional Patent Application, United States Patent and Trademark Office Serial, No. 60/628, 252.

Bernitsas, M.M. Ben-Simon, Y., Garcia, E., 2008, VIVACE (Vortex Induced Vibration Aquatic Clean Energy): A new concept in generation of clean and renewable energy from fluid flow, *Journal of Offshore Mechanics and Arctic Engineering*, 130, 1-15.

Blevins, R.D., 1990, Flow-induced vibration, Krieger publishing company, Malabar, Florida, USA.

Chamorro, L.P., Troolin, D.R., Lee, S. J., Arndt, R. and Sotiropoulos, F., 2013, Three-dimensional flow visualization in the wake of a miniature axial-flow hydrokinetic turbine. *Journal of Experiments in Fluids*, 54 (2), 1-12.

Derakhshandeh, J. F., Arjomandi, M., Cazzolato B., Dally. B., 2014-a, The effect of arrangements of two circular cylinders on the maximum efficiency of Vortex-Induced Vibration power using a Scale-Adaptive Simulation model. *Journal of Fluids and Structures*, 49, 654-666.

Derakhshandeh J. F., Arjomandi., M., Dally, B. and Cazzolato, B., 2014-b, Effect of a rigid wall on the vortex induced vibration of two staggered circular cylinders, *Journal of Renewable and Sustainable Energy*, 6, 033114, 2014.

Derakhshandeh J. F., Arjomandi., M., Dally, B. and Cazzolato, B., 2014-c, Harnessing hydro-kinetic energy from wake-induced vibration using virtual mass spring damper system, *Journal of Ocean Engineering*, under review.

Falcão, A.F.D.O., 2010. Wave energy utilization: A review of the technologies. *Journal of Renewable and Sustainable Energy Reviews*, 14 (3), 899-918.

Hodges, D. H., and Pierce G. A., 2011, Introduction to structural dynamics and Aero-elasticity, Vol. 15, Cambridge University Press.

Govardhan, R. and Williamson C., 2000, Modes of vortex formation and frequency response of a freely vibrating cylinder, *Journal of Fluid Mechanics*, 420, 85-130.

Govardhan, R. and Williamson C., 2004, Critical mass in vortex-induced vibration of a cylinder, *European Journal of Mechanics-B/Fluids*, 23(1),17-27.

Khalak, A. and Williamson, C., 1996, Dynamics of a hydro-elastic cylinder with very low mass and damping, *Journal of Fluids and Structures*, 10 (5), 455-472.

Khan, M., Iqbal M., and Quaicoe J., 2009, River current energy conversion systems: Progress, prospects and challenges. *Journal of Renewable and Sustainable Energy Reviews*, 12(8), 2177-2193.

Laitone, E., 1997, Wind tunnel tests of wings at Reynolds numbers below 70,000. *Journal of Experiments in Fluids*, 23 (5), 405-409.

Larsen, J.W., Nielsen, S.R. and Krenk, S., 2007, Dynamic stall model for wind turbine airfoils. *Journal of Fluids and Structures*, 23 (7), 959-982.

Lau, Y., 2003, Experimental and numerical studies of fluid-structure interaction in flow-induced vibration problems. PhD thesis, The Hong Kong Polytechnic University.

McKinney, W. and DeLaurier J., 1981, The Wing mill: An oscillating-wing windmill, *Journal of Energy*, 5(2): p. 109-115.

Menter, F. and Egorov, Y., 2010. The scale-adaptive simulation method for unsteady turbulent flow predictions. Part 1: Theory and model description. *Flow, Turbulence and Combustion*, 85 (1), 113-138.

Ozono, S., 1999, Flow control of vortex shedding by a short splitter plate asymmetrically arranged downstream of a cylinder. *Journal of Physics of Fluids*, 11, 2928-2934.

Peng, Z., and Zhu Q., 2009, Energy harvesting through flow-induced oscillations of a foil, *Journal of Physics of Fluids*, 21(12), 123602-9.

Roshko, A., 1954, On the development of turbulent wakes from vortex streets, National Advisory Committee for Aeronautics, NACA Technical Report 1191.

Sarpkaya, T., 1978, Fluid forces on oscillating cylinders, *ASCE Journal of the Waterway Port Coastal and Ocean Division*, 104, 275-290.

Sarpkaya, T., 2004. A critical review of the intrinsic nature of Vortex-Induced Vibrations. *Journal of Fluids and Structures*, 19 (4), 389-447.

Sheldahl, R.E. and Klimas P.C., 1981, Aerodynamic characteristics of seven symmetrical airfoil sections through 180-degree angle of attack for use in aerodynamic analysis of vertical axis wind turbines. Sandia National Labs., Albuquerque, NM (USA), Report number SAND-80-2114.

Sváček, P., Feistauer M., and Horáček J., 2007, Numerical simulation of flow induced airfoil vibrations with large amplitudes, *Journal of Fluids and Structures*, 23(3), 391-411.

Trevor L., 2013, *Future energy: improved, sustainable and clean options for our planet*, Elsevier Science, Amsterdam.

Unal, M. and Rockwell D., 1988, On vortex formation from a cylinder. Part 1, The initial instability, *Journal of Fluid Mechanics*, 190, 491-512.

Vries, O., 1983, On the theory of the horizontal-axis wind turbine. *Annual Review of Fluid Mechanics*, 15(1), 77-96.

Williamson, C., and Roshko A., 1988, Vortex formation in the wake of an oscillating cylinder, *Journal of Fluids and Structures*, 2(4), 355-381.

Williamson, C. and Govardhan R., 2004, Vortex-induced vibrations, *Annual Review of Fluid Mechanics.*, 36, 413-455.

Zdravkovich, M., 1997, 1st edition, Flow Around Circular Cylinders, Vol. 1. Oxford University Press Inc., New York.

Zhu, Q., 2011, Optimal frequency for flow energy harvesting of a flapping foil. *Journal of Fluid Mechanics*, 675, 495-517.



## Chapter 7

### Conclusions and future work

#### 7.1. Conclusions

Employing non-turbine systems, such as VIV and WIV, is a relatively new concept to generate renewable hydro energy. The dynamic response of a circular cylinder under different conditions was investigated. As the power coefficient is directly proportional to the behaviour of the cylinder, the key parameters such as amplitude of displacement needs to be evaluated. It was shown that the dynamic response of an unbounded cylinder under the VIV mechanism is different from the WIV mechanism employing two circular cylinders. This difference affects the power coefficient of the converter. Generally, the maximum amplitude of oscillation of the cylinder is obtained at lock-in, when there is synchronisation between the frequency of vortex shedding and the natural frequency of the cylinders. This leads to the maximum power coefficient of the converter. On the other hand, the WIV mechanism can arise at frequencies outside the natural frequency of the cylinder. Furthermore, as these mechanisms are applicable in the shallow rivers or installed on the seabed of oceans, other features such as the effect of a rigid wall affect the dynamic response of the cylinder. It was shown that the gap ratio of an upstream cylinder can affect the pressure field around a downstream mounted cylinder which causes different dynamic response of

the cylinder. The reason is due to the alteration of flow pattern and resulting vortices such as mode of vortices and circulation of vortices which can occur in the wake of cylinder and leads to change in the lift force acting on the downstream cylinder. Therefore, in the current dissertation, detailed investigations into the causes of alterations of the structure of the vortices, including the frequency, vorticity, lift force and phase angle between force and displacement are presented and discussed.

### 7.1.1. Study of power coefficient of a cylinder

The power coefficient for both VIV and WIV mechanisms were investigated and compared in Chapter 3. The following observations were made.

- The maximum power coefficient of the VIV power was calculated at the upper branch with a 2P mode to be approximately 10% for a single elastically mounted cylinder. This value is approximately one-third of the power coefficient (28%) when using two cylinders with a staggered arrangement of  $3.5 \leq x_0/D \leq 4.5$  and  $1 \leq y_0/D \leq 2$ ;
- Assuming linear behaviour and a sinusoidal response of the cylinder, the theoretical power coefficient of VIV can be explained as a function of four dimensionless parameters; the lift coefficient, Strouhal number, amplitude of oscillation, and phase angle between force and displacement. However, all these parameters are implicit, while the reduced velocity varies and cannot be explicitly specified. Therefore, the power coefficient of VIV for a single cylinder can be formulated only as a function of the reduced velocity.



### 7.1.2. Effect of staggered arrangement on the power coefficient

A detailed calculation of the power coefficient as a function of free stream velocity including the maximum theoretical power, the fluid power, the power density and the power coefficient is presented in Chapter 4, where the results were compared for both VIV and WIV mechanisms. From these results, the following outcomes were observed:

- In the VIV mechanism, the upper branch of amplitude occurs at a limited range of frequencies in which the shedding frequency is very close to the natural frequency of the structure. However, for the staggered arrangement of the cylinders, the WIV responses can occur at frequencies outside this range;
- A structural mechanism was designed, built and employed to investigate the WIV response of the cylinder using a virtual mass spring damper (VMSSD) instead of real spring damper. In this mechanism, the cylinder was installed vertically in the water channel. This assisted in avoiding the static load on the motor arising from the cylinder, thus reducing friction and improving the response. Therefore, the test rig was designed to operate at a low free stream velocity (or low Reynolds number, such as  $Re = 2,000$ ) without the nonlinearities observed in previous work;
- The staggered arrangement of the cylinders results in increased WIV efficiency as compared to the aligned arrangement of the cylinders. The results of water channel tests of sixteen test cases revealed that a staggered arrangement with  $3.5 \leq x_0/D \leq 4.5$  and  $1 \leq y_0/D \leq 2$  showed the highest power coefficient of the WIV converter among those test cases performed due to the minimum phase shift between force and velocity of the cylinder;

- The numerical analysis also demonstrated that for flow around two circular cylinders and the downstream one is attached to an elastic support, the mode of oncoming and downstream vortices are 2S and 2P, respectively. These modes are known as the major vortex pattern for a vibrating cylinder (Williamson and Roshko, 1988), in which the synchronisation occurs. Therefore, based on the arrangement of the cylinders, the dynamic response of the downstream cylinder is different as compared to a response of a single cylinder.

### **7.1.3. Effect of a rigid wall on the power coefficient**

To identify the effect of a rigid wall and consequently the influence of the boundary layer on the dynamic response of the downstream cylinder, numerical analyses were conducted and a detailed explanation of the vortex dynamics has been discussed in Chapter 5. In this section, twelve arrangements of a pair of cylinders were considered, with the following observations:

- The downstream elastically mounted circular cylinder was affected by the ‘jet flow’ of the upstream stationary cylinder mounted next to a rigid wall, when the upstream cylinder is mounted at small gap ratios,  $0.25 \leq G/D \leq 0.5$ . The variation of the acting lift coefficient on the upstream cylinder is approximately 33%, while for the downstream one it is approximately 27%. It was shown that the arrangements of the cylinders based on the gap ratio of the upstream cylinder affect both lift and drag coefficients acting on the cylinders;
- The lift coefficient, the maximum amplitude of oscillation, the Strouhal number and the phase angle between the exerted lift force on the downstream cylinder and the displacement of the cylinder on the power coefficient of the WIV were evaluated. Despite the

maximum lift coefficient of the downstream cylinder occurring at lower gap ratios, the maximum oscillation of the downstream cylinder occurs at higher gap ratios ( $G/D \geq 1$ ). The reason is due to the phase angle between the exerted lift force and displacement of the cylinder. It was observed that the maximum achievable theoretical efficiency of VIV power for the current test cases is approximately 37% at  $G/D = 1$  and is much higher than the power coefficient of a single unbounded cylinder.

#### 7.1.4. Effect of flutter on energy extraction

In order to investigate the effect of angle of attack, the wake flow patterns around the cylinder and airfoil was studied using CFD along with water channel tests at a transient flow regime (explained in Chapter 6). The results of the numerical modelling and experimental tests support the following observations:

- In regard to the angle of attack in capturing energy of the vortices, it was observed that the optimum angle of attack was found to be  $\alpha = 10^\circ$ . For this angle of attack, the maximum FIV efficiency of 30% is obtained for cases with  $3.5 \leq x_0/D \leq 4.5$  and  $1 \leq y_0/D \leq 1.5$  arrangements, which are limited to the narrower lateral distances;
- The locations with higher power density were determined as a zigzag pattern in the wake of the cylinder. It is found that although at higher longitudinal distances, such as fully developed-vortex-formation ( $X_3$ ), the vortices are fully developed. Due to the dissipation of vortices, the power density of the fluid gradually reduces. As a consequence, the primary-vortex-formation regime ( $X_2$ ), was identified as an ideal longitudinal distance between the cylinder and airfoil;

- It was found that the vortex shedding frequency of the wake is a function of both longitudinal distance and lateral distances between coupled cylinder and airfoil and it was varied from pre-vortex-formation regime ( $X_1$ ) to the primary-vortex-formation regime ( $X_2$ ). The Strouhal number of a coupled cylinder and airfoil ultimately converged to the Strouhal number of a single cylinder at the  $X_3$  regime. Consequently,  $X_1$  is not appropriate for harnessing the energy of the vortices with irregular frequency of vortex shedding.
- The length scale of vortices behind a cylinder becomes larger at higher longitudinal distances (e.g.  $X_2$  and  $X_3$ ) as well as the larger transverse spacing of the vortices. This provides a stronger circulation of vortices and consequently increases the lift force on the downstream airfoil. The variation of the length scale of vortices and transverse spacing of the vortices can be seen in both centre aligned and staggered arrangements of when the longitudinal distance increases. However, this variation was higher for the centre aligned arrangements.

## 7.2. Future work

The major recommendations for future work are presented in this section.

### 7.2.1. Effect of the location of the pitching axis

It has been shown that the dynamic response of the airfoil due to the lift force is a function of angle of attack. Therefore, in this project, the airfoil was only under the influence of the lift force. In the next step, the flutter of the airfoil can be considered employing both lift force and moment by choosing different locations for the pitching axis. Hence, further investigations are required to find the optimum location of the pitching axis when the airfoil is located in the wake of the stationary cylinder.

### **7.2.2. Effect of passive control on the downstream airfoil**

One of the biggest advantages of the virtual mass spring damper device used in this project is to perform a wide range of tests using a control system. In this research, only a semi-activated control system has been considered. The VMSD system still has the potential to develop into a higher level of application such as purely passive mechanism, in which the airfoil will be entirely excited by the vortices. In this case, the flutter response of the airfoil can be programmed based on a closed loop-feedback of the generated lift and torque acting on the airfoil. Consequently, in that situation, the maximum kinetic energy of the vortices would be considered and a wider range of variables are involved such as the frequency and magnitude of the torque based on the frequency of the acting vortices.

### **7.2.3. Effect of mass and damping ratios**

All numerical and experimental investigations in this project have been conducted using a constant mass and damping ratio. It has been shown that the dynamic response of the VIV and WIV are inversely proportional to the product of mass and damping ratio,  $m*\zeta$  (Govardhan and Williamson 2000, Assi 2009, Raghavan and Bernitsas 2011). In another scenario, Bokaian and Geoola (1984) showed that by varying the damper ratio, the VIV and WIV regimes can be overlapped. Following these, Assi (2009) found that the magnitude of the WIV response is more sensitive to variation of the damping ratio rather than to variations in mass ratio. Therefore, further investigations are required to highlight the effect of these parameters, particularly of the flutter response of the airfoil and consequently the power coefficient of the converter.

#### **7.2.4. Effect of upstream cylinder**

It was found that the geometry of downstream cylinder such as circular and non-circular cylinders influence the dynamic response of the body. Further analysis should be performed to study the effect of an upstream cylinder on the power coefficient of the downstream cylinder.

#### **7.2.5. Effect of roughness on cylinders**

This project has been conducted using smooth surfaces for the bluff bodies. It was shown that the surface roughness has an effect on the extraction of energy from the VIV mechanism (Chang *et al.* 2011). Further investigations need to be conducted to analyse the effect of roughness on the WIV mechanism.

## References

Assi, G., Mechanisms for flow-induced vibration of interfering bluff bodies. PhD thesis, Imperial College London, UK, 2009.

Bokaian, A. and Geoola, F., Wake-induced galloping of two interfering circular cylinders, *Journal of Fluid Mechanics*, 146, 383-415, 1984.

Chang, C. C. J., Ajith Kumar, R. and Bernitsas, M.M., VIV and galloping of single circular cylinder with surface roughness at  $3.0 \times 10^4 \leq Re \leq 1.2 \times 10^5$ , *Journal of Ocean Engineering*, 38, 1713-1732, 2011.

Govardhan, R. and Williamson, C., Modes of vortex formation and frequency response of a freely vibrating cylinder. *Journal of Fluid Mechanics*, 420, 85-130, 2000.

Raghavan, K. and Bernitsas, M.M., Experimental investigation of Reynolds number effect on vortex induced vibration of rigid circular cylinder on elastic supports. *Ocean Engineering*, 38 (5-6), 719-731, 2011.

Williamson C. H. K. and Roshko A., Vortex formation in the wake of an oscillating cylinder, *Journal of Fluids and Structures*, 2, 355-381, 1988.

## **Appendix A**

### **Conference Papers:**

In this appendix all conference papers resulting from this body of work are represented in full.



## Statement of Authorship

Title of Paper	Numerical simulation of vortex-induced vibration of elastic cylinder.
Publication Status	<input checked="" type="radio"/> Published, <input type="radio"/> Accepted for Publication, <input type="radio"/> Submitted for Publication, <input type="radio"/> Publication style
Publication Details	Derakhshandeh, J. F., Arjomandi, M., Dally, B., Cazzolato, B., Numerical simulation of vortex-induced vibration of elastic cylinder, 18th AFMC Conference, 2012.

### Author Contributions

By signing the Statement of Authorship, each author certifies that their stated contribution to the publication is accurate and that permission is granted for the publication to be included in the candidate's thesis.

Name of Principal Author (Candidate)	Javad Farrokhi Derakhshandeh
Contribution to the Paper	To investigate the dynamic response of a circular cylinder in harnessing hydro-power energy.
Signature	Date 18/03/2015

Name of Co-Author	Maziar Arjomandi
Contribution to the Paper	Supervised the work, assisted in developing ideas and manuscript evaluation.
Signature	Date 18.03-2015

Name of Co-Author	Bassam Dally
Contribution to the Paper	Supervised the work, assisted in developing ideas and manuscript evaluation.
Signature	Date 18.03-2015

Name of Co-Author	Benjamin Cazzolato
Contribution to the Paper	Supervised the work, assisted in developing ideas and manuscript evaluation.
Signature	Date 19/3/15

## Statement of Authorship

Title of Paper	Experimental and computational investigation of wake-induced vibration.
Publication Status	<input checked="" type="radio"/> Published, <input type="radio"/> Accepted for Publication, <input type="radio"/> Submitted for Publication, <input type="radio"/> Publication style
Publication Details	Derakhshandeh, J. F., Arjomandi, M., Dally, B., Cazzolato, B., Experimental and computational investigation of wake-induced, 19th AFMC Conference, 2014.

### Author Contributions

By signing the Statement of Authorship, each author certifies that their stated contribution to the publication is accurate and that permission is granted for the publication to be included in the candidate's thesis.

Name of Principal Author (Candidate)	Javad Farrokhi Derakhshandeh		
Contribution to the Paper	To study and evaluate the efficiency of power generation from wake-induced vibration using both numerical and experimental methods.		
Signature	<table border="1" style="float: right;"> <tr> <td>Date</td> <td>18/03/2015</td> </tr> </table>	Date	18/03/2015
Date	18/03/2015		

Name of Co-Author	Maziar Arjomandi		
Contribution to the Paper	Supervised the work, assisted in developing ideas and manuscript evaluation.		
Signature	<table border="1" style="float: right;"> <tr> <td>Date</td> <td>18.03.2015</td> </tr> </table>	Date	18.03.2015
Date	18.03.2015		

Name of Co-Author	Bassam Dally		
Contribution to the Paper	Supervised the work, assisted in developing ideas and manuscript evaluation.		
Signature	<table border="1" style="float: right;"> <tr> <td>Date</td> <td>18.03.2015</td> </tr> </table>	Date	18.03.2015
Date	18.03.2015		

Name of Co-Author	Benjamin Cazzolato		
Contribution to the Paper	Supervised the work, assisted in developing ideas and manuscript evaluation.		
Signature	<table border="1" style="float: right;"> <tr> <td>Date</td> <td>18/3/15</td> </tr> </table>	Date	18/3/15
Date	18/3/15		

18<sup>th</sup> Australasian Fluid Mechanics Conference  
 Launceston, Australia  
 3-7 December 2012

**Numerical simulation of vortex-induced vibration of elastic cylinder**

Javad Farrokhi Derakhshandeh<sup>1</sup>, Maziar Arjomandi<sup>2</sup>, Benjamin Cazzolato<sup>3</sup> and Bassam Dally<sup>4</sup>

<sup>1,2,3,4</sup>School of Mechanical Engineering  
 University of Adelaide, Adelaide, South Australia 5005, Australia

**Abstract**

Study of the flow around a bluff body and its effect on the flow induced vibration is relevant to design of bridges, tall buildings and similar structures. The flow around bluff bodies, arranged in tandem where one of the bodies is in the wake region of the second one, was studied using numerical simulation. This phenomenon is related to the response of bluff bodies immersed in fluid flow and is known as Vortex Induced Vibration (VIV). Vortex energy extraction is of interest to this work. This paper presents the results of a 2D numerical simulation of the wake interaction of two circular cylinders at low Reynolds number using ANSYS Fluent Workbench. The upstream cylinder is stationary, while the downstream elastic cylinder can be affected by the vortices in the wake of the first cylinder. The paper reports the behaviour of the elastic cylinder through a CFD model, with a focus on harnessing the vortical energy. Also discussed is the theoretical maximum energy that can be harvested by this method. For validation purposes, the modelled amplitude of the oscillation is compared to published data in literature. The results show that the motion of elastic cylinder can be modelled as a simple mass spring damper model.

**Introduction**

Flow induced vibration is a phenomenon which is related to interaction of fluid forces and elastic forces in the structures [9]. These phenomena are related to the response of the structure which is immersed in fluid flow and are known as Vortex Induced Vibration (VIV). The vibration induced on structures by vortices is of importance because of its potentially destructive effect of structures. In these phenomena a non-stationary excitation force is exerted on the structures by vortices, which depending on the Reynolds number can be periodic. The vortex shedding behind a cylinder is known as a vortex street and the behaviour of the vortices in the wake of the structure is similar, regardless of the geometry of the structure. Blevins [6] showed that the vortex shedding in a steady subsonic flow is a function of the Reynolds number. Zdravkovich [11] presented the detailed information of the exerted forces on the stationary circular cylinder in different regimes. The results reveal that by increasing the Reynolds number from laminar to transitional regimes,  $Re=10^4-10^5$ , the lift force on the cylinder can increase significantly.

Vortices energy can be harnessed and used as a renewable, friendly energy. A study of the flow around a pair of cylinders as a tandem body might a simple model to harness the vortices energy by downstream cylinder.

This paper investigates numerically the flow interaction between two circular cylinders to explain a new concept of renewable generation energy due to VIV. In this model the upstream cylinder is stationary while the downstream has one degree of freedom and can oscillate freely in the normal to the mean flow direction.

**Mathematical model**

A simple schematic of the arrangement of two cylinders is shown in Figure 1. The moving rigid cylinder is mounted on an elastic base with one degree of freedom in y-direction. Therefore, the elastic cylinder is a simple mass-damper-spring system [4] and the equation of motion can be defined as

$$m_{osc}\ddot{y} + c\dot{y} + ky = F_y(t). \tag{1}$$

In the equation above,  $m_{osc}$  is the total oscillating mass of system,  $y$  is the normal direction of flow,  $\dot{y}$  and  $\ddot{y}$  are velocity and acceleration of cylinder, respectively,  $c$  is damping coefficient,  $k$  is spring stiffness and  $F_y$  is the fluid force which is exerted on the cylinder boundary perpendicular to the flow.

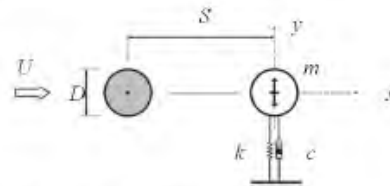


Figure 1. Schematic of two cylinders in cross flow, the upstream is rigidly mounted; the downstream is free to move

In Equation (1), it is appropriate that non dimensional parameters such as mass ratio and damping factor are considered instead of mass and damping constant. The mass ratio can be defined as the total oscillating mass of system over the specific mass of fluid,  $m^* = 4 m_{osc} / \rho \pi D^2 l$  and damping factor is  $\zeta = c / 2\sqrt{k \cdot m_{osc}}$ . In former equation,  $\rho$  is the fluid density,  $D$  is the diameter of cylinder and  $l$  is the length of the cylinder. In this research, the mass ratio and damping factor were  $m^* = 2.6$  and  $\zeta = 0.007$  based on the assumptions of Carmo [8] and the experiments of Assi [2] to validate the results. The Reynolds number,  $Re = U_{\infty} \cdot D / \nu$ , is 1500 based on the diameter of the upstream cylinder  $D$  where  $U_{\infty}$  is free stream velocity and  $\nu$  is kinematic viscosity of fluid. For this Reynolds number, the non-dimensionalised frequency which is defined as Strouhal number  $St = f_c \cdot D / U$  ( $f_c$  is the vortex frequency). The Strouhal number for the selected Reynolds number is close to 0.2 [6].

For the system under investigation, vortex shedding in the wake of upstream cylinder exerts harmonic forces on the elastic downstream cylinder. The asymmetric distribution of pressure acts on the surface of elastic cylinder and generates the translational motion. This motion has been simulated using the ANSYS Fluent Workbench 14.0. To model the behaviour of elastic cylinder a User Define Function as a UDF file has been loaded in the Fluent and it has been coupled by a dynamic mesh setup. In this interaction the sinusoidal response of the cylinder causes the fluctuating transverse amplitude and force. Therefore,

harmonic displacement, velocity and lift coefficient equations of the cylinder can be considered respectively as

$$y = y_{max} \cdot \sin(2\pi f_s t), \quad (2)$$

$$\dot{y} = (2\pi f_s) \dot{y}_{max} \cos(2\pi f_s t) \quad (3)$$

$$c_L(t) = C_L \cdot \sin(2\pi f_s t + \varphi) \quad (4)$$

Here  $y_{max}$  is maximum amplitude of oscillation and  $\varphi$  is the phase angle between the fluid forcing and the displacement,  $c_L$  is time dependent lift coefficient and  $C_L$  is the amplitude of lift coefficient of the cylinder. The position and velocity of cylinder can be interpreted by Fluent for transient flow in each time step. The work generation by the downstream cylinder is obtainable utilising the total vertical force including the pressure and viscous forces on the surface of elastic cylinder. Therefore, Equations (3) and (4) can be used to calculate the work acting on the cylinder as the inner product of fluid force which is exerted on the cylinder during a vortex-induced vibration cycle by the displacement of cylinder as follows

$$W_{VIV} = \int_0^{T_{cyl}} F_y \cdot \dot{y} \cdot dt \quad (5)$$

In the Equation (5),  $T_{cyl}$  is the one complete cycle of oscillation. By integrating the right hand side of Equation (5) and averaging over the cycle period the power due to VIV for a circular cylinder can be obtained as [5]

$$P_{VIV} = \frac{W_{VIV}}{T_{cyl}} \quad (6)$$

#### Interaction of two stationary cylinders

The behaviour of shear layers around coupled stationary circular cylinders has been broadly categorized as six regimes [10] depending on the separation distance between the cylinders. Experimental and numerical analysis of these regimes have been conducted by Igarashi [10] and Carmo [8]. They found that critical separation is located somewhere between  $S = 3.0 - 4.0$  which  $S$  is a separation distance between cylinders (see Figure 1) and the downstream cylinder can be significantly affected by shear layers. Considering to the regimes C and D illustrate that vortices after separation are symmetric and gradually they change as the asymmetric shear layers. Therefore, the more distance between cylinders causes asymmetric pressure distribution over the second cylinder. Assi [1] suggested that the vortex formation length of a coupled cylinder is directly dependent on the Reynolds number and it decreases by increasing the Reynolds number between 3000 and 13000. He also showed that turbulence intensity can also affect the angle of separation [2].

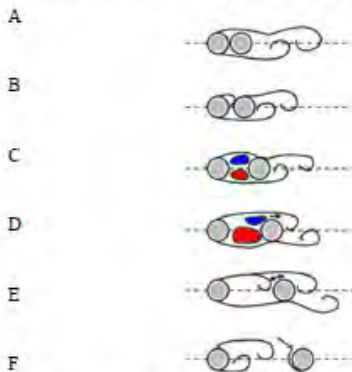


Figure 2. Patterns of flow regimes between two aligned cylinders [10]

Mixed effects of  $x_0$  and  $y_0$  (separation and lateral distance respectively) on the lift and drag coefficient of downstream body have been analysed by Bokaian et al. [7]. Their outcomes illustrate that the lateral distance to access the maximum lift coefficient is close to one diameter of the cylinder.

#### Numerical model

A numerical simulation was conducted to analyse the behaviour of the downstream elastic cylinder and to harness the energy of the vortices. The number and type of mesh elements have been selected in an iterative manner to give an accurate solution with minimal computational time. A finer mesh was incorporated near the boundary layers to capture the flow behaviour in this region in greater detail since the boundary layer flow patterns and its interaction with the free stream velocity are of major importance in this investigation. Figures 3 and 4 display the mesh for a pair of circular cylinders.

The inlet boundary and the free walls are set at  $6D$  far away from the centre of cylinders. Here  $D$  is the diameter of both cylinders and is equal to  $0.05$  m. The outlet boundary has been selected sufficiently far away from the downstream body and it is equal to  $25D$ . The separation distance between cylinders is  $S = 4D$ . The triangular mesh has been generated for flow domain as an unstructured mesh with 67,666 elements.

The location of the downstream cylinder is  $(0, 0)$  (relative to the position of the axes in Figure 1) and the location of the upstream cylinder is  $(0, 4D)$ . The natural frequency of the elastic cylinder was  $f_n = 0.3$  Hz, chosen to match the structural factors of the previous experiments [2]. The non-dimensionalised flow speed can be considered as  $V_r = U/f_n D$ . Consequently, according to the free velocity of the fluid, the reduced velocity for this simulation is  $U/f_n D = 2.0$ . It is obvious that the maximum amplitude of VIV occurs when the reduced velocity is close to  $U/f_n D$ . This means that the frequency of vortices is equal to the natural frequency of the structure.

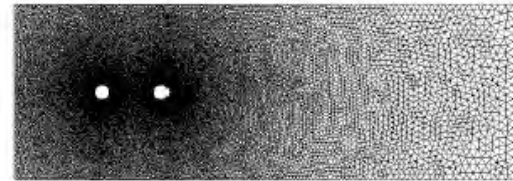


Figure 3. Triangular mesh and imposed boundary conditions of cylinders.

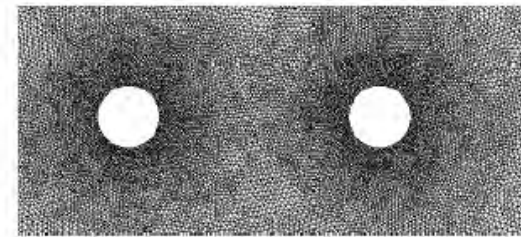


Figure 4. Unstructured fined mesh around cylinders.

The instantaneous flow field for the numerical results are shown in Figure 5. The image reflects the position of the upstream cylinder and vertical displacement of the downstream cylinder using plus sign in the centre of each cylinder.

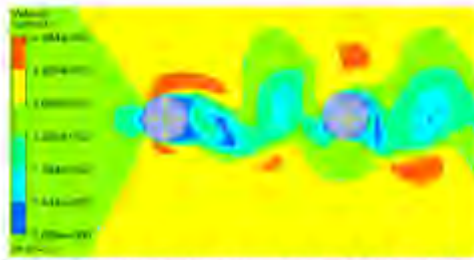


Figure 5. Instantaneous velocity contours (m/s) over two cylinders and vertical displacement of elastic downstream cylinder

**Numerical results and discussion**

The power which is produced by the elastic circular cylinder in normal direction to the fluid flow can be calculated using the velocity and lift coefficient history diagram of the downstream cylinder. Therefore, the force acting around the wet surface of the elastic cylinder ( $D$ ) can be determined using the dynamic pressure over the cylinder surface. Figures (6-a) and (6-b) show the lift coefficient history for both the stationary upstream and elastic downstream cylinders, respectively. It is clear that the exerted lift force on the elastic downstream cylinder is almost three times bigger than the lift force exerted on the stationary cylinder due to effects of the produced vortices.

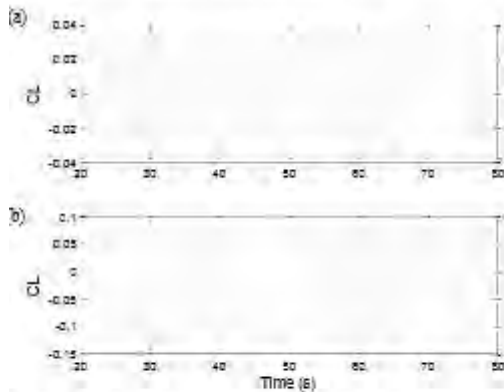


Figure 6. Lift coefficient history of cylinders: (a) stationary upstream cylinder, (b) elastic downstream cylinder.

The non-dimensionalised power can be defined as a power of VIV divided to the power of fluid [5]. Therefore, the efficiency of VIV can be written as

$$\eta_{VIV} = \frac{P_{VIV}}{P_{fluid}} \quad (7)$$

where,

$$P_{fluid} = F_y \cdot U = \frac{\rho}{2} U^3 \cdot D \cdot l \quad (8)$$

Table 1 compares the maximum amplitude of the elastic cylinder in the normal direction with available experimental data [2]. It is observed that the numerical results correspond satisfactorily with the data obtained from previous experiments.

	$Re$	$\xi$	$V_r$	$y/D$	Error
Assi (2009)	1500	4D	2.0	0.061	~6%
Present study	1500	4D	2.0	0.065	

Table1. Comparison between the numerical results and experimental data

The power of VIV can be calculated using the normal velocity and lift force of downstream cylinder for one full developed cycle. The graphs in Figure 7 show the non-dimensionalised displacement (a), velocity (b) and force (c) history of the cylinder. These graphs reveal that the phase angle between velocity and force is zero. This means that the quantity of  $\cos(\varphi)$  is maximum and it is equal to one. Hence, the power can be calculated using inner product of velocity and force. The efficiency of VIV power for one cycle of oscillation can be calculated using the Equation (7). The maximum efficiency of power for one cycle is 0.7%. Although, the value of efficiency is very small, these conditions have been selected only to validate the numerical simulation. Admittedly, by selecting appropriate parameters which involve mass ratio, damping factor, natural frequency, Reynolds number or reduced velocity and lateral distance of cylinders the extracted power can be increased. This method can be considered as a new technique for production of renewable energy which comes from ocean and shallow rivers.

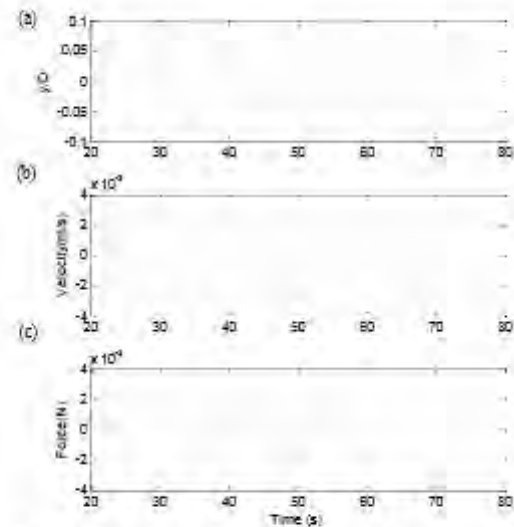


Figure 7. History of: (a) displacement, (b) velocity, (c) force for one cycle of oscillation

**Conclusions**

Two-dimensional numerical analysis of vortex induced vibration has been done to harness vortical energy which is produced from the wake of the upstream circular cylinder. Due to vortices formation, the downstream circular cylinder which is mounted on the elastic system can be oscillated perpendicular to the flow direction. This translation was modelled as a motion of simple mass-damper spring. Numerical simulation results for amplitude of oscillation have a sufficient agreement with previous experiments. The outcomes illustrate that the velocity of cylinder and normal force has the same frequency, and positive power can be generate due to this method.

**References**

[1] Assi, G., *Experimental study of the flow interference effect around aligned cylinders*, 2005, Master's thesis, University of Sao Paulo, Sao Paulo, Brazil (in

## Appendix A: Conference papers

---

- Portuguese). Available at: [www.ndf.poli.usp.br/sgassi](http://www.ndf.poli.usp.br/sgassi).
- [2] Assi, G., *Mechanisms for flow-induced vibration of interfering bluff bodies*, 2009, PhD thesis, Imperial College London, London, UK. Available at: [www.ndf.poli.usp.br/sgassi](http://www.ndf.poli.usp.br/sgassi).
- [3] Assi, G., Bearman P., and Meneghini J., *On the wake-induced vibration of tandem circular cylinders: the vortex interaction excitation mechanism*. *Journal of Fluid Mechanics*, 2010. 661(1): p. 365-401.
- [4] Bearman, P.W., *Vortex shedding from oscillating bluff bodies*. *Fluid Mechanics*, 1984. 16: p. 195-222.
- [5] Bernitsas, M.M., Raghavan K., Simon, Y. B., Garcia, E. M. H., *VIVACE (Vortex Induced Vibration Aquatic Clean Energy): A New Concept in generation of clean and renewable energy from fluid flow*. *Offshore Mechanics and Arctic Engineering*, 2008. 130. p. 1-15
- [6] Blevins, R.D., *Flow-induced vibration*. 1990.
- [7] Bokaian, A. and Geoola F., *Wake-induced galloping of two interfering circular cylinders*. *Journal of Fluid Mechanics*, 1984. 146 (1): p. 383-415.
- [8] Carmo, B.S., *Estudo numerico do escoamento ao redor de cilindros alinhados*. *Master's thesis, University of Sao Paulo, Brazil*, 2005.
- [9] Chen, S.S., *Flow-induced vibration of circular cylindrical structures*. Washington, DC, Hemisphere Publishing Corp., 1987.
- [10] Igarashi, T., *Characteristics of the flow around two circular cylinders arranged in tandem. I*. *JSME International Journal Series B*, 1981. 24: p. 323-331.
- [11] Zdravkovich, M., *Flow Around Circular Cylinders, vol. 1. Fundamentals*. *Journal of Fluid Mechanics*, 1997. 350: p. 377-378.

## Experimental and Computational Investigation of Wake-Induced Vibration

J. F. Derakhshandeh, M. Arjomandi, B. Cazzolato and B. Dally

School of Mechanical Engineering  
University of Adelaide, Adelaide, South Australia 5005, Australia

## Abstract

The use of non-turbine systems to generate hydropower energy has drawn the attention of researchers. In the current paper, Wake Induced Vibration (WIV) is experimentally and numerically studied. For this purpose, two circular cylinders were arranged in a tandem in a water channel; the upstream cylinder was fixed and the downstream one was supported by a virtual elastic base. Force and displacement measurements were conducted on the downstream cylinder in a transitional flow regime,  $Re = 2,000$ - $15,000$ . The effects of the longitudinal and lateral distances between the cylinders on the dynamic response of the WIV were investigated. It is shown that WIV can occur outside the frequency of the Vortex Induced Vibration (VIV), resulting in a higher potential of energy harnessing. The results reveal that the efficiency of power generation from WIV depends on the position of the downstream cylinder, and it is a function of the Reynolds number. In addition, Computational Fluid Dynamic (CFD) studies were performed using a Scale Adaptive Simulation (SAS) model to analyse the flow characteristics around the cylinders. The lift, displacement amplitude and frequency of oscillation calculated by the numerical modelling are in a reasonable agreement with the experimental data.

## Introduction

Increases in energy demand and global warming have motivated scholars to investigate new renewable and environmentally friendly energy generation technologies. Vortex Induced Vibrations (VIVs) is one such technology (Bernitsas and Raghavan 2004). The term of VIVs denotes to those phenomenon associated with the reaction of structures in a cross flow. There are numerous studies in the literature with a focus on the VIV phenomenon of a circular cylinder. Bernitsas *et al.* (2008) developed a converter to capture VIV energy generated from ocean currents. In their studies, the experimental and theoretical VIV efficiencies were estimated to be 22% and 37%, respectively. The response of a cylinder to VIV was modelled using a Mass-Spring-Damper (MSD) by Bearman (1984) and following his proposed model, Hover *et al.* (1997) offered the first computer model of Virtual Mass-Spring-Damper (VMSD). The VMSD system allows the operator to electronically set the desired impedance of the MSD. This facilitates the rapid examination of a wide range of experimental test cases rapidly compared to the physical MSD, which requires replacing the parts of the system to change the impedance.

Using the VMSD models opened the way for optimisation and further investigation of energy utilization. In spite of the extensive studies on VIV of a cylinder, Wake Induced Vibration (WIV) has not received similar attention, particularly to harness kinetic energy of free streams in shallow rivers or oceanic currents. In the WIV mechanism, when the downstream cylinder is displaced sideways, a lift force would act to move the cylinder towards the centreline (Zdravkovich 1977). The most comprehensive study on this field was conducted by Assi (2009), who studied the WIV mechanism of two similar cylinders and reported the dynamic response of the downstream one at a range of Reynolds number between 1,000 and 30,000. It was observed that the WIV response of the cylinder is a function of

longitudinal distance between the cylinders. In the current paper, a new design for a VMSD mechanism is presented. For this purpose, a vertically mounted cylinder in a cross-flow was utilized, as opposed to previous work, which employed a horizontally positioned cylinder. This approach eliminates the effect of weight and buoyancy forces on the drive mechanism, and consequently improves the accuracy of the data. In addition, besides the VIV effect, the WIV response of an elastic cylinder is considered for harnessing the hydrokinetic energy of the wake. In the WIV, the maximum amplitude of oscillation is not limited to the resonance frequency of the structure, which facilitates the capture of energy from the vortices outside the natural frequency of the structure.

## Experimental details

To investigate the effect of the arrangement of two circular cylinders on the efficiency of the WIV power, a series of tests were conducted in a closed-loop water channel with a test section of 2,000 mm length, 500 mm wide, and 600 mm depth at the University of Adelaide. Two cylinders with different diameters were employed. The upstream cylinder had a diameter of  $D_1 = 40$  mm and length of 600 mm and was stationary at a fixed position during the experiment. The downstream cylinder had a smaller diameter of  $D_2 = 30$  mm and length of 400 mm. This cylinder was mounted on the elastic base of the VMSD system. The longitudinal ( $x_0$ ) and lateral ( $y_0$ ) distances between the cylinders were varied as shown in figure 1. A total of sixteen arrangements of the cylinder were tested. The flow velocity was varied between 0.05 m/s and 0.37 m/s and consequently the maximum Reynolds number achieved, based on the density of water and the diameter of the upstream cylinder, was  $Re=15,000$ .

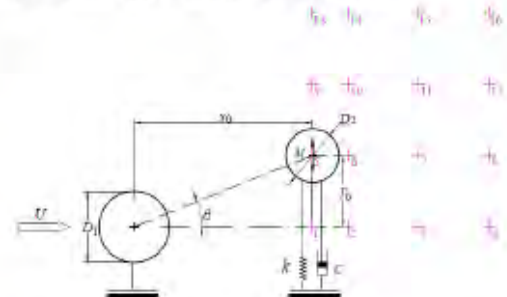


Figure 1. Schematic of the arrangements of the elastically mounted cylinder relative to the stationary upstream cylinder. Sixteen test cases are considered. (+) symbols denote the position of the centre of the downstream cylinder.

## Virtual Mass Spring damper (VMSD) and Proportional Integral Derivative (PID) control system

The VMSD used in the experiments consisted of a Maxon brushless EC-Max 30 (with 2,000 quad-count encoder) servo-motor, a gearbox of 51:1 ratio, two toothed pulleys and toothed belt which were attached to a carriage running on four linear bearings. In order to control the servo-motor a Maxon ESCON

50/5 servo controller was used. The fluidic force in normal direction to the mean flow, exerted on the downstream cylinder, was measured using two strain gauges in a half-bridge arrangement. The bridge directly measured the moment at the root of the cantilevered column, and by assuming 2D flow conditions; the lateral force was estimated. The corresponding equipment and the water channel test section are shown in figure 2. The instantaneous displacement of the downstream cylinder was measured and controlled using a Proportional-Integral-Derivative (PID) controller. The pulses generated by the embedded encoder in the Maxon motor were used for measuring the angular position of the motor shaft as well as speed (angular velocity). The position signal of the motor was used for feedback control. The angle of rotation of the shaft was converted to the real linear displacement of the carriage to which the cylinder was attached. As a result, the difference between measured oscillation of the downstream cylinder and equivalent linear displacement of the shaft was calculated as an error value. This value was defined as an input signal of the PID controller. The PID controller is tuned using Ziegler Nichols method (Astrom and Hagglund 2006).

The proportional, integral and derivative gains of PID controller set to minimize the output error of displacement to less than 1 mm. Compared with amplitude of oscillation of the cylinder, this small discrepancy was negligible.

The dSPACE software was used for the real time communication with the nonlinear PID controller and data acquisition. Despite the high flexibility of the VMSSD system, by setting various mass and damping ratios using the Simulink software, in the current study, the mass and damping ratios were kept constant in order to study the influence of the geometry and Reynolds number on the efficiency of the WIV power. In addition, to facilitate the comparison of the results with the previously published data (Assi 2009), the mass and damping ratios were kept constant at 2.4 and 0.01, respectively, and the Reynolds number was changed from 2,000 to 15,000 by adjusting the free stream velocity of the water channel.



Figure 2. Experimental setup showing the water channel, the cylinders and the VMSSD model for force and displacement measurements.

### Results and discussion

A series of force and displacement measurements were conducted in order to analyse the dynamic response of the downstream cylinder as a function of the cylinders' arrangement and the Reynolds number. In order to assess the accuracy of the VMSSD system, a similar arrangement to the previously published work of Assi (2009) was chosen and the dimensionless amplitude

of oscillation of the downstream cylinder was compared (see figure 1, Test case 3). Herein, the amplitude of oscillation is normalized by the diameter of the downstream cylinder ( $T^*$ ). As shown in figure 3, the displacement of the cylinder is in a good agreement with the published data by Assi (2009) for  $Re < 13,000$ . The small discrepancy between the data can be due to different experimental methods, and is within acceptable bounds for experimental reproducibility

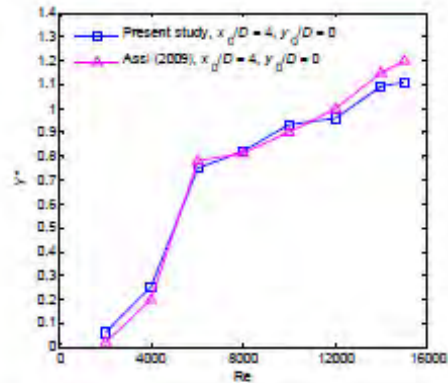


Figure 3. Comparison of the dimensionless amplitude displacement as a function of the Reynolds number with the published data by Assi (2009).

Figure 4 shows the effect of both longitudinal and lateral distances between the cylinders on the amplitude of oscillation of the downstream cylinder. As shown in the figure, the minimum and maximum displacement amplitude occur at the conditions of Test cases 1 and 11, respectively. These two test cases are marked by the lower ( $\nabla$ -) and upper ( $\Delta$ -) bounds. The amplitude of oscillation of the other test cases was found to be within these two bounds. It is observed that for lower Reynolds numbers,  $Re \leq 6,000$ , the lateral distance between cylinders has a larger effect on the displacement amplitude of the downstream cylinder, which has been not reported previously. It is also observed that with an increase in longitudinal distance between cylinders from  $x_0/D_1 = 2.5$  to 4 (Test Case 1 and 11, respectively), the displacement amplitude increases, which is agreement with Assi's work (2009), who showed that among those test cases with  $4 \leq x_0/D_1 \leq 20$ , the maximum displacement amplitude of the cylinder is achievable for  $x_0/D_1 = 4$ . The maximum displacement of the downstream cylinder was compared with the VIV response of a single cylinder in order to highlight the response of the WIV mechanism in harnessing the hydrokinetic energy. Figure 5 presents the displacement amplitudes of the VIV of a single cylinder, which referred to the initial, upper and lower branches in the literature (Williamson and Roshko 1988). Here, these responses are categorised into three zones; known as Zone 1, Zone 2 and Zone 3. In Zone 1, the WIV amplitude achieved for the staggered arrangements is higher than that of the VIV amplitude of a single cylinder. However, in Zone 2 the maximum achievable amplitude of the WIV is lower than amplitude of the VIV. It is also observed that for the staggered arrangement of the cylinders, Zone 3 shows much higher displacement amplitude compared with the one of the VIV. It is also worth noting that in Zone 3 the maximum amplitude of displacement is higher than the upper branch of the VIV response of a single cylinder in Zone 2. Thus, in contrast to the VIV, it is shown that the maximum amplitude of oscillation in the WIV is not limited to the natural frequency of the cylinder, and by increasing the Reynolds number the amplitude of oscillation increases.



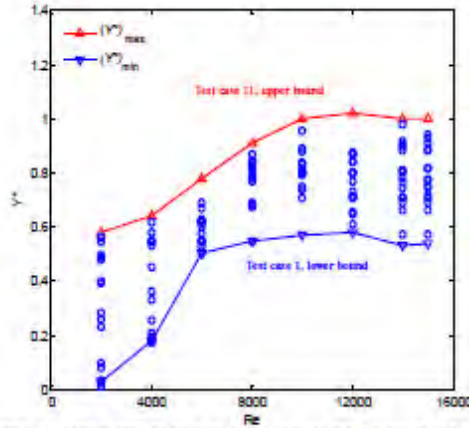


Figure 4. Scatter plot of all tests cases comprising the upper and lower bounds (Test case II and I, respectively) as a function of the Reynolds number, and the lateral and the longitudinal distances between cylinders. Circles represent different arrangements.

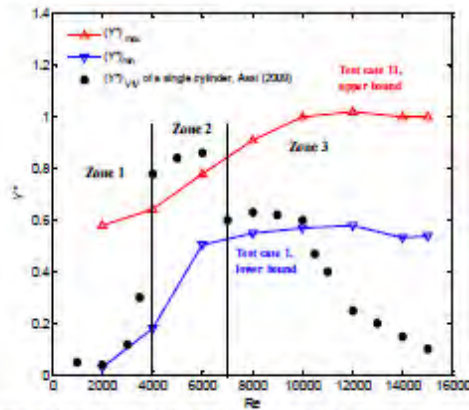


Figure 5. Comparison of the WTV response of the downstream cylinder and the WTV of a single cylinder as a function of the Reynolds number.

The fluid power was applied to compute the efficiency of the power and it can be formulated as  $P_{fluid} = FU = (\frac{1}{2})\rho U^3 D_2 L$ , therefore,

$$\eta_{WTV} = \frac{P_{WTV}}{P_{fluid}} \quad (1)$$

In above Equation  $P_{WTV}$  is the average power, which is given by

$$P_{WTV} = \frac{W_{WTV}}{T} \quad (2)$$

where,  $W_{WTV}$  is integrating the inner product of the force and the instantaneous velocity, and can be calculated over a complete cycle of oscillation ( $T$ ) as follow

$$W_{WTV} = \int_0^T F_y \dot{y} dt \quad (3)$$

In figure 6 the isolines contours of the WTV efficiency are plotted as a function of longitudinal ( $x_0/D_1$ ) and lateral ( $y_0/D_1$ ) distances between cylinders at Reynolds number 6,000. It is observed that the highest WTV efficiency of 28% is obtained for the cases in which the downstream cylinder is positioned at  $3.5 \leq x_0/D_1 \leq 4.5$  and  $1 \leq y_0/D_1 \leq 2$ .

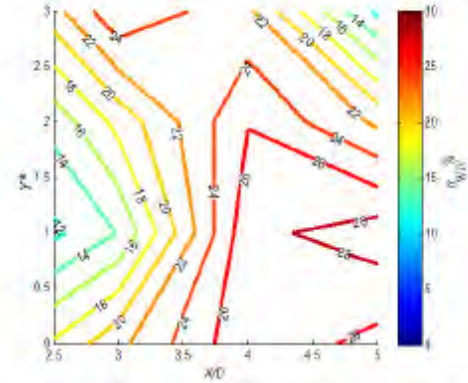


Figure 6. Effect of arrangement of the cylinders on the efficiency of WTV power ( $\eta_{WTV}$ %). Isolines contours of the WTV efficiency versus longitudinal and lateral position of the downstream cylinder at  $Re = 6000$ .

### Computational Fluid Dynamic Study

In order to investigate the flow pattern and study the characteristics of the flow, a Scale Adaptive Simulation (SAS) turbulence model was used to model a transitional flow regime over two circular cylinders. In comparison to the other turbulence models of Reynolds Average Navier Stokes (RANS) and Large Eddy Simulation (LES), the SAS model uses the von Karman length scale, which is defined as (Mentor and Egorov 2005)

$$L_{vk} = k_t \left| \frac{\partial u / \partial y}{\partial^2 u / \partial y^2} \right| \quad (4)$$

Here,  $k_t$  is the turbulent kinetic energy. The von Karman length scale enables the model to adapt its behaviour to Scale Resolving Simulation (SRS) according to the stability parameters of the flow. This allows the model to provide a balance between the contributions of the simulated and resolved parts of the turbulence stresses. The SAS model was successfully examined in the previous works by the authors (Derakhshandeh *et al.* 2014-a, and 2014-b) and its reliability for this study was demonstrated. Figure 7 shows a 2D computational domain and the structured mesh elements in the computational domain and around the cylinders.

The vortex pattern in the wake of the cylinders is shown in figure 8. It can be seen that the vortex pattern of the upstream and downstream cylinders are "2S" and "2P", respectively. The term 2S means that in each half-cycle a vortex is shed, similar to the natural Karman vortex shedding, while the term 2P highlights the formation of vortex pairs, which transfer with the flow at an angle outwards from the wake centreline. These two types of vortex patterns are known as the major vortex patterns in which the resonance or lock-in occurs compared with P or S modes of vortex patterns (Williamson and Roshko, 1988). With the 2S and 2P vortex generation modes, a synchronisation of oncoming vortices (2S) occurs with the vortices of the downstream cylinder. As a result, stronger circulation is produced which is directly proportional to the lift force acting on the downstream cylinder and causes a higher displacement. Therefore, the generated vortex pattern can considerably affect the dynamic response of the downstream cylinder when the cylinder is located in a reasonable lateral distance of the upstream cylinder.

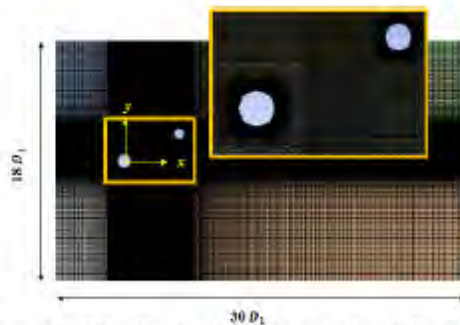


Figure 7. Quadrilateral mesh grid around two circular cylinders and the dimensions of computational domain.

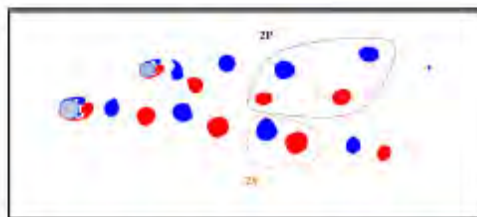


Figure 8. Contours of the vortex formation in the wake of the cylinders at  $Re = 6,000$  including vortex modes. The upstream cylinder is stationary and the downstream cylinder is elastically mounted.

### Conclusions

Experimental and numerical investigations were implemented to assess the WIV. For the experimental part, a Virtual Mass Spring Damper (VMSD) system was designed and employed. Force, displacement and frequency measurements were conducted in a closed-loop water channel using a Maxon motor and strain gauges all linked to a computer by a dSPACE control system. As the cylinders were installed vertically in the test section, the effect of gravity and buoyancy were considered negligible, hence the non-linearities observed on previous works were successfully removed. It was shown that in the VIV mechanism the upper branch of amplitude occurs at a limited range of frequencies (or reduced velocities) in which the shedding frequency is very close to the resonance frequency of the structure. However, for the staggered arrangement of the cylinders, the results show that WIV responses can occur at the frequencies outside the range in which VIV is observed. The staggered arrangement of the cylinders results in increased WIV efficiency (up to 28%) as compared to the aligned arrangement of the cylinders. The results of water channel tests also showed that of sixteen test cases the staggered arrangement with  $3.5 \leq x_0/D_1 \leq 4.5$  and  $1 \leq y_0/D_1 \leq 2$  showed the highest efficiency of the WIV power. The present experimental results showed that the Reynolds number plays an important role on the efficiency of the WIV energy. The alteration of the Reynolds number changes the upstream vortex shedding frequency which affects the phase difference of the lift and displacement of the downstream cylinder, subsequently impacting the WIV efficiency. Numerical analysis also demonstrates that for flow around two circular cylinders, when the downstream one is based on an elastic support, the mode of oncoming and downstream vortices are 2S and 2P, respectively. These modes are known as the major vortex pattern for a vibrated cylinder (Williamson and Roshko, 1988), in which the synchronisation occurs. Therefore, based on the arrangement of

the cylinders, the dynamic response of the downstream cylinder can be different.

### References

- [1] Assi, G., Mechanisms for flow-induced vibration of interfering bluff bodies. PhD thesis, Imperial College London, London, UK, 2009.
- [2] Astrom, K.J. and T. Hagghund, *Advanced PID Control*. ISA, 2006.
- [3] Bernitsas, M.M. & Raghavan, K., Converter of current/tide/wave energy. Provisional Patent Application. United States Patent and Trademark Office Serial, 2004, Serial No. 60/628,252.
- [4] Bernitsas, M.M., Raghavan, K., Ben-Simon, Y. & Garcia, E., VIVACE (Vortex Induced Vibration Aquatic Clean Energy): A new concept in generation of clean and renewable energy from fluid flow. *Journal of Offshore Mechanics and Arctic Engineering*, 2008, 130, 1-15.
- [5] Bearman, P.W., Vortex shedding from oscillating bluff bodies. *Fluid Mechanics*, 1984, 16, 195-222.
- [6] Blevins, R.D., *Flow-induced vibration*. Krieger publishing company, Malabar, Florida, USA, 1990.
- [7] Derakhshandeh, J.F., Arjomandi, M., Dally, B. & Cazzolato, B., Effect of a rigid wall on the vortex induced vibration of two staggered circular cylinders. *Journal of Renewable and Sustainable Energy*, 2014-a, 6, 033114.
- [8] Derakhshandeh, J.F., Arjomandi, M., Dally, B. & Cazzolato, B., The effect of arrangements of two circular cylinders on the maximum efficiency of Vortex-Induced Vibration power using a Scale Adaptive Simulation model. *Journal of Fluids and Structures*, 2014-b, 10.1016.
- [9] Hover, F., S. Miller, & M. Triantafyllou, Vortex-induced vibration of marine cables: Experiments using force feedback. *Journal of Fluids and Structures*, 1997, 11(3), p. 307-326.
- [10] Menter, F. & Egorov, Y., A scale-adaptive simulation model using two-equation models. 43rd AIAA Aerospace Sciences Meeting and Exhibit 1-13, 2005.
- [11] Williamson, C. & Roshko, A., Vortex formation in the wake of an oscillating cylinder. *Journal of Fluids and Structures*, 1988, 2 (4), 355-381.
- [12] Zdravkovich, M., 1st edition, *Flow Around Circular Cylinders*, vol. 1. Oxford University Press Inc., New York, 1997.



## Appendix B

### Experimental Setup and Apparatus

This section outlines a detailed of experimental setup, apparatus and system parameters used to perform the experimental tests.

Water density:

$$\rho = 1000 \text{ (kg/m}^3\text{) at } T = 20^\circ\text{C}$$

Water channel dimensions:

$$2,000 \times 650 \times 500 \text{ mm}^3$$

Mass-spring-damper parameters:

$$\text{Mass ratio: } m^* = 2.4$$

$$\text{Stiffness: } k = 50 \text{ (N/m)}$$

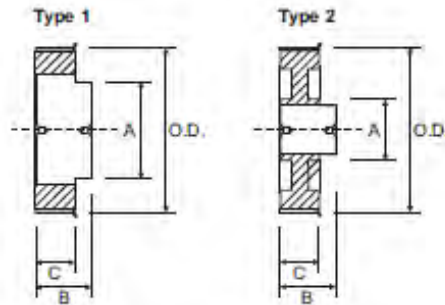
$$\text{Damping ratio: } \zeta = 0.01$$

	Diameter	Length	Material
Upstream cylinder	$D_1 = 40 \text{ (mm)}$	$L_1 = 650 \text{ (mm)}$	Aluminium
Downstream cylinder	$D_2 = 30 \text{ (mm)}$	$L_2 = 400 \text{ (mm)}$	Acrylic
Airfoil	Chord = 100 (mm)	$L_2 = 400 \text{ (mm)}$	Aluminium

# Plastic Timing Pulleys

## XL Pitch 0.200"

## L Pitch 0.375"



XL037					
Suit 9.5mm wide belt (3/8")					
Part No.	O.D.	Type	A	B	C = 13.0
PP11XL037	17.3	1	12.5	21.0	
PP12XL037	18.9	1	12.5	21.0	
PP14XL037	22.1	1	16.0	21.0	
PP15XL037	23.7	1	18.0	25.0	
PP16XL037	25.4	1	18.0	25.0	
PP18XL037	28.6	1	20.0	25.0	
PP20XL037	31.8	1	20.0	25.0	
PP21XL037	33.5	1	20.0	25.0	
PP22XL037	35.1	1	20.0	25.0	
PP24XL037	38.3	1	25.0	25.0	
PP28XL037	44.8	1	25.0	25.0	
PP30XL037	48.0	2	25.0	25.0	
PP32XL037	51.2	2	25.0	25.0	
PP36XL037	57.7	2	35.0	25.0	
PP40XL037	64.2	2	35.0	25.0	
PP42XL037	67.4	2	35.0	25.0	
PP44XL037	70.6	2	35.0	25.0	
PP48XL037	77.1	2	35.0	25.0	
PP50XL037	80.3	2	35.0	25.0	

Plastic with an Aluminium hub  
1 Flange on boss side only

L050					
Suit 12.7mm wide belt (1/2")					
Part No.	O.D.	Type	A	B	C = 17.0
PP10L050	29.6	1	20.0	25.0	
PP12L050	35.6	1	25.0	25.0	
PP14L050	41.7	1	30.0	30.0	
PP16L050	47.8	1	30.0	30.0	
PP18L050	53.8	2	30.0	30.0	
PP20L050	59.9	2	30.0	30.0	
PP22L050	65.9	2	40.0	30.0	
PP24L050	72.0	2	40.0	30.0	
PP26L050	78.1	2	40.0	30.0	
PP28L050	84.1	2	40.0	30.0	
PP30L050	90.2	2	40.0	30.0	
PP32L050	96.3	2	40.0	30.0	
PP36L050	108.4	2	50.0	40.0	
PP40L050	120.5	2	50.0	40.0	

Plastic with an Aluminium hub  
1 Flange on boss side only

L100					
Suit 25.4mm wide belt (1")					
Part No.	O.D.	Type	A	B	C = 30.0
PP10L100	29.6	1	20.0	40.0	
PP12L100	35.6	1	25.0	40.0	
PP14L100	41.7	1	30.0	40.0	
PP16L100	47.8	1	30.0	40.0	
PP18L100	53.8	1	40.0	50.0	
PP20L100	59.9	1	40.0	50.0	
PP22L100	65.9	2	40.0	50.0	
PP24L100	72.0	2	40.0	50.0	
PP26L100	78.1	2	40.0	50.0	
PP28L100	84.1	2	48.0	50.0	
PP30L100	90.2	2	48.0	50.0	
PP32L100	96.3	2	48.0	50.0	
PP36L100	108.4	2	57.0	50.0	
PP40L100	120.5	2	57.0	50.0	

Plastic with a Steel hub  
1 Flange on boss side only

## Classical Timing Belts XL, L, H & XH



	Pitch (inch)	Pitch (mm)	T	B
XL	1/5"	5.08	1.27	2.30
L	3/8"	9.53	1.91	3.50
H	1/2"	12.70	2.29	4.00
XH	7/8"	22.23	6.35	11.00

Code & Pitch	Number of Teeth	Pitch Length mm
60XL	30	152.4
70XL	35	177.8
80XL	40	203.2
90XL	45	228.6
100XL	50	254.0
110XL	55	279.4
120XL	60	304.8
130XL	65	330.2
140XL	70	355.6
150XL	75	381.0
160XL	80	406.4
170XL	85	431.8
180XL	90	457.2
190XL	95	482.6
200XL	100	508.0
210XL	105	533.4
220XL	110	558.8
230XL	115	584.2
240XL	120	609.6
250XL	125	635.0
260XL	130	660.4

Standard widths of:-  
 6.4mm (1/4") Code = Length-XL025  
 9.5mm (3/8") Code = Length-XL037  
 Off standard widths are available on request.  
 Long Length up to 12.7mm (1/2") wide is available.

Code & Pitch	Number of Teeth	Pitch Length mm
124L	33	315.0
150L	40	381.0
187L	50	475.0
210L	56	533.4
225L	60	571.5
240L	64	609.6
255L	68	647.7
270L	72	685.8
285L	76	723.9
300L	80	762.0
322L	86	817.9
345L	92	876.3
367L	98	932.2
390L	104	990.6
420L	112	1066.8
450L	120	1143.0
480L	128	1219.2
510L	136	1295.4
540L	144	1371.6
600L	160	1524.0

Standard widths of:-  
 12.7mm (1/2") Code = Length-L050  
 19.1mm (3/4") Code = Length-L075  
 25.4mm (1") Code = Length-L100  
 Off standard widths are available on request.  
 Long Length up to 25.4mm (1") wide is available.

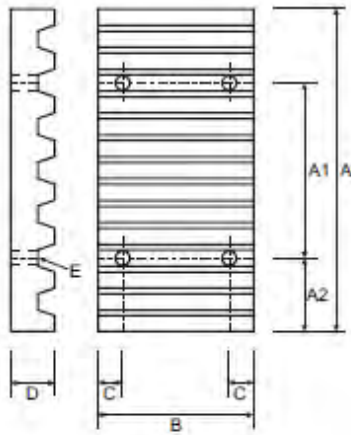
Code & Pitch	Number of Teeth	Pitch Length mm
507XH	58	1287.8
560XH	64	1422.4
630XH	72	1600.2
700XH	80	1778.0
770XH	88	1955.8
840XH	96	2133.6
980XH	112	2489.2
1120XH	128	2844.8
1260XH	144	3200.4
1400XH	160	3556.0
1540XH	176	3911.6
1750XH	200	4445.0

Standard widths of:-  
 50.8mm (2") Code = Length-XH200  
 76.2mm (3") Code = Length-XH300  
 101.6mm (4") Code = Length-XH400  
 Off standard widths are available on request.

Code & Pitch	Number of Teeth	Pitch Length mm
240H	48	609.6
270H	54	685.8
300H	60	762.0
330H	66	838.2
360H	72	914.4
390H	78	990.6
420H	84	1066.8
450H	90	1143.0
480H	96	1219.2
510H	102	1295.4
540H	108	1371.6
570H	114	1447.8
600H	120	1524.0
630H	126	1600.2
660H	132	1676.4
700H	140	1778.0
750H	150	1905.0
800H	160	2032.0
850H	170	2159.0
900H	180	2286.0
1000H	200	2540.0
1100H	220	2794.0
1250H	250	3175.0
1400H	280	3556.0
1700H	340	4318.0

Standard widths of:-  
 19.1mm (3/4") Code = Length-H075  
 25.4mm (1") Code = Length-H100  
 38.1mm (1.125") Code = Length-H150  
 50.8mm (2") Code = Length-H200  
 76.2mm (3") Code = Length-H300  
 Off standard widths are available on request.  
 Long Length up to 50.8mm (2") wide is available.

## Timing Belt Clamping Plates



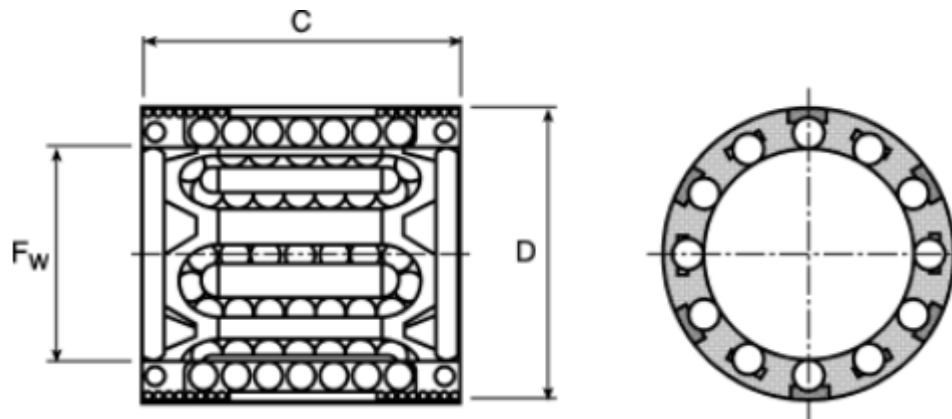
Ideal for applications where the belt must be firmly held in one spot. Perfect for use with long length belting. Naismith Engineering keep a large range of Clamp Plates on the shelf.

Classical	Part No	A	A1	A2	B	C	D	E
XL	PIA-XL025	42.5	25.4	8.6	25.4	6.0	8.0	5.5
	PIA-XL037	42.5	25.4	8.6	28.5	6.0	8.0	5.5
L	PIA-L050	76.6	47.6	14.5	39.1	8.0	15.0	9.0
	PIA-L075	76.6	47.6	14.5	45.0	8.0	15.0	9.0
	PIA-L100	76.6	47.6	14.5	51.5	8.0	15.0	9.0
H	PIA-H050	106.9	63.5	21.7	45.0	10.0	22.0	11.0
	PIA-H075	106.9	63.5	21.7	51.0	10.0	22.0	11.0
	PIA-H100	106.9	63.5	21.7	57.4	10.0	22.0	11.0

HTD	Part No	A	A1	A2	B	C	D	E
5M	PIA-5M09	41.8	25.0	8.4	28.0	6.0	8.0	5.5
	PIA-5M15	41.8	25.0	8.4	34.0	6.0	8.0	5.5
	PIA-5M25	41.8	25.0	8.4	44.0	6.0	8.0	5.5
8M	PIA-8M20	66.0	40.0	13.0	45.0	8.0	15.0	9.0
	PIA-8M30	66.0	40.0	13.0	55.0	8.0	15.0	9.0
	PIA-8M50	66.0	40.0	13.0	75.0	8.0	15.0	9.0
	PIA-8M85	66.0	40.0	13.0	110.0	8.0	15.0	9.0
14M	PIA-14M40	116.0	70.0	23.0	71.0	10.0	22.0	11.0
	PIA-14M55	116.0	70.0	23.0	86.0	10.0	22.0	11.0
	PIA-14M85	116.0	70.0	23.0	116.0	10.0	22.0	11.0
	PIA-14M115	116.0	70.0	23.0	146.0	10.0	22.0	11.0
	PIA-14M170	116.0	70.0	23.0	201.0	10.0	22.0	11.0

Metric	Part No	A	A1	A2	B	C	D	E
T5	PIA-T5/10	41.8	25.0	8.4	29.0	6.0	8.0	5.5
	PIA-T5/16	41.8	25.0	8.4	35.0	6.0	8.0	5.5
	PIA-T5/25	41.8	25.0	8.4	44.0	6.0	8.0	5.5
T10	PIA-T10/16	80.0	50.0	15.0	41.0	8.0	15.0	9.0
	PIA-T10/25	80.0	50.0	15.0	50.0	8.0	15.0	9.0
	PIA-T10/32	80.0	50.0	15.0	57.0	8.0	15.0	9.0
	PIA-T10/50	80.0	50.0	15.0	75.0	8.0	15.0	9.0
AT5	PIA-AT5/10	41.8	25.0	8.4	29.0	6.0	8.0	5.5
	PIA-AT5/16	41.8	25.0	8.4	35.0	6.0	8.0	5.5
	PIA-AT5/25	41.8	25.0	8.4	44.0	6.0	8.0	5.5
AT10	PIA-AT10/16	80.0	50.0	15.0	41.0	8.0	15.0	9.0
	PIA-AT10/25	80.0	50.0	15.0	50.0	8.0	15.0	9.0
	PIA-AT10/32	80.0	50.0	15.0	57.0	8.0	15.0	9.0
	PIA-AT10/50	80.0	50.0	15.0	75.0	8.0	15.0	9.0

## Linear bearings:



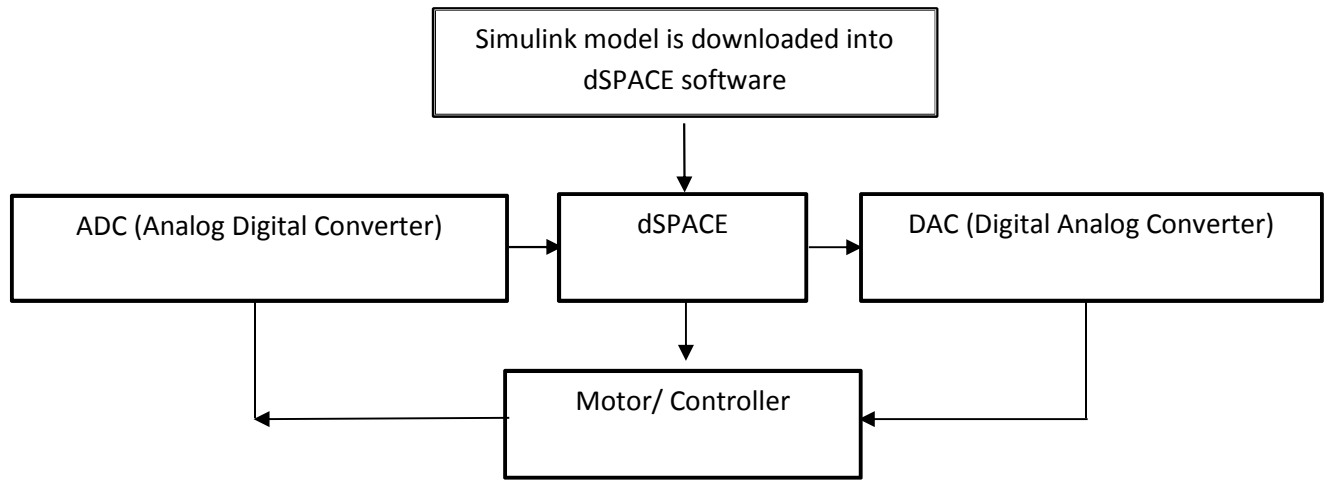
Designations	Dimensions			Basic load ratings	
	$F_w$	D	C	dynamic C	static $C_0$
	mm			N	
LBBR 3 (CAS4)*	3	7	10	60	44
LBBR 4 (CAS4)*	4	8	12	75	60
LBBR 5 (CAS4)*	5	10	15	170	129
LBBR 6A	6	12	22 <sup>1)</sup>	335	270
LBBR 8	8	15	24	490	355
LBBR 10	10	17	26	585	415
<b>LBBR 12</b>	<b>12</b>	<b>19</b>	<b>28</b>	<b>695</b>	<b>510</b>
LBBR 14	14	21	28	710	530
LBBR 16	16	24	30	930	630
LBBR 20	20	28	30	1 160	800
LBBR 25	25	35	40	2 120	1 560
LBBR 30	30	40	50	3 150	2 700
LBBR 40	40	52	60	5 500	4 500
LBBR 50	50	62	70	6 950	6 300

Example:  
LBBR 4 (CAS4)  
LBBR 20-LS  
LBBR 50-2LS

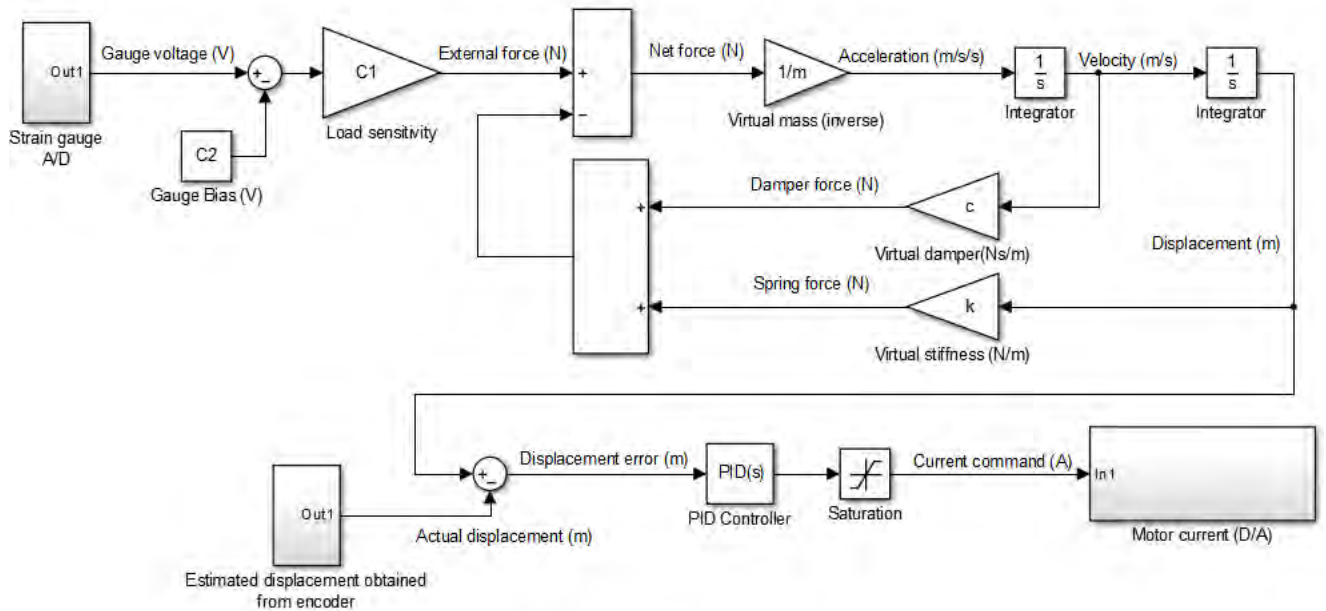
\* Without seal, 4 pieces, packed in cassette (only valid for sizes 3, 4, 5)  
<sup>1)</sup> Width 22 does not correspond to series 1 in ISO standard 10285



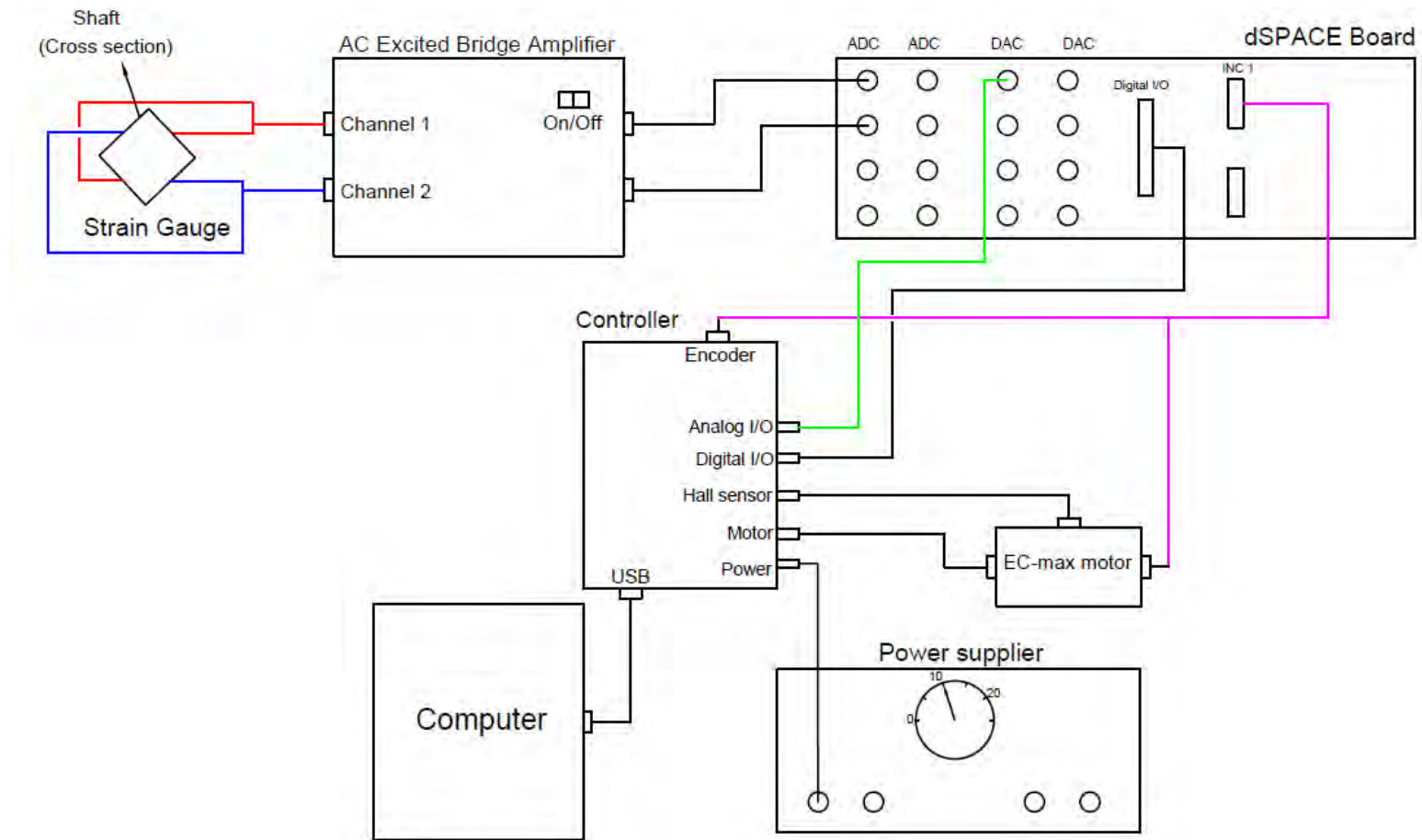
## Control system flow chart:



## Simulink model (mass-spring-damper):



## Motor and controller circuitry



## Maxon Controller technical data: ESCON 50/5 (40

ESCON 50/5 (409510)		
Electrical Rating	Nominal operating voltage $V_{CC}$	10...50 VDC
	Absolute operating voltage $V_{CC\ min} / V_{CC\ max}$	8 VDC / 56 VDC
	Output voltage (max.)	$0.98 \times V_{CC}$
	Output current $I_{cont} / I_{max}$ (<20 s)	5 A / 15 A
	Pulse Width Modulation frequency	53.6 kHz
	Sampling rate PI current controller	53.6 kHz
	Sampling rate PI speed controller	5.36 kHz
	Max. efficiency	95%
	Max. speed DC motor	limited by max. permissible speed (motor) and max. output voltage (controller)
	Max. speed EC motor	150'000 rpm (1 pole pair)
	Built-in motor choke	3 x 30 $\mu$ H; 5 A
Inputs & Outputs	Analog Input 1 Analog Input 2	resolution 12-bit; -10...+10 V; differential
	Analog Output 1 Analog Output 2	resolution 12-bit; -4...+4 V; referenced to GND
	Digital Input 1 Digital Input 2	+2.4...+36 VDC ( $R_i = 38.5\ k\Omega$ )
	Digital Input/Output 3 Digital Input/Output 4	+2.4...+36 VDC ( $R_i = 38.5\ k\Omega$ ) / max. 36 VDC ( $I_L < 500\ mA$ )
	Hall sensor signals	H1, H2, H3
	Encoder signals	A, A\, B, B\, (max. 1 MHz)
Voltage Outputs	Auxiliary output voltage	+5 VDC ( $I_L \leq 10\ mA$ )
	Hall sensor supply voltage	+5 VDC ( $I_L \leq 30\ mA$ )
	Encoder supply voltage	+5 VDC ( $I_L \leq 70\ mA$ )
Potentiometers	Potentiometer P1 (on board) Potentiometer P2 (on board)	240°; linear
Motor Connections	DC motor	+ Motor, - Motor
	EC motor	Motor winding 1, Motor winding 2, Motor winding 3
Interface	USB 2.0	full speed (12 Mbit/s)
Status Indicators	Operation	green LED
	Error	red LED

9510)

**ESCON**

**Feature Comparison Chart**




The ESCON servo controllers are small-sized, powerful 4-quadrant PWM servo controller for the highly efficient control of permanent magnet-activated DC motors.

The featured operating modes – speed control (closed loop), speed control (open loop), and current control – meet the highest requirements. The ESCON servo controllers are designed being commanded by an analog set value and features extensive analog and digital I/O functionality and are being configured via USB interface using the graphical user interface «ESCON Studio» for Windows PCs.

Legend: (✓)\* = only in use with DC Tacho or Encoder / nnnnnn = order number / O = optional

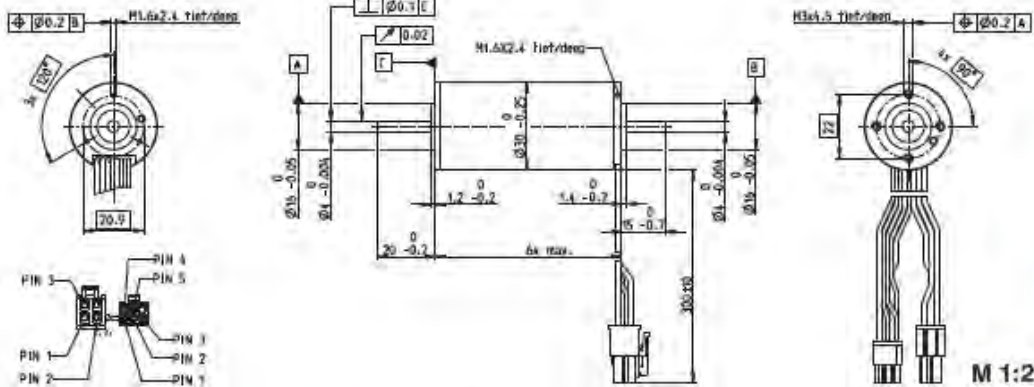


esccon@maxonmotor.com

Feature	ESCON 36/2 DC (403112)	ESCON 36/3 EC (414533)	ESCON 50/5 (409510)
Product image			
<b>Motors</b>			
DC motors up to	72 W	—	250 W
EC motors up to	—	97 W	250 W
<b>Sensors</b>			
Digital Incremental Encoder (2 channel with or without Line Driver)	✓	—	✓
DC Tacho	✓	—	✓
Without sensor (DC motors)	✓	—	✓
Digital Hall Sensors (EC motors)	—	✓	✓
<b>Electrical Data</b>			
Nominal operating voltage $V_{cc}$	10...36 VDC	10...36 VDC	10...50 VDC
Max. output voltage	$0.98 \times V_{cc}$	$0.98 \times V_{cc}$	$0.98 \times V_{cc}$
Max. output current	4 A (<60 s)	9 A (<4 s)	15 A (<20 s)
Continuous output current	2 A	2.7 A	5 A
Pulse Width Modulation frequency	53.6 kHz		

# Maxon motor:

## EC-max 30 Ø30 mm, bürstenlos, 60 Watt

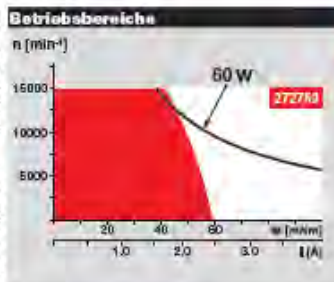


■ Lagerprogramm  
 Standardprogramm  
 Sonderprogramm (auf Anfrage)

Artikelnummern				
272762	272763	272764	272765	

Motordaten					
Werte bei Nennspannung					
1 Nennspannung	V	12	24	36	48
2 Leerlaufdrehzahl	min <sup>-1</sup>	7980	9340	9490	9350
3 Leerlaufstrom	mA	302	191	130	85.4
4 Nenndrehzahl	min <sup>-1</sup>	6590	9040	9270	8130
5 Nennmoment (max. Dauerdrehmoment)	mNm	93.6	60.7	63.7	64.1
6 Nennstrom (max. Dauerbelastungsstrom)	A	4.72	2.66	1.88	1.4
7 Anhaltmoment	mNm	381	458	522	519
8 Anlaufstrom	A	26.8	18.9	14.5	10.7
9 Max. Wirkungsgrad	%	80	81	82	82
Kerndaten					
10 Anschlusswiderstand Phase-Phase	Ω	0.447	1.27	2.48	4.49
11 Anschlussinduktivität Phase-Phase	mH	0.049	0.143	0.312	0.573
12 Drehmomentkonstante	mNm/A	14.2	24.3	35.9	48.6
13 Drehzahlkonstante	min <sup>-1</sup> /V	672	393	266	197
14 Kennliniensteigung	min <sup>-1</sup> /mNm	21.2	20.6	19.4	18.2
15 Mechanische Anlaufzeitkonstante	ms	4.86	4.73	4.21	4.17
16 Rotorträgheitsmoment	gm <sup>2</sup>	21.9	21.9	21.9	21.9

Spezifikationen	
<b>Thermische Daten</b>	
17 Therm. Widerstand Gehäuse-Luft	7.4 K/W
18 Therm. Widerstand Wicklung-Gehäuse	0.5 K/W
19 Therm. Zeitkonstante der Wicklung	2.76 s
20 Therm. Zeitkonstante des Motors	1000 s
21 Umgebungstemperatur	-40...+100°C
22 Max. Wicklungstemperatur	+155°C
<b>Mechanische Daten (vorgespannte Kugellager)</b>	
23 Grenzdrehzahl	15000 min <sup>-1</sup>
24 Axialspiel bei Axiallast < 8.0 N	0 mm
> 8.0 N	0.14 mm
25 Radialspiel	vorgespannt
26 Max. axiale Belastung (dynamisch)	5 N
27 Max. axiale Aulpreskraft (statisch) (statisch, Welle abgedübelt)	88 N
28 Max. radiale Belastung, 5 mm ab Flansch	25 N



**Legende**

■ Dauerbetriebsbereich  
 Unter Berücksichtigung der angegebenen thermischen Widerstände (Ziffer 17 und 18) und einer Umgebungstemperatur von 25°C wird bei dauernder Belastung die maximal zulässige Rotoroberfläche erreicht = thermische Grenze.

— Typenleistung  
 Kurzzeitbetrieb  
 Der Motor darf kurzzeitig und wiederkehrend überlastet werden.

Weitere Spezifikationen	
29 Polpaarzahl	1
30 Anzahl Phasen	3
31 Motorgewicht	305 g

Motordaten gemäss Tabelle sind Nennwerten.

Anschlüsse Motor (Kabel AWG 20)		
rot	Motowicklung 1	Pin 1
schwarz	Motowicklung 2	Pin 2
weiss	Motowicklung 3	Pin 3
N.C.		Pin 4

Stecker Molex	
39-01-2040	Artikelnummer

Anschlüsse Sensoren (Kabel AWG 26)		
gelb	Hall-Sensor 1	Pin 1
braun	Hall-Sensor 2	Pin 2
grau	Hall-Sensor 3	Pin 3
blau	GND	Pin 4
grün	V <sub>ref</sub> 3...24 VDC	Pin 5
N.C.		Pin 6

Stecker Molex	
430-25-0600	Artikelnummer

Schalbild für Hall-Sensoren siehe S. 33

maxon Baukastensystem		Übersicht Seite 20-25	
1 Planetengetriebe Ø32 mm 1.0 - 8.0 Nm Seite 277/279		Encoder MR 500/1000 Imp., 3 Kanal Seite 319	Encoder HEDL 5540 500 Imp., 3 Kanal Seite 329
2 Koaxdrive Ø32 mm 1.0 - 4.5 Nm Seite 281		Bremse AB 20 24 VDC, 0.1 Nm Seite 370	
3 Planetengetriebe Ø48 mm 3 - 15 Nm Seite 284		Empfohlene Elektronik: Hinweise Seite 24	
		ESCON 36/9 EC 342	
		ESCON Mod.50/4 EC-S 343	
		ESCON Module 50/5 343	
		ESCON 50/5, 70/10 344	
		DEC Module 24/2 346	
		DEC Module 50/5 346	
		EPOS2 24/5, 50/5 351	
		EPOS2 P 24/5 354	
		EPOS2 70/10 EtherCAT 357	
		MAXPOS 50/5 360	

maxon EC-max